Magnetic Studies at Low and Intermediate Temperatures

A Thesis submitted for the Degree of
Doctor of Philosophy
in the University of Oxford

Samantha J. Dawson

St.Hilda's College,
Oxford.

RADCLIFFE SCIENCE LIBRARY OXFORD
DEPOSITED
- 9 FEB 1995
THESIS

Hilary Term 1993

Magnetic Studies at Low and Intermediate Temperatures

S.J.Dawson, St Hilda's College, Oxford.
A thesis submitted for the degree of Doctor of Philosophy,
Hilary Term 1993.

ABSTRACT

This thesis contains three major areas of work.

Chapter 1 describes the various film deposition techniques available for the growth of thin films. These different growth methods, substrate preparation and vacuum techniques, are discussed in the context of the effect of the growth process and deposition environment on film structure and quality.

Chapter 2 describes the two film growth chambers.

Chapter 3 describes the origin of giant magnetoresistance (GMR) in magnetic multilayered structures, and investigates the magnetoresistive properties of ion-beam sputtered CoCu multilayered thin films. Different film structures and deposition conditions have been investigated in order to maximise the size of negative magnetoresistance seen.

Chapter 4 investigates the magnetic and giant magnetoresistive properties of sputtered CoCu and CoAg heterogenous alloys. The magnitude of the GMR effect is found to depend on the Co concentration and Co particle size.

Chapter 5 describes an investigation of molecular beam epitaxy (m.b.e.) grown Dy/Y multilayer structures. The temperature dependences of helical magnetic structure in the Dy layers is investigated in two samples of different multilayer structures.

Chapter 6 describes an acoustic interferometer which has been used to measure velocity and attenuation changes in an ultrasonic signal at frequencies of order 1GHz. Also described is the production of the thin film piezoelectric transducers used in this technique, which are grown directly onto a single crystal of the material under investigation. The acoustic interferometer is used to investigate the dynamics of of a relaxation process between two time-reversed antiferromagnetic states in DyAlG, and a model for domain growth in this system is postulated.

Chapter 7 investigates the phase diagram of $DyPO_4$ using the acoustic interferometry technique. The observations of hysteresis effects are used to define a mixed phase region below the tricritical point.

Acknowledgements

The work in this thesis was carried out under the supervision of Dr.J.F.Gregg.

I wish to thank:

Professor R.A.Cowley for extending to me the facilities of the Clarendon Laboratory.

Mr.C.R.Staddon for his help in making many of the thin films samples studied in this thesis, and for many helpful discussions.

Dr.J.S.Lord and Mr.J.Z.Pfeffer for explaining to me the fundamentals of ultrasonics and for being helpful lab-mates. I would especially like to acknowledge the computer and electronics expertise of J.S.Lord.

Professor W.P.Wolf for helpful discussions on $Dy_3Al_5O_{12}$ and for his general encouragement.

Mr.M.R.Wells and Dr.R.Ward for growing the m.b.e. samples and the X-ray analysis of several samples. I should also like to acknowledge Mr.N.Hagmann for helpful discussions.

Dr.C.Fermon for the use of the neutron beam line at C.E.A. Saclay, for his great help with the neutron experiments and for his hospitality. I would also like to thank the C.E.A. for the unlimited use of the SEM.

I should also like to acknowledge:

The Magnetic Materials Research Group at UCNW Bangor and CNRS Meudon for the use of their respective AGFMs. I should in particlular like to thank Dr.K.Ounadjela, Dr.S.Thompson and Dr.K.O'Grady.

The Department of Engineering Science for the use of their facilities to bond the thin film transducers.

The Department of Materials Science, and in particular Dr.A.Petford-Long, for the use of the TEM facilities and for the TEM photographs. Also I would like to thank Miss.M.Dellith for the supply of Si wafers.

I wish also to thank the technical staff, especially Mr.G.S.Matthews and Mr.G.Quelch for their cheerful help and advice in the Research Workshop, Mr.F.Wondre for explaining the practicalities of X-ray crystal alignment, Mr.G.Reid for optical polishing of the ultrasonic samples, Mr.T.Thompson and Mr.R.Silvester for an almost continous supply of liquid helium and conversation, Mr.T.Carter, the Photographic Unit, and Mr.K.Robinson and Mr.T.Holliday for the construction (and occasionally repair) of much of the apparatus.

Thanks to Dr.K.Atkins for his help in mastering TeX and Dr.D.A.Rabson for the loan of the book "TeX for the Impatient". I should like to thank my mother for typing much of the first draft of this thesis, and Mr.C.C.Davidson and Dr.D.A.Rabson for their great help in proof-reading.

Many thanks are also due to Mr.C.C.Davidson, Dr.M.D.Winn,
Dr.K.A.Atkins, Mr.J.Ascough, Dr.A.Burrows, Mrs.R.Winn and my parents.

Contents

1 Thin Films 8
1.1 Thin Film Deposition Methods 8
1.2 Substrate Cleaning 16
1.3 Surface Analysis Techniques 17
1.4 Surface Structural Analysis 22
1.5 Vacuum System Specifications 23
1.6 U.H.V. Techniques 25
1.7 Pumping Requirements for Sputtering Systems 27
1.8 Pressure Gauges 28
2 Thin Film Deposition Chambers 31
2.1 Introduction 31
2.2 The Large Deposition Chamber 31
2.3 The Small Sputtering Chamber 38
3 Magnetic Multilayers 41
3.1 Multilayered Structures 41
3.2 Theory of Magnetoresistance and Interlayer Exchange in Transition Metal Magnetic Multilayers 43
3.3 Sample Preparation 47
3.4 Film Deposition 48
3.5 Film Characterization Methods 51
3.6 Experimental Method 56
3.7 CoCu Multilayer MR Measurements 60
3.8 Origins of Film Anisotropy 81
3.9 Low Temperature Results 82
3.10 Possible methods of improving film quality 82
3.11 Conclusions 90
4 Heterogeneous Alloys 91
4.1 Introduction 91
4.2 Production of Alloy Films 91
4.3 Homogeneous and Heterogeneous Alloys 93
4.4 Magnetic Behaviour of Heterogeneous Alloys 95
4.5 Origin of GMR 97
4.6 Requirements for GMR in Alloys 99
4.7 Magnetometry 100
4.8 CoCu Alloys 101
4.9 CoAg Alloys 112
4.10 Magnetoresistance Measurements 118
4.11 MR as a Function of temperature 123
4.12 Conclusions 135
5 Magnetic Structure in Dy/Y Superlattices 141

5.1 Rare Earth Multilayers 141
5.2 Neutron diffraction 145
5.3 Experimental Methods 147
5.4 Experimental Results-SL13 151
5.5 Experimental Results-SL25 153
5.6 Possible Origin of the New Magnetic Structure 157
5.7 Diffraction Pattern Simulation 158
5.8 Conclusions 158
6 Microwave Ultrasonic Interferometry 160
6.1 Introduction 160
6.2 The Acoustic Interferometer 161
6.3 The Experimental Apparatus 162
6.4 Production of a Zinc Oxide Transducer 164
6.5 Dysprosium Aluminium Garnet 166
6.6 Magnetic Properties 166
6.7 Experimental Method 170
6.8 Experimental Results 172
6.9 Domain Nucleation and Growth:Theory 183
6.10 Frustrated Relaxations 188
6.11 Conclusions 193
7 Ultrasonic Investigation of $DyPO_4$ 195
7.1 Introduction 195
7.2 Measurement of Critical Behaviour 197
7.3 Dysprosium phosphate 198
7.4 Experimental Method 200
7.5 The Phase Diagram 202
7.6 The Mixed Phase 207
7.7 Conclusions 213

Figures

2.1 The Large Deposition Chamber 32

3.1 The Rotating Target 50
3.2 High Angle X-ray Diffraction 53
3.3 Low Angle X-ray Diffraction 54
3.4 SEM Micrograph 56
3.5 MR and X Measurement Circuits 58
3.6 Saturation of MR 61
3.7 Oscillations in MR 63
3.8 MR as a function of buffer layer 66
3.9 Out-of-plane Angular Dependence 68
3.10 MR and X (B$\perp$I) 71
3.11 MR and X (B$\|$I) 72
3.12 MR and X (B at 30° to I). 73
3.13 Magnetometry trace- easy direction 74
3.14 Magnetometry trace- hard direction 75
3.15 Anisotropic Magnetoresistance 78
3.16 Angular Variation of MR 79
3.17 Resistance vs temperature 83
3.18 ΔR(T) and hysteresis 84
3.19 Low Temperature Low Field Results 85
3.20 Deposition rate vs beam energy 87
3.21 MR of as-deposited and annealed sample 89

4.1 Compositional Analysis 102
4.2 Room temperature magnetometry results 104
4.3 MR as a function of distance along substrate 105
4.4 AMR 106
4.5 MR temperature dependence 108
4.6 MR at 295K and 4K 109
4.7 MR of annealed sample 111
4.8 Room temperature M-H data 113
4.9 Low temperature magnetization 115
4.10 Remanence as warmed in 4T field 117
4.11 Remanence at 4K 119
4.12 Remanence as a function of T 120
4.13 AES and MR data- CoAg alloy 122
4.14 MR as a function of T 124
4.15 MR at 294K and 4.2K 125
4.16 Position of GMR peaks as function of temperature 127

4.17 Field cycling at 4.2K 128
4.18 $\Delta(\Delta R/R)$ as function of T 129
4.19 Quadratic fit to sample 2 132
4.20 Quadratic fit to sample 1 133
4.21 Quadratic fit at 4K 134
4.22 Quadratic fit (small particles) at 4K 136
4.23 TEM photograph 138
4.24 TEM after annealing 139

5.1 A Typical Diffraction Pattern 147
5.2 SEM pictures of films 149
5.3 The Spectrometer 150
5.4 Neutron diffraction pattern-SL13 152
5.5 T-dependence of Dy turn angle 154
5.6 Diffraction pattern at 115K- SL25 155
5.7 Diffraction pattern at 139K- SL25 156
5.8 Diffraction pattern simulation 159

6.1 The acoustic interferometer 163
6.2 The ZnO transducer 165
6.3 The phase diagram 167
6.4 SEM Picture of ZnO Transducer Array 171
6.5 Relaxation from metastable state 174
6.6 Relaxation in the [111] direction 175
6.7 The angular strain distribution 177
6.8 Relaxations - [111] direction 178
6.9 Relaxations - [100] direction 179
6.10 Arrhenius plots [111] 181
6.11 Arrhenius plots [100] 182
6.12 Attenuation of ultrasonic signal 184
6.13 t^3 fits to relaxation 187
6.14 Frozen relaxation 189
6.15 The "onion skin" effect 191

7.1 Sample alignment 201
7.2 Discontinuity in ultrasonic signal 203
7.3 The phase diagram 204
7.4 Mixed phase region 205
7.5 Attenuation measurements 206
7.6 Hysteresis as a function of sweep speed 208
7.7 The mixed phase region 209
7.8 Halted sweeps 211
7.9 Halted sweeps 212

Chapter 1

Thin Films

This chapter discusses the uses and merits of a selection of the techniques available for thin film deposition and analysis.

1.1 Thin Film Deposition Methods

1.1.1 Thermal evaporation

The evaporant is directly or indirectly heated to a temperature in the region of 1000° to 2000°C causing it to evaporate and condense onto the substrate surface positioned above.

There are two widely used methods of heating,

(a) resistive heating

(b) electron-beam heating.

Resistively heated sources The substance to be evaporated is placed in a refractory metal boat which is heated resistively using a high current. Refractory metals such as W, Ta, Mo and Pt are chosen because of their high melting points and low volatility compared to the evaporants deposited in this way. In the following experiments molybdenum is used. It is obviously important that the boat does not react chemically with the evaporant and should not be volatile, so as not to lead to a chemically impure film.

The amorphous nature of the film derives from the small adatom mobility and fast deposition rate. The adatoms require enough kinetic energy to move between the various potential minima in the lattice periodic structure to find their correct lattice sites and need sufficient time in which to do so. In general films grown from substances with low melting points have larger crystallites because of their atoms' greater mobility. However the faster the deposition rate the more rapidly the atoms are trapped and the more the

time available to find their correct lattice sites is restricted. This is the advantage of a method such as molecular beam epitaxy which uses a slower rate of deposition. Generally however, the atoms arrive without enough energy to find their correct epitaxial locations and although increasing the substrate temperature may improve texture, the films remain of amorphous form.

Electron-beam heated sources The advantage of this heating method is that the evaporant surface is directly heated and therefore contamination from the boat is less probable as the highest temperature evaporant is spatially separated from it. An electron beam produced by a cathode filament is directed onto the metal evaporant which acts as the system anode. E-guns are widely used in molecular beam epitaxy (m.b.e.) for depositing high melting temperature materials and have the advantage that the material acts as its own crucible hence minimizing contamination. A further discussion of m.b.e. growth is included in Chapter 5.

In general the thermal evaporation technique is used for metals and thermally stable compounds. The advantages are rapid deposition and the ease of coating relatively uncomplicated surfaces. Film thickness can be monitored using a quartz crystal monitor. A similar deposition method is that of flash evaporation, a technique which is particularly useful for the deposition of alloys as it avoids prolonged heating which may cause fractional distillation of the constituent metals because of their varied melting points and volatilities.

1.1.2 Sputtering

Sputtering occurs when ionized gas molecules created in an electrical discharge bombard a target electrode causing its atoms to leave the surface as free atoms owing to momentum transfer from the ions. The chamber geometry is arranged such that the sputtered material is deposited onto a substrate positioned close to the target. Polycrystalline films generally result because the atoms arrive with enough energy to find their correct lattice sites and the deposition rate can be fairly slow ($\sim$ Å per second).

Sputtering can be carried out under either dc or rf conditions. In either case

sputtering rates can be improved by the use of a magnetron configuration. For the case of d.c. sputtering the single cathode, termed the target, is bombarded by positive ions and is eroded. The material liberated is deposited on the opposite electrode. The sputtering discharge can also be used specifically to etch the target itself. The disadvantage of d.c. sputtering is that cathode materials must be electrically conducting. When an electrical discharge occurs the electrons leaving the cathode move towards the anode, colliding with the gas atoms and causing ionisation. The ions then drift towards and collide with the cathode producing further electrons from the target by secondary emission. For low voltages and currents the electron multiplication is insufficient to start to a self-sustaining discharge. As the applied voltage is increased the current will increase and the discharge strikes. The voltage required to maintain the discharge once it has struck is however smaller than this, leading to a negative I-V characteristic in this region; each electron ionization must lead to at least one further electron being produced.

Consider two electrodes with an applied d.c. voltage sufficient to cause a discharge to strike. This voltage is needed for the generation of secondary electrons to maintain the glow. There is a dark space seen at the cathode and the voltage between the cathode and the anode is dropped almost entirely across this region, leaving the glow space or plasma at almost uniform potential and containing equal numbers of ions and electrons. If a low frequency field is applied then the system behaves as though it has two cathodes since a dark space appears at both electrodes. This can be considered as a succession of shortlived d.c. discharges of alternating polarity. If the frequency is increased further to above 50KHz it is found that the minimum pressure at which the discharge will operate is reduced indicating that there is an additional source of ionization other than secondary electrons from the electrodes. This source is the electrons in the glow space that oscillate in the field and make elastic collisions with gas atoms and can acquire sufficient energy to cause ionisation. Thus the high voltage electrode required in a d.c. glow discharge is no longer needed [1].

Rf magnetron sputtering deposition

Rf sputtering does not have a defined cathode as both electrodes are bombarded

by positive ions during alternate phases of the rf cycle, and can therefore be used for the deposition and etching of insulating and conducting materials. The relative ion bombardment of each electrode depends on the size of each and the bias voltage between them; these parameters can be adjusted according to whether deposition or etching is required [2]. Controlled ion bombardment of a substrate can result in enhanced film properties (see Ion beam assisted deposition). The applied field appears largely between the two electrodes and therefore if an electron is scattered out of the inter-electrode space it will no longer oscillate in the field and will be unable to cause ionization.

The required pressure for sputtering can be maintained by leaking a pure, inert gas into the chamber [3]. A typical magnetron utilizes a magnetic field to trap electrons in a region directly above the substrate. The resulting trapped electron cloud greatly increases the probability of ionization of an atom which passes through the region because of the greater electron concentration. This has the advantage that a lower background gas pressure is needed for a discharge to be maintained. A higher pumping rate can be utilized, thereby reducing contamination of the film particles which continually desorb from the vacuum chamber walls. A greater flux of positively charged ions also impinges on the target which self-biases to a negative potential giving rise to an increased sputtering rate of the target molecules.

The heavier ions pick up relatively little energy from the rf field owing to their mass. They are accelerated towards the target because the glow discharge develops an appreciable positive potential with respect to the two electrodes. This occurs because the electrons have a much higher mobility than the ions and so are easily collected on the electrode when it is positive causing a depletion of the dark space and an increase in the potential of the glow region. The size of the potential is such that the electrons in the glow space cannot leave it for most of the rf cycle, whereas the positive ions are attracted by the electrodes and reach them within a few cycles. The majority of ions reaching the target have sufficient energy to cause sputtering; the impact of the ions cause momentum transfer to atoms within the target causing some of them to travel towards the substrate where a thin film is formed.

The US Gun II radio-frequency magnetron sputtering source can be operated using either a DC power source or an rf 13.56MHz supply. The targets used should be 50.8mm in diameter and ~3mm thick. The argon pressure required is of the order of 10^{-3} to 10^{-5}torr.

The magnetic field is typically generated using two magnets. One annular magnet is situated beneath the outer edge of a circular target, whilst a small cylindrical magnet is situated below the target centre. Opposite poles are placed uppermost in order that the field lines should run from one magnet to the other. The heavier ions are relatively unaffected by the magnetic field, whilst electrons are trapped in this region. It is found experimentally that maximum sputtering occurs where flux lines lie parallel to the target surface. This results in a circular path roughly half way between the magnets covering approximately 20% of the target area where a large amount of target erosion occurs. For most metals this does not pose any specific problems, but necessitates regular target replacement. For precious metals significant financial constraints are imposed and the targets cannot simply be discarded once perforations appear. Target reprocessing is costly, time consuming, and can introduce impurities. A new design of magnetron [4] which uses a rotating field is being developed within the group which will be more cost effective for the small user. The simplest design based on this theory employs two bar magnets fixed side by side pivoted about the centre of their length. The flux lines generated run from one to the other generating a hemi- cylindrical electron cloud whose axes runs along the length of the bar magnets. This would generate a single line of erosion across the target were it not for the additional rotation of both magnets round the central pivot. Total uniformity of target erosion can be produced by increasing the field strength towards the ends of the bar magnets increasing the sputtering rate at the outer edge. Target heating will also be spread over the entire target reducing heat damage. A further interesting aspect of the design is that the rotation is provided not by a motor, but by a turbine driven by the cooling water present in all magnetrons to prevent target overheating. A rotation rate of 100 rpm is anticipated. The magnetron design is also simplified because the rf voltage signal can be carried on the two concentric water carrying

metal tubes which act as the magnetron's vertical support. Separate water and electrical connections are no longer necessary because an electrical motor is not used to provide rotation. Rf interference is not a problem. This type of magnet arrangement can easily produce a balanced magnetron arrangement as the strength of each bar magnet will in any case be approximately equal and few flux lines will escape. Unbalanced magnetrons however have important uses in cases where electron bombardment of the film during growth improves film quality.

1.1.3 Ion beam deposition

A collimated beam of ions (e.g. argon) of energy 100ev to 1000ev is produced from an ion gun and used to sputter a target, producing a beam of target material atoms which is directed towards the substrate. The main advantage of this technique is that

a good vacuum can be maintained so that a film with low gas contamination can be grown whilst still maintaining the merits of a sputter deposited film. Another advantage is that the chemical nature, incidence angle and energy of the impinging ion species is known and can be varied almost independently, and in-situ diagnostics can be used at all stages of the deposition. The ion gun used can be a broad beam or Kaufman source [5], [6] which can have a current flow of up to 10mAcm^{-2}, ion energies of up to 2000eV and a beam divergence of less than 8°.

The gas to be ionized is introduced into the rear of the ion gun chamber and the discharge is struck producing a conducting plasma composed of nearly equal numbers of electrons and ions in a background atmosphere of neutral atoms. Owing to their small mass and high velocities the electrons escape to any electrode that is positive with respect to the plasma. The magnetic field from the pole pieces, however, forces the electrons to follow long paths before reaching the anode, thus increasing the probability of ionizing collisions within the chamber. The ions that are produced are focused by the positive screen grid which is at the cathode potential. They are then extracted and accelerated through the apertures in the accelerator grid that is biased to a potential of 1000V relative to the discharge, thereby producing a directed beam of high energy ions. The

neutralizer can be placed anywhere within the area of the conducting ion beam and acts as an electron source to produce roughly equal numbers of electrons and ions. The net result of this is that an insulating or floating potential sample experiences no charging effects and can be bombarded in exactly the same way as a grounded metal target. A further advantage is that beam divergence is reduced.

1.1.4 Ion plating

Ion plating [7] is a plasma or ion activated deposition technique in which the substrate is made the cathode of a glow discharge and is therefore subjected to a flux of energetic ions and neutrals which cause appreciable sputtering before and during film formation. The material to be deposited is evaporated into the gas discharge; the evaporated atoms become ionized and are attracted to the substrate which is held at the negative potential. There are two important advantages in this process. Firstly, the collisions between the evaporant and the plasma give rise to diffusion so that all surfaces (however irregular) are covered; secondly, the ionised evaporated material arrives with higher energy than if the discharge was absent giving rise to higher adatom mobility and better film quality. A high voltage rf signal may be used instead of d.c. biasing of the substrate in order that non-metallic films can be grown.

The surface can be atomically cleaned using argon bombardment in an Ar d.c. discharge, and then without interrupting the sputtering process the coating material is evaporated from a resistively heated vaporisation source. The deposition rate must obviously be greater than the sputtering rate for a film to form.

The films produced are of good quality, being dense and non porous; this occurs due to the positive ion bombardment of the growing film increasing the average kinetic energy of the surface atoms, so that they can move into the correct crystallographic sites, removing contaminant gas atoms and giving better film adhesion [8]. The advantage of this method is the fact that good quality films can be produced quickly. the speed of deposition being limited only by the evaporation rate of the material to be deposited. The main contribution to film contamination is from discharge gas atoms. a problem

arising from the fact that the deposition pressure is approximately 25×10^{-3} torr .

1.1.5 Ion beam assisted deposition

Ion beam bombardment of the film during growth can be used to modify the physical and chemical properties of thin films and can be used in conjunction with all of the above methods. The two most common methods involve

(a) the use of a broad- beam ion source directed at the substrate in conjunction with an evaporation deposition process and

(b) dual beam ion deposition.

With the latter method one ion beam is used to sputter atoms from a target to produce a beam of sputtered atoms to be deposited on the substrate whilst the other beam is directed at the substrate surface. The two sources operate at sufficiently low flux that there is little interaction between them even though their paths may cross.

Physical changes occur because the incident energetic particles in the bombarding ion beam contribute energy and momentum to change irreversibly the nature of the film. Changes in film density and stress, in the modification of the lattice constants and degree of orientation of the grains[6] are seen. It has been observed [9] that the ion bombardment of a copper film gave rise to reduced grain size.

Chemical changes can also be induced in the film; incident ions may be incorporated into the film or compounds may be formed. The film can be made with better adhesion to the substrate, wide variations in stoichiometry are possible and metastable compounds, which cannot be produced by conventional methods, can be formed. This method can favourably modify properties of the thin film including film density, stress, degree and direction of orientation, and grain size [6]. The incident beam contributes some of its energy and momentum to change irreversibly the structure of the film surface. Chemical changes can be induced; for example compounds may be formed or the incident gas ions may be incorporated into the film thus changing its nature. Such effects are often not able to be duplicated by simply raising the film temperature. This is because the spatial extent of the impact of the incident particles is small and the effects

are localized with the subsequent events occurring quickly after impact. An example of reactive deposition is the use of low energy oxygen ions (ie less than 200eV) to bombard a resistively evaporated film of copper, producing a Cu-O compounds including CuO, Cu_2O and a new metastable compound Cu_5O_4 [9]. The chief advantage of ion beam bombardment during film growth is that by careful selection of ion energy, flux and species a high degree of control over the local energy and chemical constitution of the film is possible.

1.2 Substrate Cleaning

The hardest and most adherent coatings can be deposited onto a substrate that is free from contaminants, such as grease or adsorbed layers. Electrically insulating materials cause particular problems as surface electrostatic charges can build up and small particles are powerfully attracted to the surface and lead to holes in the deposited film. A problem also arises if moisture (or in the case of plastics, plasticizer) remains incompletely degassed when deposition occurs. The deposition itself results in a heating effect due to energy transfer to the substrate and can lead to an increase in vapour liberation and hence a poorly adherent film.

1.2.1 Chemical methods

Chemical methods can be used for initial cleaning of a surface. Solvents can be used to remove traces of grease and other materials at a macroscopic level. In our experiments Genklene is used to remove oil or grease, followed by acetone or a solution of the alkali industrial detergent, Decon, in distilled water. From this point in time, the surface should be carefully handled using gloves or tweezers. Of course any surface exposed to the atmosphere quickly becomes contaminated by adsorbed atoms or molecules including water. These however can be easily removed by either baking under vacuum or by ion bombardment. Another cleaning method involves the use of ultrasonic vibration whilst the substrate is soaked in a solvent or acid/alkali bath.

1.2.2 Ion bombardment

This method uses a high voltage glow discharge between metal electrodes in a continuously pumped vacuum vessel. Initially a rise in pressure is observed as the adsorbed gas molecules are rapidly removed from the vacuum chamber inner surfaces under ion bombardment. As this process is continued the pressure falls as the gases are pumped away; a fast pumping rate is needed in order to prevent significant readsorption on collision of the gas molecules with the walls.

The electrons in the glow discharge have much smaller masses than the positive ions and therefore have a greater mobility. Thus the vacuum chamber walls and other surfaces develop a negative potential with respect to the discharge, causing these surfaces to be bombarded by positive ions. Glow discharge cleaning is generally effective in removing surface contaminants such as grease that remain untouched by baking, because the energy is transferred directly to the contaminants themselves. Baking can lead to the formation of compounds that are difficult or impossible to remove.

In all cases deposition must quickly follow cleaning to prevent significant contaminant adsorption from occurring. Other problems occuring during d.c. glow discharge include contamination of the substrate surface by material sputtered from nearby dark space shielding [10]. The amount of contamination by this mechanism is related to the electrical potential of the shielding and is therefore minimized for grounded shields.

A further type of cleaning utilizes rf sputtering, which is again useful for non-conducting substrates. Ion beam cleaning also works on the bombardment theory and involves the use of accelerated argon ions to etch the surface.

1.3 Surface Analysis Techniques

Many surface techniques involve the detection of electrons emitted or scattered from the surface. The surface sensitivity is derived from the fact that electrons in the energy range 5eV to 2000eV have large inelastic scattering cross-sections. Thus any detected electrons with unchanged energies (ie that have been elastically scattered) are therefore derived from a thin surface layer. The techniques are thus surface-specific.

1.3.1 Investigation of the Surface Chemical Constitution

The most common methods of surface chemical analysis use electron spectroscopy. When a surface is bombarded by photons or electrons, the energies of the electrons emitted are characteristic of particular combinations of energy levels of the constituent atoms and of particular chemical states of the surface which can be identified by comparison with theoretical or experimental values. Such methods include Auger electron spectroscopy, XPS and UPS which will now be described.

Types of electron analyser The following types of analyser are the most common and have different resolving powers and sensitivities and are therefore useful in different situations,

(a) retarding potential analyser (RPA)

(b) cylindrical mirror analyser (CMA)

(c) cylindrical hemispherical analyser (CHA)

(d) magnetic double focusing spectrometer

The resolving power, ρ ,is given by

$$\rho = \frac{E}{\Delta E_A} \tag{1.1}$$

where ΔE_A equals the spread of energies passed by the analyser.

The most common analyser in use is the RPA as this is also available as part of the electron optics of a LEED system; it can be used for identification of elements present and for simple quantitative studies. The cylindrical mirror analyser is also commonly used and has good resolving power. It has a high collection efficiency (as it may be placed close to the sample), togther with a reasonable physical size and fast data collection. It is therefore more widely used than the latter two analysers which are more beneficial for detailed electron spectral analysis. The CMA consists of two concentric cylinders which for any given potential difference will only pass electrons of a certain energy, which will then be focused on the collector.

1.3.2 Auger electron spectroscopy (AES)

The Auger process occurs when a core level atomic electron is ionized, and an electron from a higher energy level E_B relaxes into the hole; the excess energy is passed to another electron from energy level E_C which is ejected taking with it a well defined kinetic energy,

$$K.E. \simeq E_A - E_B - E_C \tag{1.2}$$

which is characteristic of the particular species and is sensitive to its chemical state. The core electron is bound by a large amount of energy E_A and as such this mechanism for energy release is an alternative to X-ray emission.

The electron energies can be analysed either using a CMA or RPA as part of a LEED system. When a CMA is used (with preretardation grids) the energy spectrum is found by sweeping the voltage on the outer cylinder, V, and hence varying the passed energy, E.

$$\frac{\Delta E}{E} = const$$

$$\Delta E \propto E_0$$

Thus for an input N(E), the output is EN(E).

Alternatively, using an RPA the measured current is

$$I = \int_{E_0}^{\infty} N(E)dE = \int_{E_0}^{E_P} N(E)dE \tag{1.3}$$

where E_P is the primary beam energy.

Consider now the measurement of a current arriving at the collector with a retarding voltage V_0 and $V_0 + \Delta$V. Thus the difference between the two currents is given by

$$\int_{E_0}^{E_0+\Delta E} N(E)dE$$

where ΔE = eΔV =ΔE N(E), for small ΔE. The difference is therefore proportional to the energy distribution as required.

We can therefore see that the resolution, ΔE, decreases with ΔV whilst the signal N(E)ΔE increases by the same ratio. The resolution ($\sim$1eV) is limited by the non-spherical nature of the grids and field penetration between them destroying the system s

radial geometry. This method has a poor signal to noise ratio. There is a constant background signal due largely to secondary electron emission from underlying atoms which may be able to able to ionize surface atoms. This background noise carries no information about the type of atoms involved and can be an order of magnitude larger than the signal that is to be observed.

An improvement can be made by applying a modulating voltage, $\Delta V \sin\omega t$. In Auger electron spectroscopy the second harmonic of the current, $\sin(2\omega t)$, is measured using a phase sensitive detector which is referenced by a frequency doubled signal. The amplitude of this signal is found, using a Taylor series expansion, to be given by

$$A_2 = \Delta E^2 / 4.\mathrm{N}'(E_0) + \ldots$$

Thus it is the differential of the energy distribution that is measured; this differentiation has the effect of removing the constant background and also produces a more easily observable peak.

AES is a useful technique for surface analysis, providing an indication of chemical composition and in particular surface cleanliness. This sensitivity is derived from the fact that there is a high probability of Auger electron emission. For a K-shell hole in an atom with Z less than 20, Auger emission is more likely than X-ray decay, and for atoms with Z less than 15 it is the sole process. For electrons of energy less than 1000eV the AE process dominates for most values of Z for energy levels higher than K. In order to obtain the greatest sensitivity the incident electron beam should strike the surface at a grazing angle; a typical sensitivity is 1% of an atomic layer.

1.3.3 XPS and UPS

X-ray photon spectroscopy (XPS) and ultraviolet photon spectroscopy (UPS) involve the ejection of an electron of binding energy E_B with kinetic energy E_K by an incident photon with a large enough energy, $h\nu$. E_K can be measured using an analyser and so if the incident photon energy is known the binding energy can be found.

$$E_K = h\nu - E_B \qquad [1.4]$$

The two methods use different sources of very different energies. UPS uses a

helium discharge lamp which can operate at 21.2eV and 40.8eV; these energies are capable of ionizing valence bands. XPS uses an X-ray tube as a source with Al or Mg rods producing photons of energies 1487eV and 1254eV which are capable of ionizing core levels.

The width of the observed signal in each case depends on

(a) the intrinsic width of the level from which the electron is ejected

(b) the bandwidth of the incident radiation.

(c) the bandpass width (or window), ΔE_A of the analyser.

The dominating factor in the case of UPS is the bandpass, 0.1eV, the bandwidth of the radiation being ~1meV. For XPS the bandwidth of the incident radiation is 1-1.4eV and is thus the limiting factor, unless a monochromator is used. The detector must have a high collection rate as few photons are produced and the lines seen are of low intensity.

The spectra produced by these two methods are of the same general form, but UPS produces a more detailed spectrum not only because of the greater energy resolution but because UPS is a low energy process and the electrons produced have larger scattering cross-sections. The inelastic collisions also involve production of phonons and other excitations. The spectra of XPS show lines due to core levels of width ~1.3eV, whereas conduction band levels can be up to 10eV wide. Bonding information can be obtained using either method by studying the changing shape of the spectra as the surface species are added.

In general the atoms can be identified by comparing the results with calculated or experimentally derived standard spectra. The binding energy is however difficult to calculate as the atomic wave-functions appear to relax before the electron has left the atom.

1.3.4 Comparison of AES and XPS techniques

AES and XPS are the most common surface analysis techniques involving electron spectroscopy and have nearly uniform sensitivity to surface species (except for the light nuclei

H,He). However AES has the greatest spatial resolution.It uses an intense electron beam making it faster and more sensitive than XPS, owing to the electrons larger excitation cross-section and the ease of producing an intense beam. AES is therefore a useful process for routine checking of inhomogeneous surfaces, as long as the intensity of the electron beam causes no surface damage.

XPS on the other hand has a poor spatial resolution but is better for determining the exact chemical nature of fairly homogeneous films. The resolution can be slightly improved by using an X-ray monochromator. Although the techniques described above are particularly useful for quantitative analysis of surface layers, the peak height gives only an approximate value for film depth. Other techniques must be employed to discover the topography and distribution; these include secondary ion mass spectroscopy (SIMS) and the use of an atom probe.

1.4 Surface Structural Analysis

The techniques used to investigate surface structure can give information about

(a) the symmetry of the surface unit cell,

(b) the atomic positions within that cell.

The symmetry, size and shape of the unit cell can be found by using X-ray, neutron and electron scattering from a single crystal, and also, in the case of X-rays, a fine powder. Neutrons are particularly useful for investigating magnetic systems via their spin interaction with the sample magnetism. The size of the surface unit mesh can be determined to 1 part in 10^3.

By comparing the intensity of the diffracted beams with calculated values, the location of an atom within the unit cell can be determined. This is made more difficult by the effects of multiple scattering, especially in the case of LEED.

1.4.1 LEED and RHEED

Low energy electron diffraction (LEED) and reflection high energy electron diffraction (RHEED) are the most common methods of surface structural analysis, and

involve the detection of elastically scattered electrons from the surface which form a diffraction pattern, a map of the structure in reciprocal space.

LEED provides a simple convenient method of determining surface long-range order, using low energy electrons (ie less than 1000eV) which are incident normally upon the surface. For electrons in this energy range surface effects are most important as they have a short inelastic mean free path, and the structure is revealed from their diffraction pattern as λ is of the order of the atomic spacing.

In contrast the electrons used in RHEED have longer inelastic mean free paths, but are incident at nearly grazing angles. This is important for two reasons;

(a) the penetration depth achieved is small despite the high electron energy

(b) the apparent wavelength of the electrons increases and so is of the order of the periodic spacing of the surface atoms.

This is necessary because

$$E = \frac{hc}{\lambda} \tag{1.5}$$

spacing must be of the same order magnitude as the wavelength for diffraction to occur. The form of a RHEED diffraction pattern can also provide information about the topography of the surface. For example a smooth surface gives rise to streaks, whereas a rough surface tends to give a pattern composed of spots more reminiscent of the three dimensional bulk object.

1.5 Vacuum System Specifications

A typical vacuum system consists of a vacuum chamber, a pumping system and a set of pressure gauges to monitor pressure in several parts of the system. Any system will contain leaks, however small, and will be subject to outgassing from components within the system as the pressure falls. The pumping rate decreases as the pressure falls. The base pressure occurs when the pumping rate equals the leak rate into the chamber. The effective pumping speed of a system is almost always less than the pumping speed as determined under test. This shortfall is due to the impedance of the connecting tube.

and can be shown as follows.

Consider the pumping speed at the inlet port, S and the conductance of the tubing, U, between the pump and the vacuum chamber. S_E the effective pumping speed is given by,

$$\frac{1}{S_E} = \frac{1}{S} + \frac{1}{U} \tag{1.6}$$

$$S_E = \frac{SU}{S+U} \tag{1.7}$$

For the fastest pumping speed S >> U and S_E = U. The pumping speed is therefore limited by the rate at which the gas can flow through the connecting tubing. This rate is maximized for a wide short pipe.

The pumping system in general consists of a rotary pump which is initially used to pump down the chamber to $\sim 10 \times 10^{-2}$ torr and then to back a pump capable of reaching pressures of 10×10^{-7}torr and lower such as an ion or diffusion pump. The rotary pump is connected in series with the diffusion pump and pumps away the gas expelled at the diffusion pump outlet.

1.5.1 Types of pump

Rotary pump The rotary pump works by a rotating vane sweeping inside a metal container so that the two surfaces are nearly in contact. The air intake is connected to a volume that increases as the vane rotates allowing the gases into a volume that becomes sealed and then finally decreases in size compressing the gas and forcing it out through a sprung valve into oil.

The vane rotates at 300-700 r.p.m. and can pump typically 60 litres of gas per second at atmospheric pressure, which decreases to zero at 10×10^{-2} torr slowing significantly below 1 torr. There are leaks in the system due to the fact that the two metal surfaces can never fit perfectly as there has to be a finite clearance so that the blade can rotate fast enough.

Roots pump The Roots pump works on a similar principle to the rotary pump, except for the fact that there are two perfectly fitting rotor blades that rotate in opposite

directions squeezing the air through the pump. A pump of this type can handle large quantities of gas between 1×10^{-3} and 1 torr, and is therefore useful on an industrial scale pumping up to 200,000 litres per minute.

Diffusion pump The diffusion pump is the most common type of vapour pump; in such a pump a stream of vapour above heated oil flows from the base of the pump upwards and out of a jet pointing in a downwards direction. The gas molecules at the inlet are subjected to this jet of vapour molecules and on collision the momentum of the vapour molecules tends to drag the gas molecules downwards in the direction of the outlet to a rotary pump connected in series with the diffusion pump which provides the backing pressure for the diffusion pump. An actual diffusion pump is made up of several cascaded jet stages, each stage operating at a successively lower pressure.

A typical diffusion pump works in the pressure range 10^{-2} to 10^{-7} torr with the help of a cold trap (e.g. a liquid nitrogen trap) which condenses out water vapour and backstreaming oil or mercury depending on the pump type. The limiting factor in the low pressure region is the effect of backstreaming which involves small numbers of molecules of diffusion oil travelling in the wrong direction from the top jet and entering the vacuum chamber. This effect can be caused by bad jet design leading to turbulence effects or by collisions of the vapour molecules with gas molecules in the stream that have large velocities in the direction of the vacuum chamber (again possibly owing to turbulence). Backstreaming can generally be prevented by using a baffle in front of the inlet, which may be water cooled. The oil vapour then condenses on the baffle and is allowed to flow back down in a direction towards the walls of the pump away from the main jet stream. Use of a baffle will, however, reduce the pumping speed.

1.6 U.H.V. Techniques

Ultra high vacuum (UHV) techniques for reaching pressures below 10^{-10}torr have special requirements. Below 10^{-7}torr standard vacuum system components such as rubber, grease, mild steel or brass cannot be used because of their out-gassing factors.

Instead materials such as stainless steel or copper must be used. Glass can be degassed by baking and metals by electron bombardment or induction heating. Getter ion and turbomolecular pumps can be used to obtain pressures below 10^{-7}torr.

Ion, Getter-Ion and Sorption Pumps

An ion pump is a vacuum pump which utilizes an electric or magnetic field to transport ionized gas molecules in a direction in which they can be removed by either sorption or by being directed towards a second pump. A gettering pump is one with a continuously or intermittently renewable sorbent surface, which reduces the partial gas pressures by adsorption, absorption or chemisorption of contaminant gases present. The main advantage of these types of pump is that a lower pressure can theoretically be obtained because there is no chamber contamination due to oil vapour backstreaming. Such pumps are therefore sometimes known as "clean" pumps.

One of the most widely used getter-ion pumps is the titanium pump, which can obtain pressures of 10^{-10}-10^{-12}torr. The method of operation of a titanium pump initially requires the use of a standard pumping system to reduce the chamber pressure, for example a mechanical rotary pump and a diffusion pump plus a cold trap . The system is then baked, typically at 300° for six hours, and on cooling, the pumps are isolated from the chamber. Titanium wire is then fed onto a graphite post heated by electron bombardment to a temperature of 2000°. A typical quantity of titanium used is 10 to 20mg per minute.

Two types of gettering occur. Dispersal gettering arises from sorption during evaporation, whilst contact gettering occurs when atoms arrive at the walls and are adsorbed, absorbed or chemisorbed and embedded by subsequent layers of Ti. Chemisorption occurs for the cases of N_2, O_2, CO and CO_2 and stable low vapour pressure solids are formed. Inert gas ions are not gettered, but small amounts may be trapped under a fresh layer of Ti.

Electrons from the electron source used to heat the graphite rod are also used to ionize gas molecules, and then a grid held at 1000V is used to provide an accelerating potential for the positive ions formed on collision with these electrons. Thus singly

charged ions arrive at the wall with a maximum kinetic energy of 1000eV helping their sorption onto the Ti film.

Turbomolecular Pumps

Rotating blades impart an impulse to the gas molecules in the direction of the backing port. The advantage of this pump type is low hydrocarbon contamination, the wide range of working pressures and UHV base pressure.

No oil is required either as a lubricant as for a rotary pump or as the pumping mechanism as for a diffusion pump. The pumps also have a high compression ratio for heavy hydrocarbons. These factors are the main reason for the importance of the turbo pump in the production of a hydrocarbon free environment.

The pump is connected directly to the vacuum chamber via a large flange so there is no decrease in throughput. The turbine blades are attached to a stator and rotor. The rotor shaft is dynamically balanced to reduce vibration and is driven by a motor to run at rotational speeds of upwards of 25000 rpm. The motor is internal to the pump and means that no unnecessary connections to atmosphere are needed.

The upper blades are of large radial dimension and are used as a vacuum stage to suck the molecules into the compression stage compound of smaller blades. The backing port is pumped by a 2 stage rotary pump. Magneto-bearing turbo pumps are magnetically suspended using electromagnets which lift and stabilize the rotor. No lubrication is needed and an entirely hydrocarbon free pump can therefore be produced.

Turbomolecular pumps can be used over the entire pressure range down to 10^{-11}torr provided UHV methodologies are followed. Blade rotational speed decreases above 10^{-2}torr owing to the threshold of laminar viscous flow in this pressure region. At the lowest pressure the residual gas is largely H_2 which originates from the chambers' metal walls. Under test conditions water is the next most significant contaminant and molecular masses of greater than 44 were not seen [11].

1.7 Pumping Requirements for Sputtering Systems

The pumping requirements for sputtering include some apparently contradictory factors. Films require conditions of high vacuum cleanliness yet are grown in a gas discharge at a pressure in the range 10-20 mTorr. Initially leaks in the system must be minimized and the chamber can be baked at $\sim 200°$ to help the out-gassing process. The pumping system must operate at a high through-put in order to reduce backstreaming and to flush out the system. This, however, may cause turbulence and jet instabilities which can again lead to backstreaming and lack of pressure control, causing the pumping action to stop. The gas pressure can be kept at the required 10mTorr by leaking an inert gas into the system which will not react with contaminants in the system and by controlling the pumping rate by varying the baffle valve on the pump inlet.

The so-called clean pumps do not have a high enough throughput for noble gases to be of use in maintaining low pressures. However they can be used instead of the baking period to initially reach low pressure, followed by the use of a diffusion pump designed to have minimum backstreaming at the working pressure to reduce oil contamination [12].

1.8 Pressure Gauges

1.8.1 Penning gauge

The Penning gauge is a type of cold cathode ionization gauge useful in the pressure range $10^{-2} - 10^{-6}$ torr. The gauge consists of two plate cathodes 1 inch apart but electrically connected with a ring shaped anode in between situated in a glass tube connected via a thin tube to the chamber; 2kV p.d. is maintained across them. Permanent magnets positioned outside the tube above and below the cathode provides a 0.04T field perpendicular to the electrode plane. Electrons originate at the cathodes as a result of collisions by the positive ions, and are constrained by the magnetic field to pass through the anode. Electrons travelling in non-normal directions undergo helical motion, increasing the probability of ionization of the gas molecules until they eventually collide with the anode. The μA current produced is linearly related to the pressure in the range $10^{-3}$to 10^{-5}torr.

1.8.2 The Pirani gauge

This is a hot wire gauge which utilises the variation in the thermal conductivity of the gas with pressure in the range 10^{+2} to 10^{-4}torr. A wire filament is mounted in a glass envelope and heated by an electric current. This wire is placed in one arm of a Wheatstone bridge and a constant p.d. maintained across the bridge. The thermal conductivity of the gas increases with the number of gas molecules present and so therefore does the resistivity of the wire situated within the gas, as the greater thermal conductivity of the gas causes the equlibrium wire temperature to fall. The change in off-balance current can therefore be taken to be a measure of the pressure change. The temperature of the wire is also dependent on radiation and conduction down the wire itself. However these processes have a negligible effect when compared to the thermal conductivity of the gas atoms. A lower limit to the useful operating pressure range of this gauge occurs when the mean free path of the gas molecules becomes comparable with the dimensions of the glass vessel and thus is no longer pressure dependent.

1.8.3 The Ion gauge

A generalised ion gauge consists of a three electrode tube containing a thermionic filament cathode that emits electrons which are then accelerated towards an electron grid held at +200V. Positive ions are produced by the collisions of these electrons with residual gas atoms, and these ions are collected at an electrode (the ion collector). The ion current recorded is dependent on the pressure as described by the expression,

$$\mathrm{I}_{+} = S.p.\mathrm{I}_{-} \tag{1.8}$$

where

I_{-}=electron current

p=pressure

I_{+}=ion current

S=the sensitivity of the gauge which is dependent on the design and geometrical factors involved.

The low pressure limit arises from X-rays produced by electrons of energy greater than 150eV. These X-rays cause photoelectrons to be produced at the ion collector resulting in a current I_X which cannot be distinguished from I_+. At 10^{-8} torr these two currents are of equal magnitude and so the collector current is thus effectively pressure independent.

The **Bayard-Alpert** gauge is a refinement of the ion gauge by which pressures of 10^{-10} torr and below can be measured. This is achieved by altering the geometry of the gauge to give a structure factor such that only 1% of the produced X-rays are detected. In this case the ion collector is a narrow axial wire in the centre of the tube surrounded by the accelerating grid, with several thermionic filaments situated outside.

1.8.4 Residual Gas Analysis

One of the most common methods of residual gas analysis involves the use of a mass spectrometer. Atoms are ionized and the ions are then sorted according to their mass/charge ratio and then detected, the relative amount of each constituent being related to the measured ionization current.

There are two methods of separating different mass/charge (m/q) ratios in current use:

(1) Ions are passed through a electric or magnetic field in which the deflection of their trajectories depends on m/q. This has the advantage that only ions with the selected m/q ratio are collected. A typical piece of apparatus using an electric field is the quadrupole mass spectrometer.

(2) All ions follow the same path and their time to travel a set distance is measured. This travel time is related to the m/q ratio.

Chapter 2

Thin Film Deposition Chambers

2.1 Introduction

Two deposition chambers have been constructed. The original chamber was designed specifically to produce small batches of identical ZnO transducers. The larger chamber is a multi- deposition system and can produce up to eight different samples in one deposition session.

2.2 The Large Deposition Chamber

The sputtering chamber is a multi-gun facility with the capability for deposition using the techniques of

(a) thermal evaporation,

(b) rf magnetron sputtering,

(c) ion-beam deposition,

(d) ion plating,

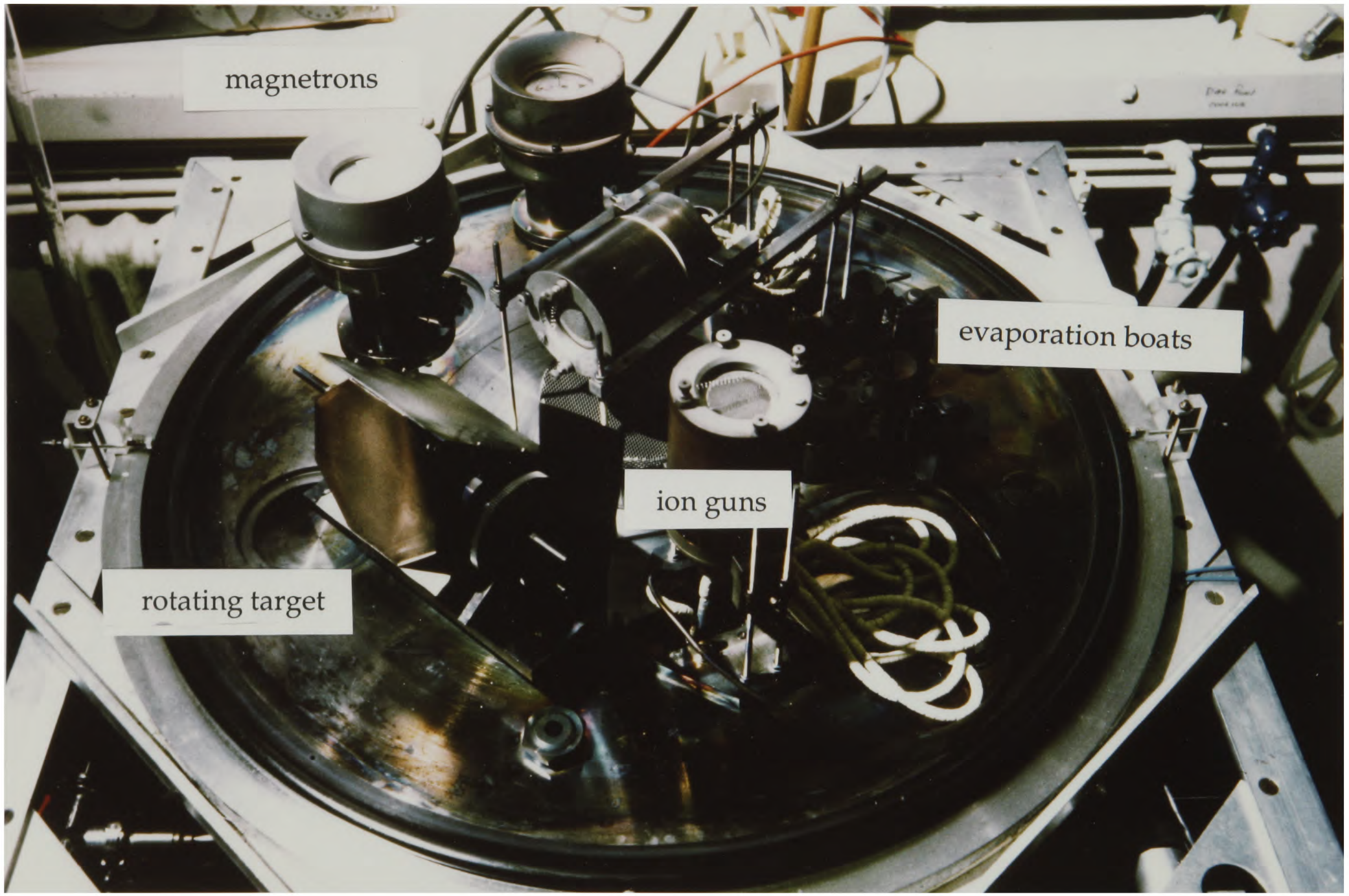
(e) ion-beam assisted deposition.

The chamber can contain up to three magnetrons, an ion gun, two evaporation boats and a rotating target holder and substrate table thus enabling different combinations of guns and geometries to be used in the deposition process (Fig.2.1).

2.2.1 The Vacuum Chamber

A circular glass cylinder of diameter 0.6 metres and height 0.5 metres forms the vertical chamber walls. The horizontal surfaces consist of two large flat discs of 1 inch thick stainless steel, in which holes of various sizes have been drilled to accommodate the necessary monitoring gauges, gas and power supplies.

The top plate is semi-permanently attached and sealed with an 'O' ring to the


magnetrons
evaporation boats
ion guns
rotating target

circular upper edge of the chamber. A padded clamping ring which fits loosely beneath the upper lip of the glass and is held in place by 4 inch long bolts clamps the top plate to the glass cylinder. These bolts must be evenly tightened to ensure that no unbalanced stress is placed on the glass. Any changes in temperature and of course internal vacuum pressure would cause a further and possibly fatal increase in strain within the chamber.

A winching system is mounted in the ceiling above the chamber and is attached via 3 bolts embedded in the top plate and provides a means of gaining access to the chamber. The base plate is integral with a substantial metal frame. The vacuum seal with the glass is again made using a rubber 'O' ring of 1cm thickness and 0.6 metre diameter greased using Apiezon M vacuum grease.

The base plate features a central hole and flange which connects to the pumping system. The mouth of the system is covered by a 2mm wire grating to prevent objects from dropping into the pump below whilst not significantly restricting the pumping capacity. The inside of the chamber is covered with Mylar transparent sheeting which prevents build-up of sputtered material on the glass surface of the rig and allows viewing during deposition. It has been shown that Mylar does not outgas significantly.

The main support of the substrate table is a rotating tube which is at atmospheric pressure internally, whilst the externally attached substrate holders are obviously at vacuum pressure. The entire structure can be rotated using a gearing system fitted to the external part of the main support. The vacuum seal around the main support is maintained using 'O' rings and close contact between the smooth interfaces of the metal tubes. When the substrate table is rotated the chamber pressure rises slightly, but falls again quickly once the rotation stops and the 'O' rings efficiently reseal the vacuum. This problem has been alleviated in later designs by using a well balanced substrate table for which stresses are equally distributed.

The substrate table itself was initially of rectangular shape, counterweighted for stability and water cooled to control the temperature increase that occurs on sputtering. The substrate holder was a circular steel plate separate from the main table and rotatable separately from it, with no method of direct cooling.

The latest design under construction at the present time consists of a 10cm thick hollow circular plate, which is well balanced and uses P.T.F.E. bearings to permit free rotation. An external coil of copper tubing is soldered to the substrate table base, through which a nitrogen flow can be maintained for cooling purposes. A copper plate acting as the substrate holder can be bolted directly beneath this.

The main support tube in both cases contains wiring for:

(a) the motor to rotate a shutter to prevent the substrate being exposed to unwanted sputtered ions,

(b) the rf supply which has been isolated from other wiring as far as possible,

(c) other b.n.c. connectors to pins on the underside of the substrate table, which may be used to supply power to detectors and other devices inside the chamber such as the quartz thickness monitor and thermocouples.

The pins used must have PTFE protecting shields around them to prevent sputtered metals coating the area, and thus causing shorting between the connections. These are removable and are changed frequently.

2.2.2 The Pumping System

The chamber is initially roughed out using a two stage Edwards rotary pump. In order to prevent contamination of the chamber due to oil backstreaming a filter is connected in the pumping line above the pump inlet. When a chamber pressure of 7 x 10^{-1} mbar has been reached, the rotary pump is used to back a diffusion pump. The water-cooled Speedivac oil vapour diffusion pump is centrally mounted beneath the base plate. The pump has a throughput capacity of 1000 litres/second, and is connected via a butterfly valve to the chamber. The base pressure of the system is of order 1x10^{-6} torr, which can be reduced by further extended pumping and the use of a Meissner trap to the 10^{-7} high vacuum range. The vacuum system can be run continuously using a nitrogen autofill syphon and an electrical timer to control the flow of liquid nitrogen which is kept under pressure using a valve connected to the compressed air supply.

The Meissner Trap The Meissner trap is a coil of copper tubing of a diameter

designed to fit within the walls of the chamber and is connected to two vents which emerge through the top plate of the chamber. When pressures within the chamber are limited by the presence of water the trap may be filled with liquid nitrogen, producing a cold surface onto which water and any other contaminants with boiling temperatures above about 80K may condense. The filling of the trap can improve the vacuum pressure by typically an order of magnitude. It is important the trap should be kept full of nitrogen, as a large amount of heat is generated during the sputtering processes and hot spots may quickly develop causing a pressure increase detrimental to the film quality.

One advantage of a metal chamber is that it is easy to use a baking procedure, which causes absorbed substances in the wall to be driven off and pumped away. Thus base pressures of 10^{-9} torr are easily achieved. Glass chambers have the disadvantage that external heating must be applied with care to avoid the development of large thermal stresses.

The base pressure is limited by the pump capacity and in addition by

-leaks (non-detectable)

-oil contamination

-outgassing.

The system has been leak tested using a built-in mass spectrometer leak test facility. Helium gas is sprayed about vacuum seals and joints. Any leak present results in an increased helium pressure within the system; the detection limit is of order 10^{-10} torr. There are no significant leaks present.

Oil contamination in a vacuum system largely arises from backstreaming from the pump. A filter is connected in the pumping line of the rotary pump in order to reduce this.

Outgassing from surfaces within the chamber is a factor that can be decreased by extended pumping times and by baking of the chamber. The baking of a glass chamber has inherent difficulties, and for a system in regular use in which the pumping cycle is repeated every approximately 24 hours an extended pumping period is not practicable. The working base pressure is thus found to be 10^{-7} torr.

The oil contamination problem will be largely eliminated with arrival of a Leybold TurboVac 360 V turbomolecular pump. This pump has a throughput of 350 litres a second. The pumping method depends solely on a rotating blade system and should therefore result in a reduction in contaminants in the system. Any remaining oil contamination may come from the argon used to backfill the chamber to a workable sputtering pressure. Although high purity (99.995%) gas is used, contamination may result from the oil used in the gas cylinder filling process. The argon is filtered using a Balston filter which has been further sealed using epoxy to reduce air leaks.

Using a Dataquad mass spectrometer the major contaminants at low pressures are found to be water and hydrocarbons of mass numbers in the range 40 to 80 from the rotary and diffusion pump oils, some of the ions of the above and in addition some cracking fractions of oil. There are also small amounts of helium and hydrogen which are difficult to remove using any pumping system owing to their small mass. Air leaks can be identified by the presence of peaks in the atomic mass spectrum at 28 and 32, corresponding to nitrogen and oxygen respectively, in an approximate ratio of 4:1. In general for a system with no significant air leaks the largest partial pressure will be that of water ($\sim 10^{-6}$torr). This need not be due to a water leak and is in fact usually entirely due to water adsorbed by the chamber walls being desorbed as the surrounding pressure falls. This water can be removed by baking the chamber or by the use of a cold trap. The latter method is used in this chamber as described above.

2.2.3 Pressure Gauges

The system contains 6 pressure gauges. An Inficon Model CC3 vacuum gauge combines a Pirani and Penning gauges, used for general measurements made at low and high vacuums respectively.

Two Balzers ion gauges (HP and BA) and a capacitance gauge are used for high vacuum conditions. The high pressure HP gauge and the BA gauge are controlled by a Balzers IMG 060B and together provide accurate measurements over a range of 10^{-2} to 10^{-8}. The capacitance gauge is invaluable during magnetron sputtering processes as it

is unaffected by the presence of rf radiation, which restricts the use of the other gauges. The mass spectrometer analysis facilities are available at pressures below $1x10^{-4}$ mbar.

2.2.4 Deposition Facilities

The available deposition facilities comprise

- up to 3 magnetron sources,
- two tungsten evaporation boats,
- two ion guns.

An argon supply is fitted to the rig to produce an atmosphere suitable for a gas discharge. Other gases such as oxygen can also be added to the atmosphere for sputtering compounds in which the presence of another gas is required for stoichiometric deposition (e.g. an oxygen/argon mix is required for the sputtering of ZnO). The desired flow rate can be provided using a needle valve and by controlling the butterfly valve at the throat of the diffusion pump. The working pressure is of order of 3×10^{-4}. The argon supply also provides a method by which the chamber can be brought up to atmospheric pressure without the reintroduction of contaminants that would otherwise be admitted if the vacuum is let up to air, though in practice easily produced and less expensive nitrogen gas is used. The gas in both cases is fed into the chamber via a Vernier leak valve to enable a high degree of control in the gas pressure.

The magnetrons are run in rf mode and are supplied using anAdvanced Energy RFX-600 rf power supply. A wide range of metallic and non-conducting films can therefore be deposited. They can be run singly using a Advanced Energy MTN500 power matching circuit, or simultaneously using a home made power splitting and matching box. In this case the power is fed to a single socket from which 2 copper wires emerge effectively splitting the power. Each matching circuit consists of inductance of order 3μH in series with a 500pF variable air capacitor and in parallel with a 1000pF variable air capacitor. The inductance was calculated using the following equation

$$\mathrm{L} = \frac{\mathrm{N}^2 d}{3.5 + 8l/d} \tag{2.1}$$

where d is the coil diameter and l is the coil length in inches. The variable capacitors

permit matching of both circuits to the rf power supply, by minimizing the total reflected power from the two magnetrons as monitored by the power supply. A sharper resonance position is found for two magnetrons than for a single magnetron, since if the discharge of one gun strikes it tends to cause the second gun to strike drawing more power and exerts a correcting effect on the power balance between them.

The chamber contains two IonTech ion-guns, one mounted horizontally to perform ion beam depositions and the other vertically for direct substrate cleaning to remove any surface contaminants prior to deposition. The beam currents are controlled by an IonTech.Inc. MPS 3000 FC supply. The targets used in ion beam sputtering deposition are thin 2 inch squares of material screwed to the 3 square faces of stainless steel target holder of triangular cross-section as shown in Fig.3.1. In order that contamination of the sputtered material does not occur the screws are placed at the corners away from the area sputtered by the ion beam. The original target holder rotated in the horizontal plane, however this was modified as it was found that the geometry of the target holder and substrate table was such that the maximum deposition rate could not be achieved. The current target holder is rotated in the vertical plane and during the sputtering process there is an angle of 45° between the incident beam and the target, and similarly between the target and the substrates such that the substrates are directly above the sputtered region. The target holder can be rotated into position by a computer controlled RS stepper motor which provides accurate angular positioning to within approximately 0.5°. A multilayer can therefore be produced very easily using a simple program.

2.3 The Small Sputtering Chamber

The small sputtering chamber was designed [85] to produce ZnO transducers. As will be discussed in more detail in Chapter 6 such a transducer consists of two successive layers of evaporated Cr and Au onto which the ZnO transducer was deposited. An array of gold top dots was then deposited on top. The initial chamber design contained a single designated ZnO magnetron and two evaporation boats. The sample itself was mounted

on a horizontal rod that could be manually rotated from outside the chamber and moved linearly in the horizontal plane such that the substrate could be positioned directly above either the evaporation boats or the magnetron.

The chamber is of metal construction and small volume enabling a good base pressure to be obtained typically of less than 1×10^{-6}. The system is also easily baked and contains a Meissner trap which results in a significantly lower working base pressure than this. (This pressure is lower than can be measured using the Penning gauge available.) An additional advantage occurs because the system is pumped using a mercury vapour pump which introduces no oil contamination. The rotary pump used for the initial evacuation of the chamber to a pressure of 0.2 torr and backing the diffusion pump is the only source of such contaminants.

2.3.1 Modifications to the Chamber

It was found that some experimental runs produced better films than others. The addition of the Cr layer had been found to improve film adhesion [85], however some film peeling problems still occurred. A further problem arose when bonding gold wires to the top dots. In many cases the dots became detached from the ZnO even when very small strains were applied.

In order to solve these problems the chamber has undergone major alterations. Firstly a mass spectrometer head was added to monitor any contaminants that may be present. Secondly a 5cm diameter horizontal side arm was fitted connecting to a 8cm diameter chamber containing an ion gun. The elevation was such that the emergent ion beam was located at the same height as the sample holder in order that the sample may be precleaned by rotating it to face the ion beam. It was hoped that in this way that film adhesion would be greatly improved by the removal of surface contaminants.

A third improvement was made by adding the facilities permitting ion plating of the gold top dots. A discharge was struck using a rf signal applied to the sample via a copper coil (of 1 inch diameter and 3 turns) in an argon atmosphere. A slow evaporation process through the discharge then proceeded over a time of order 15 minutes.

Bombardment of the gold film during deposition should produce a better adhesion of the gold atoms to the transducer. Transducers made subsequent to these improvements have shown no signs of peeling or bonding problems.

Finally a quartz monitor is being fitted to the chamber. This should result in more accurate and repeatable film thicknesses, and successive batches of ZnO transducers having well defined structure resulting in similar piezoelectric properties.

Chapter 3

Magnetic Multilayers

There has been great interest recently in the study of magnetic multilayers, owing to the presence of novel magnetic properties not seen in bulk material, which can be tailored to fit specific requirements by altering the structure on an Å scale.

3.1 Multilayered Structures

The motivation for the study of multilayered structures can be divided into two main areas. Firstly there is a great deal of theoretical interest in two dimensional (2D) magnetic layers. 2D systems, and also a new class of pseudo-2D materials, can be now be experimentally realised and tested. Secondly lattice parameters, exchange interactions and anisotropies can be varied in such structures with the consequence that film characteristics can be modified in such a way as to produce a variety of technologically useful properties.

Multilayers that have been widely investigated include FeCr, CoRu, CoPt and CoCu. Currently CoPt films are being widely researched because of their perpendicular anisotropy and high coercivity which make them ideal materials for optical storage discs. CoCu multilayers have recently been found to exhibit magnetic field dependent changes in sample resistance of 60%. These giant magnetoresistive properties have practical applications as magnetic sensors and are specifically being developed to enable fast reading of the magnetically stored data. Reading heads for discs currently in use utilize induction loops producing output voltages that depend on the rate of change of magnetic field rather than giving signals directly proportional to the magnetisation.

The generalized structure of a magnetic multilayer consists of alternate layers of magnetic material e.g. Co, Fe interspersed by spacer layers usually of a non-magnetic material e.g. Cu, Cr, Au,. Both types of layer are of the order of Å thickness. A magnetic layer and its adjacent spacer layer form a bilayer, the characteristic repeat

distance of the multilayer structure that can be accurately established using X-ray and neutron scattering.

3.1.1 Magnetoresistance

A metal in a steady uniform magnetic field may show a change in resistance from that present in zero field. This effect is called magnetoresistance (MR). MR will be defined as the value (R(0) – R(H)/R(0) × 100 which will be referred to as ΔR/R%. MR effects seen in pure metals are usually positive and of a relatively small magnitude. A typical value for copper at room temperature is 2% in 24T applied field [13].

These effects are due to a precession of the charge carriers in an applied magnetic field. The applied field causes the conduction electrons in the sample to undergo a helical path at the cyclotron frequency, given by

$$\omega_c = \frac{eB}{m^*} \tag{3.1}$$

where m* is the effective mass of the electron. The chance of collision for a given distance travelled in the current direction increases with the increased effective path length. The MR thus increases with the magnitude of applied field. In general the magnitude of the magnetoresistance change depends on the applied field strength and the structure, purity and crystallinity of the sample. The direction of current flow with respect to the field orientation also affects the size of MR seen. In some conditions a negative magnetoresistance can be found eg. in long narrow samples where the electron mean free path is comparable with the sample size. The main appearance of negative MR, however, occurs when ferromagnetic materials are present. The conduction electrons are polarized and the scattering is spin-dependent.

In magnetic multilayers the GMR found by Parkin is negative and of order 60% at room temperature. There is currently much discussion concerning the requirements for this GMR to exist. Initial m.b.e. grown films showed little or no GMR and no oscillations between ferromagnetic and antiferromagnetic interlayer coupling [14]. Oscillatory GMR was first discovered [15] in magnetron grown multilayers. This chapter is a study of ion-beam grown multilayers, made in an attempt to investigate further the influence of film

deposition method on the interlayer interactions and the presence of GMR.

3.2 Theory of Magnetoresistance and Interlayer Exchange in Transition Metal Magnetic Multilayers

An interesting feature found in multilayer systems is that the interlayer exchange gives rise to an oscillatory function of ferro- and antiferro- coupling as a function of spacer layer thickness. The effect of this was first observed by Parkin *et al* in FeCr, CoCr and CoRu sputtered multilayer systems as an oscillation in the GMR [16] as discussed above. The oscillation period is generally found to be of order 10Å as a function of the spacer layer thickness [17], [18], but this figure is material dependent as is the phase of the oscillation in coupling. These oscillations can also be of different wavelength in the same material for different orientations of the crystal axis. For example Co (111)/Cu (111) and Co(001)/Cu(001) have oscillations of 12.5Å and 10.5Å respectively and different relative oscillation phases [18], [19]. It has been demonstrated that interface roughness can influence the structure of the oscillations themselves as well as their magnitude [20].

There are therefore two basic effects occuring in multilayers that need explanation. Firstly it is necessary to provide a theory for the basic scattering mechanism and its field dependence; secondly the origin of the interlayer interactions and the resulting long period of oscillation of the interlayer coupling needs to be explained. It has been shown that the GMR is observable in uncoupled [21] or pinned [22] antiferromagnetic transition metal sandwiches. This proves that the GMR is entirely a consequence of the relative magnetic orientation of the layers rather than being dependent on the coupling mechanism. The theories of the interlayer coupling and the GMR can therefore be treated separately.

3.2.1 Interlayer Exchange

Rare earth multilayer structures were the first systems in which indirect interlayer exchange was clearly observed. For Dy/Y it is seen that interlayer exchange between the magnetic Dy layers is an oscillatory function of the non-magnetic Y spacer layer thickness

(see Chapter 5). This oscillation can be described using an Rudermann-Kittel-Kasuya-Yosida (RKKY) like model.

3.2.2 RKKY Interaction

The RKKY model of indirect interactions evolved because it became clear that direct exchange theory provided insufficiently large interactions in the rare-earth and 3d transition metals to cause magnetic ordering. A direct exchange interaction relies on overlap between the localized 3d and 4f electrons responsible for the magnetisation. Non-localised electrons must therefore play a large part in the ordering interaction, although their contribution to the spontaneous moment is negligible. The mechanism for this so-called indirect exchange occurs via the polarization of the itinerant electron gas by the ions. The polarization is found to oscillate in sign with distance from any given point with amplitude which varies as a function of r^{-3}.

Simple RKKY theory gives rise to an oscillation period fixed at the reciprocal of twice the Fermi wave vector, K_F, ie. a lattice constant. This gives rise to short oscillation periods ($\sim$ 1-2Å) for many systems including CoCu multilayers. It is clear from experimental evidence that an RKKY-like indirect exchange interaction is capable of providing a model for interpreting the experimental results.

Whether two successive magnetic layers are ferromagnetically or antiferromagnetically coupled depends critically on the thickness of the spacer layer, and not on the magnetic layer thickness. This suggests that the interaction between the 2 layer types occurs largely at the interfaces, for example by hybridization of the non-magnetic and the magnetic states at the interface leading to an indirect coupling by polarization of the spacer layer. There is a tendency for the conduction band of the non-magnetic layer to become magnetic. Experimentally Parkin found that the amplitude of the interlayer exchange increases from the left to the right of the transition metal series and from 5d to 3d elements [17]. The exchange interaction is smaller for the noble metals. This is consistent with an indirect exchange model. Further if the spacer layer thickness is increased to a distance where a RKKY interaction could no longer couple the layers, the

oscillations in the GMR also gradually disappear. There may still be a significant MR effect remaining, which is due to randomly oriented domains which are aligned when an external field is applied.

More realistic calculations using representative band structures and including interface roughness can result in the prediction of long period oscillations. Wang *et al* [23] found that calculations for FeCr which took into account s-d mixing interaction and surface roughness predicted long oscillation periods. Short oscillation periods (related to the Cr nesting properties) were regained if the roughness was removed.

Other types of model include those based on aliasing [24]. A RKKY type short period oscillation is assumed but because of atomic spacing the exchange coupling is sampled at discrete intervals. This produces an oscillation with longer apparent wavelength. This theory also provides a simple explanation for why multilayers of same elements but different crystal axis orientations can produce such differences in oscillation period and phase. A small change in the short period wavelength can lead to larger changes in the longer aliased oscillations.

3.2.3 The Two Current Model of GMR

The MR effects seen in multilayered samples can produce a decrease in sample resistance by up to 60% when a field is applied at room temperature [15]. This has been explained in terms of a simple spin dependent scattering model. Consider a multilayer consisting of magnetic layers and non-magnetic spacers. A magnetic field is applied in the plane of the film. The basic assumption is that the spin of the conduction electron is conserved for distances much longer than the mean free path. This is true for ferromagnetic metals when the temperature is low compared to the Curie temperature. The current is therefore carried by two separate spin channels which correspond to spins aligned parallel (spin $\uparrow$) and anti-parallel (spin $\downarrow$) to the applied field. The multilayer resistance can therefore be modelled as two resistances connected in parallel. The electrons with spins aligned with the field are termed the majority carriers. They are in the energetically favoured state and are scattered less strongly than minority (spin anti-parallel) carriers.

For a multilayer in which all layers are ferro-aligned the scattering is weak in one of the spin channels giving rise to a small resistance only, whilst the other channel has a large resistance. The low resistance channel short circuits the larger resistance channel and gives a lower overall resistance, given by the equation for parallel resistors,

$$\frac{1}{(R_T)} = \frac{1}{(R_\uparrow)} + \frac{1}{(R_\downarrow)} \tag{3.2}$$

where $R_\uparrow \ll R_\downarrow$.

For antiferromagnetic (AF) alignment of adjacent layers, an electron experiences alternately weak or strong scattering. Both channels experience significant scattering in this case giving a higher resistivity overall. When a magnetic field is applied the layers (which are AF coupled in zero field) become ferro-aligned in the applied field direction at the saturation field H_{sat}. It can therefore be seen that application of an external magnetic field to an AF coupled multilayer will give rise to a decrease in the film resistance.

3.2.4 Causes of scattering

In the previous sections the only assumption made was that the scattering is spin dependent. This difference in scattering is due to the different densities of states available at the Fermi level for up and down spins. Scattering occurs at both interfaces and in the bulk of a layer. The relative importance of these two scattering mechanisms and the way in which each is represented in calculations is a region widely explored by theoretical models. There are 2 main theories for the mechanism and location of scattering events. The first invokes diffuse scattering from the rough interfaces between the magnetic and non-magnetic layers. The second theory is based on a bulk scattering mechanism ie. scattering of electrons within a magnetic layer. In both cases an electron is more strongly scattered if its spin is aligned anti-parallel to the field produced by the orientation of the magnetic ions.

Camley and Barnas [25] developed one of the first theoretical models, based on a semi-classical approach, in which bulk and boundary scattering were modelled by defining spin dependent mean free paths for the bulk magnetic regions and spin-dependent transmission coefficients at boundaries.

The quantum model [26] uses spin dependent scattering potentials to model the scattering processes. Electron wave packets are scattered by the inhomogeneous distribution of scattering centres that results. Expressions for interface roughness and impurity concentrations can also be included in the expression. Scattering potentials localised at interfaces can produce phase shifts in RKKY oscillations [27].

Fits to experimental data have been made for both of these methods taking the magnitude of the MR at its first maximum as a reference point. The quantum model has the advantage of agreeing with absolute values of MR, whereas the semi-classical model leads to values that are a factor of 0.6 times too small.

3.3 Sample Preparation

3.3.1 Substrates

Glass and single crystal (100) silicon wafer substrates were used, the typical substrate size was 1cm^2. All substrates were thoroughly chemically cleaned before being placed in the vacuum chamber for ion cleaning. The chemical cleaning procedure involved three stages; firstly the substrates were washed in a solution of 1 part Decon (an industrial cleaner) to 3 parts distilled water to remove any grease present. The substrates were then rinsed several times in distilled water to remove any detergent traces, and rinsed again in acetone to remove any traces of moisture which would otherwise remain. The samples were gently wiped using a Whatman 301 lens tissue soaked in acetone to remove remaining residue. Acetone has the advantage of evaporating quickly to leave a dry surface.

The substrates were then attached via 2 clips to the rotating substrate table. The substrate table had initially been cleaned with Genklene (tri-chloroethane) to remove grease and then wiped with acetone to remove any traces of Genklene and any moisture. The substrate table was positioned within the large vacuum deposition chamber which was then evacuated.

3.3.2 Ion Beam Cleaning of Substrates

When the chamber had reached base pressure, the substrates were then ion-cleaned in order to remove any remaining surface contaminants. Argon ions of energy 500eV were used.

3.3.3 Heating of Substrates Prior to Deposition

Several substrates were heated by direct radiation from the ion gun neutraliser filament (without an ion beam present) prior to deposition. Normally substrate temperatures increase gradually during the deposition process. The substrates used are all poor thermal conductors and their temperature increases with increased deposition time. It is thought that substrate heating during film deposition may improve the film and multilayer structure, and reduce stress within the plane. If the sample temperature is still increasing during deposition the film quality may change throughout the multilayer; if this is indeed the case, pre-heating a substrate may result in a more uniform film quality.

3.4 Film Deposition

3.4.1 General description of films

The films to be discussed are of the following general structure. A buffer layer is grown directly onto the substrate in order to produce a better growth surface for the subsequent multilayer. Following the buffer layer a multilayer of N bilayers is grown where N = No. of cobalt layers = No. of copper layers. A capping layer may be grown to protect the film. The elements used as buffer and capping layers have been varied and for several batches of samples were not included at all. The total thickness of the capping and buffer layer must be taken into consideration. If the resistance of these two layers is comparable with or less than that of the multilayer they will tend to act as a short circuit and decrease the magnitude of the MR effect. In addition to the multilayer samples 200Å films of pure Co and Cu were made. These samples were made in order to verify that the properties observed in multilayer films arise as a consequence of their multilayered structure.

Following the preparative steps described in the previous section the multilayer films could then be deposited.r The materials used were of high quality, with guaranteed purity of at least the following values

Carbon 99.8%

Silver 99.95%

Iron 99.5%

Gold 99.998%

Copper 99.90% (with unquantified silver impurities, controlled low O_2)

The argon gas was industrial grade of minimum 99.995% purity; however there is a possibility of oil contamination derived from the cylinder.

Two alternative deposition techniques are available for multilayer deposition. The majority of films have been grown using the ion-beam sputtering technique.

Rotating Target Method- Ion Beam Sputtering

This method uses the horizontal ion gun aimed at the triangular cross-section rotating target. One side bears a sheet of buffer layer material (e.g. Fe) if used, the other two being covered by cobalt and copper targets respectively (Fig. 3.1).

A stepper motor is used to rotate the targets. A series of 8 samples can be made as there is a further degree of freedom arising from the use of a rotatable substrate table so that the process may be repeated. Each substrate position may be exposed in turn with the use of a rotating shield of the same diameter as the substrate table with a hole of 8cm diameter at the radius of the centre of the samples. This design limits possible cross contamination of neighbouring substrates.

A copper-constantan thermocouple was used to measure the substrate temperature during deposition. It was found that the temperature rose to $\sim 50°$ within a few seconds. The subsequent rate of heating depended on the target being sputtered. The heating rate produced for a copper target was 2 degrees per minute whilst for cobalt a rate of 5 degrees per minute was found. A typical deposition temperature would thus be in the range of 50° for a 900eV beam rising to 100° for longer deposition times.

The Rotating Substrate Method - Rf Magnetron Sputtering

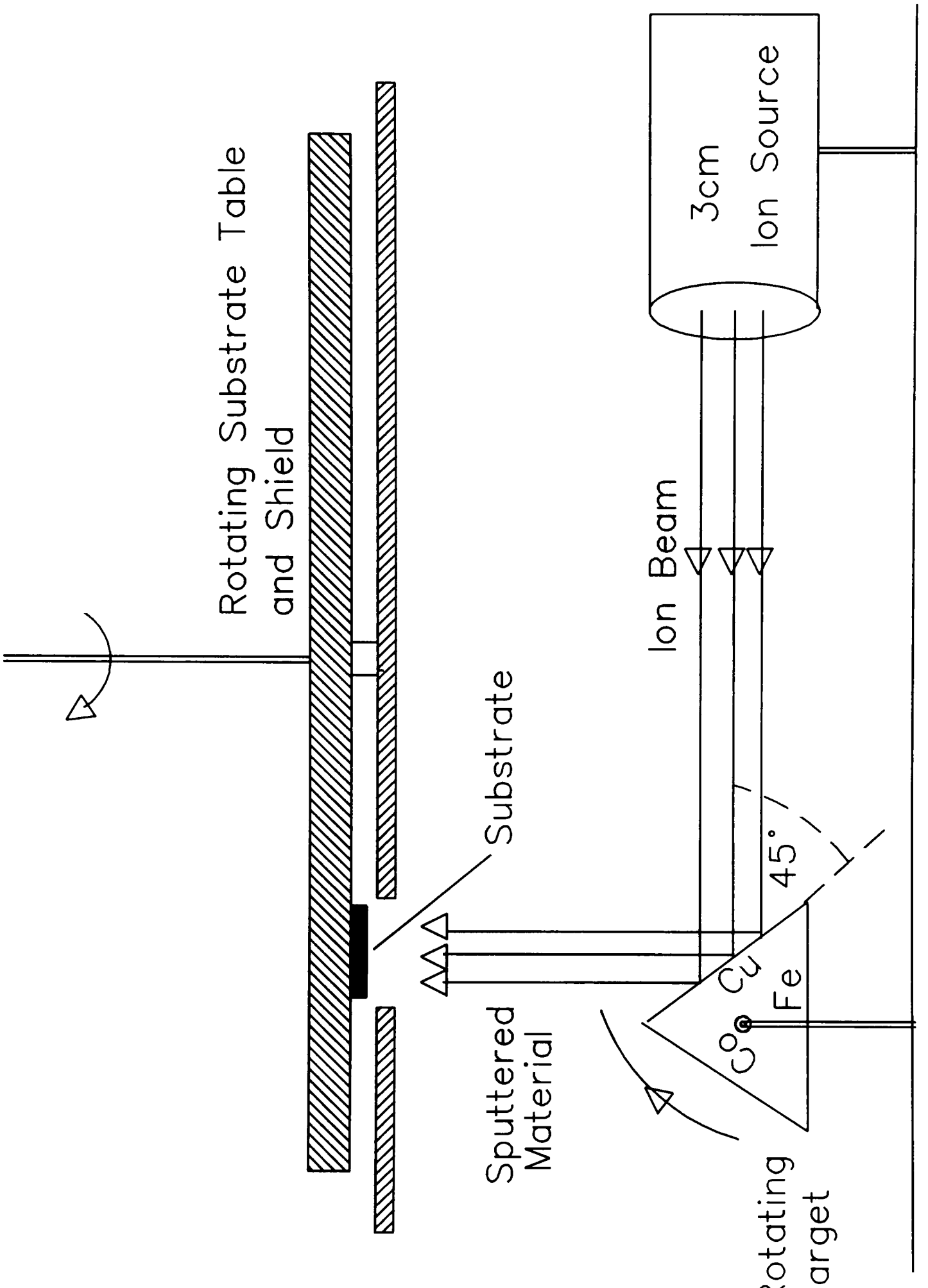

Rotating Substrate Table
and Shield
Substrate
Sputtered
Material
Ion Beam
3cm
Ion Source
45°
Cu
Fe
Co
Rotating
Target

Figure 3.1

In this method a computer controlled stepper motor built into the substrate table rotates a small rotor to which a single substrate is attached. The rotor oscillates over two rf magnetrons which are running simultaneously and halts over each for a programmed time. The deposition temperature in this case was found to be of order of 40°. This temperature is similar to the deposition temperature used by Parkin [15] when producing films of very large MR.

3.5 Film Characterization Methods

The magnetic, structural and transport properties of the films have been characterized using a variety of methods.

Structural

- X-ray Diffractometry
- Scanning Electron Microscopy (SEM)

Magnetic

- Magnetometry
- Rf Susceptibility

Transport

- Magnetoresistivity

3.5.1 X-ray film Characterization

Samples have been examined using X-ray diffraction. We shall consider films grown on both substrate types.

High Angle Diffraction

A single crystal possesses a set of reciprocal points in k-space which correspond to the mean separation of the atomic planes. These reciprocal points correspond to the position of the Bragg peaks in a diffraction pattern resulting from an X-ray scattering experiment on the sample. Multilayering in a sample is evidenced by a series of satellites that occur about each Bragg peak, corresponding in k-space to the bilayer repeat distance in real space. Amorphous films and polycrystalline multilayers have very weak Bragg

reflections owing to the tiny crystallite sizes and the fact that only small number of these crystallites contribute to the signal. The structural satellites are too small to be seen. The predominant orientation of crystallites in the direction perpendicular to the film is known as texturing and can be identified using high resolution large angle diffraction methods.

Magnetoresistance has been shown to depend on film texturing; Egelhoff *et al* found that m.b.e. grown CoCu multilayers films with Cu (100) growth direction exhibited magnetoresistance whereas those with Cu (111) growth did not [28]. Polycrystalline films that show magnetoresistance [15] have been described as (111)-textured. However it has recently [28] been shown that these samples contain a significant proportion of other crystallite orientations, including (100).

Figure 3.2 shows the high angle diffraction pattern for Sample 2. The peaks have been identified as arising from (0001) Co, (111) Cu and (200) Cu (from low to high angles). The peaks for both copper orientations are seen to be of comparable height.

Low Angle Diffraction

Low angle diffraction is an important tool in the investigation of multilayered amorphous structures as the structural satellites about the origin of reciprocal space are of measurable amplitude. A diffraction pattern produced from a periodic structure represents the Fourier transform of that structure. Thus the number of satellite peaks depends on the sharpness of the boundary between a layer of magnetic and non-magnetic material. For a sinusoidal distribution of cobalt through the film thickness only one satellite is seen because the chemical profile contains only the first Fourier component. For a squarer cobalt distribution with sharper chemical interfaces higher order Fourier components are needed to adequately describe the distribution shape; improved film quality therefore produces more satellite peaks.

Figure 3.3a shows the results obtained for low angle X-ray diffraction on the glass sample, and shows only one peak, indicating a sinusoidal film composition. However if one considers that the resulting diffraction pattern is an average over the sample area exposed to the X-ray beam it can be seen that a film with a square composition profile on

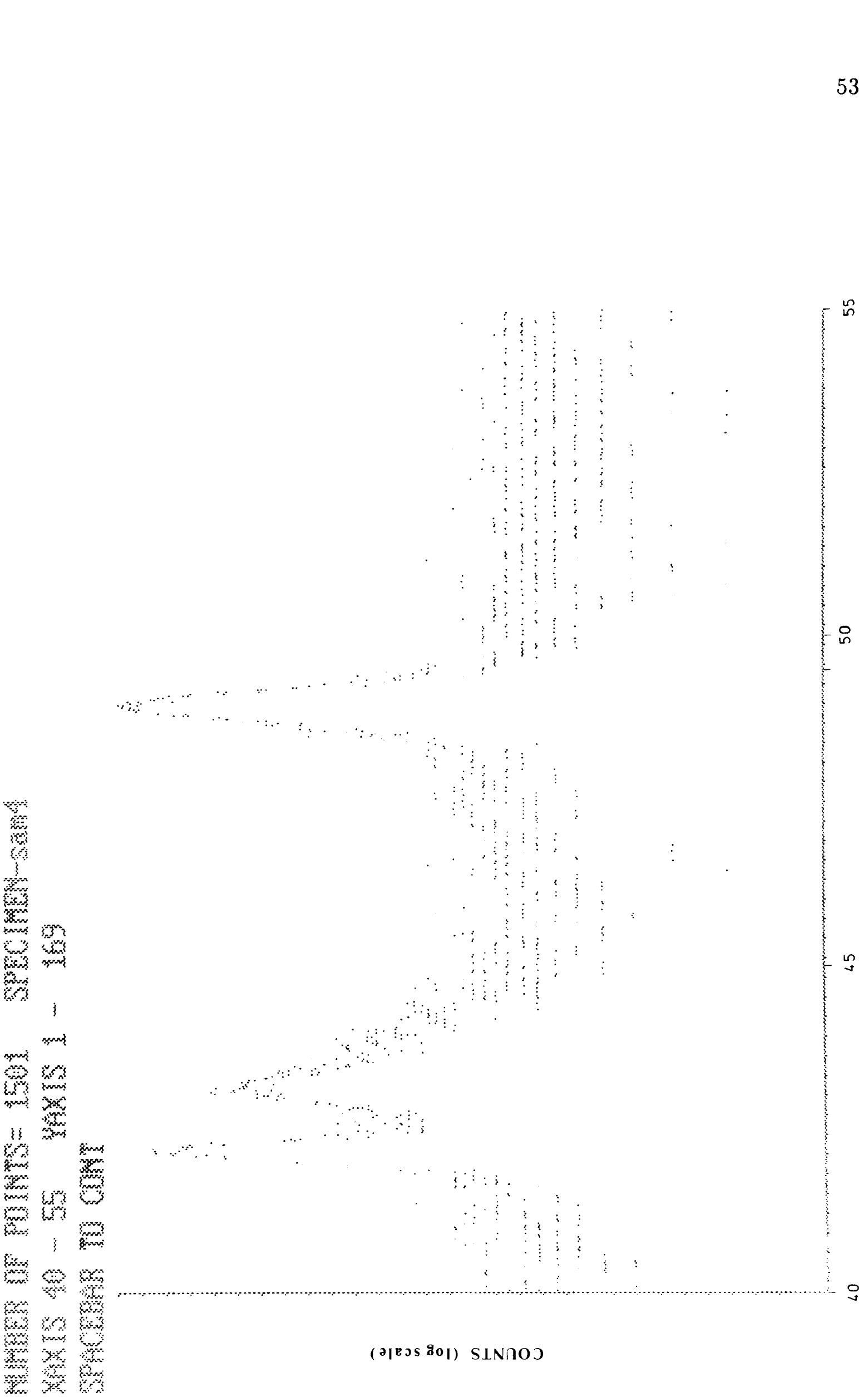


Figure 3.2

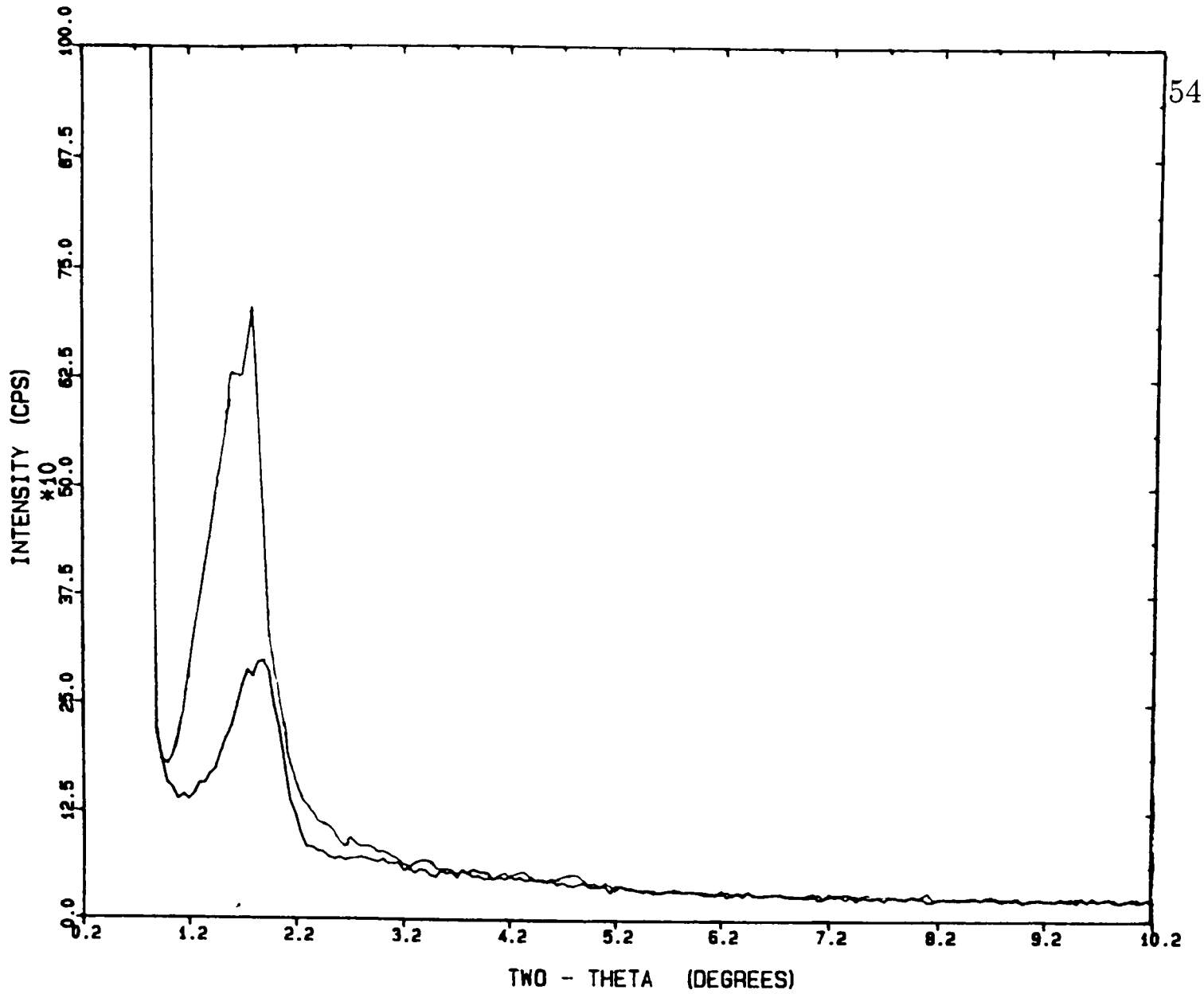


Fig. 3.3 (a)

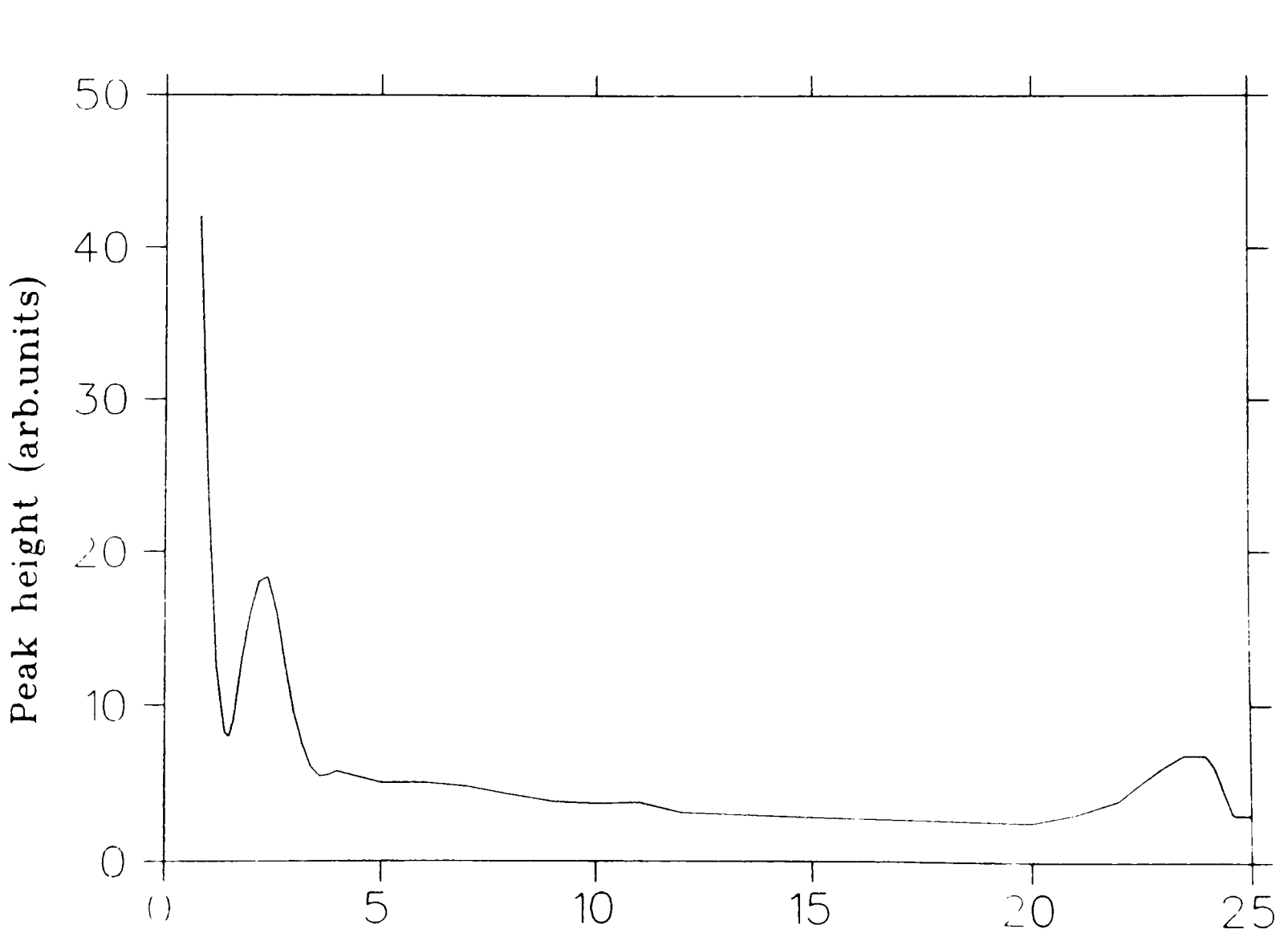


Figure 3.3 (b)

a short length scale such as that grown on a rough substrate, or with buckled layers and with no interdiffusion could also give rise to fewer diffraction peaks than would otherwise be expected.

The X-ray diffraction data for a film composed of CoCuCoCuCo where each layer is 13Å thick grown on epitaxial Si is shown in Fig.3.3b. The trace shows the first and fourth order diffraction peaks. The missing second and third order diffraction peaks can be accounted for by modelling the expected diffraction pattern for Co and Cu thicknesses of roughly equal magnitude. It is found that with the layer thicknesses given in the ratio of 0.8 to 1.3 (instead of the assumed 1:1), these peaks are suppressed. It is difficult to establish accurately the thickness of the individual bilayer components, although the overall bilayer thickness can be found to within 1Å. The film thicknesses calculated using the quartz monitor agree well with the bilayer values found by diffraction. This film was grown using the same ion-beam technique; the difference in the number of diffraction peaks seen could be explained by the better quality of the Si substrate.

3.5.2 SEM Results

SEM micrographs were taken of the films as shown in Fig 3.4. The film surface is seen to be pitted on a 0.5μm scale.

3.5.3 SEM Examination of Substrates

Six substrates (two glass, and two unprepared and two chemically etched crystalline silicon substrates) were chemically cleaned as previously described. One of each pair of substrates was further cleaned using the ion beam. Using a scanning electron microscope each surface was examined to assess the effect of the ion cleaning, if any, on the substrate.

The glass sample showed a gently rippling structure in one direction on a scale of 1μm. The unpolished silicon substrate showed a mountainous structure on a scale of 5-10μm. The roughness of the surface was little affected by the ion cleaning process. The epitaxial silicon substrate was initially very flat on all scales apart from a few small lumps of Å magnitude. No similar surface defects were seen on the ion-cleaned sample.

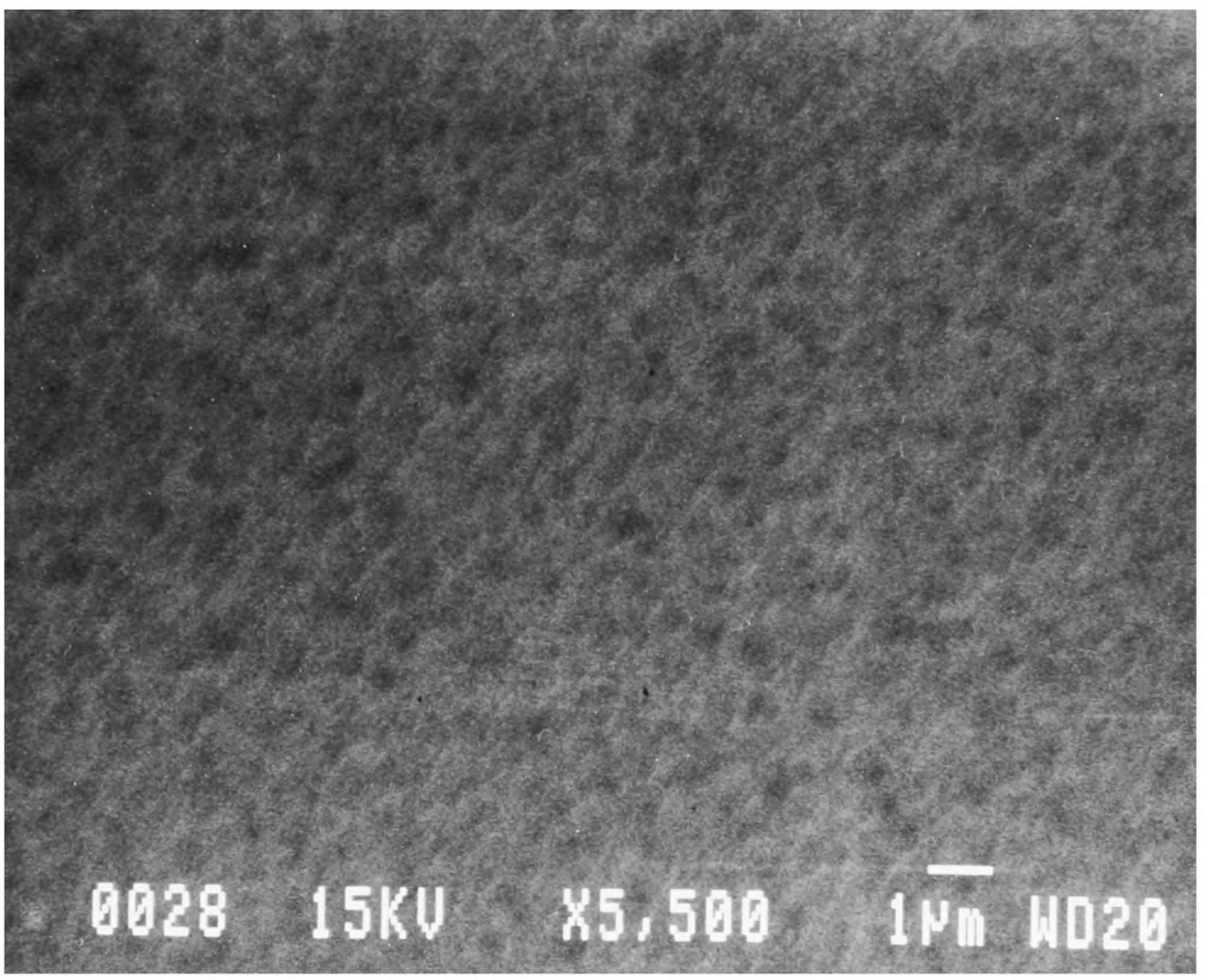


Figure 3.4 SEM micrograph

We conclude that ion beam cleaning does no superficial damage to substrate surface smoothness (at least on a 1000Å scale) and may be beneficial in eradicating small surface blemishes.

3.6 Experimental Method

Measurements were made in an Oxford Instruments variable temperature continuous flow cryostat (VTC). Temperature measurements have an accuracy of ± 0.1K. Care must be taken to allow time for the temperature of the sample and that measured by the VTC to equilibriate. The magnet used was designed for experimental work using nuclear magnetic resonance (n.m.r) and therefore produced a field homogeneous to 1 part in 10^4 over a 1cm^3 volume and of magnitude up to 1.3T. The rf susceptibility and the

magnetoresistance of the samples were measured simultaneously. Initially, susceptibility and MR data were taken separately to verify that no electrical interference between the two occurred. The sample was attached to the end of the cryostat insert which carried the electrical connections for both measurements. The d.c. connections for the MR measurement were decoupled at the top of the cryostat insert using 5nF capacitors, to prevent pick- up from these wires which could cause interference with the rf signal.

3.6.1 Magnetoresistance Measurements

A standard four point measurement MR method was used. Four electrical contacts are attached using silver dag at equal spacings along the sample length. The two outer contacts pass a current through the sample from a constant source. The circuit diagram is shown in Fig 3.5a.

The two inner contacts measure the voltage dropped over that length of the sample. An ac or dc measuring current can be used for the magnetoresistance measurements. The dc voltage drop across the two central contacts can be directly converted to give a value for the film resistance for a known current. The advantage of the a.c. method is that it is insensitive to voltages induced in the connecting wires as a result of thermal gradients along the cryostat length, and other similar effects. However more sophisticated electronics is needed to extract the results. The dc method is the experimentally simpler, and has been utilized for the following experiments. The analogue voltage signal is converted using an analogue to digital converter to a digital signal which is stored by the computer as a function of the magnetic field sweep. The constant current source could produce currents ranging from 300 μA to 100 mA, by means of a 10 pole switch which connects a range of resistances into the circuit. Film resistances of order 0.1 to 200 Ω can be measured.

3.6.2 Susceptibility Measurements

The rf susceptibility was measured using an LC circuit as shown in Fig 3.5b. The oscillation frequency is given by

$$\omega = (LC)^{-2}$$

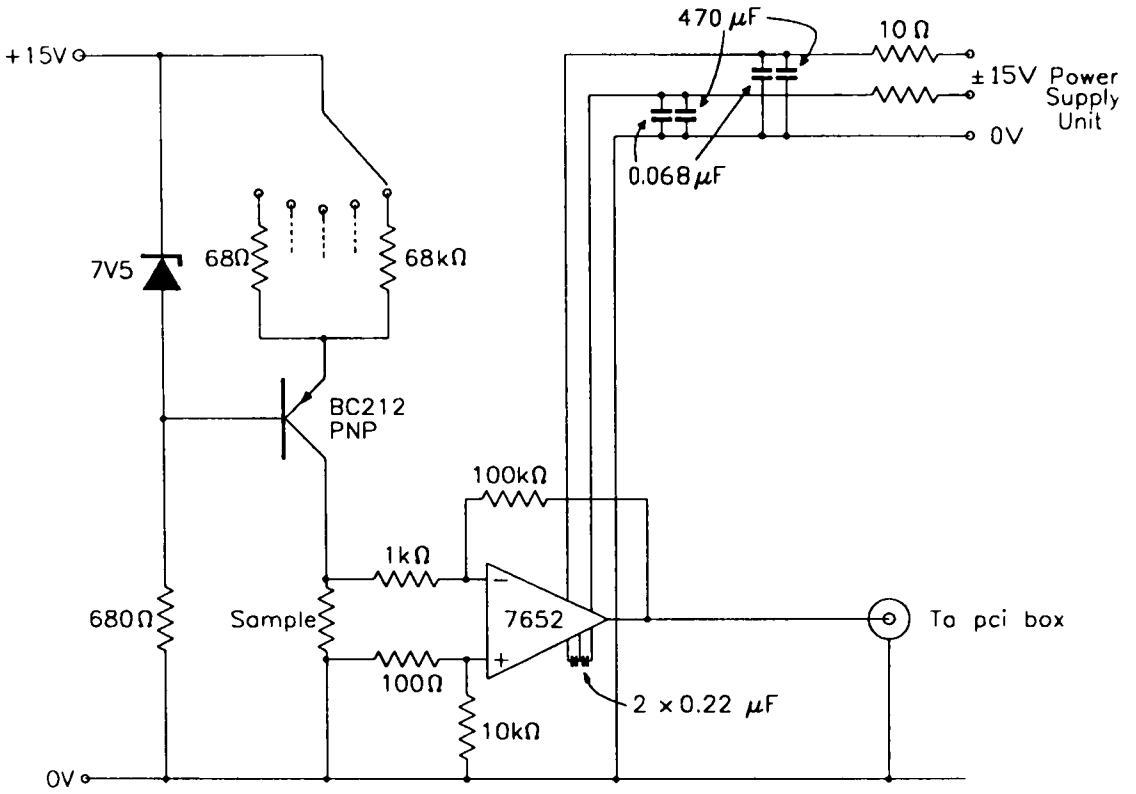


Fig.3.5(a)

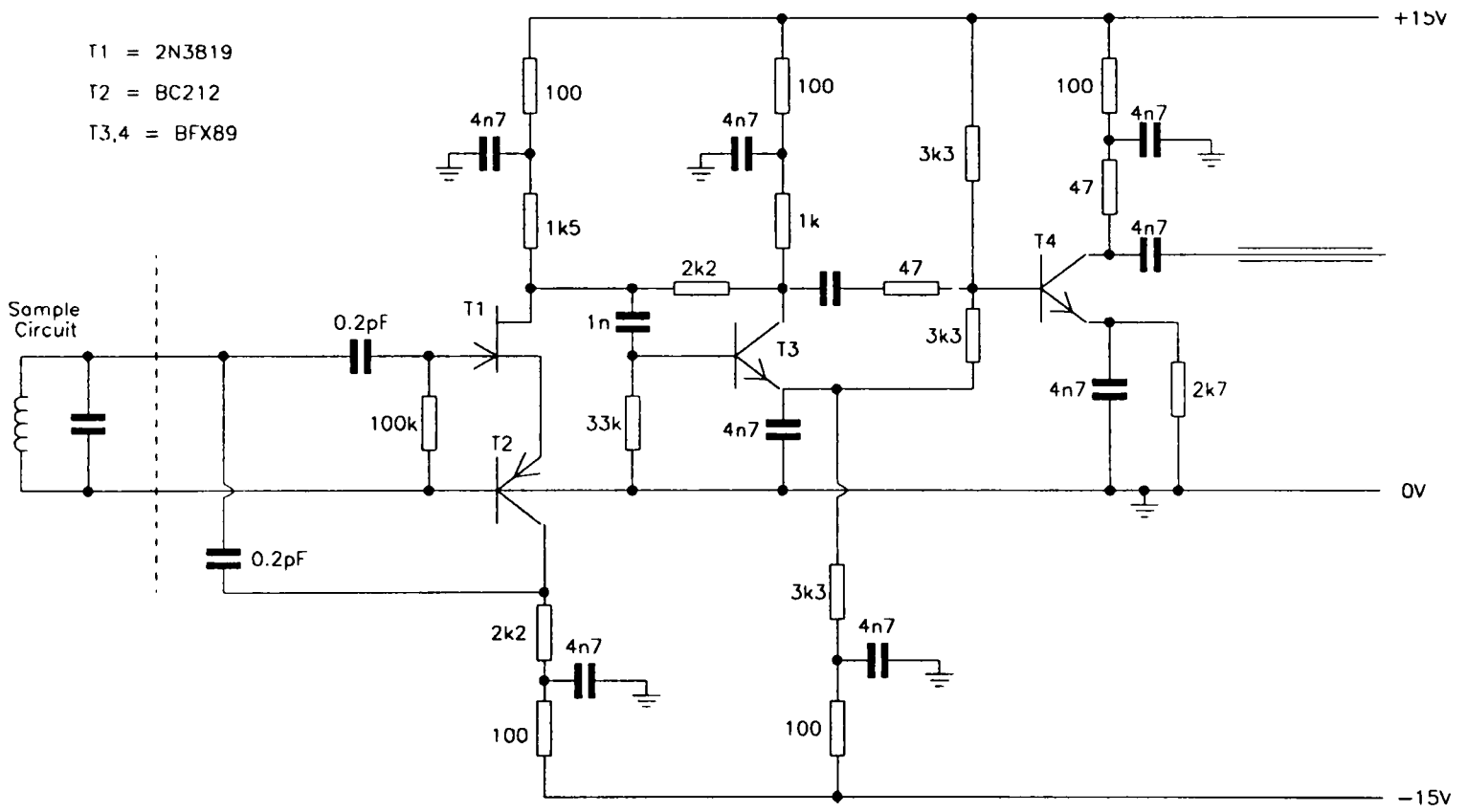


Figure 3.5(b)

and was of order 9.0 MHz for this circuit. The inductance of the coil changes with the magnetic susceptibility of the adjacent film as the dc field is swept, resulting in a change in the measured frequency of the rf signal. The quantity measured, χ_{rf}, is the differential of the magnetisation with respect to the coils' magnetic field. The dips in the resulting susceptibility trace therefore correspond to steps in the film magnetisation. The rf flux through the coil is given by

$$\Phi = NABe^{-j\omega t}$$

where A=cross-sectional area of coil=$1 \times 10^{-4}\mathrm{m}^2$, N=number of turns in coil= 20, ω=oscillation frequency=9MHz and B=magnitude of field due to the coil.

$$V = -\frac{\delta\Phi}{\delta t} = jNAB\omega e^{-j\omega t}$$

$$|B| = \frac{V}{NA\omega} = \frac{2}{20 \times 10^{-4}}.2\pi.9 \times 10^6$$

=0.02mT. In these experiments the fastest sweep used had a field step of 0.3 mT. No over-modulation occurred and therefore no detail in the susceptibility data was lost. Susceptibility measurements were made over a range of sweep rates and it was verified that the data was identical in all cases.

A Racal-Dana 1998 digital frequency counter with a frequency resolution of 0.2Hz at 9MHz was used to measure the resosnant frequency which was then directly recorded by the computer as a function of the applied dc field value. It should be noted that this coil/sample geometry produces a slightly unusual measurement. Typical susceptibility measurements are made with the sample placed within the coil. The field direction and hence the direction in which the susceptibility is measured is then defined. In these experiments the plane of the sample is placed across one end of the coil and the rf field lines thus spread through the film in all directions both in and perpendicular to the plane. Consequently this technique is sensitive to susceptibility changes in the film both perpendicular and parallel to the sample plane.

The sensitivity of this method is evident from that fact that a measurable signal was obtained from a sample containing just two 10Å Co layers separated by Cu. The

saturation moment of the sample was 37μemu. A background susceptibility trace with no sample present shows that there is some residual field dependence from the cryostat or sample holder probably due to magnetic impurities in the steel or solder. Shielding of the circuit did not result in any significant improvement; these background effects, however, make only a small contribution to the signal at low fields.

3.7 CoCu Multilayer MR Measurements

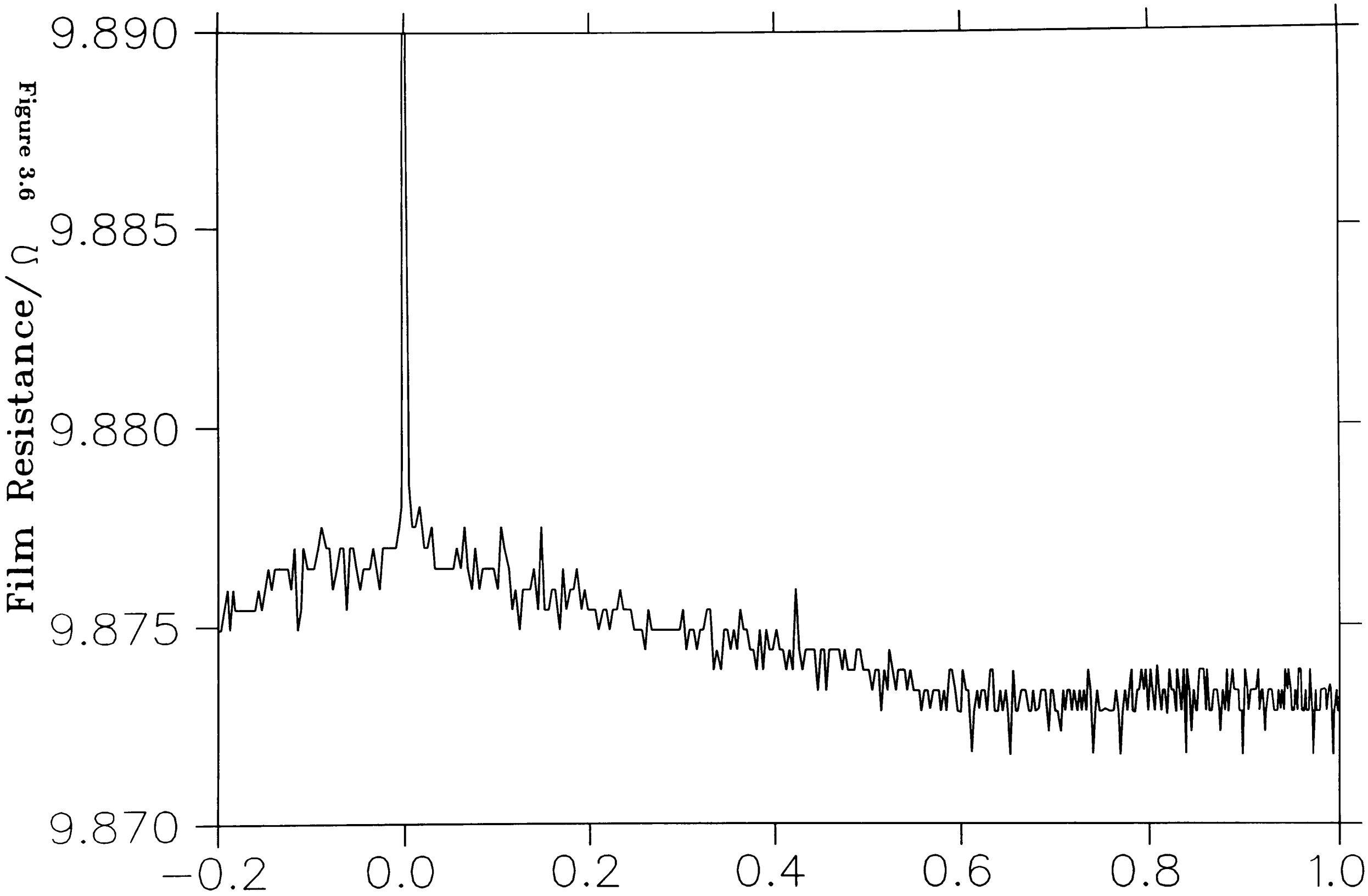
A transverse magnetoresistance measurement (B$\perp$I) is defined as one made with the direction of the applied field perpendicular to the measuring current and is the most widely used measurement condition. Typical transverse MR data for our CoCu multilayer sample consists up to 3 regions as a function of the applied field. For fields within the region of $\pm$ 10mT a sharp drop in magnetoresistance is seen for the B$\perp$I configuration. The drop is of comparable magnitude to the decrease which occurs more gradually over the 10mT to 1T range. Saturation of the MR is seen to occur in several samples for applied fields in the range 600mT to 800mT. The graph shown in Fig.3.6 shows a typical graph featuring the low field spike and the higher field negative MR shoulder approaching the saturation field. The sample is $[Co_{13\text{Å}}Cu_{13\text{Å}}]_{20}$.

3.7.1 The 10mT-1T Field Range

Using the standard model of GMR we expect to find a negative magnetoresistance for all field values until saturation occurs. As the magnitude of the applied field is increased the RKKY coupling between the layers is no longer strong enough to maintain the antiferromagnetic layer configuration and the multilayer system tends towards the lower resistance ferromagnetic configuration. It is noted [29] that the outer layers may turn first as they are more weakly bound than layers in the centre part of the multilayer stack. Our results show this general form in the high field range, but the magnitude of these effects is significantly lower than that necessary for commercial use. The largest result we have seen is 0.25% at room temperature. and 0.9% at 4.2K.

There are two possible types of coupling that could be present in our samples.

Figure 3.6


Film Resistance/ Ω
9.890
9.885
9.880
9.875
9.870
−0.2
0.0
0.2
0.4
0.6
0.8
1.0
Applied Field/T

which can be distinguished by the variation in MR that occurs with increasing space layer thickness.

- Dipolar coupling
- AF coupling with an RKKY -like origin. RKKY coupling is characterised by the oscillation in coupling sign as a function of increasing Cu layer thickness. The coupling strength effect may be weakened owing to bad layer definition, interdiffusion or impurity scattering.

3.7.2 Oscillations

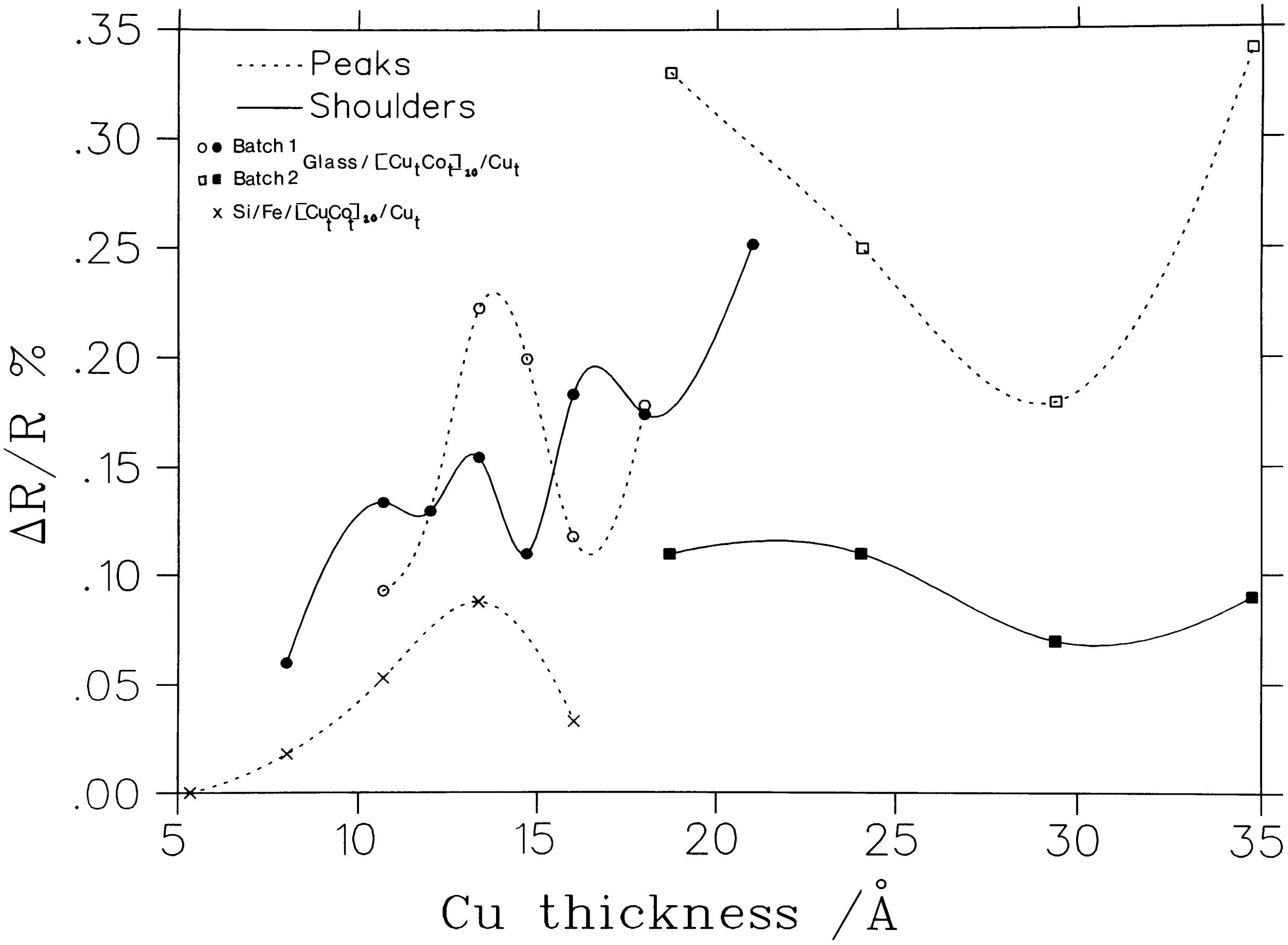
The oscillations in interlayer coupling are manifested as oscillations in the size of the measured MR.

Fig.3.7 is a plot of the size of the MR for the peaks and shoulders for all multilayer series grown, as a function of varying Cu thickness. The circles represent samples from batch 1 which are of the general form glass/$[Cu_tCo_t]_{20}/Cu_t$. where t is a single layer thickness. The squares represent batch 2 of the same general form. The crosses represent batch 4 of the general form doped silicon/Fe/$[Cu_tCo_t]_{20}/Cu_{1\text{Å}}$. The open symbols represent the MR of the low field peaks, the filled symbols that of the higher field shoulders.

Clear oscillations can be seen in both the peak and shoulder data for all samples and this is suggestive of an RKKY-like interaction as the dominant mechanism. The oscillation period is of order 13Å, in good agreement with the results of Mosca *et al* [18]. Parkin [15] found a period of 10Å. The size of the second peak is larger than that of the first. There is some evidence in the trace of the shoulders in batch 2 for superposition of two oscillation periods. Short periods have been widely predicted because of the dimensions and topology of the Fermi surface, and superimposed 2.6 and 8.0 monolayer periods oscillations have been seen recently by Johnson *et al* [91] in Co/Cu/Co sandwiches.

It is generally found and predicted theoretically [31] that the MR will increase with Co thickness up to about 10 Å and then decay as a function of approximately $1/t^{-2}$.

Figure 3.7


Peaks
Shoulders
Batch 1
Batch 2
Glass / [Cu$_t$Co$_t$]$_{20}$/Cu$_t$
Si/Fe/[Cu$_t$Co$_t$]$_{20}$/Cu$_t$
ΔR/R %
.35
.30
.25
.20
.15
.10
.05
.00
5
10
15
20
25
30
35
Cu thickness /Å

It should be noted that for the cases shown the layer thicknesses t_{Co} and t_{Cu} are the same and for small Cu thicknesses the same Co thickness is too small to obtain the maximum MR value.

3.7.3 Improving Multilayer Film Quality

Much research has been involved with the study the effect of film quality on the magnetoresistive properties of multilayers. There are two factors which may affect film quality and layer flatness in general. Substrate flatness is widely regarded as an important key to successful film growth. Large MR has been seen in films grown on silicon [15], glass [32] and MgO [33], [32]. We have investigated the effect of surface flatness on MR by growing films on a variety of substrates including glass, epitaxial (100) silicon, unprepared silicon wafer and Kapton, an amorphous polymer film. In all cases we have seen no marked difference in the size of the ΔR observed. Typical resistance was of order 1-5Ω for film grown on glass and Si producing a MR value of order 0.3%. Films grown on Kapton had resistances of order 70-100Ω and consequently had a smaller value of ΔR/R. That this result was achieved for both chemically etched and unprepared silicon is significant. Unprepared silicon is very rough on a 1-10μm scale whilst chemically prepared silicon appears flat on a scale of less than 0.1μm. Glass has surface ripples on a 1μ scale. As discussed in Section 3.5.1 films grown on glass result in fewer low angle X-ray diffraction peaks than those grown on silicon which was interpreted as implying inferior film quality. However lack of film flatness on a micron length scale appears to have no effect on the size of GMR found in these samples. It can concluded that surface flatness is not a limiting factor on the size of GMR found in these films.

The second important factor which can improve film quality is the use of buffer layers. The reasons for including such a layer include the fact that the constituents of the multilayer may react with the substrate or may tend towards island formation when grown on a given substrate type. For example, as will be described below samples made with a copper layer deposited directly onto silicon show reduced MR , implying poor film quality. This effect was also seen by Parkin [34] who confirmed the low quality with

transverse electron micrographs through the film cross- section. It was found that an iron buffer layer reduced numbers of stacking faults in the film compared with a multilayer with no buffer and resulted in an improved GMR [15]. It has been shown [35] that a 60Å iron buffer layer thickness is optimum. This thickness of iron is required to produce a good quality iron film onto which the multilayer can be grown. Thicker iron films offset this improvement in film quality by effectively short circuiting the multilayer resistance.

A series of samples were grown, each consisting of 20 bilayers containing 13Å Co and 13Å Cu layers. In this series films were grown with and without iron buffers, and of the form $[Co,Cu]_{20}$ or $[Cu,Co]_{20}$. For films with Cu grown directly on silicon the MR was small and in some cases negligible. No significant improvement in magnitude of the MR was found. Films with iron buffer layers showed a slight improvement in their MR ratios over other systems. However in later magnetometry experiments on these system the iron moment masks the behaviour of the multilayer moments. Further investigations will largely neglect these films, as in all other respects, the results are very similar for films with and without Fe.

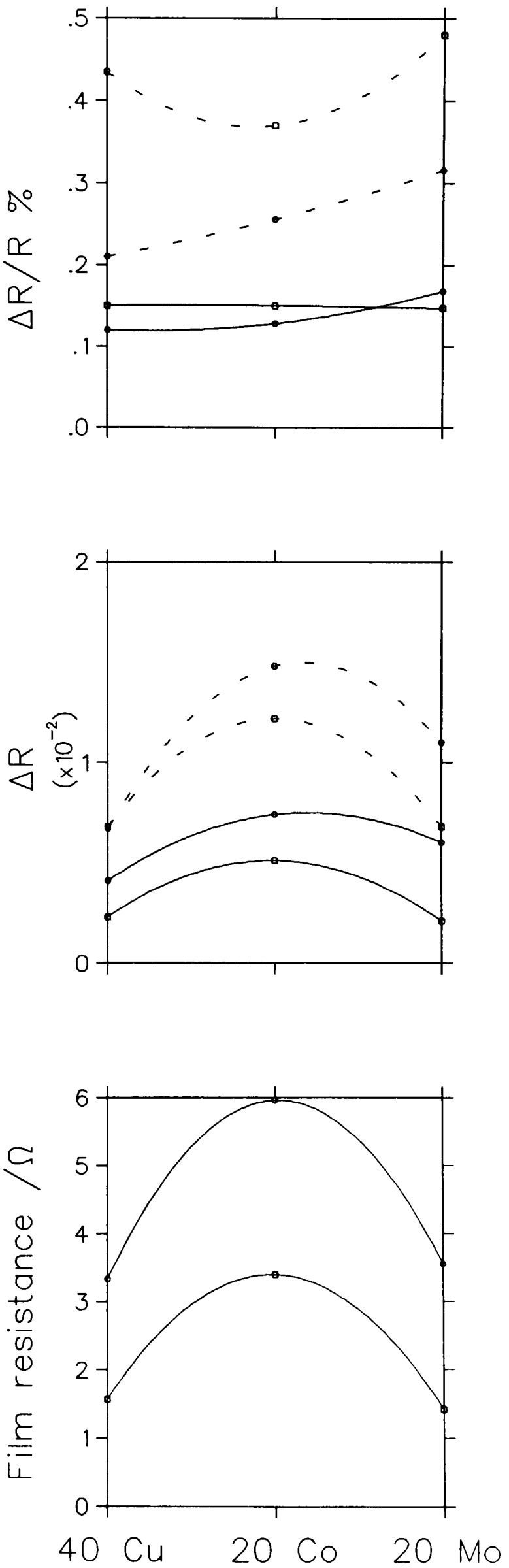
In conclusion it has been found that the MR of a multilayer is largely independent of the substrate on which it is grown. It is found that systems featuring Cu layers grown directly on Si have a poorer than average MR. In the following section multilayers featuring a range of buffer layers will be investigated.

3.7.4 Buffer layers

A series of samples of the form glass/X$[CuCo]_n$ where X was Mo,Cu,Co and n = 20,40 were grown. It was found that for the same value of n there was a measurable variation with buffer element as shown in Fig. 3.8. A second series of samples was grown on a carbon buffer layer.

None of the buffer layers produced a significant improvement in MR, the effects being of order 0.3%. The fact that the series n = 40 shows no significantly larger MR implies that the electrical shorting effect of the buffer layer is not pronounced.

Because such a wide range of buffers (Fe,C,Mo,Cu,Co) and substrates have been



peaks - - -
shoulders ——

Figure 3.8

utilized it is extremely unlikely that island growth or clumping are resulting in poor film quality. We conclude that there are factors other than the effects of a buffer layer which are significant in dominating the MR effect. These could involve impurities or interdiffusion due to high ion beam deposition energy.

3.7.5 The Low Field Range

The sharp central peaks seen for the B⊥I measurement configuration in the ±10mT range are not so easily explained. All effects of this type which have been seen in the MR measurements have corresponding features in the χ results; this suggests a correlation between the magnetic structure and the low field transport properties of the films. Peaks in resistance of similar size and at similar field values have been seen for other multilayer, spin valve and permalloy samples [36], [37], [38] [39], [21], [40], [41], [42]. A similar effect was widely reported during the 1970s [43], [44] in iron and cobalt and was identified with domain nucleation and growth effects. A theory of this residual resistivity proposed by Cabrera and Falicor (1974) [45] concludes that a Bloch wall may produce a sizeable contribution to the electrical resistivity of ferromagnetic metals when the density of states for spin up and down electrons are highly dissimilar. This is indeed true in the system currently considered.

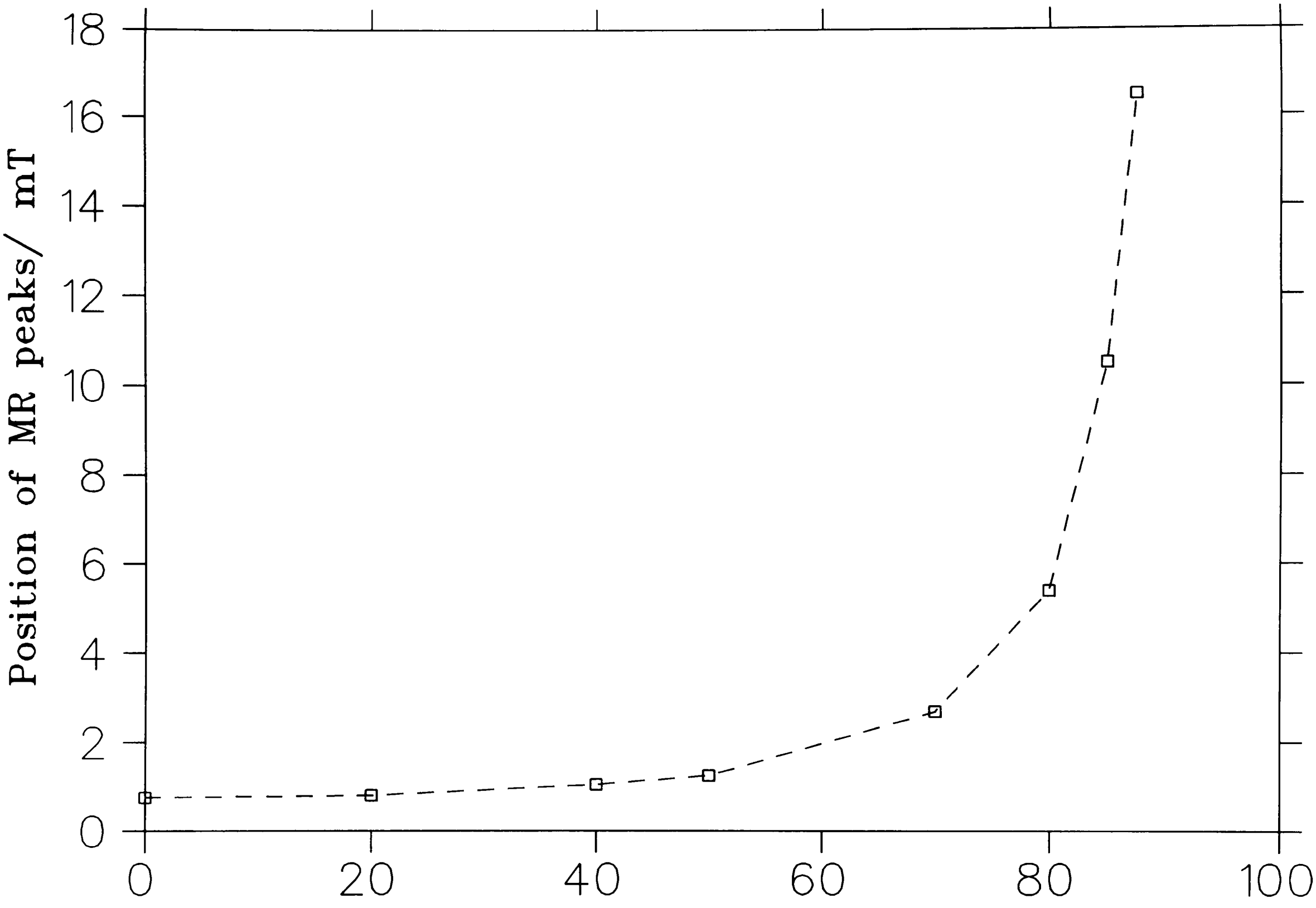
An alternative explanation is that the zero field state possesses out of plane cobalt moments, which could be pulled into the layer on application of a field in-plane. This would produce a change in electric field along the sample due to the extra-ordinary Hall effect as will be described in Section 3.7.8. This hypothesis has been tested by making measurements with the applied field H at an angle θ to the plane and perpendicular to the current direction. It is found for films of t_{Co}=t_{Cu}=13Å that the variation in the coercive field can be fitted with great accuracy to an equation of the form,

$$H_c(\theta) = \frac{H_c(0)}{\cos\theta} \qquad [3.3]$$

where θ equals the angle between the applied field and the sample plane, indicating that the cobalt spins do not lift out of the plane to any measurable extent (Fig. 3.9).

For thicker films (21Å Cu and Co thickness) it was found that the position of

Figure 3.9


Position of MR peaks/ mT
0
2
4
6
8
10
12
14
16
18
0
20
40
60
80
100
Angle between applied magnetic field and sample plane/deg

the peaks varied little with the field angle to plane until $\theta = 90°$. This suggests that for increased Cu thickness the spins can tilt out of plane in the direction of an applied field. However similar in-plane MR and χ data resulted from both these films eliminating out-of-plane anisotropy as a cause of the low field effects.

Camley *et al* [29] have suggested that the outer layers in a multilayer stack are less tightly AF coupled. It was proposed that these outer layers are free to flip to point in the direction of the reversed field before the whole stack turned, then there would be 2 less AF boundaries to scatter an electron resulting in a decrease in resistance over a small region. This is similar behaviour to that observed in spin valves. More sophisticated models involving several loosely coupled layers could give rise to maxima and minima in the small field region. The problem with this model is that one would expect the low field peak heights to be a maximum of approximately 5-10% of the full change over the 1T field range. This maximum can be defined because the decrease in MR resulting from the ferro-alignment in low field of one or two AF scattering boundaries can at most be this percentage of the decrease in MR due to the alignment of the remaining 19 AF scattering boundaries at 1T. This in fact is not the case as the central peak is often comparable in magnitude to, or sometimes greater than, the full large field magnetoresistance decrease.

3.7.6 Single Magnetic Layers

In order to find out whether any one constituent of the film was contributing to the low field effects or whether this was a consequence of multilayering,films of Co and Cu were ion beam sputtered for 100s onto glass substrates and investigated using identical MR and susceptibility techniques. Cobalt exhibited a small central peak (of magnitude 0.1%) in its transverse MR. The size of this peak was measured as a function of the angle of applied field relative to the current direction. It was found that the peak height decreased and then became negative for B parallel to the current I. MR measured for this configuration is known as longitudinal magnetoresistance (B||I). This result provides evidence for the identification of such peaks as being produced by domain effects within the Co film. No measurable MR was seen in the region 10mT to 1T for these single layer

films. This emphasizes the fact that the multilayering of the sample does induce a change in the electrical transport properties of the films.

3.7.7 Angular Dependence of MR in the Sample Plane

The above experiment was repeated for the multilayered films. The field, B, was rotated in the plane of the film with respect to a fixed current direction. The magnetoresistance and susceptibility were measured, and peaks and dips at low field were found as a function of angle of applied field relative to the current direction in both sets of data.

Figures 3.10, 3.11 and 3.12 show the results obtained for B$\perp$I, B$\|$I and with B at 30° to I for a sample of the form $[Co_{11\text{Å}}^{\circ}Cu_{11\text{Å}}^{\circ}]_{20}$. The film resistance and the rf susceptibility are shown in green and blue respectively. In addition to the peaks and dips in the B$\perp$I and B $\|$I directions unexpected MR and χ effects were seen, which featured both maxima and minima. The effect was largest in one particular direction in the plane of the film (Fig.3.12).

Several samples were characterized using a alternating field gradient magnetometer (AGFM) which confirmed the presence of magnetic anisotropy in the sample plane. The traces shown in Fig. 3.13 and Fig.3.14 show two traces made at 90° to one another on a sample $[CoCu]_{20}$. The sample shown appears to be ferromagnetically coupled with the easy direction lying in or close to the direction shown in Fig.3.13.

It is noted when using an AGFM, that the alternating field modulation has to be of very small amplitude for samples with a small coercive field. Sample demagnetisation can be achieved by sweeping the field backwards and forwards in loops of smaller and smaller amplitude. In this way over-modulation of the field signal tends to cause sample demagnetisation and results in an apparently lower coercive field and remanence. Although the modulation amplitude can be decreased, for samples with very low coercivity a true measurement cannot be obtained. This limiting factor must be taken into account when comparing this data with results from other techniques such as MR and susceptibility measurements.

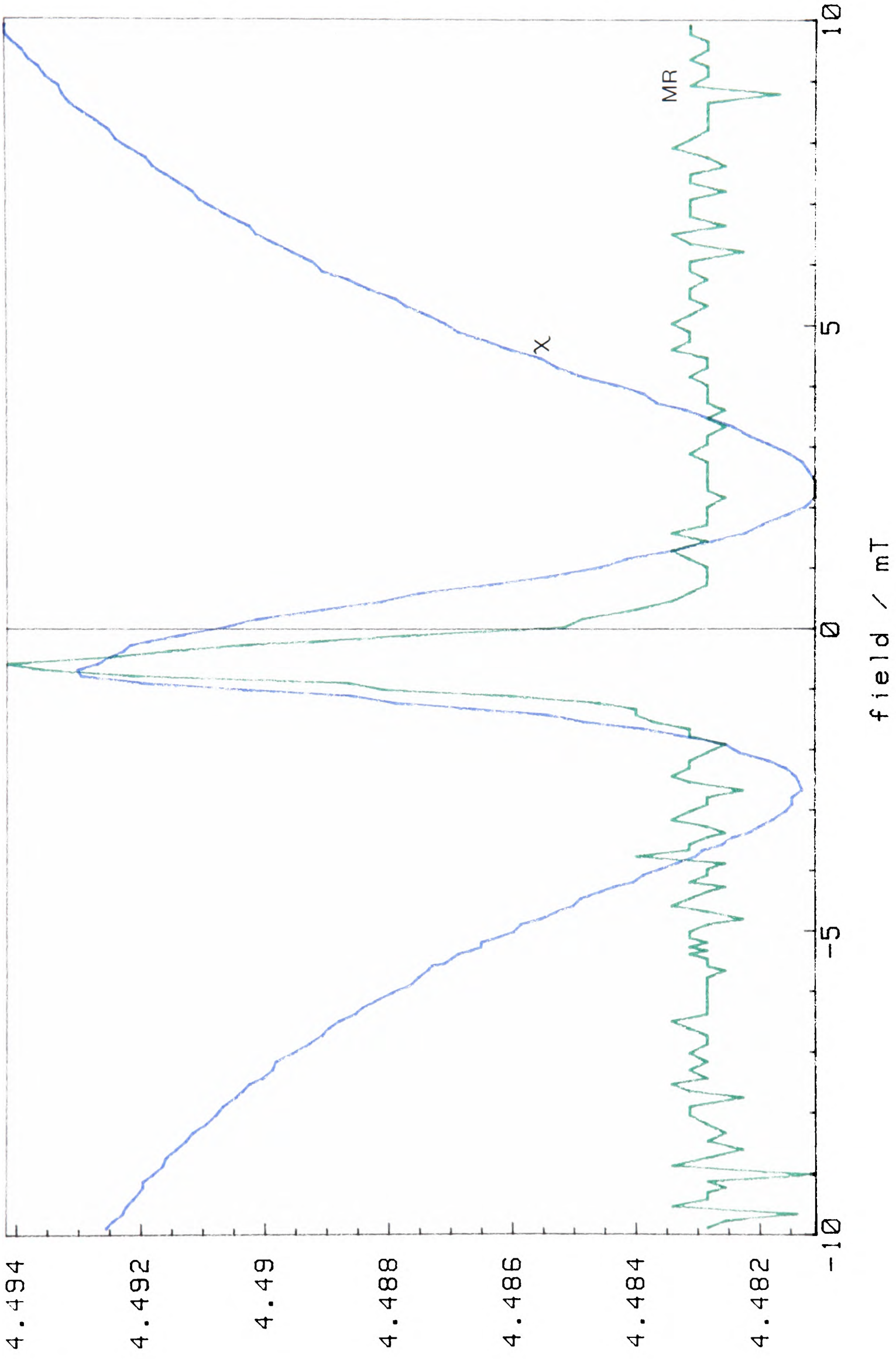

MR
X
10
5
0
-5
-10
field / mT
4.494
4.492
4.49
4.488
4.486
4.484
4.482
resistance / ohms

Fig. 3.10

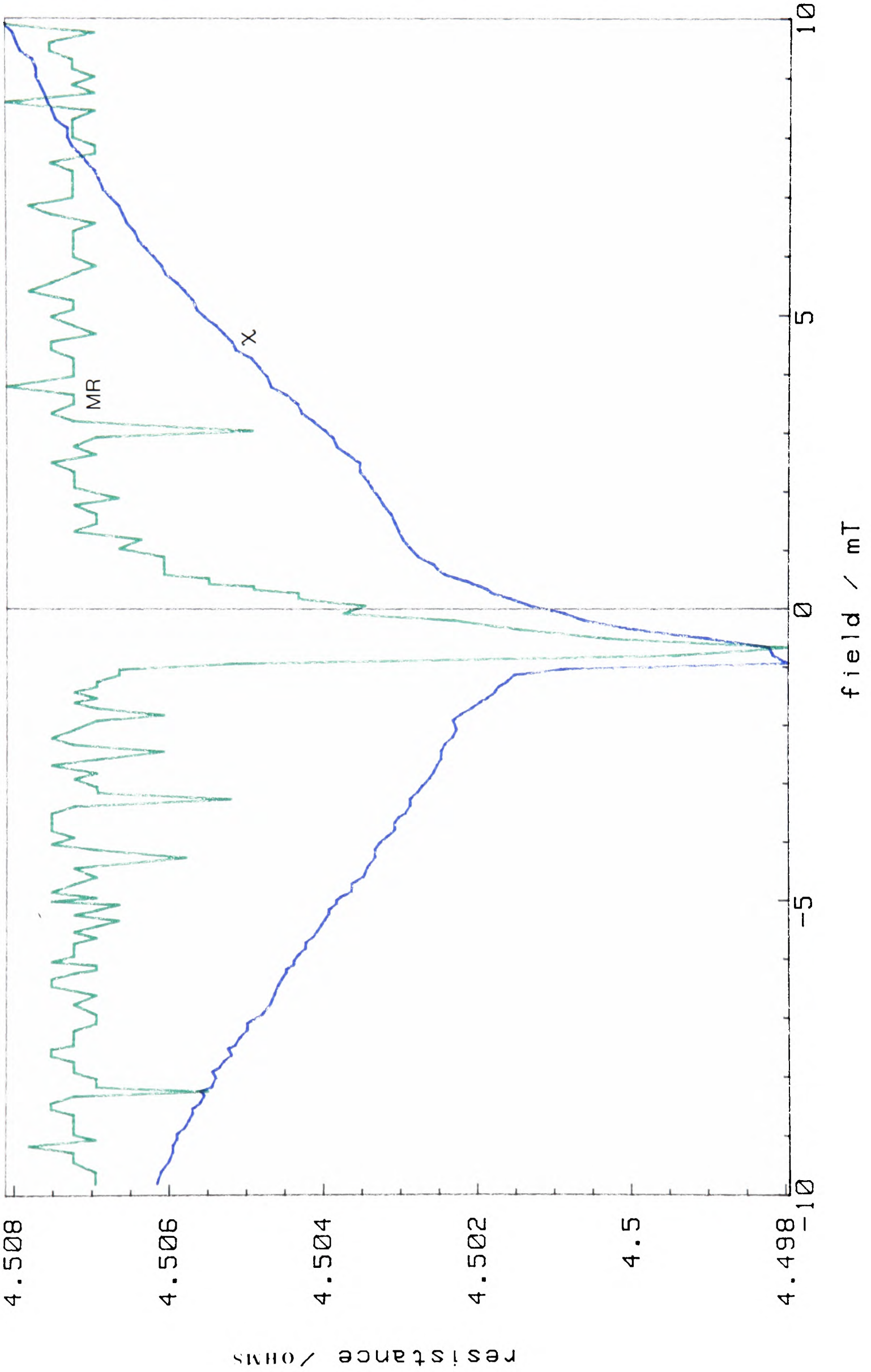

MR
χ
4.508
4.506
4.504
4.502
4.5
4.498
10
5
0
-5
-10
field / mT
resistance / ohms

Fig. 3.11

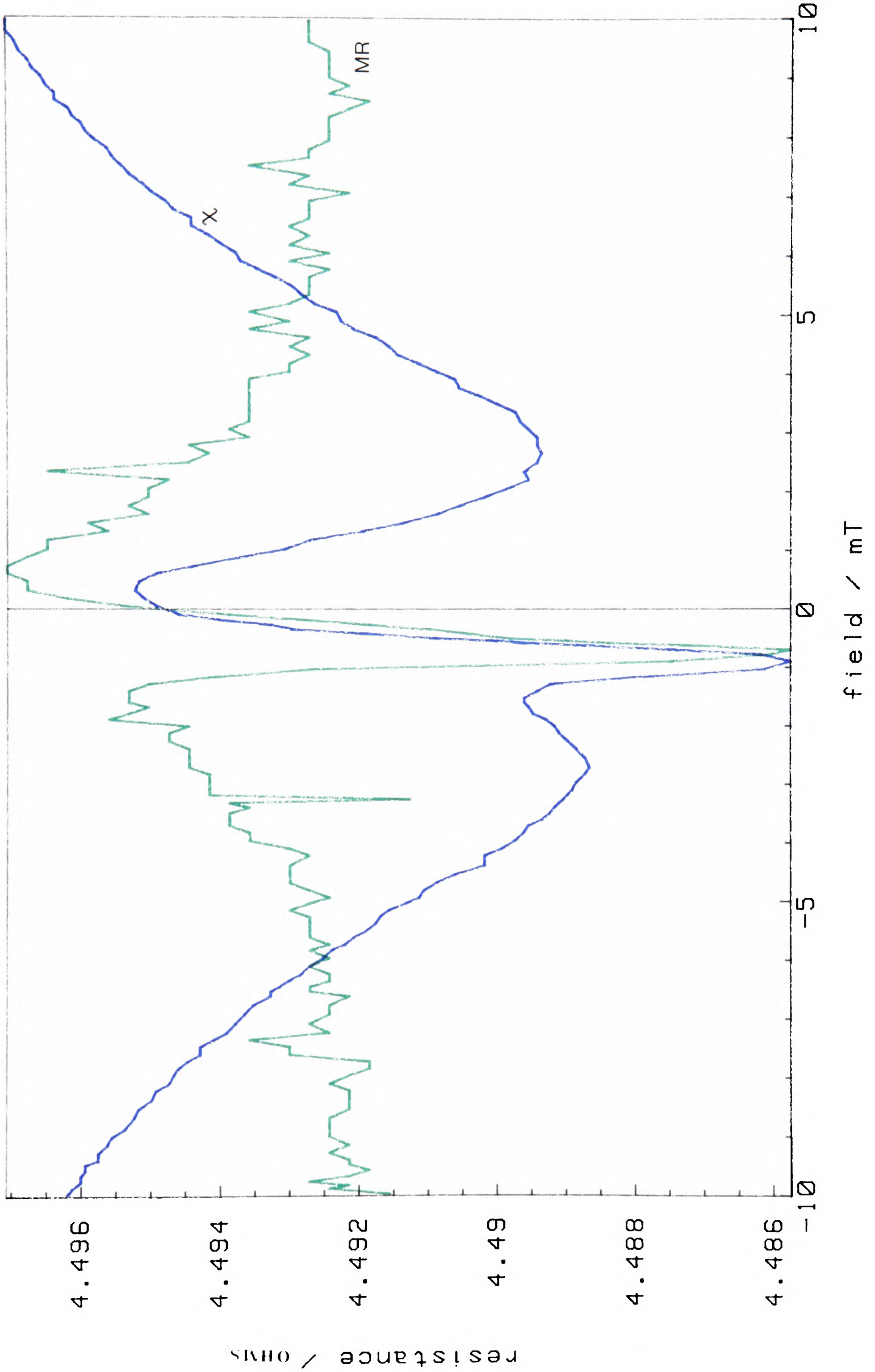

χ
MR
4.496
4.494
4.492
4.49
4.488
4.486
resistance / ohms
-10
-5
0
5
10
field / mT

Fig.3.12

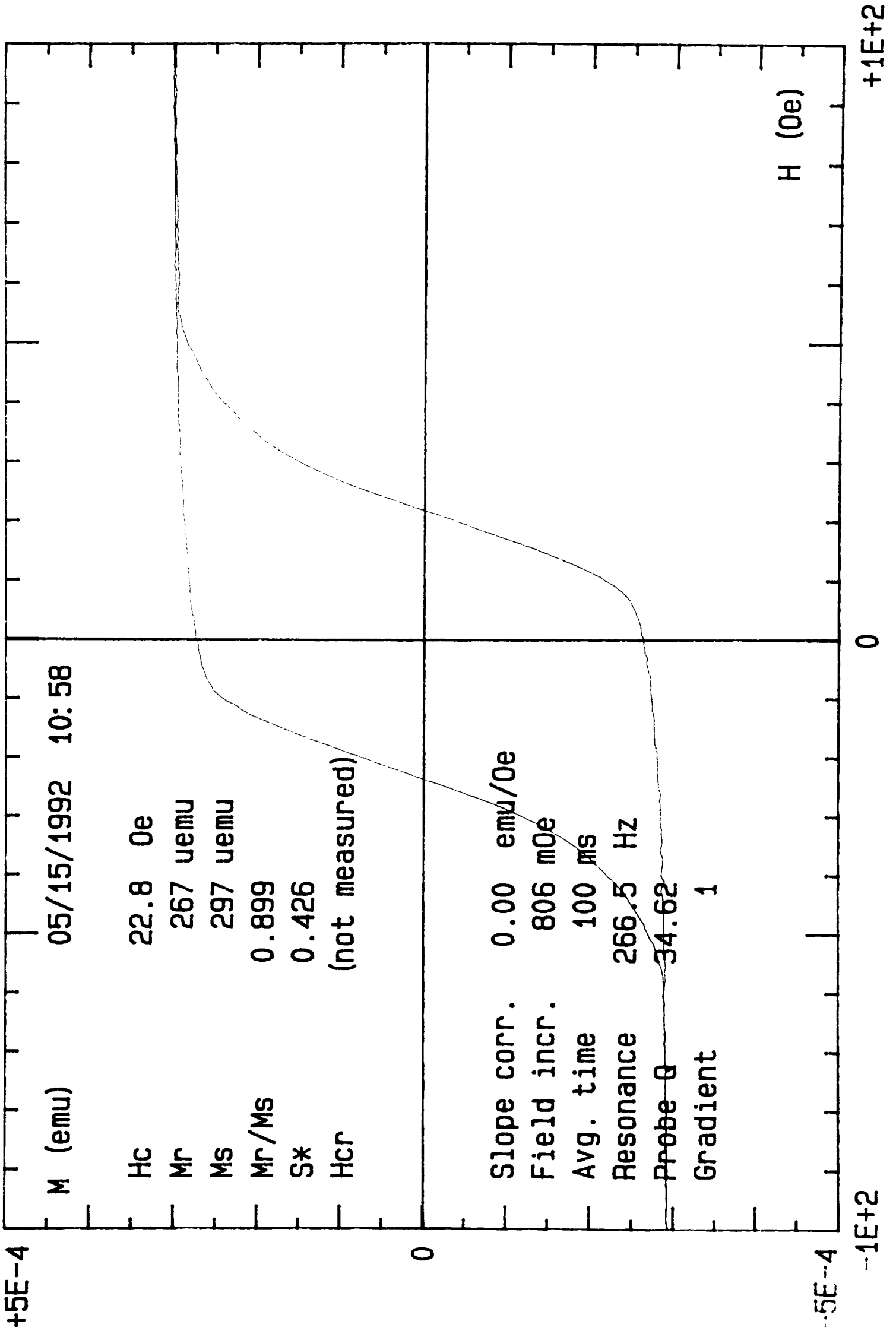
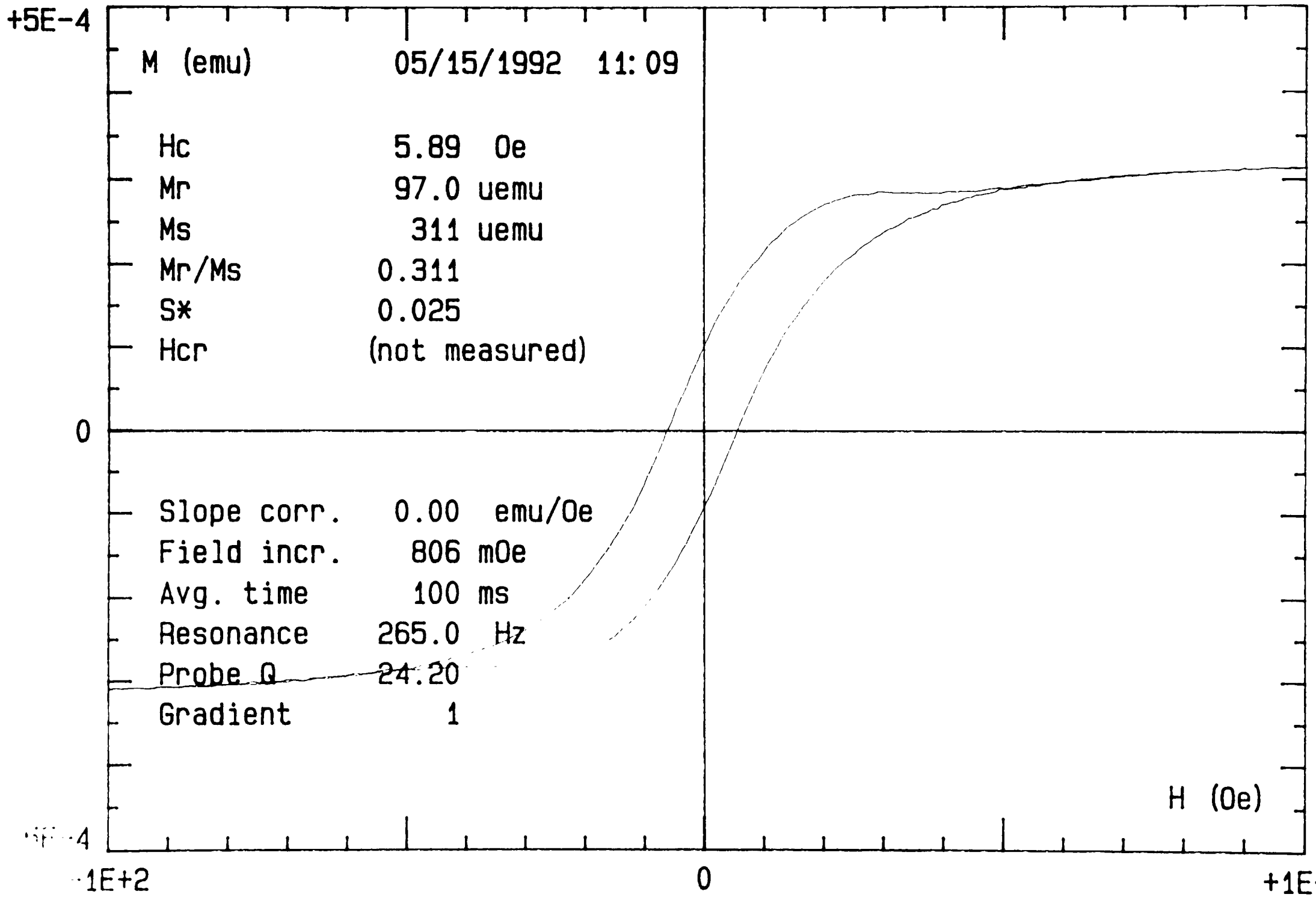

+1E+2
H (Oe)
0
-1E+2
+5E-4
0
-5E-4
M (emu)
05/15/1992 10:58
Hc 22.8 Oe
Mr 267 uemu
Ms 297 uemu
Mr/Ms 0.899
S* 0.426
Hcr (not measured)
Slope corr. 0.00 emu/Oe
Field incr. 806 mOe
Avg. time 100 ms
Resonance 266.5 Hz
Probe Q 34.62
Gradient 1

Figure 3.13

Figure 3.14


+5E-4
M (emu)
05/15/1992 11:09
Hc 5.89 Oe
Mr 97.0 uemu
Ms 311 uemu
Mr/Ms 0.311
S* 0.025
Hcr (not measured)
0
Slope corr. 0.00 emu/Oe
Field incr. 806 mOe
Avg. time 100 ms
Resonance 265.0 Hz
Probe Q 24.20
Gradient 1
H (Oe)
-4
-1E+2
0
+1E+2

3.7.8 Anisotropic magnetoresistance

It was discovered that the background film resistance at low applied magnetic fields (but neglecting the peaks) oscillated sinusoidally between maximum and minimum values which occurred in the longitudinal and transverse measurement configurations respectively. This apparent variation in the measured film resistance for these configurations is known as anisotropic magnetoresistance (AMR) and is defined as the difference between the resistivities for the configurations in which the in-plane magnetisations are respectively parallel and perpendicular to the current $\rho_{\parallel}$ and $\rho_{\perp}$. It depends on the direction of magnetisation relative to the measuring current. This AMR effect is different from the ordinary magnetoresistance effect which depends only on the magnitude and direction of the applied field relative to the current.

The electric field produced by AMR is given by McGuire and Potter [46]

$$\mathbf{E} = \rho_{\perp}\mathbf{j} + \mathbf{a}(\mathbf{j}.\mathbf{a})(\rho_{\parallel} - \rho_{\perp}) + \rho_H \mathbf{a} \times \mathbf{j}$$

where $\mathbf{a}$ is a unit vector in the direction of the magnetic moment in a single domain at an angle α to $\mathbf{j}$, the current density. The last term is the extraordinary Hall effect which may give rise to an additional voltage term for magnetisation components out of the plane and hence give a false reading for the film resistance. Ignoring this term we find that

$$E = \rho_{\perp} j[1 - \cos^2\alpha] + \rho_{\parallel} j \cos^2\alpha$$

Thus

$$\rho(\alpha) = \rho_{\perp} \sin^2\alpha + \rho_{\parallel} \cos^2\alpha$$

$$\rho(\alpha) = \rho_{\perp} \Delta\rho \; cos^2\alpha$$

where $\Delta\rho = \rho_{\parallel} - \rho_{\perp}$. In general it is found that $\rho_{\parallel}$ is larger than $\rho_{\perp}$.

An attempt has been made to separate the effect of the AMR from any effects due to film anisotropy. As explained above the AMR effect can be described clearly by the $\cos^2\theta$ term. The measurements were made in an applied field of 10mT to ensure that the low field "domain effects" would not play a part.

Figure 3.15 shows a plot of R, the film resistance at a field of +20mT as a function of angle between B and I for a sample of the form $[Co_{11\text{Å}}^{\circ}Cu_{11\text{Å}}^{\circ}]_{20}$. A fit to $\cos^2\theta$ is shown as a solid line.

It is found that ΔR for all angle θ is approximately constant at 0.012±0.001 Ω. Any angular variation in $\frac{\Delta R}{R}$ is therefore entirely due to the change in R_0 dictated by the AMR effect.

That the low field peaks/dips are not due to AMR is evidenced by the corresponding changes observed in the susceptibility measurements over the same field range; these results can in no way be affected by the geometry of the electrical measurements. However consideration of the relationship between the peaks and dips and the AMR provides strong clues about the origin of the former as will be discussed in the following section.

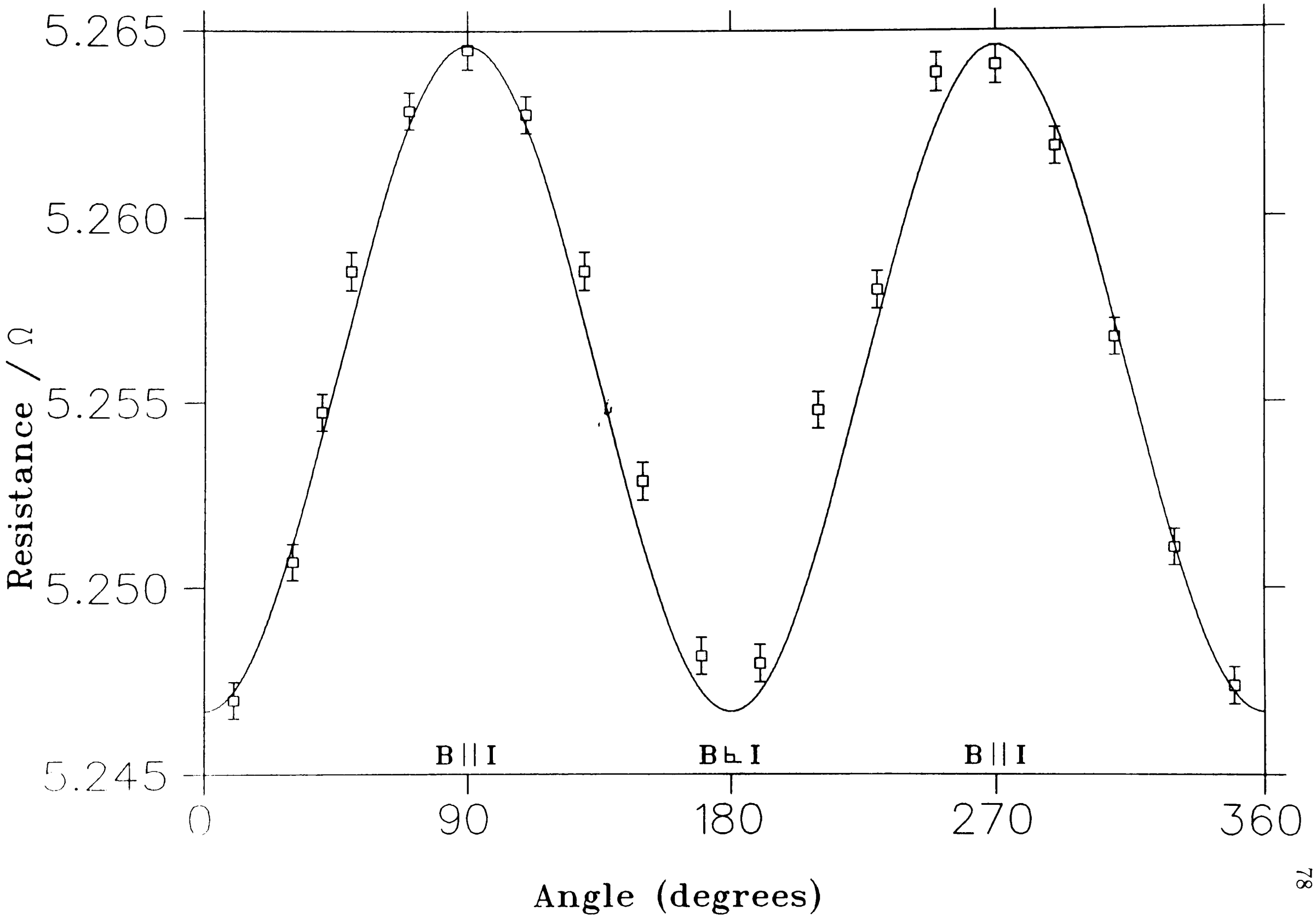
3.7.9 Domain Growth and Rotation

If the ±10mT field range is carefully considered it is noticed that the peaks occur close to the minimum AMR resistance value B⊥I and the dips close to the maximum AMR resistance values (B||I), and that the peaks and dips in the resistance fall within the upper and lower bounds of the AMR (Fig. 3.16).

As discussed in Section3.7.8 the size of the AMR depends on the relative orientation of the magnetisation M and the direction of current flow. In general M will lie in the direction of the applied field B. However in the situation where magnetisation reversal occurs by domain rotation, this is not the case. It must be noted that domain rotation can only occur if there is a tendency for the domain magnetisations to lie in a direction other than that of the applied field, that is to say the film has an in-plane anisotropy. For samples without anisotropy, domain growth is the only mechanism of domain reversal. The presence of in-plane anisotropy was confirmed using magnetometry techniques. In general this anisotropy direction is not located in the $B_\perp$ and $B_{||}$ direction. Domain rotation is therefore a possible mechanism for magnetisation reversal.

For $B_\perp$I in a large field the domain magnetisation is parallel to B and the AMR

Figure 3.15


5.265
5.260
5.255
5.250
5.245
Resistance / Ω
B||I
B⊥I
B||I
0
90
180
270
360
Angle (degrees)

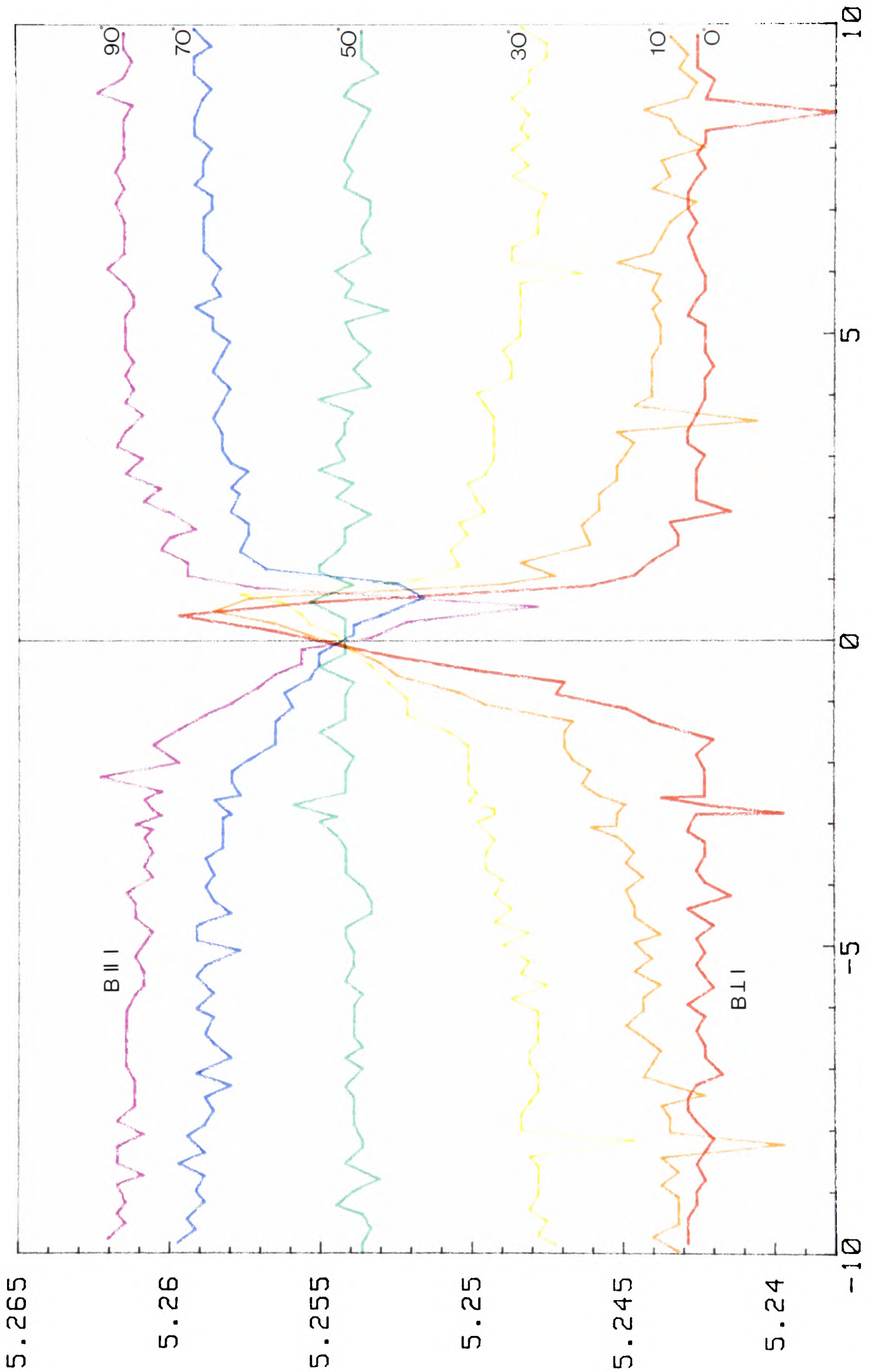

90°
70°
50°
30°
10°
0°
B II I
B T I
5.265
5.26
5.255
5.25
5.245
5.24
resistance / OHMS
10
5
0
-5
-10
applied field / mT

Fig. 3.16

is minimized. If the field direction is reversed as the domain rotates it can be seen that its magnetisation vector will at some point pass through the direction parallel to I, where the AMR is maximized. Thus it can be seen that a sharp maximum will occur for the range of the field values over which the domain rotates. The reverse situation obviously produces a minimum. That the maximum and minimum AMR resistances are often not obtained at the peaks and dips could be accounted for by incoherent rotation over the whole sample due to local fluctuations in the direction and magnitude of the anisotropy field.

Cabrera and Falico's theory [45] of electron scattering from Bloch walls can account for the appearance of sharp maxima at the coercive fields. However this model cannot provide an explanation for the observed decrease in M.R.

In the rare cases in which the in-plane anisotropy lies close to the $B_{||}$ direction it is found that a small deviation above the maximum AMR value occurs. This can be satisfactorily explained by assuming a distribution of anisotropy directions in different parts of the sample; thus in this special direction some parts of the sample will have an anisotropy axis parallel to the field (and current) direction and as such magnetisation reversal must occur by domain wall movement. This will lead to a resistance value greater than the maximum AMR value. No excursion below the minimum AMR value occurs as is to be expected. It is proposed that a trace which features both maxima and minima could be produced by a process involving both rotation and domain growth.

This explanation of the origins of maxima and minima was confirmed in two experiments in which for a given field direction relative to the sample, identical field sweeps were made with the current flowing in directions perpendicular and parallel to the applied field direction within the sample plane. The traces featured complementary characteristics. The minimum in the result of the first current direction was found to be replaced by a maximum of equal magnitude in the current direction perpendicular to it. This clearly agrees with the model of domain rotation.

3.8 Origins of Film Anisotropy

Anisotropy found in thin films and magnetoresistance measurements has been attributed to epitaxy (or partial epitaxy) of the film [39] which can occur even in non-mbe films [33], as a result of an applied field [48], [46] or strain during deposition [50], or abrasion of the substrate surface [49] producing easy and hard directions in the magnetisation.

The films have been shown to be highly polycrystalline which eliminates partial epitaxy as a possible cause of the anisotropy. A magnetic field of order 1mT-10mT applied during deposition can produce a preferred direction in the magnetic properties of a film. The process by which this occurs is not fully understood as the fields involved are very small, however it is thought that only polycrystalline films are affected in which the smaller crystallites may well tend to grow in a favoured direction specified by an applied magnetic field. Using a Hall probe the stray fields inside the chamber were measured. These appeared mainly in the vicinity of the magnetrons and horizontal ion gun where deposition occurs; it is therefore quite conceivable that these fields could induce an anisotropy direction in the polycrystalline films grown. The field directly above the magnetrons was 4.5mT falling to 0.63mT at the sample position. The new substrate table will have radial recesses behind the substrate positions in which 80mT field strength NdB bar magnets can be placed to see if any significant film anisotropy can be induced in a controlled direction.

It is likely that the 2 clips used to hold the substrate in position would exert strain on the silicon. The clips were used to hold the ends or 2 corners on the same edge of the sample depending on the shape of the substrate. A film grown on a sample under stress will be strained when released from the clips even if there was no strain present during growth. The strain was not found to be in the same direction for all samples; this is explained by small variations in the positions of the two clips and the varying amounts of strain exerted by them.

3.9 Low Temperature Results

Cooling the samples produced some interesting results. In all cases as the samples were cooled to liquid helium temperatures the films showed a decrease in the value of R_0, owing to the decrease in the number of phonons (Fig. 3.17). The sample structure is $[Co_{13\text{Å}}^{\circ}Cu_{13\text{Å}}^{\circ}]_{20}$.

The remaining resistance is due to impurity and fault scattering. It is noted that film resistances are noticeably higher than for those of Parkin [15] grown under UHV conditions. This finding agrees with X-ray results which showed that the film is highly polycrystalline. A high impurity concentration could also be invoked to explain this finding. It is found that magnitude of ΔR and the field at which the low field peaks occurred increased with decreasing temperature (Fig3.18).

The data shown here are for a sample structure $[Co_{29\text{Å}}^{\circ}Cu_{29\text{Å}}^{\circ}]_{20}$. However low field sweeps produced results reminiscent of spin valve effects (Fig.3.19).

Such effects are usually seen in trilayer sandwiches featuring one pinned ferromagnetic layer separated by a non- magnetic spacer AF coupled to another ferromagnetic layer. In these samples pinning is not intentionally introduced into the systems; however in-plane anisotropy pinning may be playing a significant role at these low temperatures.

3.10 Possible methods of improving film quality

The variations in the MR caused by changes in film composition and substrates have been investigated above. This section discusses methods of film growth and film treatment, which may affect film structure.

3.10.1 Preheating of sample

It was found that all films produced using the pre- heating method on silicon showed no magnetoresistance peaks in low fields. However the background slopes were found to be unaffected by the heating process. This indicates that substrate preheating affects film growth and suggests a possible lack of film anisotropy direction which would force magnetisation reversal to occur by domain wall movement.

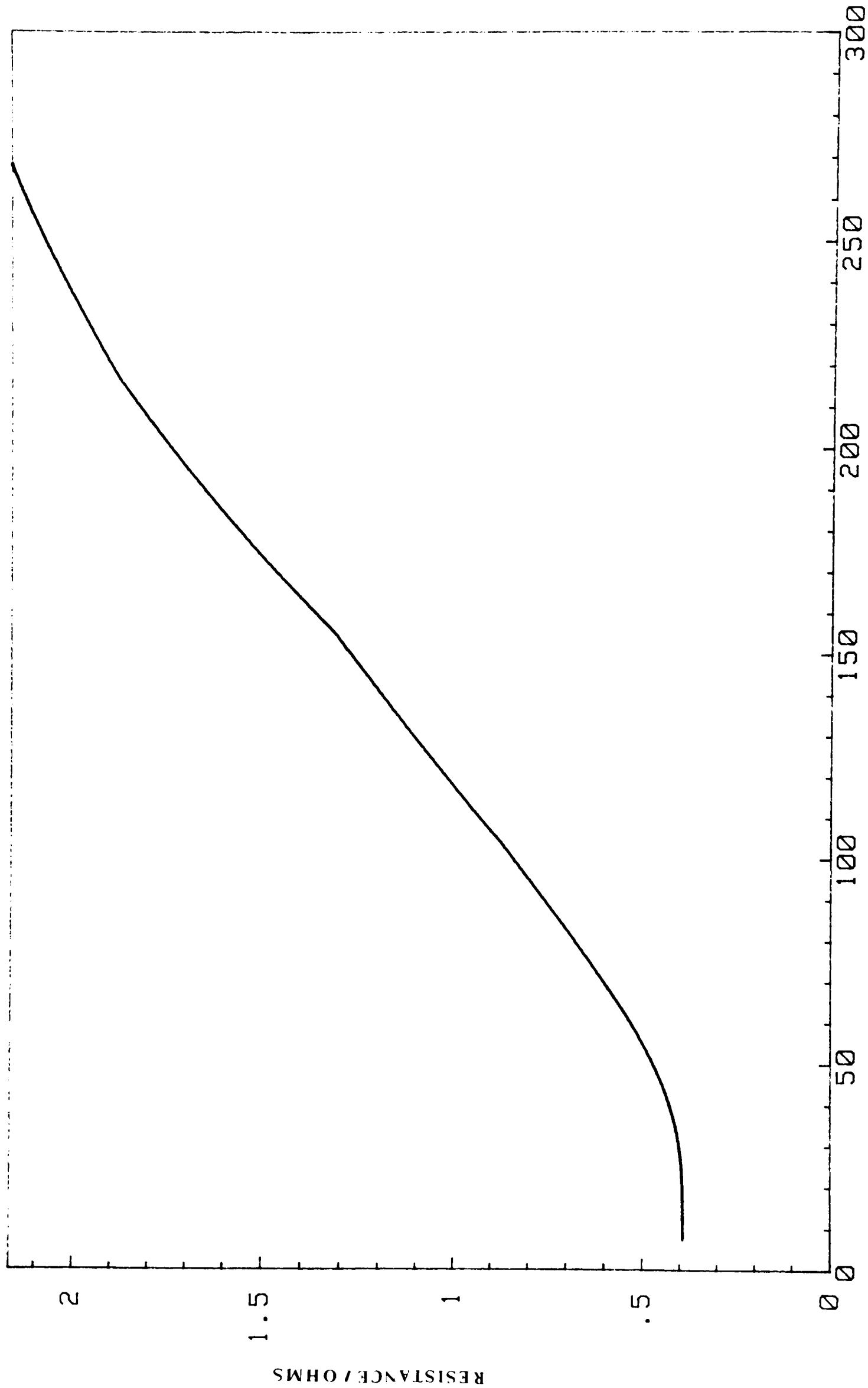

0
50
100
150
200
250
300
TEMPERATURE / K
0
.5
1
1.5
2
RESISTANCE / OHMS

Figure 3.17

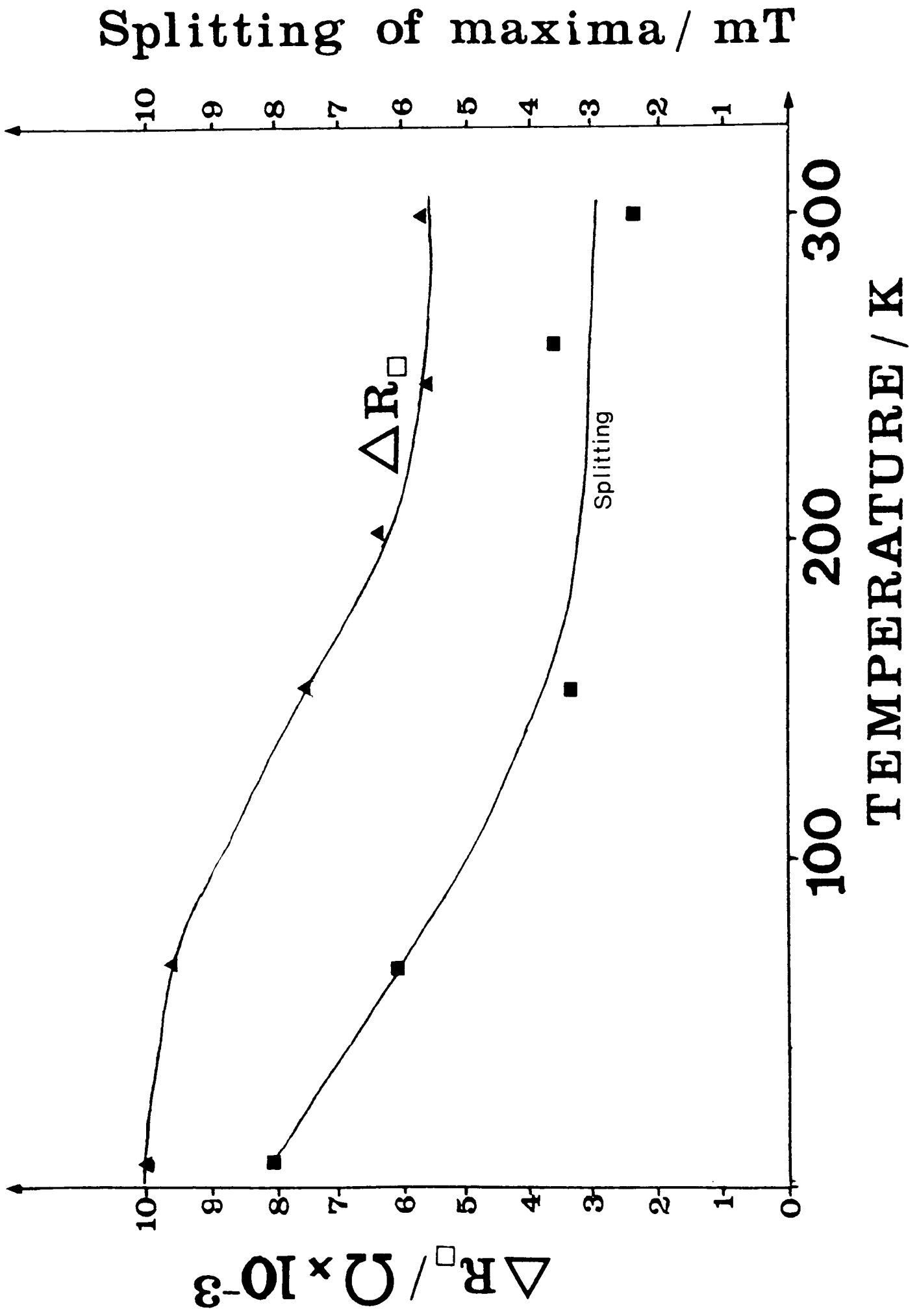
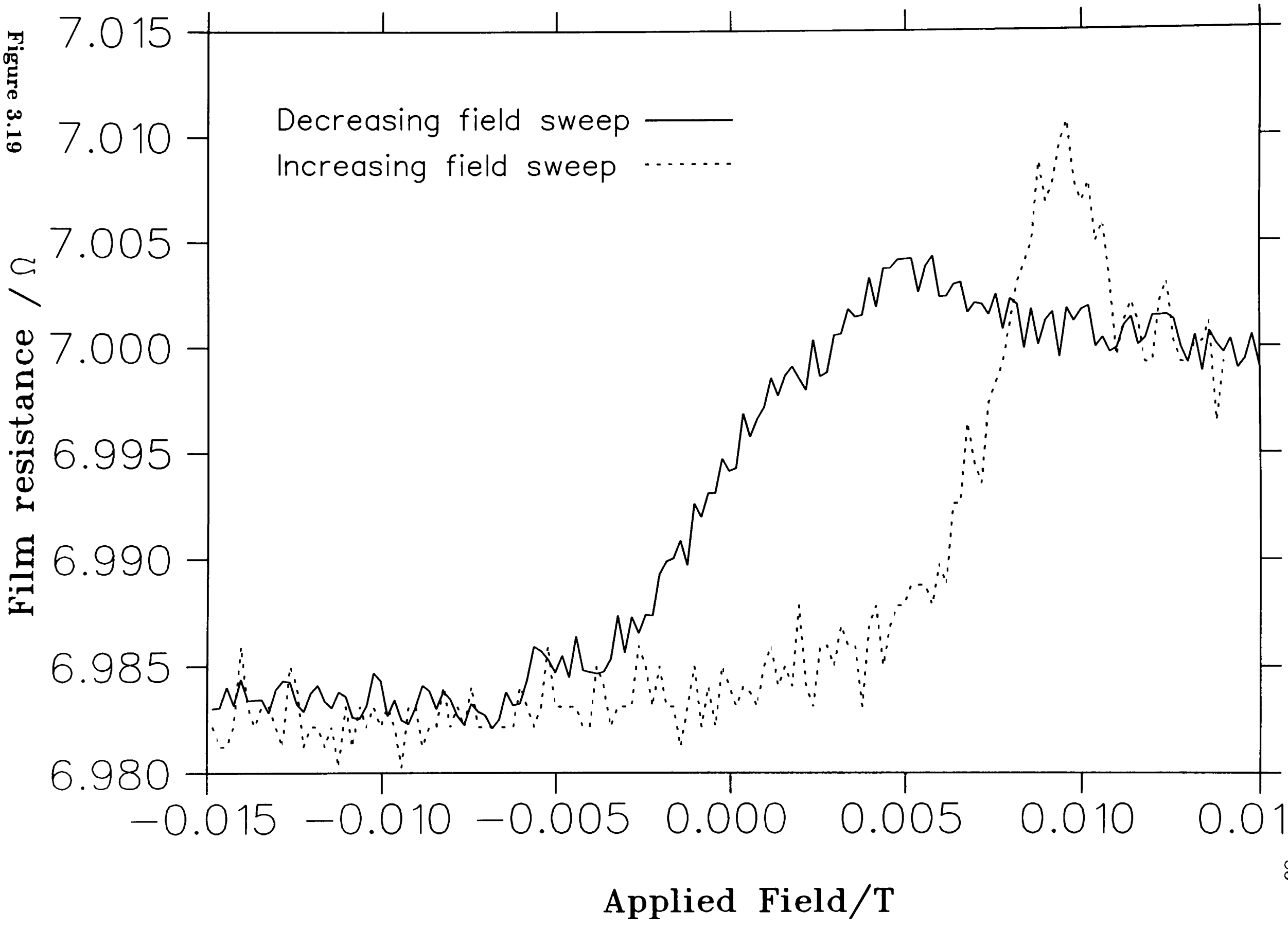

Splitting of maxima / mT
10
9
8
7
6
5
4
3
2
1
0
300
200
100
TEMPERATURE / K
ΔR□
Splitting
ΔR□ / Ω x 10-3

Figure 3.18

Figure 3.19


Decreasing field sweep
Increasing field sweep
Film resistance / Ω
7.015
7.010
7.005
7.000
6.995
6.990
6.985
6.980
−0.015
−0.010
−0.005
0.000
0.005
0.010
0.015
Applied Field/T

3.10.2 The Effect of Changing Ion Beam Energy

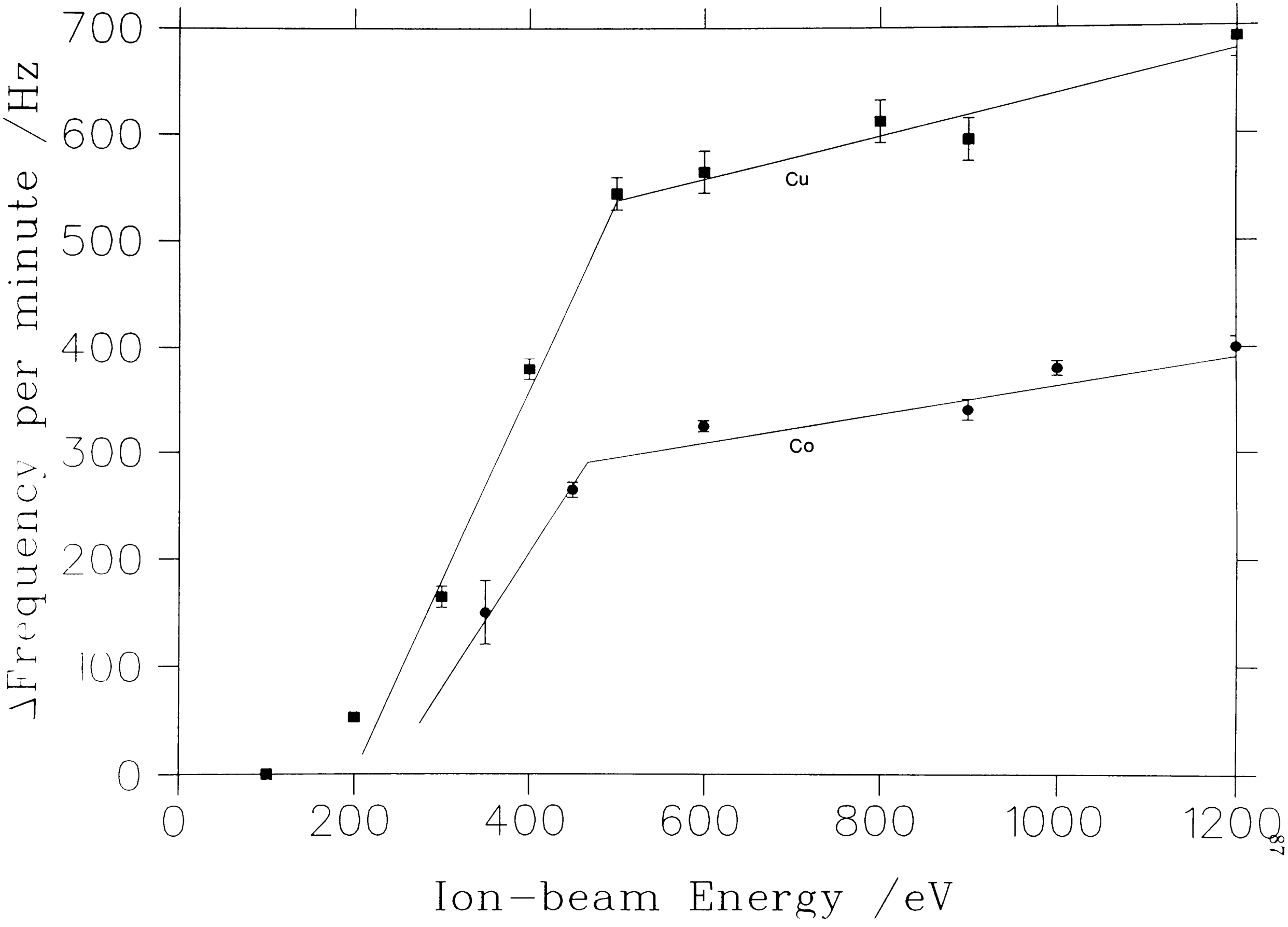
As discussed in chapter one, it is possible to vary the energy with which the electron strikes the target by varying the accelerating voltage. This energy is then transferred to the sputtered atoms and is important because it affects the physical structure of the film of which the atoms become part. A particle that arrives with a high energy may cause a cascade of collisions of atoms already within the film causing disorder and hence interdiffusion. Initially the films were grown using a 900eV ion beam. A series of specimens were made in which the ion beam energy was varied over a range 200 - 1100 eV. For 300eV and 350eV beam energies the resulting MR was negligible although some low field peaks were observed. The size of the MR increased as the beam energy was increased to 600eV for which a 0.1% MR was seen. For higher beam energies similar values were observed to those normally seen ($\sim$ 0.3%). No significant MR was obtained. However Saito *et al* [33] have recently successfully produced GMR using this method. By varying beam energy over a similar range they have found a maximum of 60% MR ratio at 600 eV whilst seeing effectively no MR at energies 150 eV either side of this value. A possible cause of the lack of a significant improvement in our results could be the fact that below 600 eV the rate of sputtering falls off very rapidly as shown in Fig 3.20. The deposition rate is shown as the change in frequency of oscillation of the quartz monitor.

To deposit at 800 eV takes approximately 3 seconds per 10Å layer, whilst at 200 eV the same thickness takes 36 seconds. This long deposition time means that relatively more impurity atoms may be incorporated into the films resulting in poor film quality. This is a problem which arises because film growth occurs under non-UHV conditions.

3.10.3 Sample Annealing

It is known [62] that copper has very low solubility in cobalt and vice versa. It was thought that by annealing multilayers it may be possible to reverse the effect of any interdiffusion that may have occurred during deposition, by whatever mechanism, at the layer interfaces. The MR of a sample of multilayer structure $[Co_{19\text{Å}}^{\circ}Cu_{19\text{Å}}^{\circ}]_{20}$ was measured before (Fig.3.21a) and after annealing (Fig.3.21b) at 400° for 24 hours. Results

Figure 3.20


ΔFrequency per minute /Hz
700
600
500
400
300
200
100
0
0
200
400
600
800
1000
1200
Ion-beam Energy /eV
Cu
Co

after annealing show that $\frac{\Delta R}{R_0}\%$ has increased from 0.22% to 0.49% for the peaks and from 0.12% to 0.28% for the slopes. The size of ΔR/R for the slopes has increased by a factor of 2. It can be seen that the value of R_0 has decreased by a factor of 5; this could be due to reduced strain and scattering owing to structural faults which could relax during the annealing process and may be in part due to increased crystallite size. The value of ΔR/R for the low field peaks is found also to have have increased by a factor of 2. It is seen that the width of the peak is seen to be broadened over a 200mT field range about the origin. This could be explained by a decrease in the coherence of the anisotropy direction across the sample resulting in less coherent domain rotation.

The increase in MR, though a significant improvement on the non-annealed sample, did not result in a GMR of the required magnitude.

3.10.4 Rf Magnetron Sputtered Multilayers

As described in Chapter 1 the different film production methods produce films of different qualities. Many of the multilayers that show giant magnetoresistance have been grown using rf or dc [15],[18] magnetron sputtering. Therefore an attempt was made to grow multilayers using the rf magnetron in the chamber in order to establish whether the lack of GMR was due to structural differences or contamination problems. The resulting samples produced a maximum MR of 0.4 % for a sample of nominal $[Cu_{11\mathring{A}}Co_{8\mathring{A}}]_{20}$ structure. Samples with Cu thickness lower or higher than this showed smaller MR. All $\frac{\Delta R}{R_0}$ results were of comparable magnitude to those previously obtained from ion-beam sputtered samples. However there are difficulties in maintaining a constant deposition rate owing to variations in the background argon pressure and it is therefore uncertain as to whether individual layer thicknesses are highly accurate. During a typical deposition the deposition rate was measured before and after deposition and was found to vary by up to 10% over a 1 minute period. The average deposition rate over a 5 minute period was used for all calculations of film thickness. Low angle X-ray measurements were made and indeed there appeared to be drift in the bilayer thickness indicated by an broad and irregularly shaped peak. The overall film thickness was, however, as expected. A

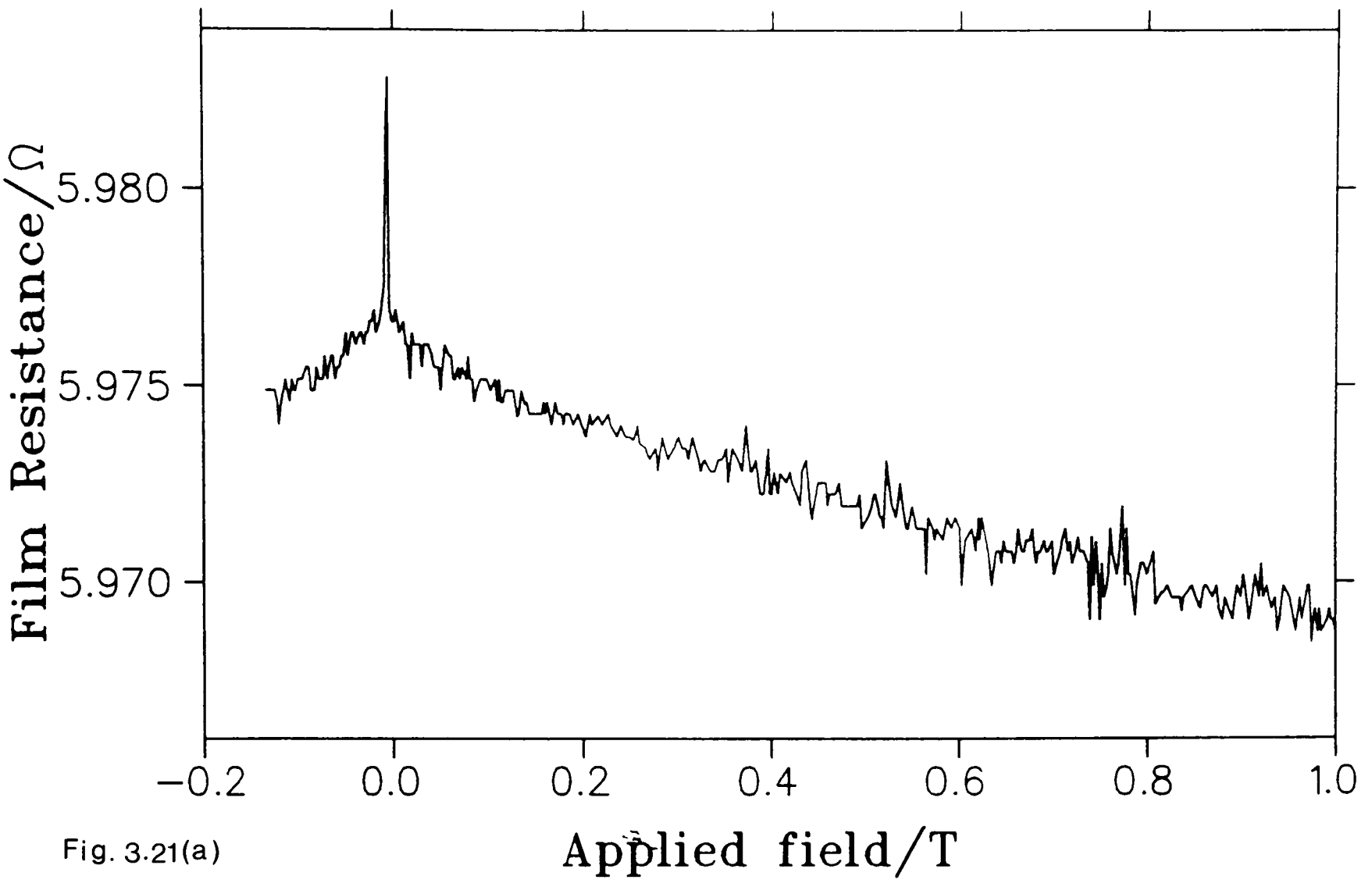


Fig. 3.21(a)

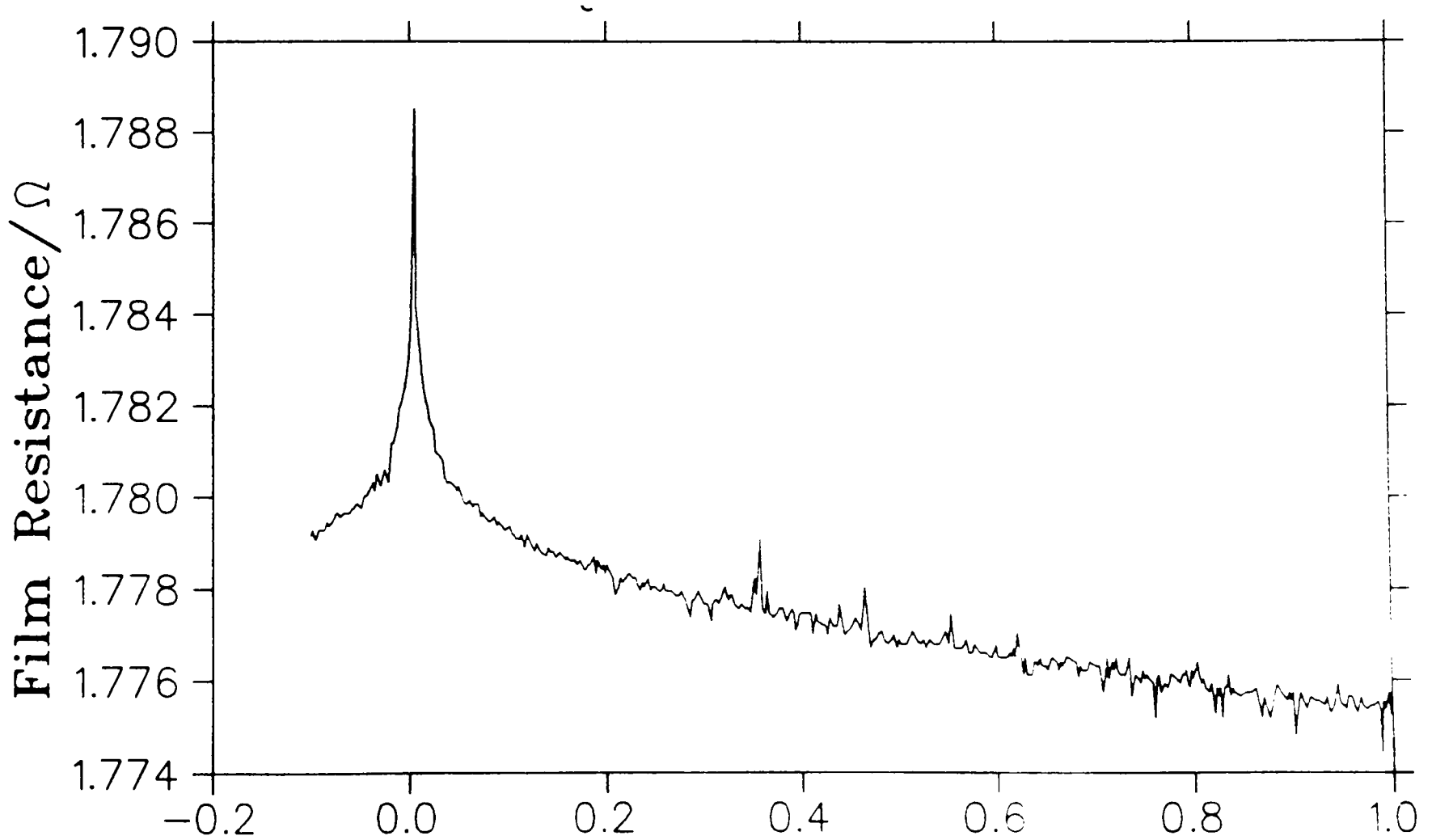


Figure 3.21 (b)

feedback system is needed to attain uniformity of layer thickness.

It is difficult to assess whether films are non-uniform enough to destroy GMR, but the fact that samples made by two different methods exhibit small negative MR of the same order of magnitude suggests a common limiting factor. This points towards a possible contamination problem. Auger electron spectroscopy results have identified oxygen as a contaminant; however it is uncertain as to whether this is merely due to surface oxidation and the presence of silicon oxide or whether the oxygen is internal to the film itself. One source of contamination for both methods could be the proximity of the magnetrons and ion beam targets to the Meissner trap. Local heating could result in the condensed contaminants being desorbed from the "cold" surface directly into the sputtering regions. The impurities arise from the fact that the vacuum chamber has only high vacuum capabilities. The most successful GMR samples have been grown in UHV systems by magnetron sputtering [15],[18], [19] and ion-beam deposition [33].

3.11 Conclusions

In conclusion we have grown CoCu multilayer films of good structural quality on (001) Si wafer with interesting anisotropy properties. The magnetoresistance properties have proved to be insufficiently large for commercial applications despite variations in film growth techniques, magnetic and spacer layer thickness, buffer layer material, substrate, substrate pre-heating and post-deposition annealing. It is therefore concluded that the limiting factor on the GMR must be either impurity scattering which results in a very short electron mean free path, or possibly that the degree of interface roughness is not conducive to high GMR.

Chapter 4

Heterogeneous Alloys

4.1 Introduction

Giant magnetoresistance (GMR) was initially observed in antiferromagnetically coupled multilayer systems [51]. It is generally agreed that the GMR effect arises from spin-dependent scattering at the multilayer interfaces or in the bulk of the ferromagnetic (FM) layers. Alignment of these coupled layers under a large applied field causes a decrease in film resistivity. Much emphasis has been placed on the effect of layering, the size of magnetic domains, connectivity between layers and the role of the interlayer exchange interaction. Later work on uncoupled magnetic sandwiches [21] confirmed that the GMR effect is entirely due to reorientation of magnetic layers, and is not an effect of the exchange coupling. The orientation of the domain magnetisation is random at the coercive field, H_c, so statistically a significant number of domains in one layer will be arranged with their magnetisation anti-parallel to those in the next layer. Application of a magnetic field produces moment alignment and a corresponding decrease of resistance.

By extension it is apparent that a random array of magnetic granules in a non-magnetic (or weakly paramagnetic) matrix might also show GMR effects. Such systems have been prepared by simultaneous deposition of 2 immiscible metals, one ferromagnetic and the other non-magnetic. Recent results [52],[53] show that GMR is found for an alloy containing single domain cobalt particles in a copper matrix. Thus it has been demonstrated that multilayered geometry is not a prerequisite for GMR.

4.2 Production of Alloy Films

In the work described in this chapter CoCu alloy films were initially grown using an ion-beam technique. The first of two methods tried involved rapid rotation of two

targets in front of the ion beam producing in effect a "multilayered" sample in which each layer was $\sim$ 1Å thick; these very thin layers effectively result in the formation of an alloy. The second method utilised a single target of cobalt covered by a punched sheet of copper. The area of the holes was calculated to give a 20% Co concentration in the final alloy taking into account the faster Cu sputtering rate. Neither of these techniques produced samples which exhibited outstanding MR effects. This was probably because of the sensitivity of the magnitude of the GMR effect on Co concentration as described in Section 4.5.

A method which dispenses with the need to make many trial concentration samples and which ultimately proved successful, used an rf magnetron source, with a circular split target of which one half consisted of pure cobalt and the other pure copper. Two strips of single crystal (001) silicon (1cm x 6cm for magnetoresistance measurements and 0.5cm x 6 cm for AES measurements) were attached to the substrate table above the target area at a height of 4cm which was estimated to be at the correct distance from the target for an alloy with an approximately linear concentration gradient to be deposited; the long dimensions of the substrates were aligned perpendicular to the join between semi-circular Co and Cu targets.

The substrates were initially chemically cleaned as described in Section 3.3.1and were ion cleaned prior to deposition for 2 seconds using a 500eV beam. A short cleaning time was used because whilst it was necessary to remove any remaining impurities from the substrates, it was desirable that some of the silicon oxide layer should remain. This was advantageous because the silicon used was doped to an extent which reduced substrate resistivity to 10Ωcm. The SiO_2 thickness has been estimated for a similar substrate to be 5000Å [54].

Samples were rf sputter-deposited at a rate of 50Å per second. Initially Co and Cu alloys were grown as these were the metals used in the multilayered systems for which the largest GMR was found [55]. Other alloys whose constituents were totally or largely immiscible were also tried. These included Co alloys containing respectively Ag, Au and Pb, and nickel alloys with Ag and Au. (All these samples have been grown using one

magnetron and 2 semi- circular targets in order to produce a continuous concentration gradient). The Co-Cu and Co-Ag alloys produced the largest GMR, and the magnetometry and MR results for these samples will be described in more detail. The Co-Ag samples and Co-Cu samples were grown consecutively and so the conditions under which they were grown can be considered to have been identical as far is experimentally possible.

For experimental convenience each silicon strip was cut into five samples of 1cm length, the other regions being of no practical use, having been partially covered by the attachment clips. An Ar atmosphere is essential to prevent sample oxidisation. Auger electron spectroscopy (AES) and energy dispersive X-ray (EDX) elemental analysis measurements were made on the second set of samples. From the AES results the relative concentration of each of the constituents was calculated from the ratio of the Cu (or Ag) to Co peak heights from the resulting spectra. Several measurements were taken for each sample and the average values have been plotted in the graphs shown later in this chapter. The EDX method produces results proportional to the mass fraction of each element, which can then be corrected and converted to the atomic fraction.

It was found that the atom% gradient was non-linear across the sample as seen in Fig. 4.1 and Fig. 4.13a owing to the geometry of the sputtering plasma. The target is of radius 2.5cm. The sputtering area has an approximate radius of 2cm with maximum sputtering rate tending to occur in an annulus with inner and outer radii of 1cm and 1.6cm respectively. This effect is enhanced by the magnetic properties of the cobalt target, which tends to bind the discharge closer to the target centre. The region of substrate above the outer edge of the Co target was therefore not the area which contained the largest Co concentration.

4.3 Homogeneous and Heterogeneous Alloys

Although the combinations of metals chosen for alloying are to a large extent immiscible, a rapid quench process such as sputtering onto a low or ambient temperature substrate will tend to suppress phase separation. If complete suppression is achieved

a chemically homogeneous metastable alloy is produced with the two elements evenly distributed on an atomic scale. This system is characterized by a single lattice parameter which may be shifted away from that of the pure non-magnetic matrix as a result of lattice strain. Owing to the relatively high free energy of such an alloy it is difficult to produce a sample in this state.

Relaxation within the material occurs by migration of cobalt atoms to form localised regions with increased Co concentration which will be referred to as clusters. This process reduces the free energy of the system and results in a chemically heterogeneous material. The system can still be characterized by a single set of X-ray diffraction peaks; however density fluctuations may appear as asymmetry in these peaks.

A granular or heterogeneous alloy system is formed if the chemically inhomogeneous state undergoes complete relaxation to a phase separated state. In the limiting case the cobalt clusters become well defined expelling any matrix atoms present. The lattice parameter (and in some cases structure) of these magnetic particles is different from that of the matrix. It is difficult to make a clear distinction between the inhomogeneous and the phase separated states as the evolution of the system during annealing between these two states occurs gradually. In each case the magnetic regions are randomly dispersed in the non-magnetic matrix.

4.3.1 Deposition Temperature and Annealing

The evolution of a system from homogeneous to heterogeneous alloy obviously depends on atomic mobility. The sputter-deposition process itself provides adatoms with sufficient energy to form a polycrystalline film; this is further aided by plasma bombardment of the substrate. Adatom surface mobility is greater than mobility within the film bulk. It is therefore not unexpected that some diffusion will take place within the film during the growth process, resulting in a chemically inhomogeneous film.

The substrate temperature rose to above ambient during the deposition process owing to the close proximity of substrate and target, necessary for the production of a concentration gradient. This temperature rise was measured to be approximately 100°C

above the target centre falling to 75°C at the edge of the sputtering target. Alloys can be grown deliberately on heated substrates to provide in-situ annealing and phase separation [56]. The disadvantage of this technique is that the annealing process cannot be as precisely controlled as when post deposition annealing is used. Careful post deposition annealing can be used to achieve the optimum GMR if the film is initially as homogeneous as possible. These samples were subsequently annealed at 484°C.

In summary, when the metastable homogeneous alloy undergoes relaxation clusters of Co atoms begin to appear, which develop into cobalt granules within the matrix. As the relaxation continues the granule size increases. It can be inferred from recent literature that the annealing temperature and annealing time are the main factors in determining final grain size. It is found that for any given sample there is an optimum combination of annealing time and temperature [58] for which the maximum GMR is found. The necessary conditions for the appearance of GMR will be discussed in Section4.6.

4.4 Magnetic Behaviour of Heterogeneous Alloys

Depending on the degree of relaxation that has occurred within an alloy and the concentration of magnetic atoms present, different types of magnetic behaviour may be expected.

It is noted that the grain structure of the film is important because the anisotropy axes of the grain will define the anisotropy direction of any Co particles within that grain. The grain size will also be a determining factor in the length of the conduction electron mean free path.

4.4.1 Large magnetic particles

The production of domain walls within a Co particle takes a finite energy and walls will only be formed if this energy is compensated for by the decrease in magnetic dipolar energy. Large magnetic granules which result from extended annealing times may be of sufficient size for domain formation to be energetically favoured. In such a system

magnetisation reversal occurs by domain wall motion.

4.4.2 Small magnetic particles

For small particles it is energetically unfavourable for domain walls to be produced. If a field is applied there can be no domain wall motion, and moment reversal can only occur by rotation of the net moment. At high temperatures, single domain magnetic particles exhibit superparamagnetism [57] which is characterised by the lack of hysteresis in the M-H loop and by a net moment which follows the Langevin relationship,

$$\frac{M}{M_S} = \coth(y) - \frac{1}{y} \qquad [4.1]$$

where

$$y = \frac{MB}{kT}$$

and M is the total moment of each cluster or particle.

The anisotropy energy of a single domain particle is proportional to the particle volume. At low temperatures the thermal energy is less than this anisotropy energy and the single domain particle cannot thermalise on an experimentally observable time scale. The temperature below which this occurs is defined as the blocking temperature, and is characterised by the appearance of hysteresis. The thermal energy required to rotate the particle moment is given by

$$E_A \propto exp(\frac{-KV}{kT}) \qquad (4.2)$$

where K = anisotropy energy per unit volume which has terms arising from crystalline and shape anisotropy.

4.4.3 Spin Glass Behaviour

A hierarchy of interactions within the alloy is apparent, the strongest being the exchange interaction which ensures that adjacent cobalt atoms act as a single "super spin". It is this strong interaction that enables the superparamagnetic system to be described by the Langevin equation for paramagnetic systems.

Inter-granular interactions can couple these magnetic granules or clusters. Spin glass behaviour can occur if there is both randomness and frustration present in a system.

It is apparent that there is an essentially random distribution of granules and grains in the alloy. Less evident is the type of inter-granular interaction that could be the origin of frustration within the system. There are several possible sources of interaction: dipolar, nearest neighbour exchange and oscillatory exchange of the type seen in magnetic multilayer systems. A system of clusters which exhibits frustration and randomness is described as a spin cluster glass. The existence of such a state has been identified by the appearance of a cusp in the zero field cooled susceptibility at 40K [58] for a Co-Ag alloy. It is experimentally difficult to distinguish a collection of superparamagnetic spins from a spin glass or spin cluster glass system. Results of a similar form for an alloy of Co-Cu [52] showing a much broader peak in the zero field susceptibility at 100K has been identified as arising from the blocking of superparamagnetic spin clusters.

4.5 Origin of GMR

It has been previously noted that the GMR is caused by the decrease in spin-dependent scattering due to the field induced alignment of initially random moments of magnetic particles in a non-magnetic matrix. The degree of spin dependent scattering depends on the angle between the moments of neighbouring particles [59].

Consider the types of scattering involved in the MR effect. Spin dependent scattering can occur in the bulk of the granule and at the interfaces between magnetic and non-magnetic phases. Small particles or clusters tend to be superparamagnetic and their moments cannot be aligned except at very low temperatures; very small clusters provide only small fluctuations in the potential seen by an electron and are less likely to cause spin-dependent interface scattering. They are also too small for a significant number of bulk scattering events to occur within them. An additional loss of moment may occur for small magnetic particles in a matrix of a different metal, owing to the contact potential between them causing an electronic redistribution at their interface. This effect will be large for particles with a large surface to volume ratio. It has been shown [60] for a homogeneous Co-Cu alloy system that for a Co concentration of less than

24% that no spin moment was present; this was interpreted as being due to electrons being added to the alloy by the Cu atoms and effectively resulting in the filling of the Co 3d bands.

Annealing processes give rise to phase separation and hence to an increase in particle size. For a useful GMR device to be obtained, there must be a significant number of magnetic particles present of sufficient size to cause scattering events and whose moments can be readily aligned. The probability of scattering however decreases with increasing particle size for a constant volume of magnetic material; this can be considered to be due to the decrease in surface area relative to the volume of magnetic material. This will produce a particularly pronounced decrease in the size of the GMR if the interface spin-dependent scattering term is dominant.

Phase separation and the formation of stable Co particles on annealing also gives rise to a decrease in overall film resistance because the disorder in the system is reduced; grain sizes may be increased and internal stresses reduced. The mean free path for an electron in the matrix is important in determining the size of the GMR, because a low background film resistance will increase the magnitude of $\Delta R/R$. In addition to this effect however a mean free path of less than the average spacing between magnetic particles means that the spin-dependent scattering term is less significant owing to spin-flip scattering within the matrix which results in loss of coherence in the spin channels. This is similarly true for particles of diameter larger than λ. It can be concluded that particle size and concentration are therefore important factors in achieving maximum GMR.

4.5.1 Theory for MR in alloys

As yet only one paper concerning GMR in alloys has been published [61] using a model of spin-dependent scattering from single domain particles. The parameters used are broadly similar to those used in GMR models of multilayered systems: the mean free path in the magnetic particles λ_m, the non-magnetic matrix λ_{nm} and the interfacial scattering parameter λ_s are common parameters. Large MR arises for long mean free

paths in the matrix and also for large interface roughness (ie small λ_s). New parameters include particle size and concentration.

The MR ratio for a single domain ferromagnetic particle system at low temperatures is found to be given by

$$\frac{\Delta R}{R} = \frac{\rho(H) - \rho(H = H_S)}{\rho(H = H_S)} = \frac{\rho_2^2}{\rho_1^2 - \rho_2^2}[1 - \alpha^2(H)] \tag{4.3}$$

where $\alpha = \frac{M(H)}{M_S}$ and ρ_1, ρ_2 are functions of the two spin channels involving particle concentration and size. The maximum magnetoresistance occurs at the coercive field, H_c which occurs by definition when $\alpha = 0$. A quadratic relation between the MR ratio and the applied magnetic field is predicted.

The largest MR is predicted for a system of the smallest particle size and high concentration. In real systems however there are other effects that come into play for small particle sizes. As described in Section 4.5 very small particles tend to lose their moments as a result of interaction with the non-magnetic matrix, and scattering potentials become spin independent for these cases.

This model has been found to be in qualitative agreement with the observed resistivities and MR effects in heterogeneous alloy systems [53]. Quantitative comparisons with experimental results have not yet been made owing to the lack of data quantifying particle size at the present time, and the difficulty in determining whether a totally phase separated Co particle is required or whether a cluster of high Co concentration is sufficient to cause spin dependent scattering.

4.6 Requirements for GMR in Alloys

The requirements for an alloy which is to exhibit a large GMR can be summarised:

(1) the two components should be immiscible so that magnetic precipitates can form in the non-magnetic matrix. For example phase diagram [62] for Co-Cu alloys indicates less than 9 atom % solubility of Cu in Co at the temperatures used and negligible solubility of Co in Cu, making this an ideal candidate in which to find GMR.

(2) In order to achieve a long mean free path (MFP) the non-magnetic metal should have as low a resistance as possible, hence the use of the noble metals such as Cu and Ag. For a film of low matrix resistance the resistance caused by spin dependent scattering will make a larger contribution to the total scattering within the film.

(3) The maximum GMR will be achieved for an alloy which is inhomogeneous on the scale of an electron mean free path. Alloys of homogeneous composition or which contain particles whose dimensions are large compared to the MFP will show no GMR.

It should be noted that GMR has only been found in alloys of magnetic transition metals. Xiao *et al* [53] attempted experiments using $Gd_{25}Ti_{25}$, which although satisfying the above requirements failed to show GMR. It is thought this is probably due to the fact that the 4f electrons, the origin of the magnetism in the lanthanide series, exist in inner shells and hence have only a small interaction with current carrying electrons.

4.7 Magnetometry

The magnetic properties of the samples have been investigated using a range of magnetometric techniques. There are 2 types of magnetometer widely used for investigating magnetic thin films including

- the alternating gradient field magnetometer (AGFM)
- the Superconducting Quantum Interference Device (SQUID) magnetometer

AGFM The sample to be investigated is mounted using a small amount of grease on the end of a quartz fibre rod attached to a piezoelectric transducer. It is then placed between two Helmholtz coils connected in opposition. These are fed from an audio oscillator and generate an alternating magnetic field gradient. For a constant current in the gradient coils the deflection is proportional to the magnetic moment of the sample, depending on the gradient direction,

$$F = mdB/dz$$

The oscillation frequency is tuned to the mechanical resonance of the rod and sample. This is important because the amplitude of vibration of the rod is proportional to the

force exerted by the field on the sample magnified by the quality factor of the resonating system, resulting in a greater sensitivity. This is essential in the characterization of thin film samples which contain very little magnetic material compared to a bulk specimen. To derive a hysteresis loop an electromagnet must be used to produce a variable uniform field.

A sensitivity of $10e^{-8}$ emu can be achieved using an AGFM. One factor which must be considered when using an AGFM is that for a sample with a small coercive field the alternating gradient may tend to demagnetise the sample. This will manifest itself as increased gradient of the M-H loop around the coercive field (ie an increase in S*, the loop squareness) and also a small reduction in the coercivity values themselves [63].

The SQUID magnetometer A SQUID magnetometer has a sensitivity of $10e^{-9}$emu. The sample is moved slowly through a set of pick-up coils and the induced current flows through the signal coil of a SQUID. The applied magnetic field is provided by a superconducting magnet.

The AGFM has the advantage that results can be quickly and easily obtained. This is in contrast with data collection for the SQUID magnetometer which can take of the order of days to produce a hysteresis loop. However this device produces the most sensitive results and can easily be used to make magnetisation measurements at low temperatures and whilst sweeping temperature in constant applied field.

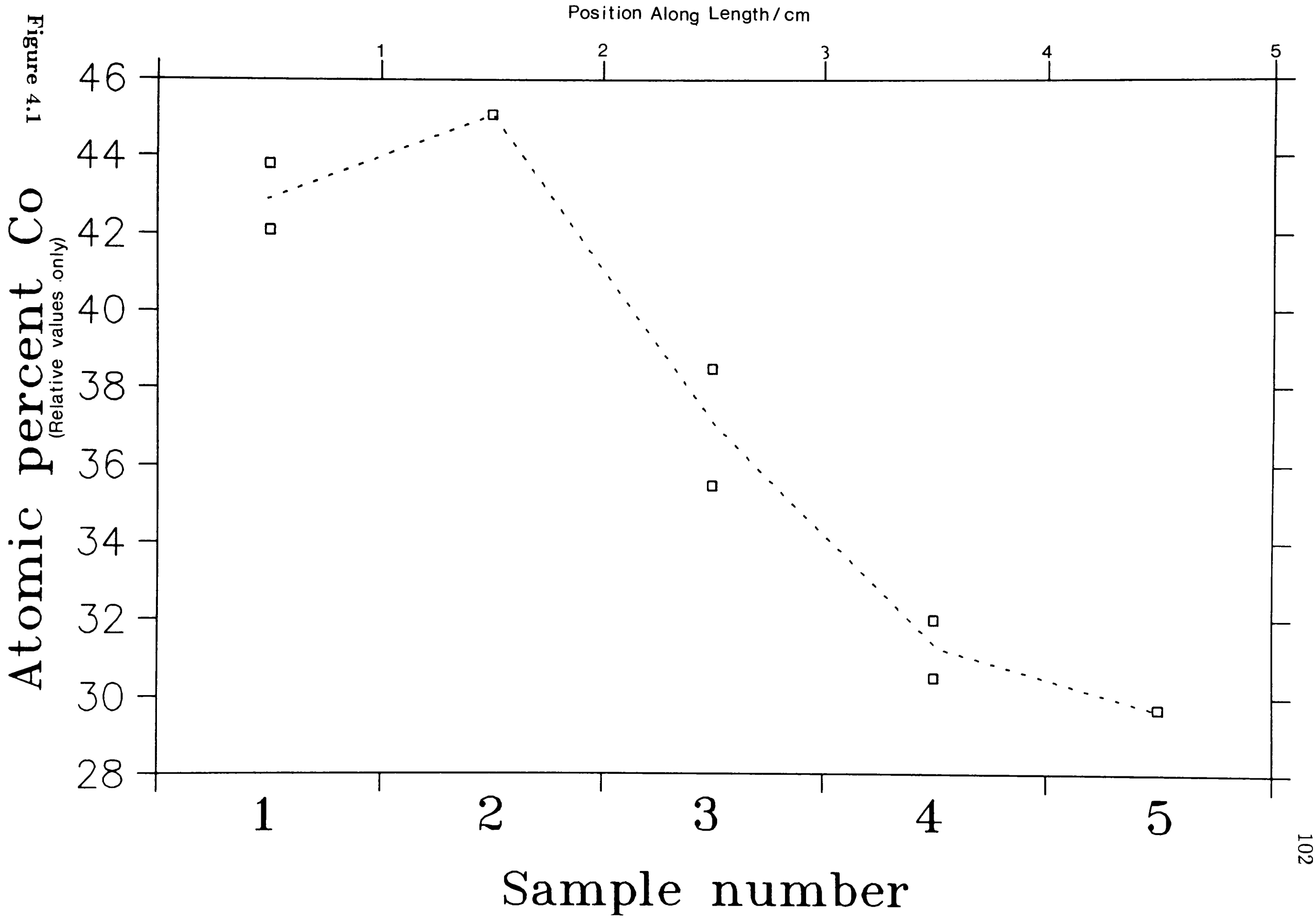
4.8 CoCu Alloys

The results of the compositional analysis is shown in Fig. 4.1.

The position in centimetres along the length of sample and the corresponding sample reference number are given on the x-axis. The composition as calculated from the Auger spectra, was found to vary from 29% - 45% Co (Fig. 4.1). The Co concentration across the sample is lower than that of Cu indicating that Co has a slower deposition rate than Cu, as is to be expected.

4.8.1 Magnetometry Results

Figure 4.1


Position Along Length / cm
1
2
3
4
5
Atomic percent Co
(Relative values only)
46
44
42
40
38
36
34
32
30
28
1
2
3
4
5
Sample number

AGFM magnetometry results indicate the presence of a majority of superparamagnetic particles as shown in Fig.4.2 for position 4. The hysteresis in low fields could arise from the existence of larger particles whose moments are blocked or which reverse by domain wall motion or from ferromagnetic interactions between a number of smaller particles which then act as a larger single moment.

4.8.2 Room Temperature MR Results

A summary of room temperature MR results for the B⊥I measurement configuration is shown as a function of position along the sample length in Fig. 4.3 (solid line). The largest MR of 2.3% was found to occur for position 4 which has a Co concentration of 30% .

This can be compared with the results of Berkowitz *et al* [52] who found a GMR of up to 10% at 10K for samples deposited at ambient temperature and Chien *et al* [53] who found negligible MR in samples deposited at 77K.

B Parallel to I Measurement Configuration Measurements were made with the applied field along the measuring current direction. A sharp positive MR dip was seen in samples 1 to 3 which contain Co concentrations of greater than 38%; the magnitude of this positive MR is comparable to (and in sample 1 greater than) the negative MR over the range 0T-1.3T. The width of the dip decreased from ± 10mT to ± 100mT and decreased in magnitude from a $\Delta R/R$ value of 0.43% to 0.06% along the substrate length from positions 1 to 3. It is postulated that this effect is due to AMR (as described in Section 3.7.8) which is of comparable magnitude to the GMR of the sample. The trend in size and width of the AMR as described above may explain that fact that peaks are not seen for samples 4 and 5; the addition of a very broad but small AMR peak/dip to the GMR peak will not be as easily distinguishable from the GMR itself.

Fig.4.4 shows the effect of AMR for sample 2. The red and blue curves represent the resistance data for the B‖I and for the B⊥I measurement configurations respectively. Similar results have recently been observed by Dieny *et al* [64] in heterogeneous alloys consisting of permalloy magnetic particles in a Ag matrix. It was found that the size of

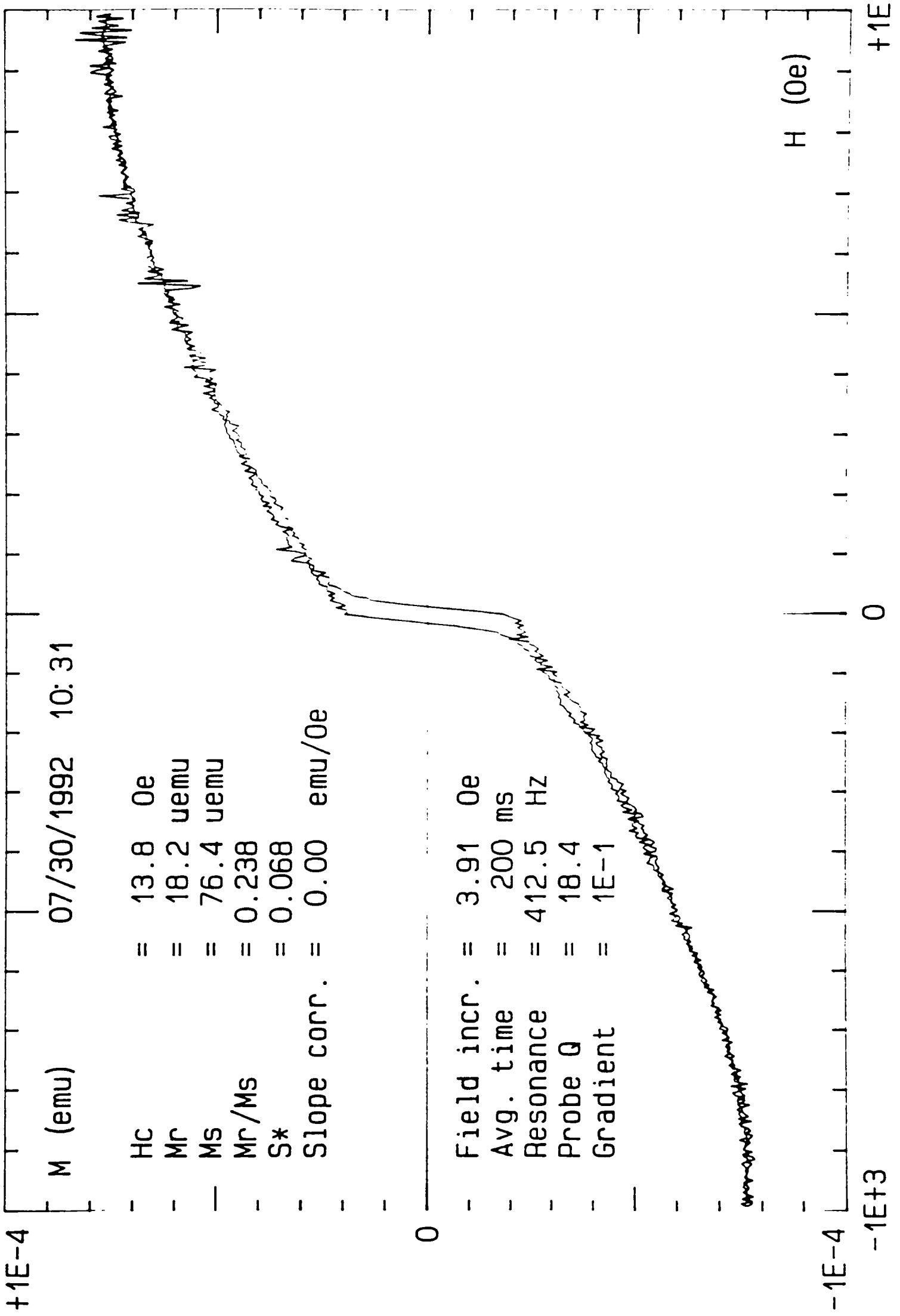
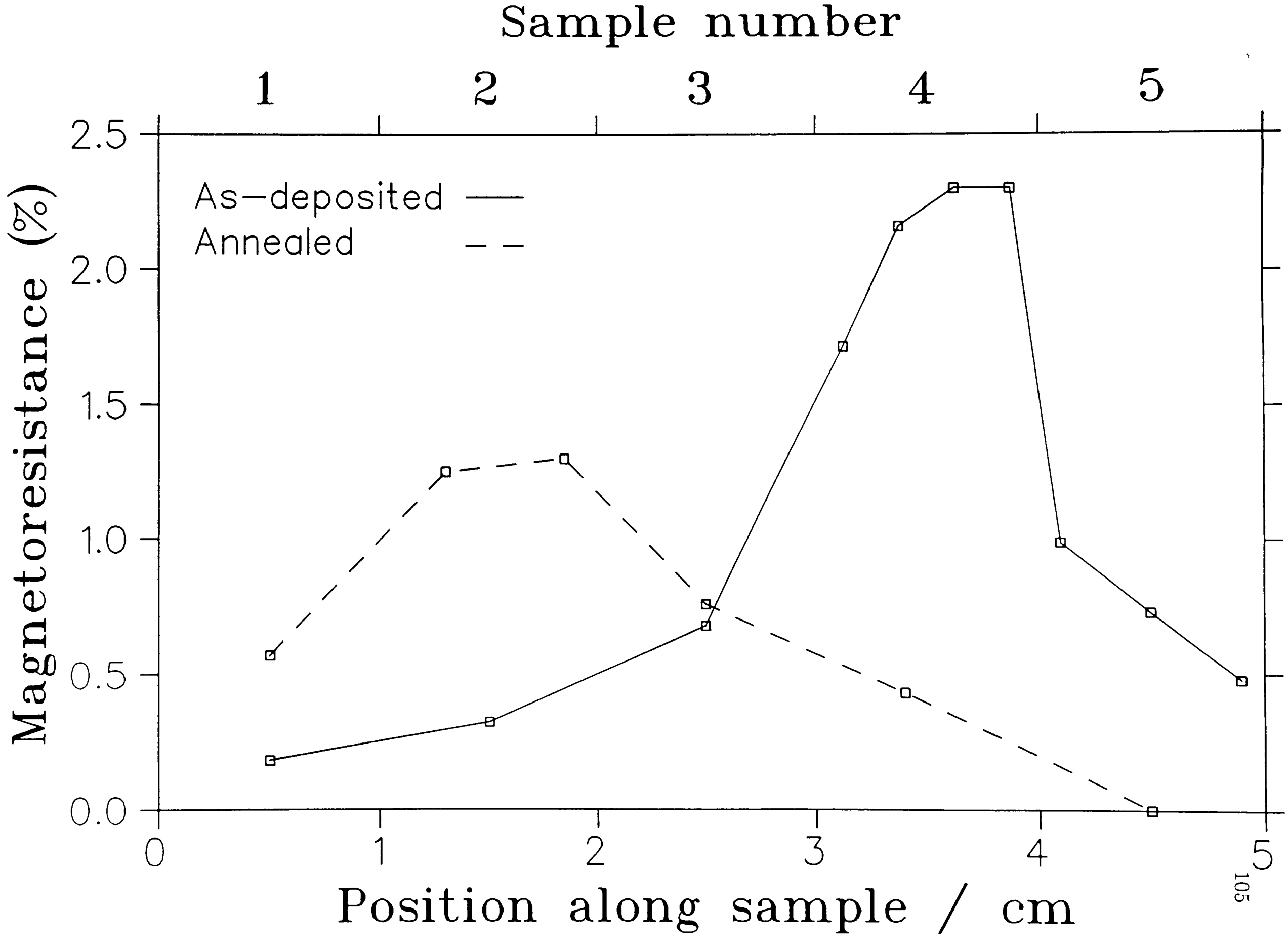

+1E+3
H (Oe)
0
-1E+3
+1E-4
M (emu)
-1E-4
07/30/1992 10: 31
Hc = 13.8 Oe
Mr = 18.2 uemu
Ms = 76.4 uemu
Mr/Ms = 0.238
S* = 0.068
Slope corr. = 0.00 emu/Oe
Field incr. = 3.91 Oe
Avg. time = 200 ms
Resonance = 412.5 Hz
Probe Q = 18.4
Gradient = 1E-1

Figure 4.2

Figure 4.3


Sample number
1
2
3
4
5
As–deposited
Annealed
Magnetoresistance (%)
2.5
2.0
1.5
1.0
0.5
0.0
0
1
2
3
4
5
Position along sample / cm

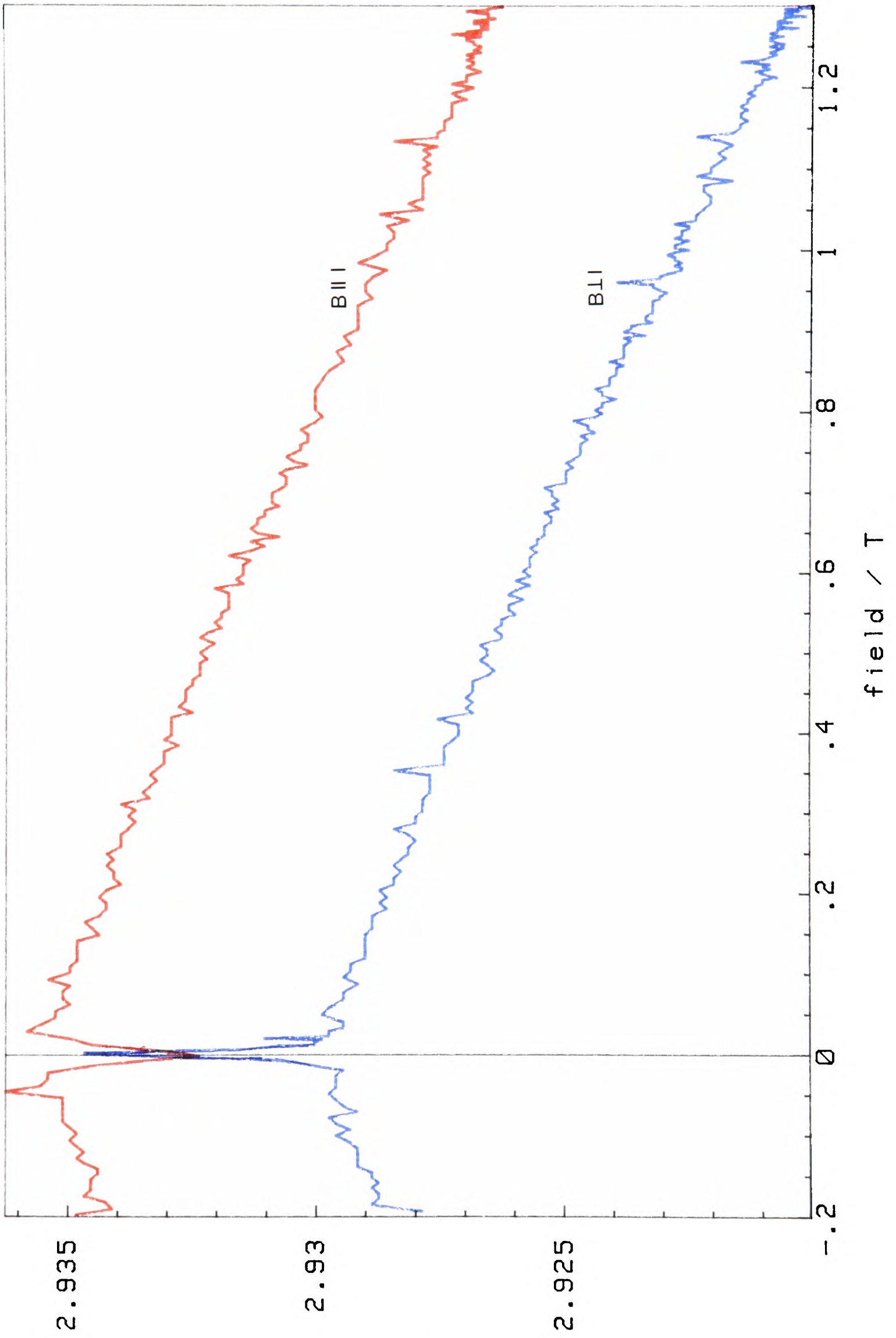


Fig.4.4

the AMR effect was larger in samples with higher permalloy concentration.

4.8.3 Low Temperature Results

The temperature dependence of the MR for Sample 4 is shown in Fig. 4.5 . Fig.4.6a and Fig.4.6b show sample resistance plotted against applied magnetic field at 294.7K and 4.2K respectively.

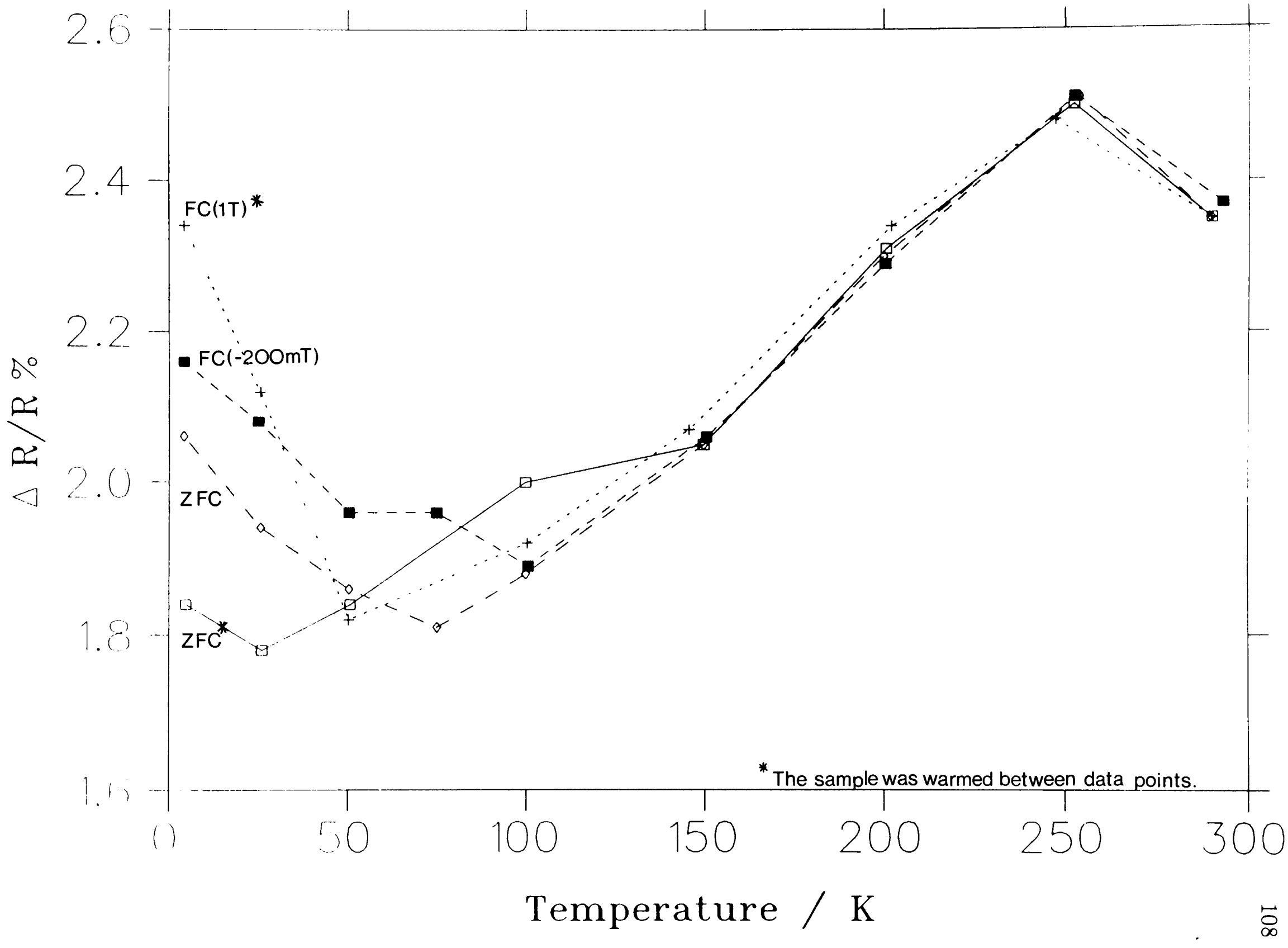
The maximum MR obtained was found at 250K. At temperatures below 150K hysteresis became apparent for all samples, whilst below 100K the magnitude of the MR effect is seen to be strongly dependent on sample history. The open squares and crosses indicate respectively the results made after the sample was cooled in zero field and cooled in a 1Tesla field, and for which the sample was warmed to room temperature between the measurements at different temperatures. The diamond shapes and filled squares indicate results for which the sample was respectively cooled in zero field and cooled in a -200mT field, but in which the sample was not warmed to room temperature between each measurement temperature. Hysteretic behaviour is indicative of blocking of a number of the superparamagnetic particles. Spin glass and spin-cluster glass behaviour has been identified in other as-deposited CoCu samples [53] and similar phenomena may contribute to history dependent effects observed.

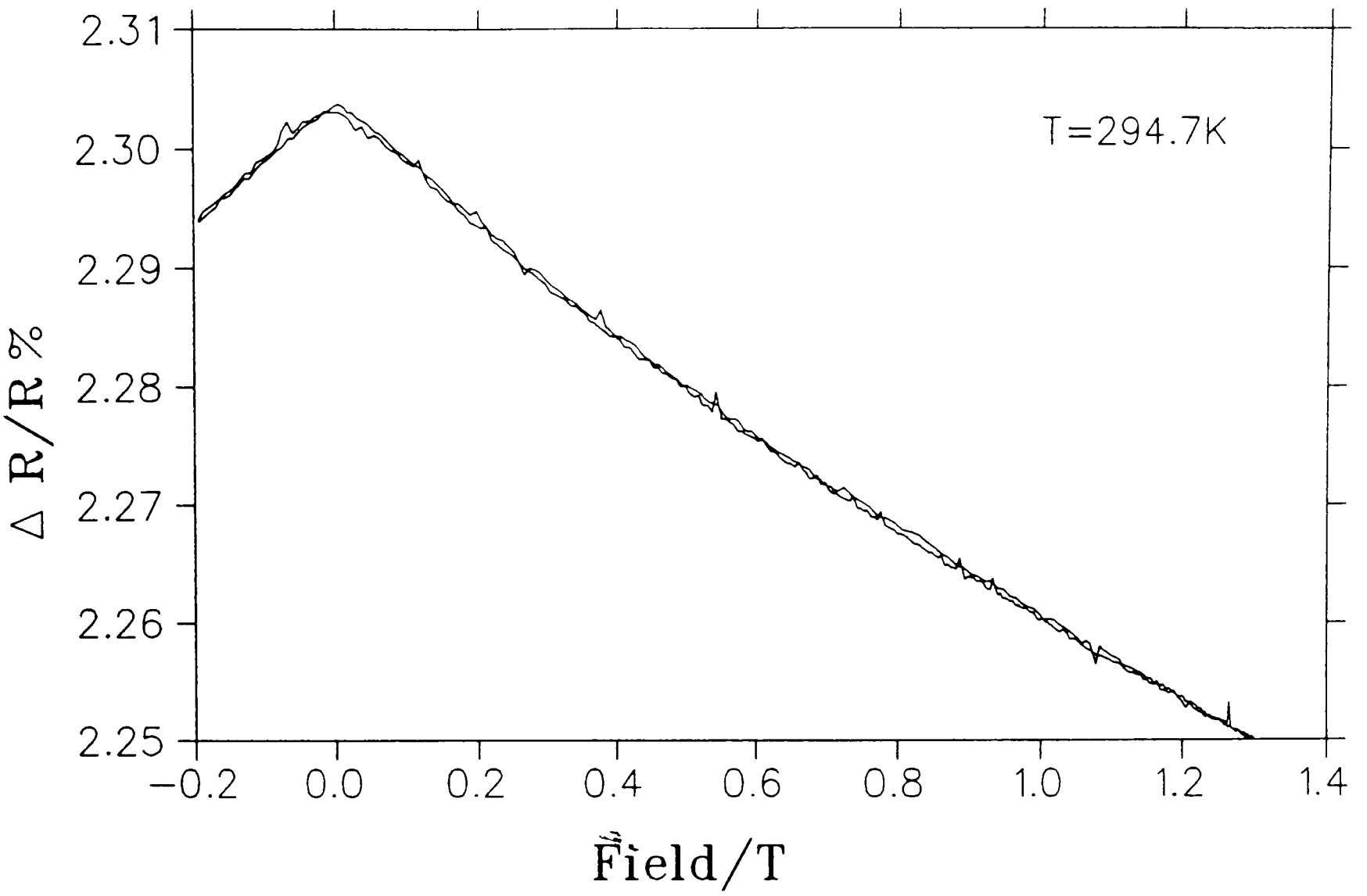
Fig.4.6b shows the low temperature resistance results for sample 4. The sample was cooled in zero field and a magnetic field applied; the resistance data for this first field sweep is shown as a dashed line. The resistance data for subsequent field cycling is shown as a solid line and clearly has a higher resistivity at M=0 than the ZFC state. This difference in magnetoresistance between the FC and ZFC traces will be defined as $\Delta(\Delta$ R/R %). This effect has also been seen in the CoAg alloy samples and will be discussed in more detail in later sections.

4.8.4 Annealing

As discussed above, an annealing process can be used to improve phase separation and increase Co particle sizes, both of which may give rise to larger spin-dependent scattering. The samples were annealed at 484° for 10 minutes. The resulting MR is

Figure 4.5


2.6
2.4
2.2
2.0
1.8
1.6
Δ R/R %
FC(1T)*
FC(-200mT)
ZFC
ZFC
0
50
100
150
200
250
300
Temperature / K
* The sample was warmed between data points.


T=294.7K
Δ R/R %
2.31
2.30
2.29
2.28
2.27
2.26
2.25
−0.2
0.0
0.2
0.4
0.6
0.8
1.0
1.2
1.4
Field/T

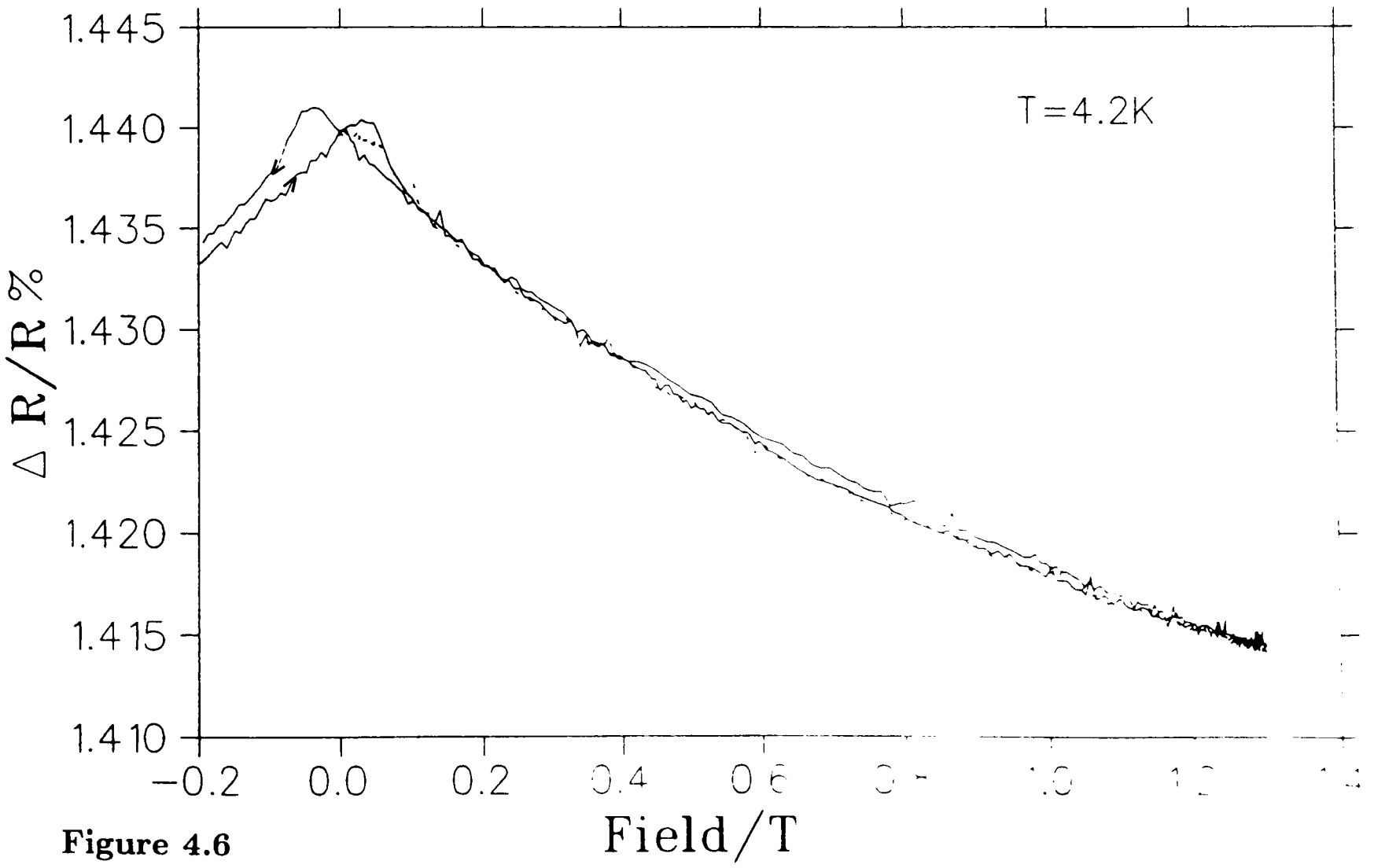

T=4.2K
Δ R/R %
1.445
1.440
1.435
1.430
1.425
1.420
1.415
1.410
−0.2
0.0
0.2
Field/T

Figure 4.6

shown shown as a dashed line in Fig.4.3. It is seen that the annealed results are of slightly smaller in magnitude and are shifted towards a higher cobalt concentration; the maximum MR now appears for a sample with an average Co concentration of 45%. It is therefore concluded that it is unlikely that we have obtained both the optimum combination of Co concentration and particle size either before or after the annealing process. It is possible that the MR is limited by problems of contamination and therefore impurity scattering. This would result in a decrease of electron MFP in the matrix and hence a reduction in the value of $\Delta R/R$ owing to a decrease in the spin-dependent to spin-independent scattering ratio. This figure can be compared to a GMR after annealing at of order 500K of 22% at 10K for a Co atom fraction of 19% found by Berkowitz *et al* [52], and a GMR of 18% at 5K for a sample of 20% atomic percent Co by Chien *et al* [53]. This variation in GMR values highlights the importance of producing an alloy with both the optimum Co concentration and the optimum particle size.

It is noted that although the MR ratio was larger for unannealed samples, the graphs were of a linear nature. For the annealed samples the MR was somewhat smaller, but the drop in MR occurred at smaller field values producing data of a concave form (Fig.4.7). A sharp fall off in film resistance with applied field (ie. a large change in GMR for a small applied field) is a property that is important for commercial applications. In addition hysteresis of order $\pm$8mT to $\pm$20mT is now present in the annealed samples at room temperature. These two findings indicate that magnetic particle size distribution has shifted and that the average particle size has increased as expected. In the former case larger superparamagnetic particles can be more easily aligned in an applied magnetic field which would result in steeper decrease in the sample resistance. In the latter case very large particles are more likely to exhibit hysteresis at room temperature because of their high blocking temperatures.

4.8.5 Conclusions

We have found a maximum value of $\Delta R/R$ of 2.5% in a Co-Cu alloy sample, which is significantly larger than the MR found for the CoCu multilayer films discussed

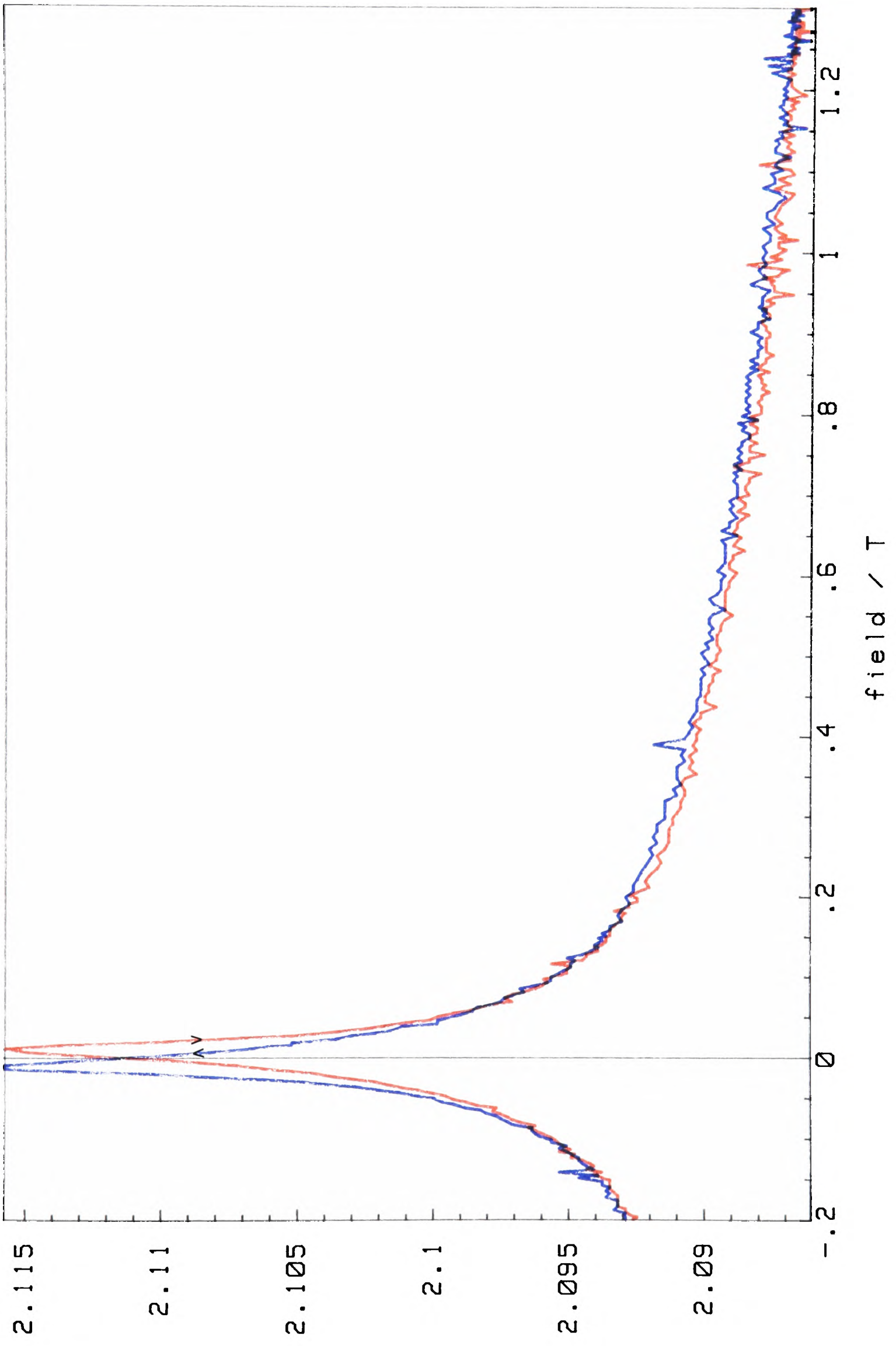


Fig.4.7

in the previous chapter. It may be that the structural character of the multilayers was the reason for the small MR seen in these earlier samples. However it remains uncertain as to whether in both cases contaminants are introduced into the films limiting the MFP and hence the GMR value, but which have a less disruptive effect in an inhomogeneous alloy structure.

4.9 CoAg Alloys

4.9.1 Magnetometry Results

Magnetisation measurements have been made at room temperature and low temperatures using a Princeton Measurement Systems AGFM and a SQUID magnetometer respectively.

Room temperature Magnetometry Results

In order to establish the magnetic properties of the samples M-H loops were measured at room temperature. Fig.4.8a shows the data for part of sample 2, (indicated by circles) which has been found using EDX measurements to have a Co atomic percentage of 38%± 6%.

The samples showed only slight hysteresis for all Co concentrations indicating that the granules are predominantly superparamagnetic. As discussed in Section 4.4.2 the magnetisation of a superparamagnetic system as a function of field can be fitted to a Langevin function. The best fit to the data is shown as a solid line and resulted from choosing a particle moment of (12600±350)μ_B. Assuming the Co moment is 1.715μ_B, the average particle radius is found to be 25-26Å . The fit is good, but not perfect indicating that there may be a small distribution of particle sizes about this average value. The room temperature M-H curve appears to saturate at 2.53 $\times 10^{-5}$ emu at fields of order 0.5T (as also shown in Fig.4.8a). It is noted however that there may be a small paramagnetic correction due to very small superparamagnetic particles which cannot be saturated at these temperatures. A small amount of hysteresis is visible about the origin.

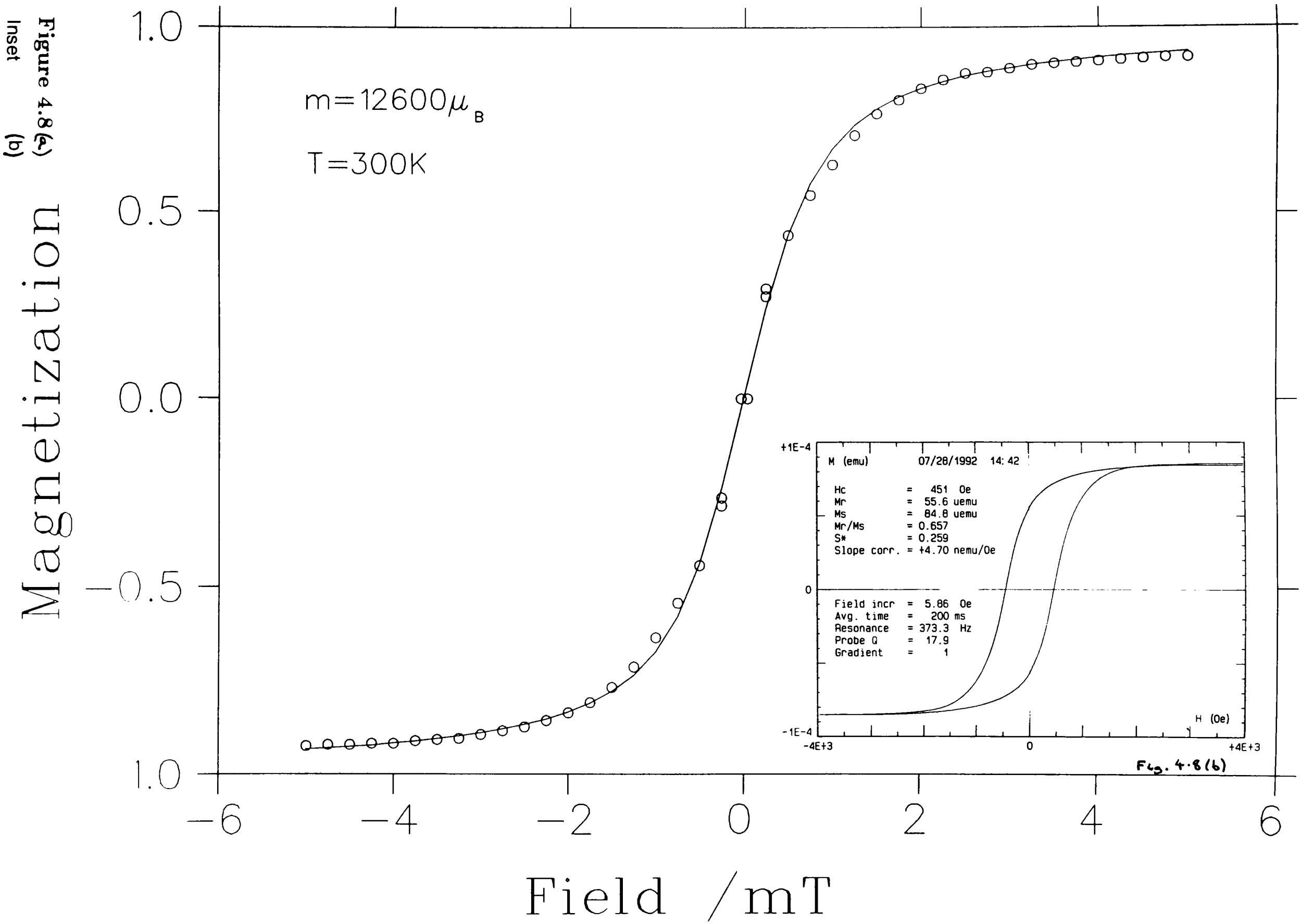


Figure 4.8(a) Inset (b)

which could arise from large particles which are blocked at room temperatures or in which magnetisation reversal occurs via the movement of domain walls, or from ferromagnetic interactions between the particles. The relatively high concentration of cobalt in this sample may mean that interactions are more likely between individual Co particles.

Following this the samples were annealed twice in a vacuum sealed test-tube initially for a period of 10 minutes at a temperature of 200°C and for the second time at 400°C for 10 minutes. Fig.4.8b shows the M-H loop for sample 2 after annealing at 484° for 10 minutes. Hysteresis of order 500Oe(50mT) is seen, which clearly arises from a dramatic increase in particle size.

Low Temperature Magnetometry Results

Figure 4.9 shows SQUID magnetometry results for the as-deposited sample 2 as a function of temperature. The largest moment of $1.5\times10^{-4}emu$ is obtained at 2K.

It is noted that there is a discrepancy in moment values at fields above 4T. The data has been corrected for the diamagnetic and paramagnetic corrections arising from the Si substrate, sample holder and cellophane used to hold the sample in place. The corrections are larger at high fields relative to the measured moment and therefore any errors will become more significant at high fields. It is seen that at 2K-4.5K the largest obtainable moment is approximately a factor of six larger than that found at room temperature, and that the majority of this low temperature moment does not appear until temperatures below 10K are achieved and fields of order 8T are applied. This can be explained by postulating that this extra moment derives from very small superparamagnetic clusters that cannot be saturated under normal temperature and field conditions. In order to estimate a typical particle size Langevin fits have been made to larger particles acts as a base line which has been subtracted off the moment values at lower temperatures. It is assumed that these larger particles will be blocked at these lower temperatures. It is found that for all field values a satisfactory fit is obtained for the data for particle moments of between $6\mu_B$ and $9\mu_B$. A very good Langevin fit is obtained for fields of up to 4T using $6\mu_B$; several points have been marked (as open squares) on the

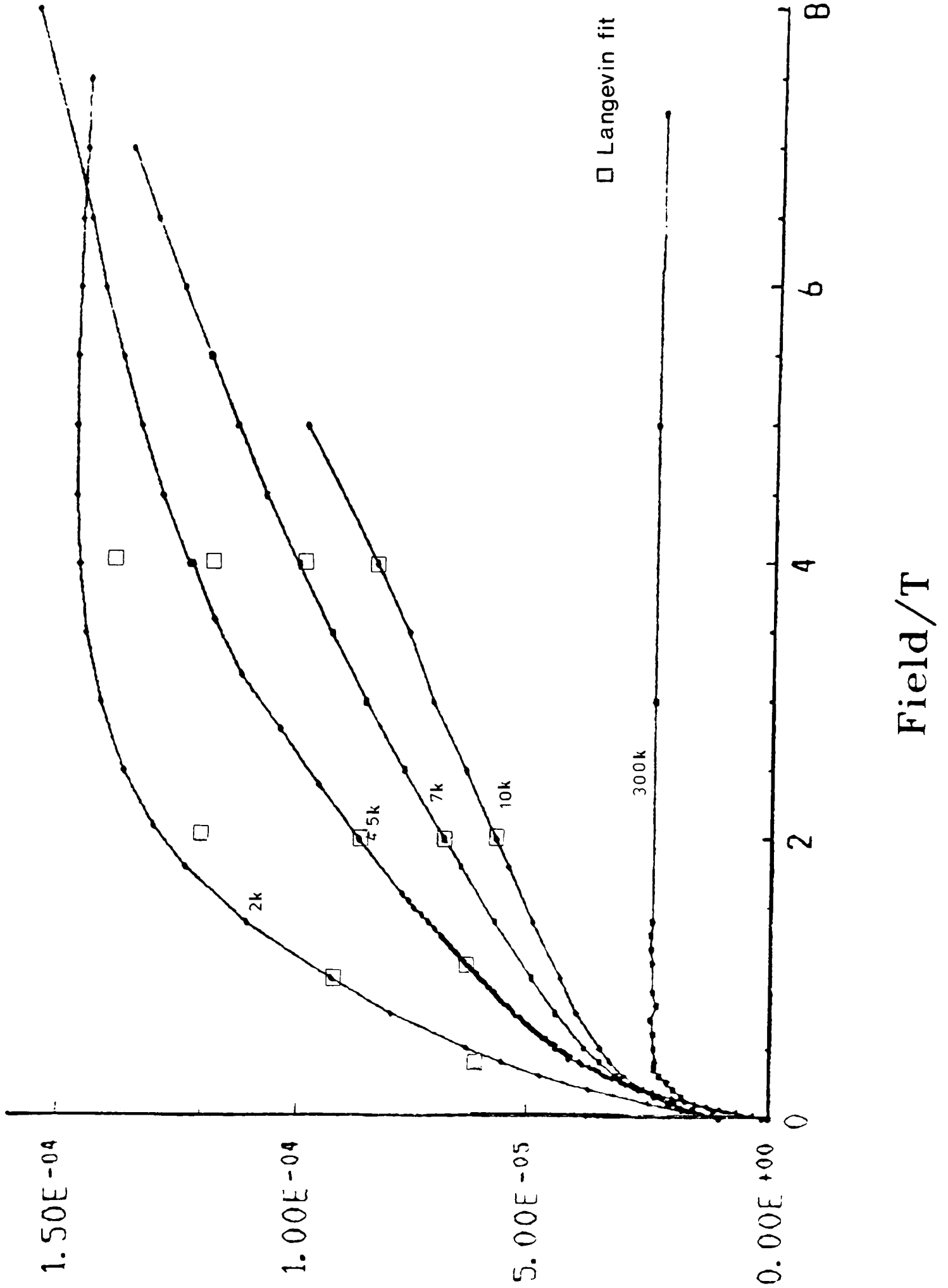

Moment/ emu
1.50E-04
1.00E-04
5.00E-05
0.00E+00
0
2
4
6
8
Field/T
Langevin fit
2k
5k
7k
10k
300k

Figure 4.9

data traces corresponding to each temperature. Assuming the Co moment is $1.715\mu_B$, this corresponds to a cluster size of order 4 atoms. Charge transfer between the Co and the surrounding Ag atoms can reduce the magnetic moment of outer atoms in the cluster; therefore for such small clusters this effect is likely to result in a smaller moment per atom and there therefore may be more Co atoms present in these clusters than calculated. It is clear that these particle sizes will produce only a small additional moment ($\sim 0.2\times e^{-5}$ emu) to the saturation moments of the larger particles at room temperature. These small particles will have a blocking temperature of 0.04K assuming they are hcp. In fact, small Co clusters are likely to assume the structure and the lattice spacing of the surrounding fcc Ag lattice; the blocking temperature in this case is estimated to be of order 1mK.

The magnetometry results can therefore be well explained by a model of Co particles of two sizes with moments of $12600\mu_B$ and $6\mu_B$ respectively. There are two models for this observation. Firstly, it is postulated that these larger particles arise because of the surface tension effects at crystallite boundaries which leads to the formation of larger cobalt regions. The smaller clusters probably occur in the centre of the crystallites where surface tension effects are negligible and they remain relatively unchanged in size. Secondly, where a larger amount of phase separation has occurred the film may consist of many small crystallites with composition of predominantly Co or Cu. The crystallite, which consists largely of Co, acts as a large moment whereas a minority of Co atoms in a predominantly Cu crystallite acts as a small particle. The Fig.4.10 shows the sample magnetisation as the sample is warmed in a field of 4T. The moment falls off very rapidly with increasing temperature, indicating that the small particles can only be saturated at very low T.

4.9.2 Remanence

The hysteresis and remanence seen in sample 2 in its as-deposited state at room temperature remains constant until the measured temperature is below 100K; below this temperature hysteresis and remanence increase rapidly. Fig.4.11 shows the M-H loop at 4.5K. The remanence is found to be of the order 1×10^{-5} emu compared to a

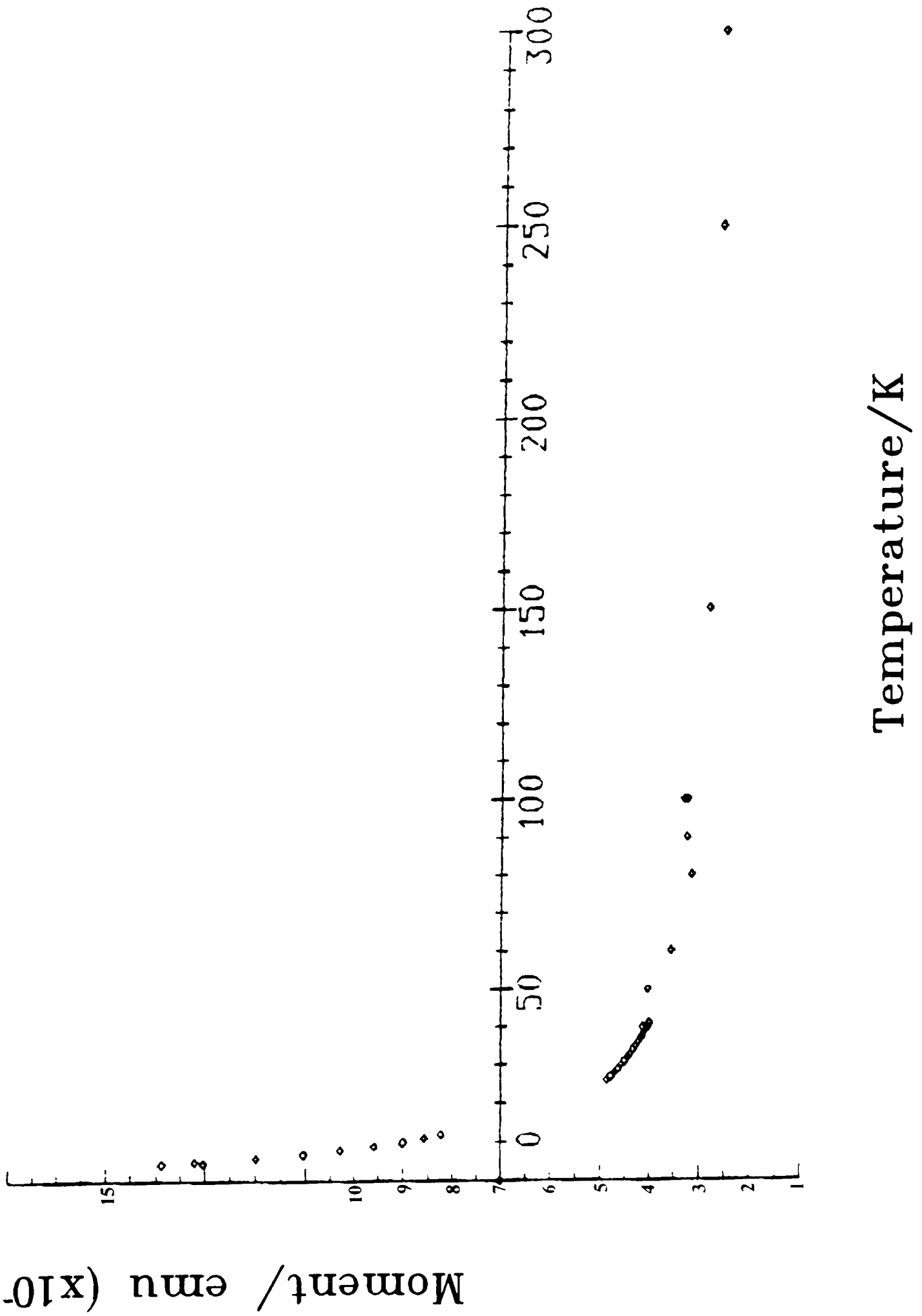

Moment/ emu (x10⁻⁵)
15
10
9
8
7
6
5
4
3
2
1
0
50
100
150
200
250
300
Temperature/K

Figure 4.10

room temperature saturation moment of 2.3×10^{-5}. It is therefore seen that a significant proportion of the particles that can be saturated at room temperature are blocked at low temperatures and will exhibit hysteresis.

Fig.4.12 shows the sample remanence as a function of sample temperature. The moments were aligned in a field of 8T at 4.5K; the field was then removed and the remanence measured as the sample was warmed up. The decrease in remanence with increasing temperature yields the distribution of blocking temperatures of the particles (and hence approximate particle size) as a function of temperature. Some size distribution is seen to exist. The majority of particles however are seen to block at a temperature of 30K corresponding with the sharp increase in remanence below this temperature. This blocking temperature corresponds to a Co particle size of 19Å and is in good agreement with the value calculated from the Langevin fit to the room temperature M-H curve. The room temperature Langevin fit discussed above was of good accuracy which suggested an alloy of mono-dispersed particles; however a better fit may be obtainable using a weighted superposition of Langevin functions. It is noted that particles or clusters of the same volume may have varying blocking temperatures as a result of variations in shape and other anisotropy; this effect is not significant above their blocking temperatures.

It is observed that there is an almost constant remanent moment of 2×10^{-6} above 50K which is maintained to 300K. This small remanence may arise from a small number of particles that are blocked at room temperature and would therefore correspond to a Co particle radius of 72Å or greater. From this data it would seem unlikely that a few very large particles would exist as this would imply a considerable gap in the distribution of particle sizes. A second possible origin of the remanence is that ferromagnetic interactions exist between smaller particles which act as a single cluster, as discussed previously in connection with the observed room temperature hysteresis in the M-H loop.

4.10 Magnetoresistance Measurements

In order to determine what contribution each class of particles makes to the

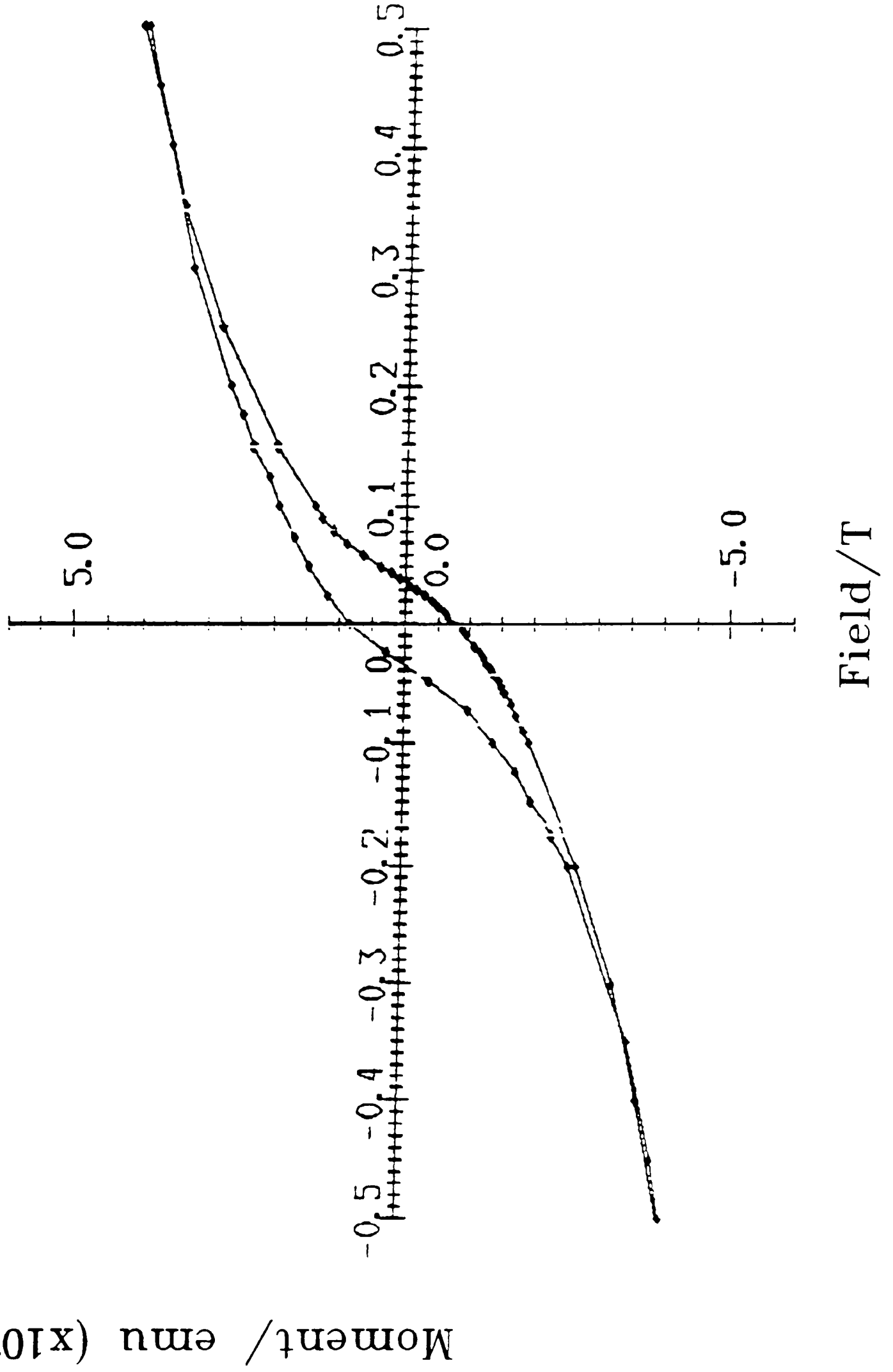


Figure 4.11

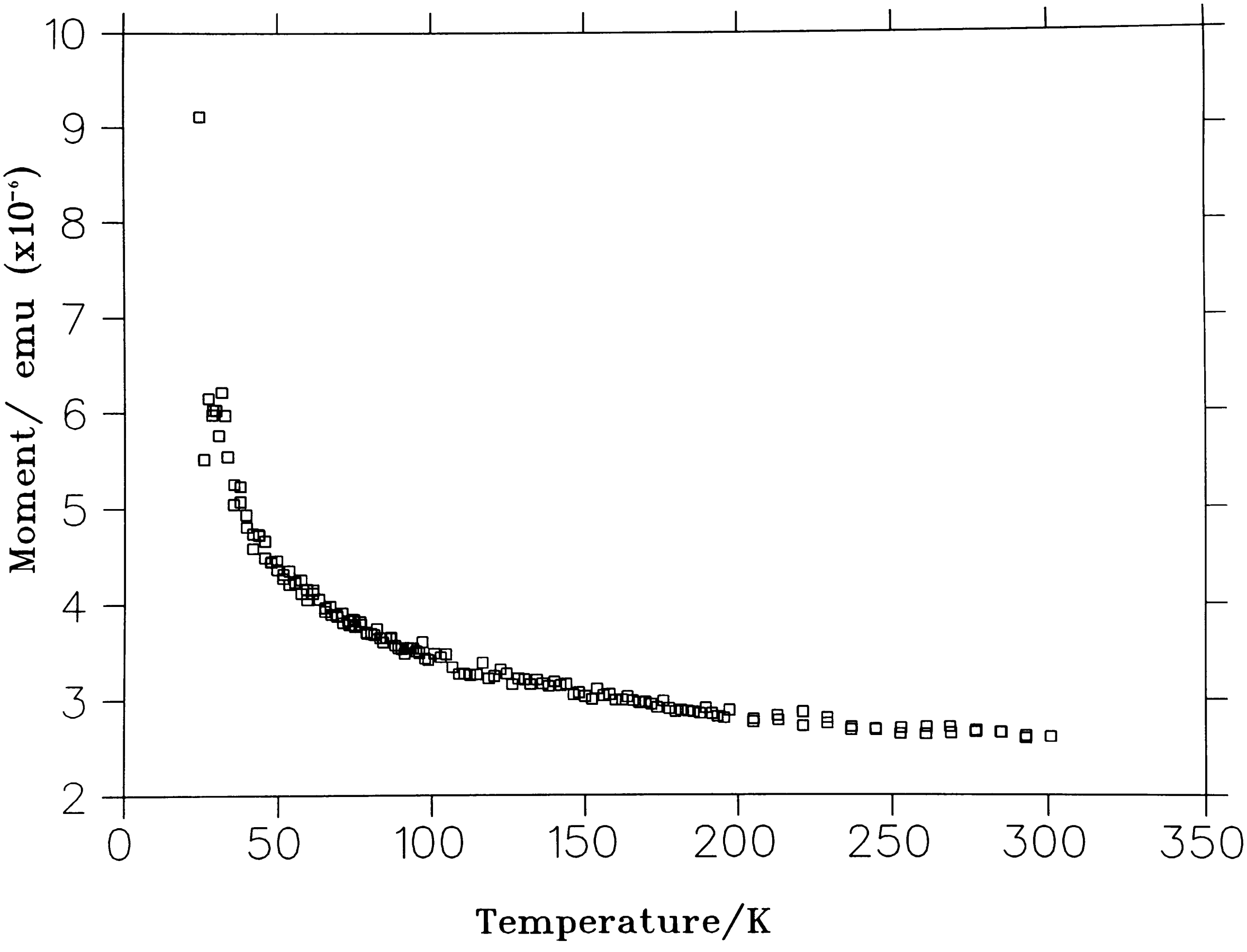

Moment/ emu (x10⁻⁶)
10
9
8
7
6
5
4
3
2
0
50
100
150
200
250
300
350
Temperature/K

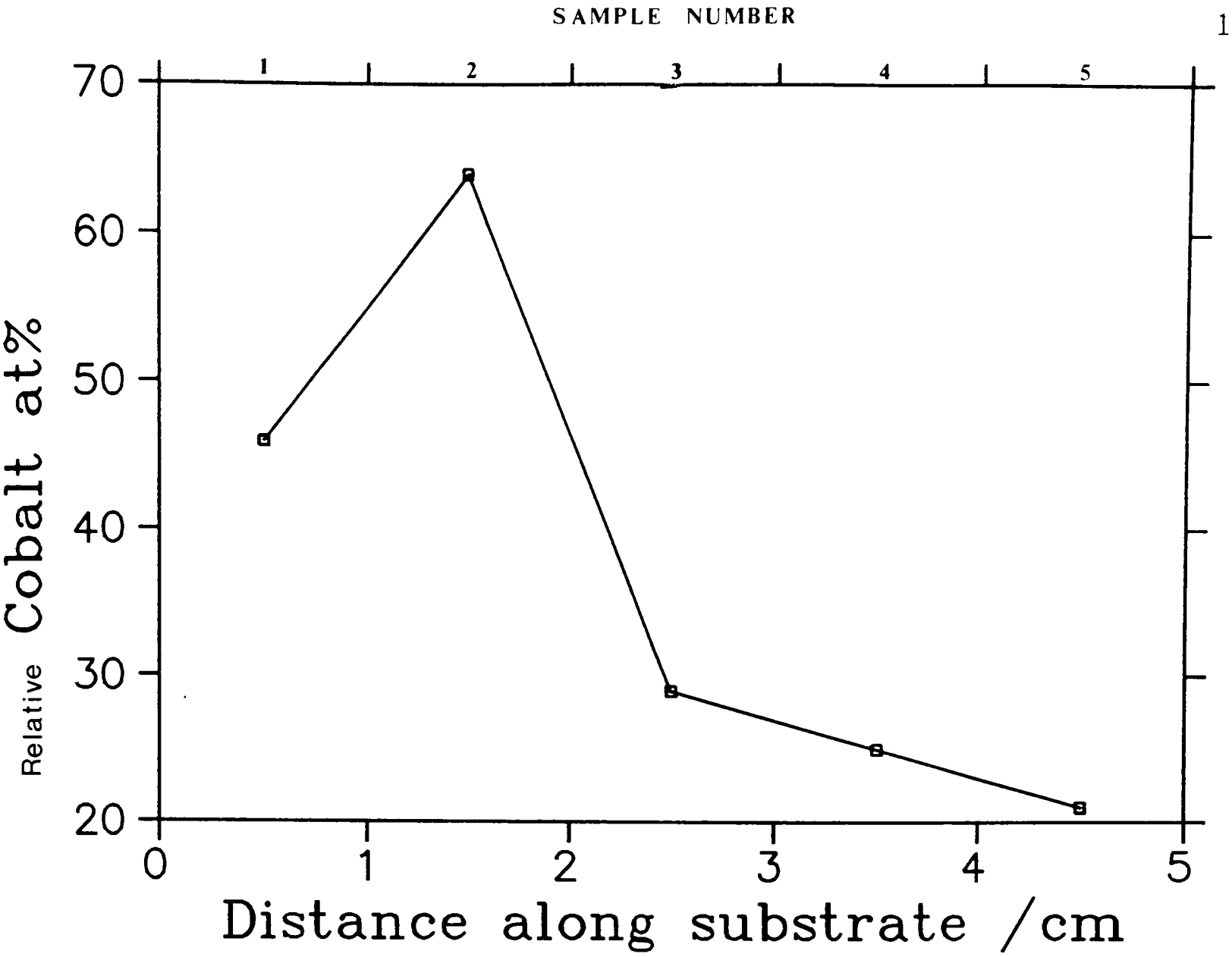
Figure 4.12

GMR, transverse magnetoresistance measurements were made in the usual manner, with the current direction perpendicular to the concentration gradient.

4.10.1 Room Temperature MR Results

Fig.4.13b shows the GMR measured in a field of 1.3T for the as-deposited (solid line) and annealed (dashed line) samples as a function of position along the substrate. The Co concentrations for these positions were shown in Fig4.13a. It is noted that the GMR does not saturate in the applied field of 1.3T despite the fact that the large particles appear to saturate in a field of order 500mT. A smaller tail in the GMR data has been experimentally observed by other groups [53],[52] and is likely to arise from the gradual alignment of very small magnetic clusters. In our samples the high Co concentration may result in slightly larger cluster size; such magnetic particles have more easily aligned moments which will make a more significant contribution to the GMR for a similar applied field value. The maximum GMR found was 10% for sample 2, which has a Co concentration of approximately 50-60%. It is this sample which will be discussed in the following sections unless specifically stated otherwise. The annealing process (10 minutes at 484°C) resulted in a much smaller GMR and it is noted that the position of the GMR peak has undergone a shift to lower cobalt concentrations. This is because the initially small cobalt granules which form in regions of low cobalt concentration grow during the annealing process forming particles that are of the optimum size to produce a large GMR. There is however an insufficient number of these particles to produce a large GMR effect. The film resistance was found to have decreased by roughly a factor of 3 for all films; this would tend to result in a larger GMR if all other factors were to remain unchanged. The reduction in film resistance could arise from increased crystallite size resulting in less boundary scattering, or from a reduction in the internal strain of the sample.

That no increase in GMR is found indicates one of two possibilities. The annealing process could have been at too high a temperature so that the optimum particle size was passed through. Secondly the as-deposited particle size could have been larger than the optimum value. A liquid nitrogen cooled substrate table is under construction. This


SAMPLE NUMBER
1
2
3
4
5
70
60
50
40
30
20
Relative Cobalt at%
0
1
2
3
4
5
Distance along substrate /cm
Sample Number

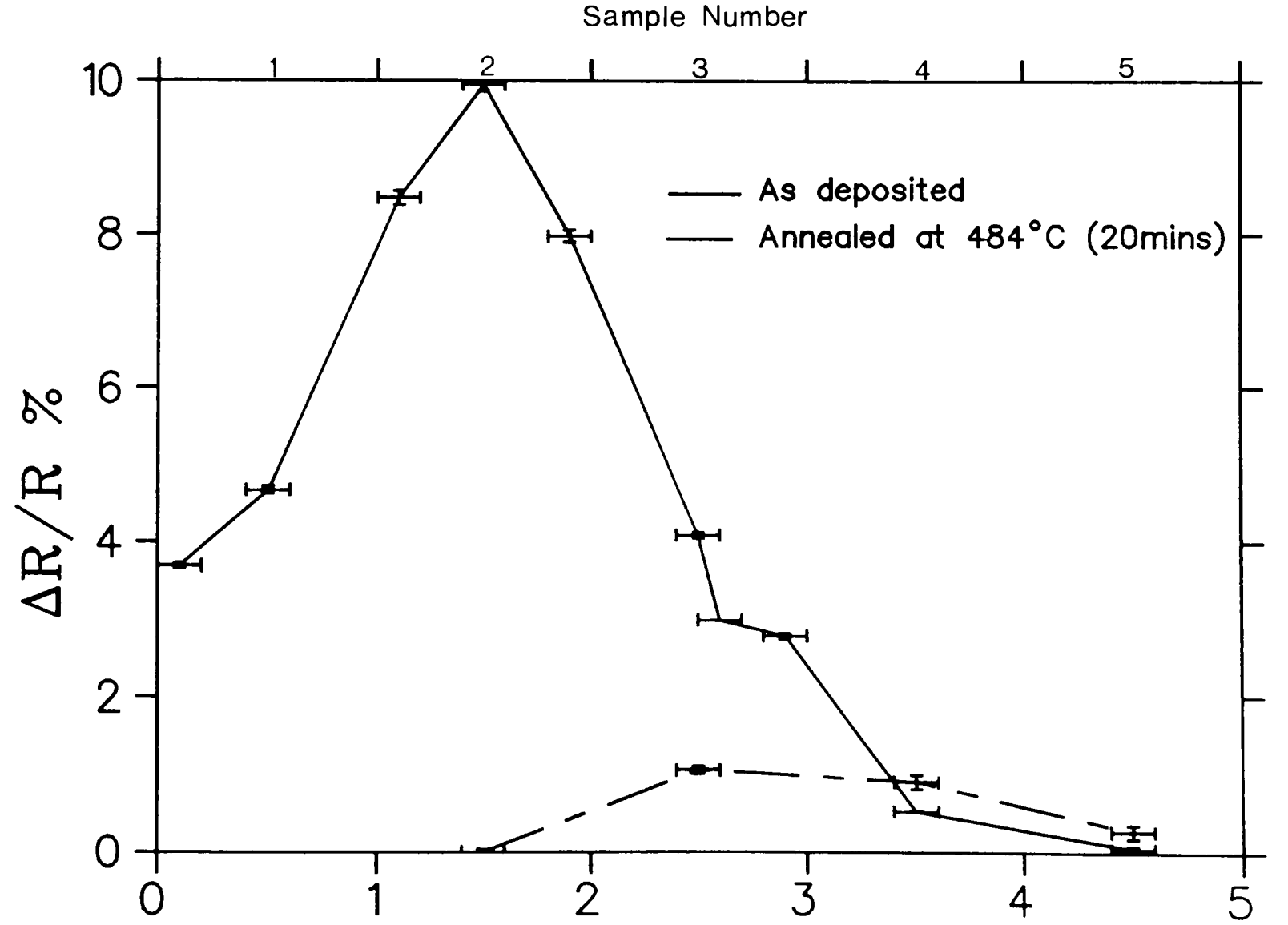

1
2
3
4
5
10
8
6
4
2
0
ΔR/R %
As deposited
Annealed at 484°C (20mins)
0
1
2
3
4
5
Distance along substrate /cm

Figure 4.13

will enable a less granular alloy to be deposited and will permit a greater control over final particle size with careful subsequent annealing.

At present we have no accurate measure of particle size distribution to confirm values calculated from magnetometry data. Preliminary TEM measurements are under way. Berkowitz *et al* [52] utilized bright field micrographs to estimate an average spherical particle size of 40Å at an average spacing of 80Å in Co-Cu alloys with maximum GMR. Barnard *et al* [65] found maximum GMR in an as-deposited Co-Ag alloy which featured grains of 20Å size. Individual grains of a specific orientation appeared to be clustered into larger particles of 150Å size.

4.11 MR as a Function of temperature

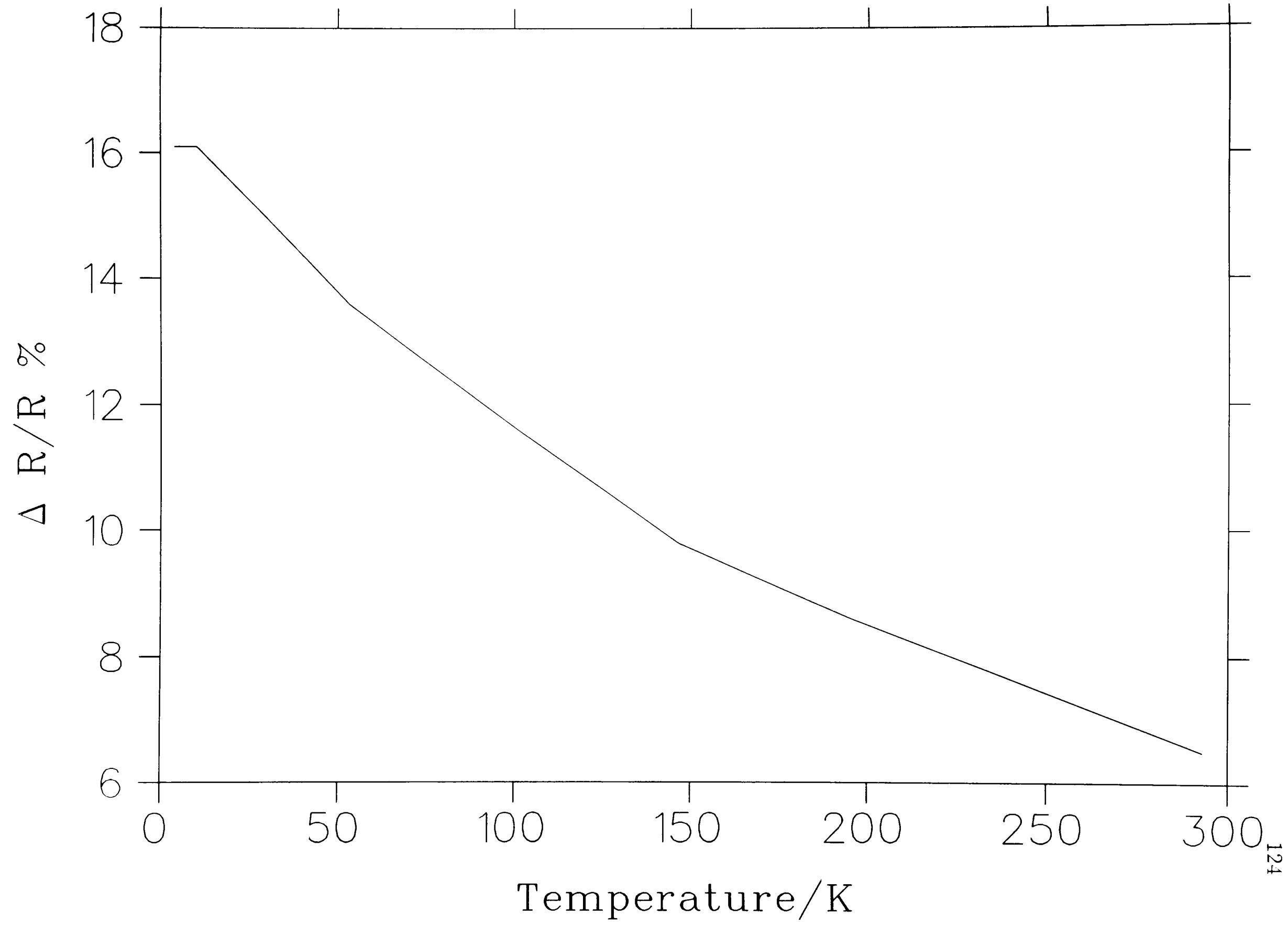
Fig. 4.14 shows the temperature dependence of the MR for sample 2. It was found that the MR increased as a function of decreasing temperature, resulting in a maximum MR value of 16.1% at 4.2K. The increase of Δ R/R% on cooling is a consequence of effects which cannot be easily deconvoluted. Firstly the background film resistance will fall owing to the decrease in the number of phonons present at lower temperatures. This effect does not appear to be very pronounced indicating that scattering from crystallite boundaries or impurities is dominant.

Secondly it can be seen from Fig.4.15 that saturation of the GMR has not occurred either at room temperature (upper trace) or at 4.2K (lower traces). It is possible that the increase in GMR at lower temperature arises because it is easier to saturate superparamagnetic spins at low T. This is a consequence of equation 4.1 ; an identical set of superparamagnetic particles will undergo greater alignment in the same applied field at lower temperatures. It is noted that some of the smaller class of particles present are partially aligned at low temperatures may give rise to a small contribution to the GMR.

4.11.1 Hysteresis

It is observed(Fig. 4.15) that hysteresis is apparent in the 4.2K GMR trace. Fig.4.16 is a plot of the applied field values at which the maximum film resistance occurs

Figure 4.14



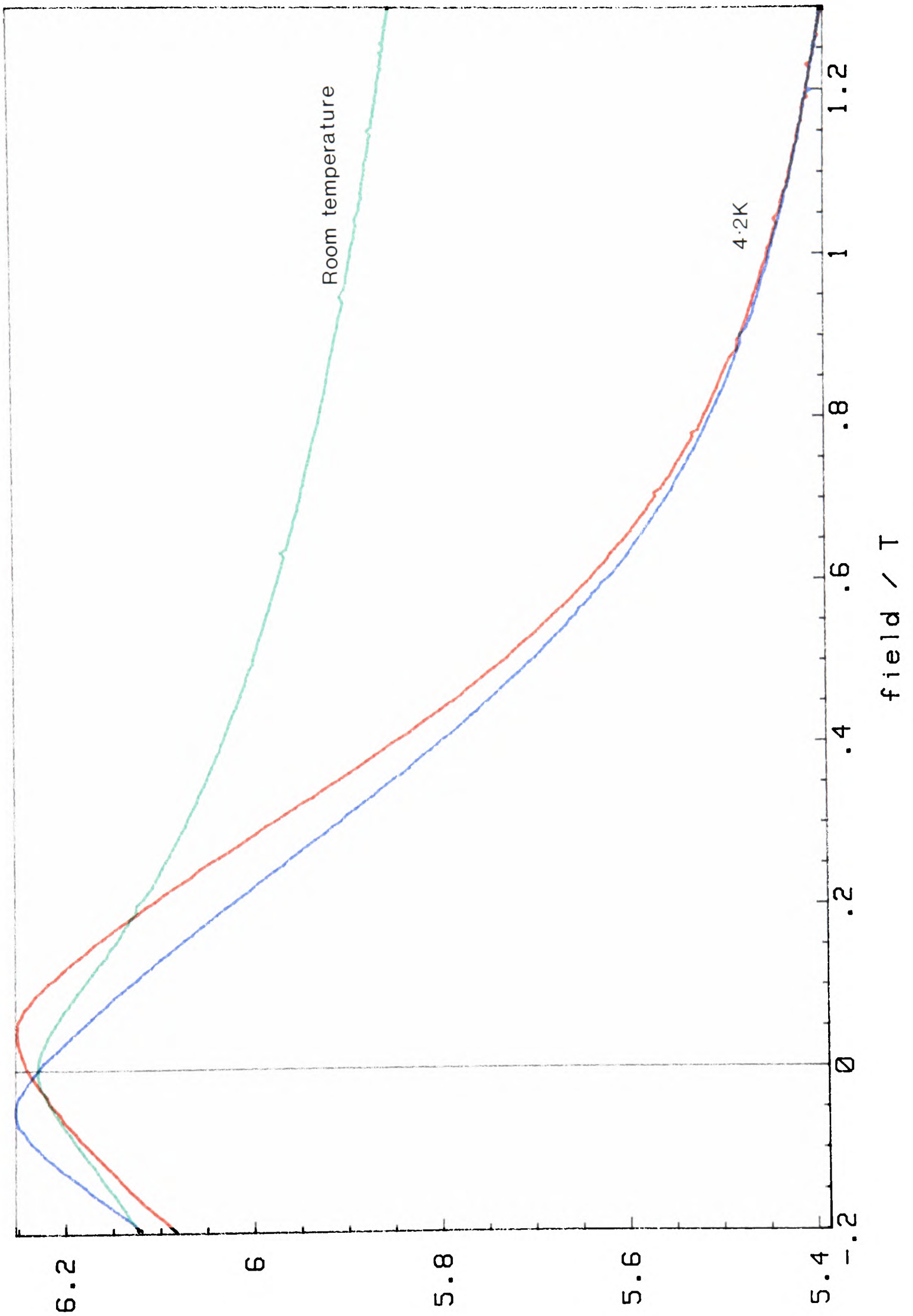

Room temperature
4·2K
6.2
6
5.8
5.6
5.4
-.2
0
.2
.4
.6
.8
1
1.2
resistance / OHMS
field / T

Fig.4.15

as a function of temperature.

A measurable hysteresis was found for temperatures below 100K, and this can be explained by the presence of superparamagnetic particles below their blocking temperature which exhibit hysteresis (as discussed in Section 4.4.2). Good agreement is found between the location of the coercive points (Fig. 4.11) and the field value at which the maximum film resistance is seen. A blocking temperature of 100K corresponds to a particle size of 28Å. There is a significant increase in hysteresis for temperatures below 30K, indicating that the majority of particles that are responsible for the GMR begin to block at this temperature. As expected there is good agreement with the value of particle size obtained from the room temperature Langevin fit and remanence results.

Fig. 4.17 shows 3 traces made after cooling in zero applied field (ZFC) to a temperature of 4.2K. The initial field sweep is indicated by the dashed line. The subsequent field cycles (solid lines) are found to have higher resistance values at the coercive fields, implying a state of increased disorder in the magnetic system as a consequence of that field cycling.

The solid line Fig. 4.18 shows the difference in the value of ΔR between the initial and subsequent traces (i.e. $\Delta(\Delta R/R)$) as a function of temperature. It is found that the size of this effect increases dramatically below 100K. The positive value of $\Delta(\Delta R/R)$ indicates the initial ZFC state exhibits more order than a truly random state would in zero field. It is noted that for temperatures in the region of 150-160K $\Delta(\Delta R/R)$ has a slightly negative value. Such negative $\Delta(\Delta R/R)$ effects have also been seen by Chien [53] in CoCu alloys and also in CoAg multilayer systems [66].

4.11.2 Origins of $\Delta(\Delta R/R)$ Effect

Fig. 4.18 shows a comparison of the magnitude of the $\Delta(\Delta$ R/R %) effect with that of remanence (shown as a dashed line); a clear correlation between the sizes of the two effects is observed. The GMR data therefore agrees well with a model which assumes that the dominant contribution to the GMR arises from the larger particles, the majority of which will block at temperatures below 30K.

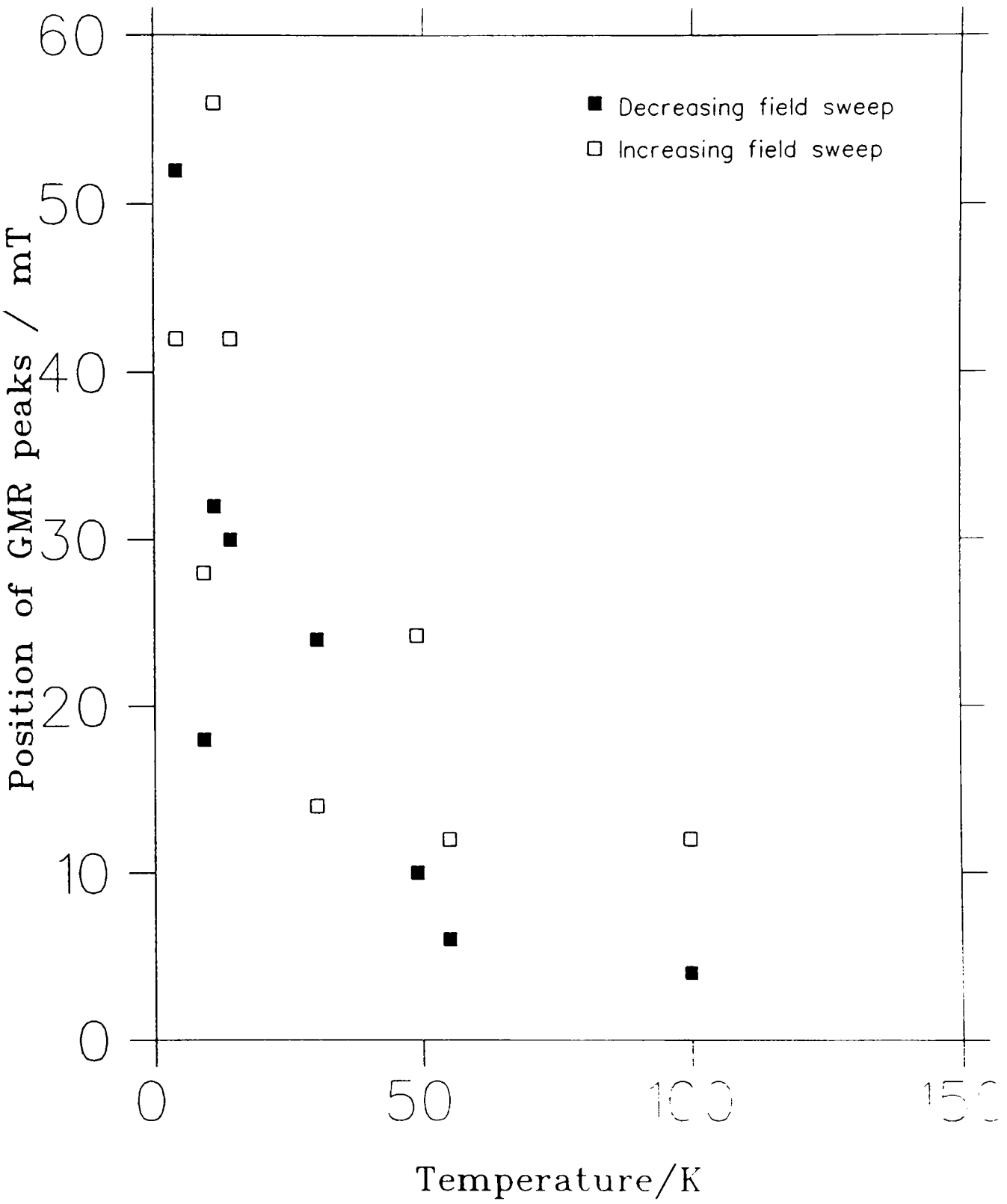

Decreasing field sweep
Increasing field sweep
Position of GMR peaks / mT
60
50
40
30
20
10
0
0
50
Temperature/K

Figure 4.16

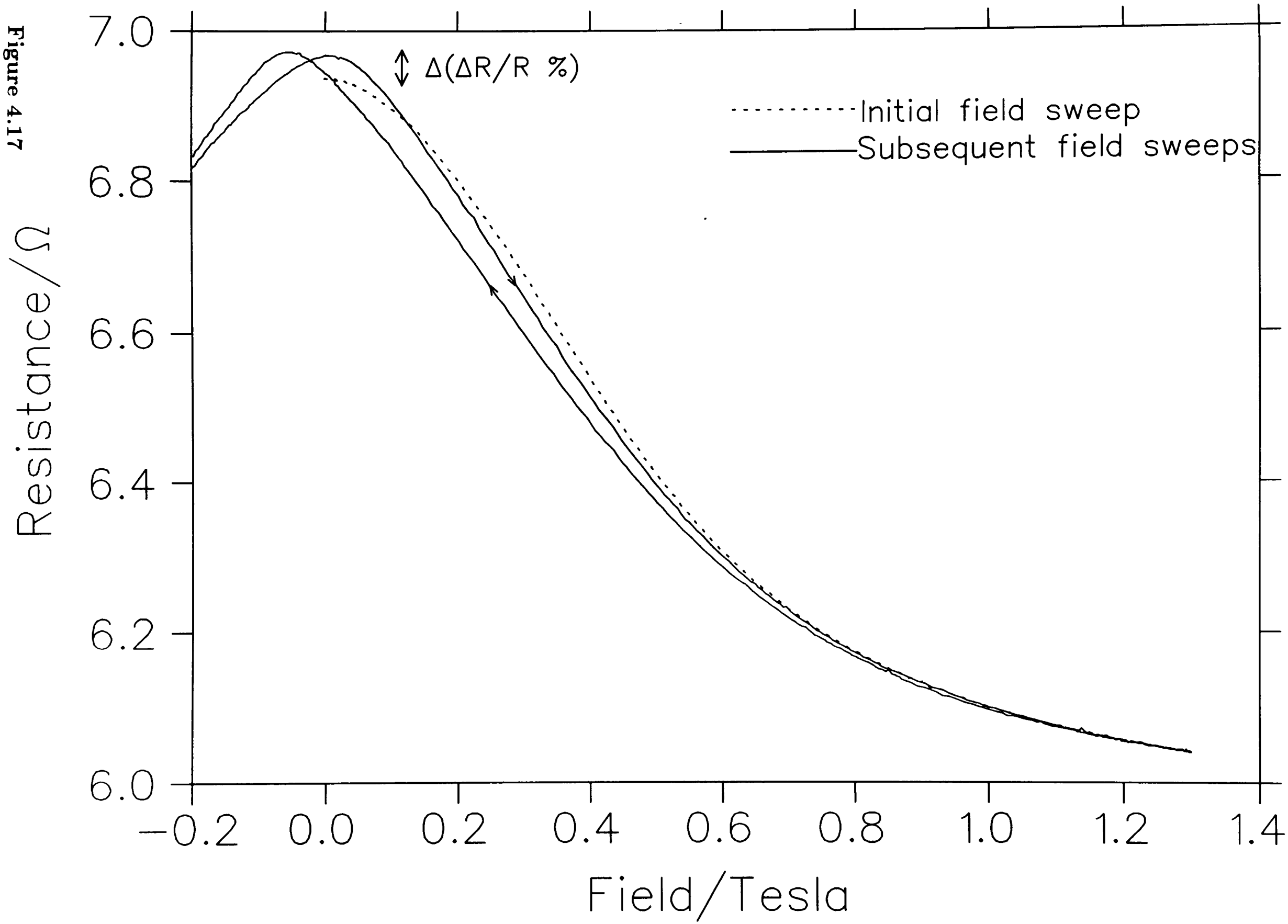

7.0
6.8
6.6
6.4
6.2
6.0
Resistance/Ω
Δ(ΔR/R %)
Initial field sweep
Subsequent field sweeps
−0.2
0.0
0.2
0.4
0.6
0.8
1.0
1.2
1.4
Field/Tesla

Figure 4.17

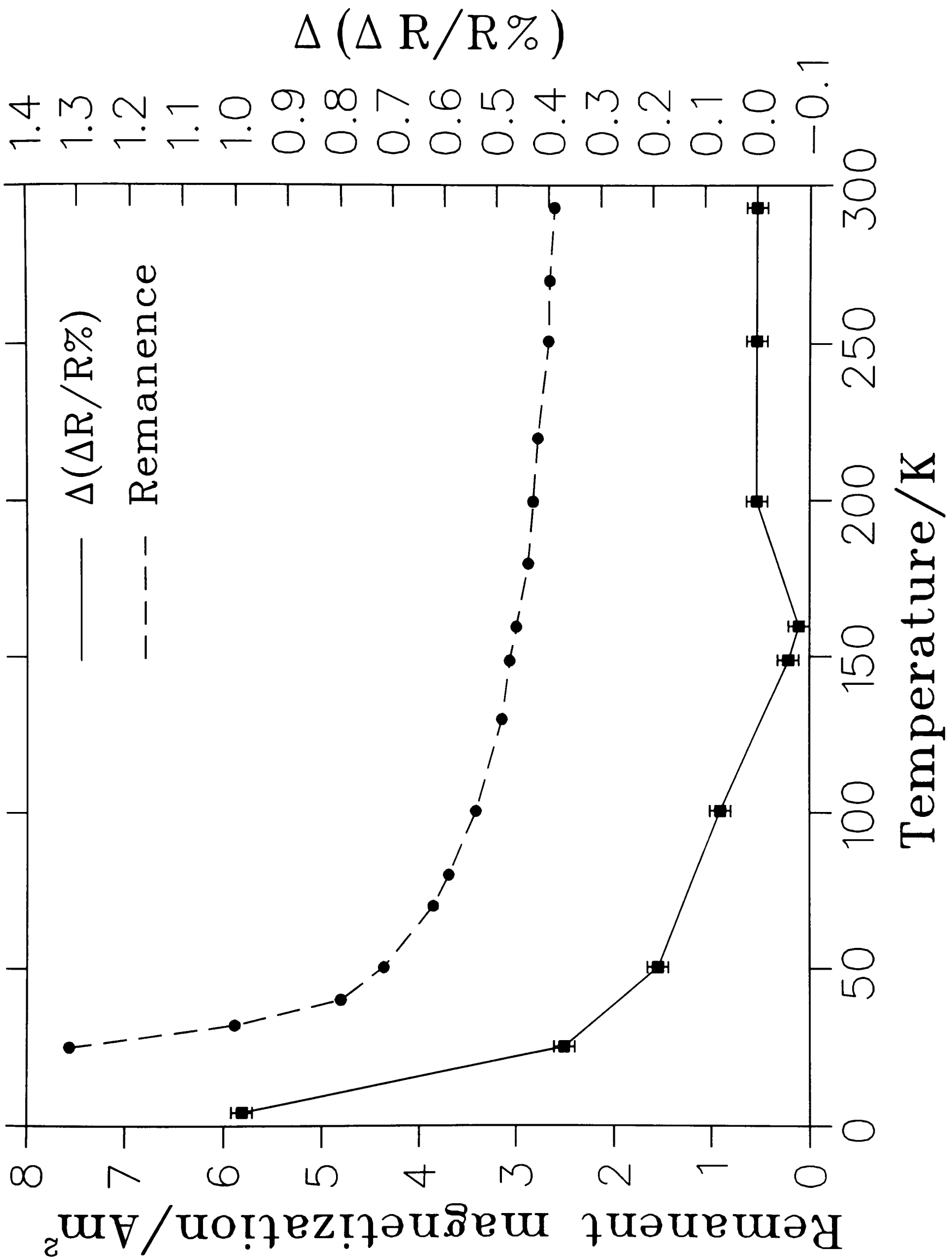

Δ(ΔR/R%)
1.4
1.3
1.2
1.1
1.0
0.9
0.8
0.7
0.6
0.5
0.4
0.3
0.2
0.1
0.0
−0.1
Δ(ΔR/R%)
Remanence
300
250
200
150
100
50
0
Temperature/K
8
7
6
5
4
3
2
1
0
Remanent magnetization/Am²

Figure 4.18

In order that the ZFC state should have a lower resistance than found subsequently at the coercive fields, it is necessary that the magnetic system in the ZFC state should be more ordered before the field cycling process. The maximum GMR appears at roughly the coercive field for the following reason. Consider a system of non-interacting magnetic particles with a range of small and large sizes in zero applied field. The small particles will be superparamagnetic for the entire range of temperatures to be considered. The larger particles will have blocking temperatures in this temperature range. Above the blocking temperatures of the large particles the moments in the system will be randomly oriented; as the temperature is decreased the large particles become blocked and the system of large particles is frozen into a random ZFC state. An applied magnetic field will tend to result in the rotation of particles and alignment of the moments of both particles sizes in this applied field direction. As the field is removed the small paramagnetic moments rotate anhysteretically. The larger particles however show hysteresis effects and will therefore exhibit remanence when the applied field is zero. The field required to rotate these particles depends on particle size and shape anisotropy and will result in a distribution of coercive fields. As a magnetic field is applied in the reverse direction the coercive point occurs when M=0 ie. the point at which as a field is applied in the reverse direction in which the sum of the moments arising from both the large and small particles is zero. The size of the GMR is dependent on particle size; we have postulated and will confirm in a later section that for our samples the larger particles contribute most effectively to the GMR. It is therefore possible that the GMR peaks and coercive points will not coincide exactly.

A positive $\Delta(\Delta$ R/R %) value can be explained by the presence of positive coupling interactions between neighbouring single domain particles, which is present at all temperatures. As the temperature is reduced below the blocking temperature of the larger particles this order is frozen into the system. If the FM coupled regions are of dimensions comparable with or larger than the MFP, the partially ordered ZFC state will therefore have a lower resistance than a randomly aligned ZFC state. Thus when a magnetic field is applied the resulting decrease in ΔR will be smaller. The coercive field

of a given particle will depend on its size and anisotropy [67]; there will therefore be a loss of ordering between the initially FM coupled particles. Field cycling produces a magnetic configuration at M=0 which is different and more disordered than the ZFC state. Because the particles are now below their blocking temperature hysteresis will occur. The hysteresis and $\Delta(\Delta R/R)$ effect will become more pronounced as the temperature is decreased because the number of blocked particles increases. This explains the clear correlation between the $\Delta(\Delta$ R/R %) effect and remanence in the sample.

4.11.3 Quadratic fit

As discussed in Zhang's theory of GMR, for a system of non-interacting particles the magnitude of the GMR should vary quadratically with the magnetic moment at low temperature. An attempt has been made to fit our room temperature and 4.2K data to a parabolic curve. The room temperature data for sample 2 cannot be satisfactorily fitted to a parabola. The data is shown in Fig4.19 . Fig 4.20 shows the data for sample 1 and it is seen that a good fit is obtained for magnetisation of magnitude greater than $\frac{M}{M_S}$=0.35 allowing for the presence of slight hysteresis. The low field GMR is clearly independent of the applied field. This can be explained by:

(1) a model of ferromagnetic interactions between a significant proportion of particles such that field alignment occurs between groups of coupled clusters but that the orientation within the groups is unchanged

(2) Large particles whose moment reversal occurs by domain wall movement.

This effect cannot be explained by the rotation of smaller particles that contribute little to the GMR as their contribution to the moment at room temperature will also be negligible. This model can clearly be applied to the results of sample 2. It is noted from the fit to sample 1 that it appears that the fit to the quadratic should be made to the regions close to saturation. The fit also indicates that there are no significant high T corrections to be made for non-interacting particles, contrary to the claims of the theory discussed in Section 4.5.1 [61].

Low temperature fits have also been made for sample 2 at 4.5K (Fig.4.21). As-

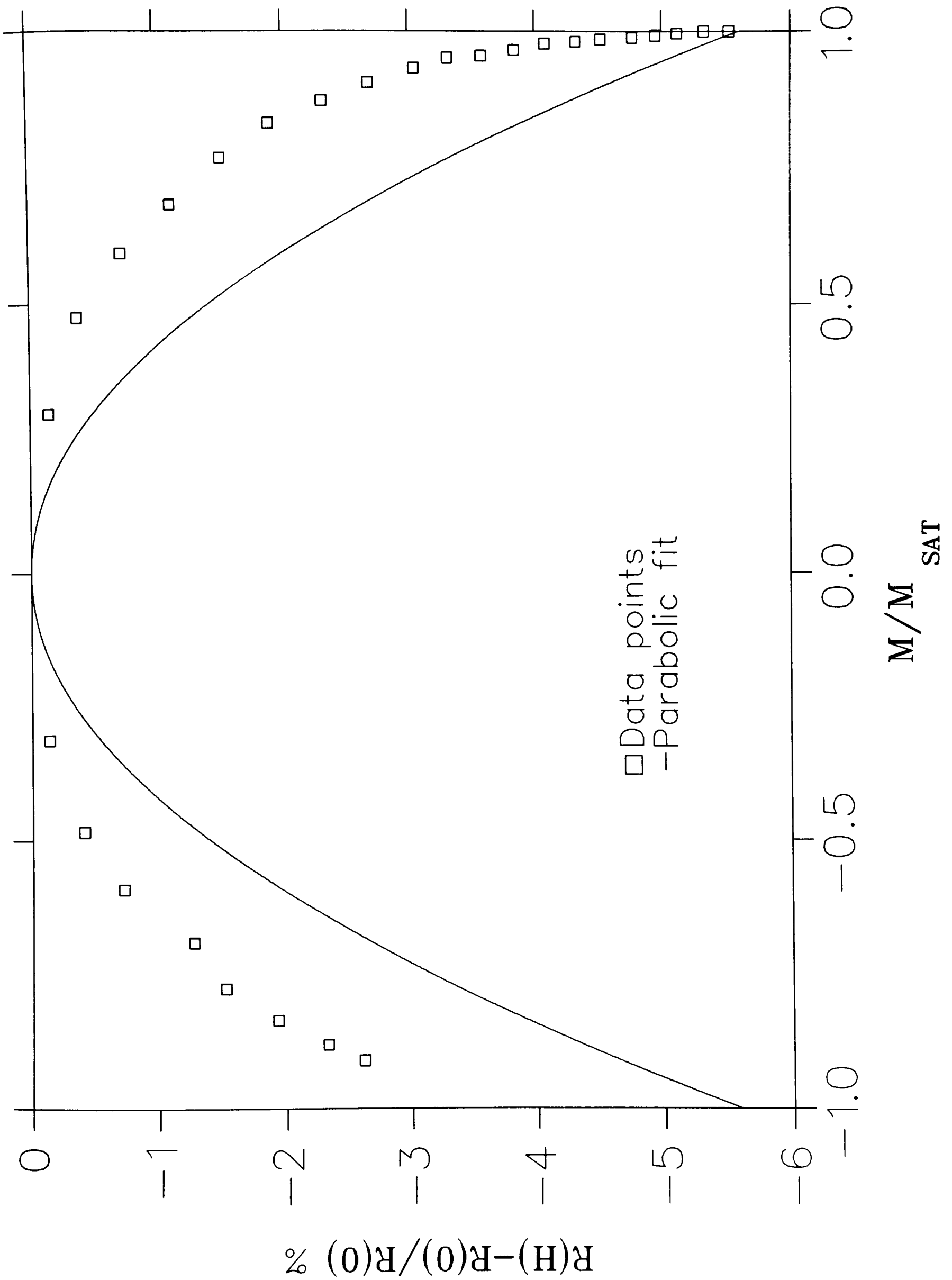
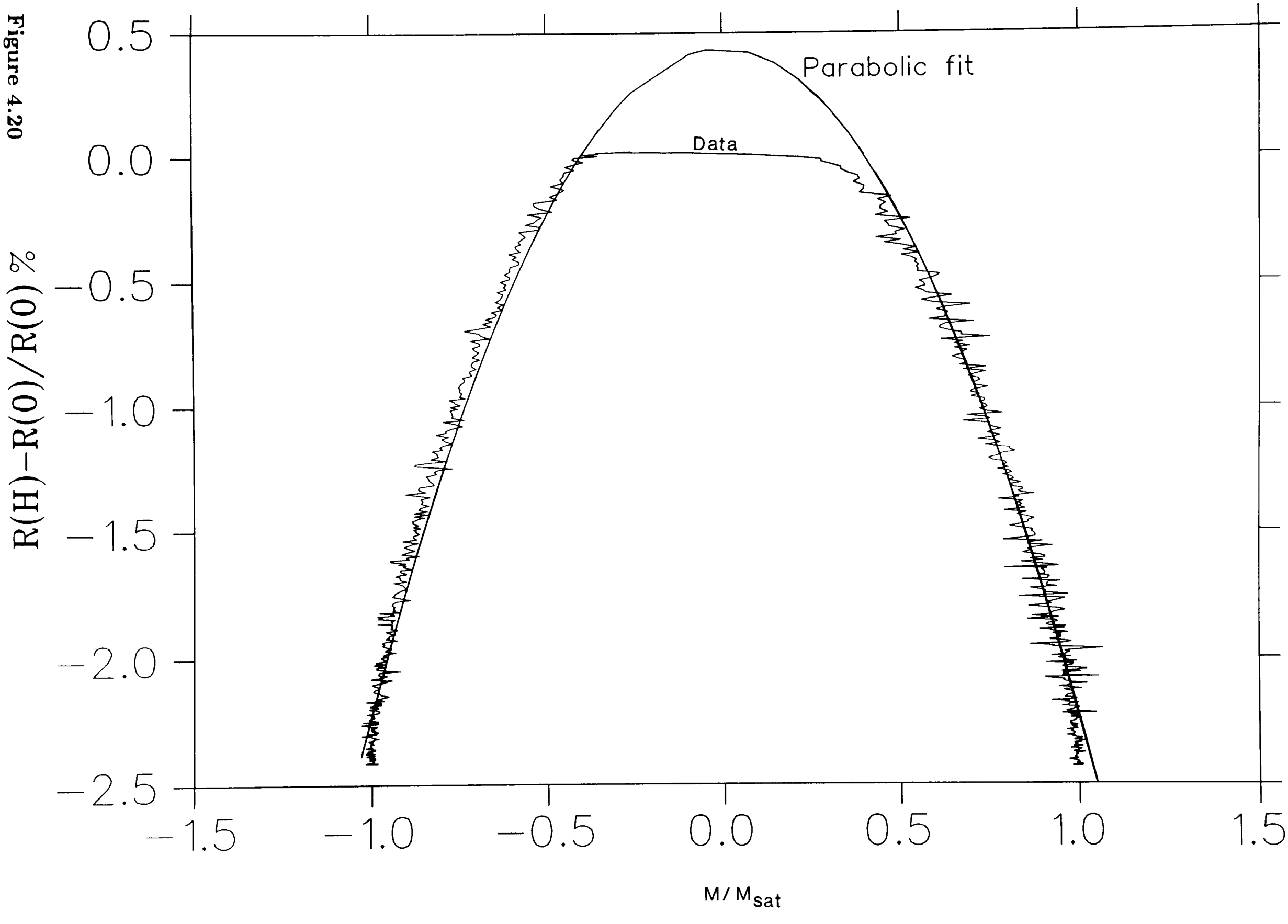

□Data points
-Parabolic fit
M/M SAT
1.0
0.5
0.0
-0.5
-1.0
R(H)-R(0)/R(0) %
0
1
2
3
4
5
6

Figure 4.19

Figure 4.20


Parabolic fit
Data
0.5
0.0
−0.5
−1.0
−1.5
−2.0
−2.5
−1.5
−1.0
−0.5
0.0
0.5
1.0
1.5
R(H)−R(0)/R(0) %
M/ M_sat

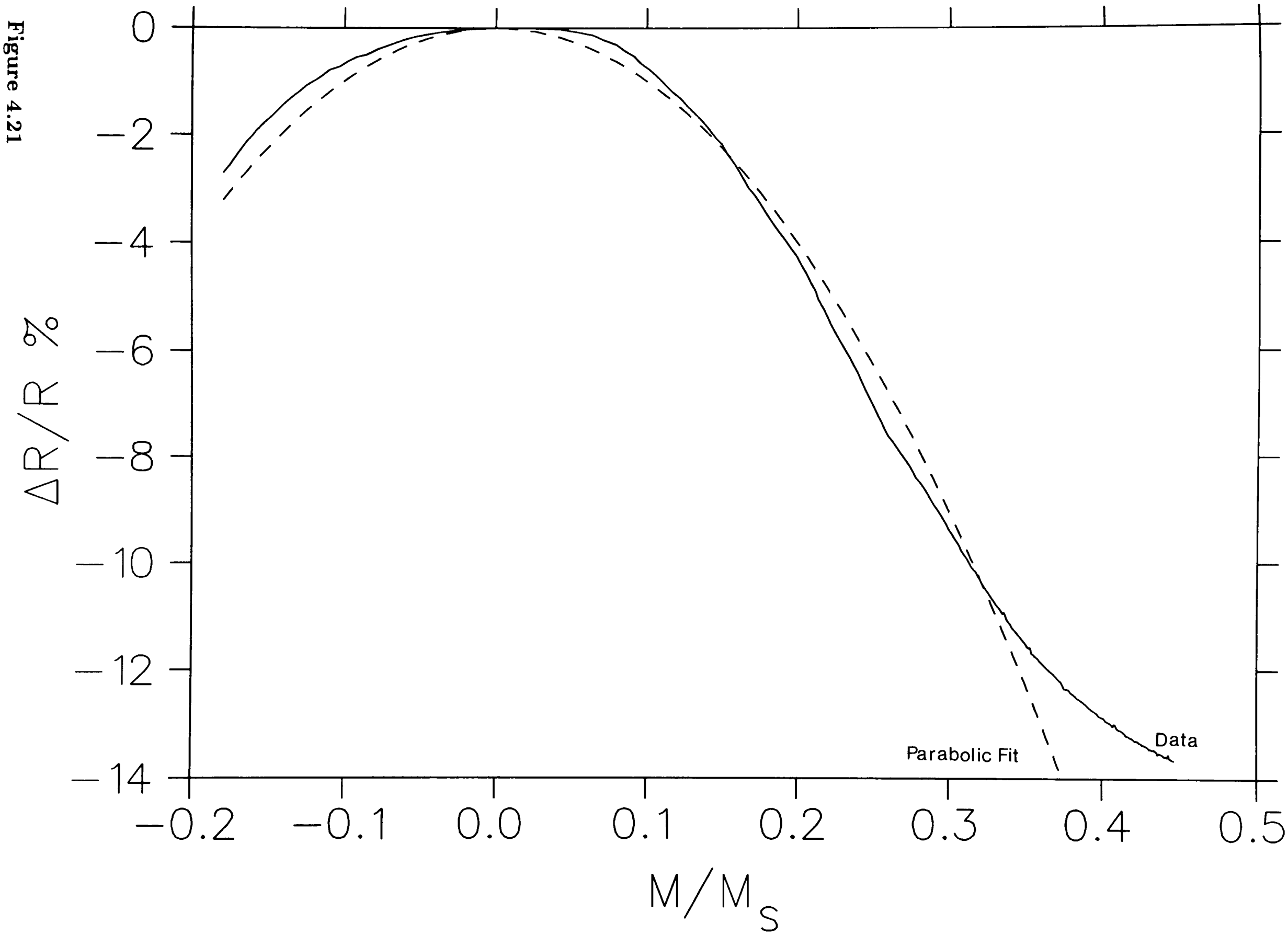


Figure 4.21

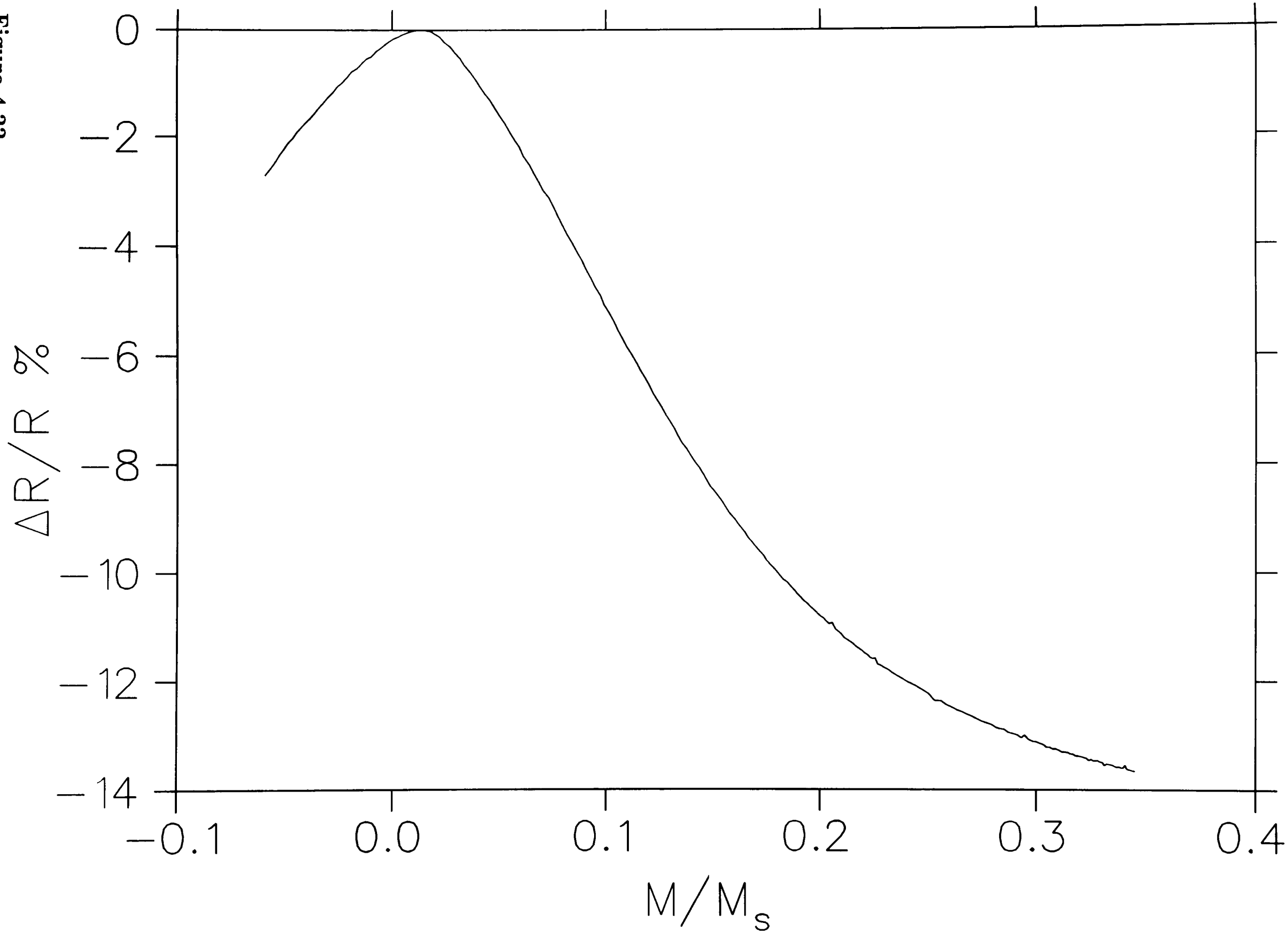
suming the full 2K moment ($\sim 1.5 \times 10^{-4}$emu) to be the saturation moment, a parabolic fit cannot be found. The GMR begins to saturate at 1.3T where M/M_s=0.4. As shown in Fig.4.21 a roughly parabolic fit can be made assuming a much smaller saturation moment ($\sim 5 \times 10^{-5}$emu). This clearly confirms the idea that at low temperatures the magnetic moment arises from two classes of particle. At low temperatures the small particles contribute very significantly to the moment and yet do not play a major role in the GMR. The magnetometry data from the two particle sizes must be deconvoluted prior to fitting a quadratic to the data. Fig.4.22 shows a plot of GMR against M/M_s as calculated from a Langevin function for $6\mu_B$ particles at 4.5K. Clearly a parabolic fit cannot be made to this data, confirming the original hypothesis that scattering from the large particles contributes most to the MR. A similar fit to the moment of the large particles produced a more parabolic curve reminiscent of the room temperature results shown in Fig.4.19.

Chien made a quadratic fit to his experimental data [53] and found good agreement with the theory at 5K except at close to the points M/Ms= $\pm$ 1. This would indicate that the alloys contained a largely uniform particle size distribution contributing equally to the spin dependent scattering.

4.12 Conclusions

In conclusion it has been demonstrated that there are two classes of magnetic clusters in the system. Particles of moment $12600\mu_B$ of approximately 7360 atoms and smaller clusters of moment $6\mu_B$ containing roughly 4 atoms. The ratio of magnetisation derived from the large and small particles at 2K is 1:5. There is therefore approximately 1 large particle for every 10000 small clusters. It is found that the small particles are not responsible for the majority of the GMR; this can be deduced from the fact that at room temperature no significant alignment of the small moment particles occurs and yet there is still a significant GMR. The magnetisation of the small particles will vary as a function of 1/T. Thus at low temperatures when the moments can be aligned the MR ($\propto T^{-2}$ from equation 4.3) of these particles may become significant. This however

Figure 4.22

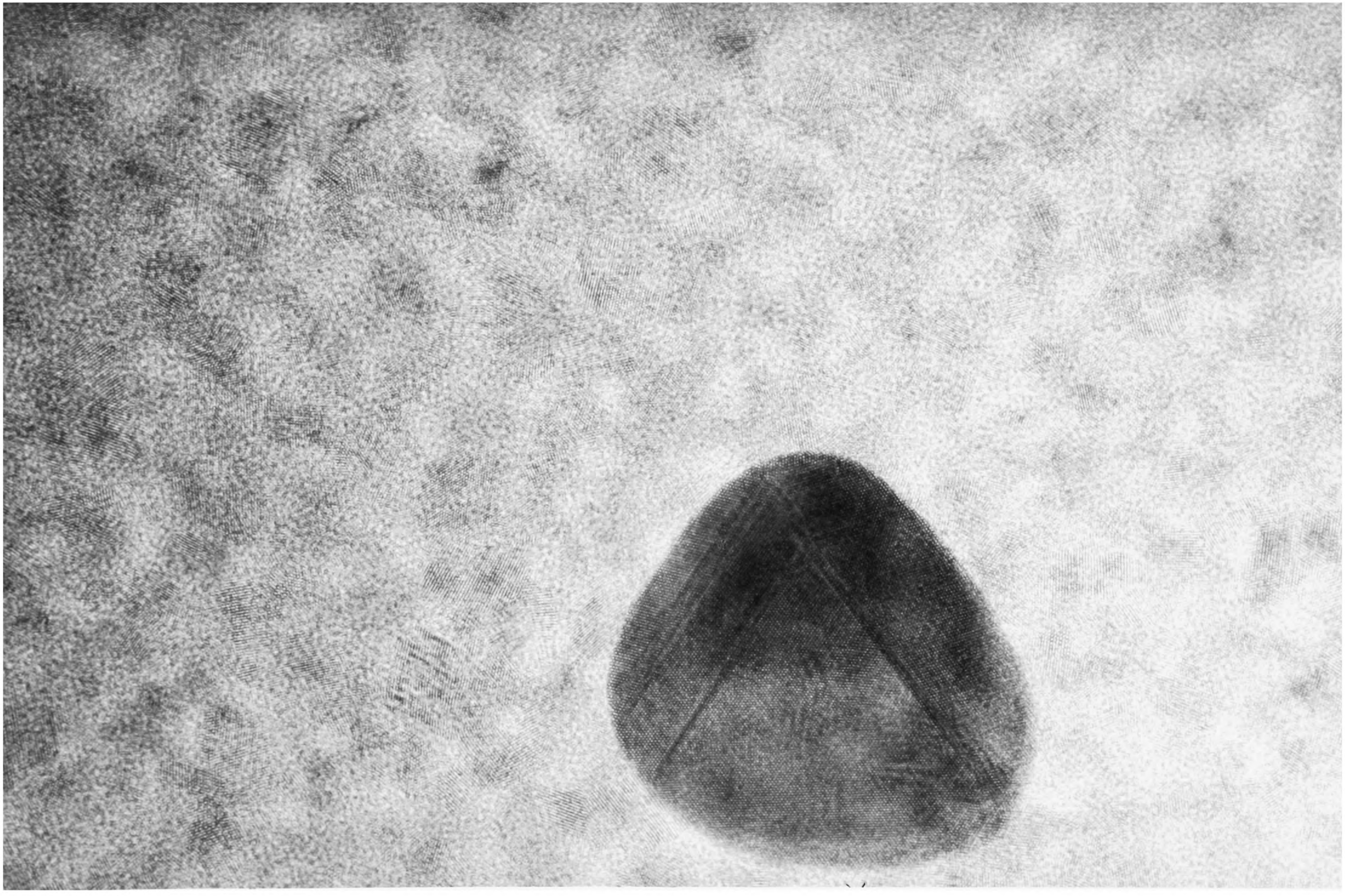


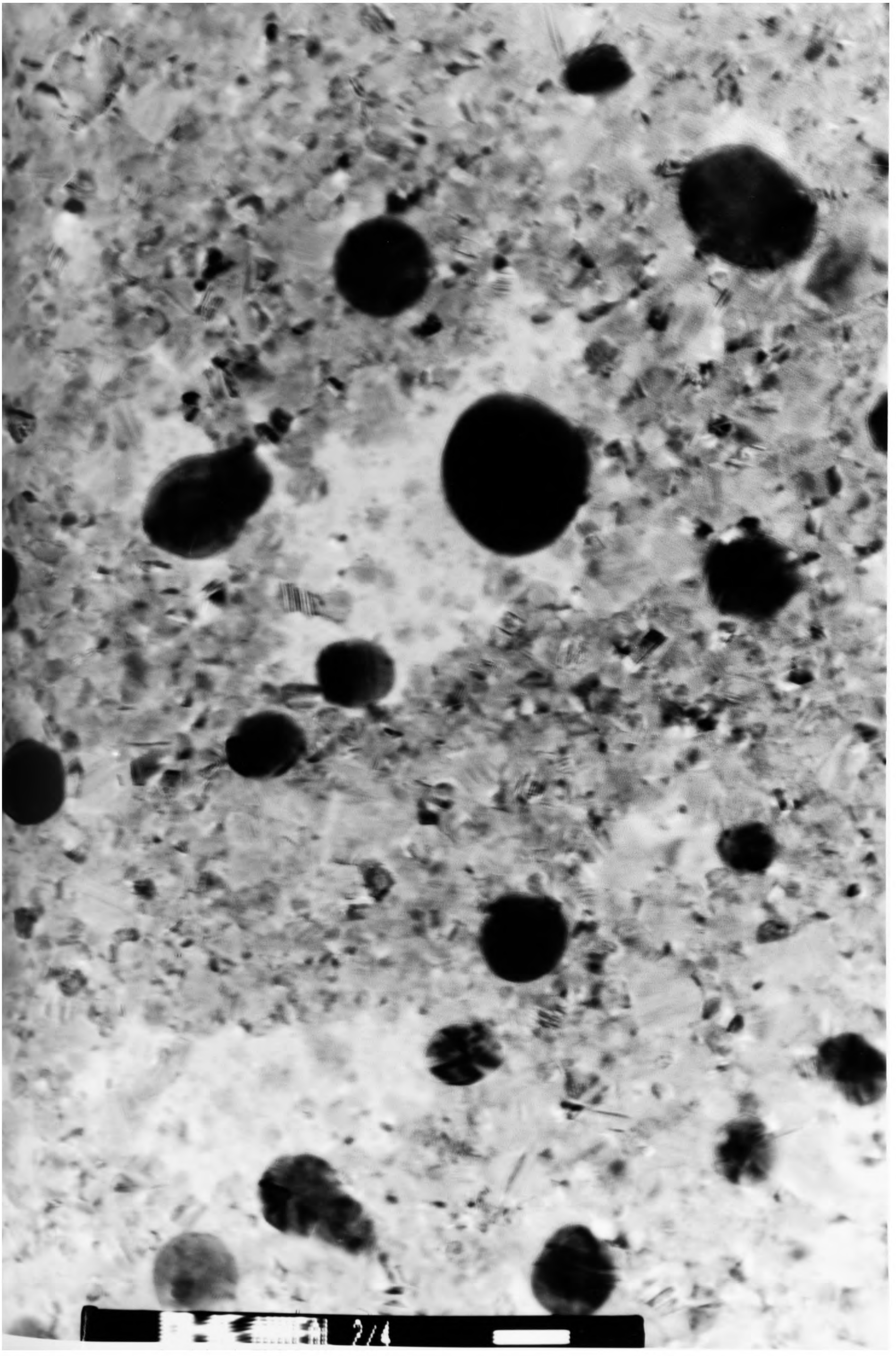
is not found experimentally. That a significant proportion of the GMR arises from the large particles is further confirmed by the appearance of hysteresis in the GMR traces. The GMR must arise at least in part from those large particles which become blocked at low T. This postulate has been confirmed by the increase in remanence and the size of $\Delta(\Delta R/R)$ effect at lower temperatures and the correlation between these effects.

Ferromagnetic interactions between blocked neighbouring particles have been invoked to explain the $\Delta(\Delta R/R)$ results. It is apparent from the deviation from a simple quadratic fit as seen in Section 4.11.3 that interactions are present. The low temperature fits to a quadratic form are not good; the moment increases rapidly whilst no change in GMR is seen. This could arise from strong inter-cluster ferro-coupling and also the large field dependent contribution to the magnetisation provided by the small clusters which do not make a significant contribution to the GMR.

Further research will be directed towards identifying the optimum particle size and Co concentration for the maximum GMR in a sample of uniform concentration. This will be achieved by the growth of various alloys of different concentrations on a liquid nitrogen cooled substrate table to produce films which are as homogeneous as possible. The evolution of the film structure and magnetic domain size will be observed during the annealing process by using TEM techniques, with the aim of correlating particle and grain size with the magnitude of GMR in a similarly annealed film.

Preliminary TEM results (Fig.4.23 Scale 3cm=100Å) for 25% Co sample grown at 77K show the existence of particles of 200Å dimensions which consist of clusters of smaller particles or which in some cases are of single crystal form; using EDX measurements these particles have been found to consist of predominantly Ag ($\sim$ 85%). Between these large particles are polycrystalline regions on a scale of tens of Å; the chemical composition of this polycrystalline region is found to be a mixture of Co and Ag. The identification of small grains as being of either pure Co or Ag is difficult to establish using the EDX technique owing to the small physical size of these regions. It is not inconceivable that these small grains could be regions of high Co or Ag concentration. Regions of these dimensions which consist of predominantly Co could clearly be identified with the





$13000\mu_B$ Co particles. Small clusters of Co within predominantly Ag grains (of either size) can be identified with Co particles of $6\mu_B$ moment.

Annealing starts to result in increased phase separation at a temperature of 240K increasing to a significant rate of change above 300K. As the annealing process progressed the large Ag clusters grew in size and in some case forming particles of 1000Å dimensions (Fig.4.24 Scale 3cm=500Å). The composition of these Ag particles increased to over 95% after annealing. The grain size is found to increase as the annealing process proceeds. Such structural changes would result in a lower film resistance as was observed experimentally. Further experiments are under way to identify the composition of the individual grains in the polycrystalline regions and to identify the magnetic domain structure of the films.

Chapter 5

Magnetic Structure in Dy/Y Superlattices

5.1 Rare Earth Multilayers

The rare earth (RE) elements such as Gd, Ho and Dy have been widely studied because of interest in their fundamental interactions which give rise to unusual magnetic orderings [68]. These metals exhibit an indirect exchange coupling mechanism between the 4f electron moments which is mediated by the conduction electrons. Many complex structures occur which depend on the balance of exchange, crystal field and magneto-elastic energies. In artificial layers the balance of these factors can be altered by changing layer thickness and the crystal field symmetry. Competing temperature dependent interactions can result in highly complex phase diagrams for these systems.

Prior to advances in m.b.e. growth technology investigations of these interactions centred on alloys of rare earth and non-magnetic materials [68]. Now with the advent of modern u.h.v. deposition techniques superlattice structures with artificial compositional periods are now possible; these are found to be experimentally interesting because the bulk properties of the rare earths can be modified by the introduction of non-magnetic spacer layers or even layers of other magnetic rare earths. In principle it is now possible to investigate the strength and range of interactions between magnetic layers by varying the thickness and composition of a conducting but non-magnetic spacer layer. Non-magnetic spacer layers can be used to produce essentially hundreds of thin films in one sample for low dimensional study that would otherwise be too mechanically fragile to handle or in which the magnetic signal would otherwise be too small to measure. It is possible that quantum effects could be found (c.f. Quantum wells in low dimensional semiconductor systems.)

5.1.1 M.b.e. deposition

The m.b.e. technique uses slow deposition rates producing structures that are highly crystalline and which can contain thin layers on an atomic scale with well defined interfaces occurring over 3 atomic planes in the best rare-earth superlattices. M.b.e requires an ultrahigh vacuum with a maximum base pressure of 10^{-10} torr and an operating pressure in the range of 10^{-8} to 10^{-10} torr. This results in the formation of atomically pure layers as very few impurities are present in the residual atmosphere. The substances are evaporated from water cooled copper boats heated by means of electron beams and also thermally heated K-cells. The evaporated particles have energies of order 0.1eV on arrival. The improvement in structure quality over films produced by sputtering and normal evaporation techniques is due to the fact that the adatoms have a longer time in which to arrange themselves in a structure which reflects the crystallinity of the layer below. The m.b.e plant was initially used to grow Dy/Y multilayer systems. When setting up a new growth apparatus it is useful to grow a materials system which has previously been investigated and whose optimum growth parameters are known. The Dy/Y multilayer stack was grown at a deposition rate of $0.5 Å sec^{-1}$, at 500 -600°C.A quartz monitor and mass spectrometer provide feedback to control the deposition rate and to monitor film thickness resulting in accurately known layer thicknesses.

The temperature of the substrate needs to be controlled in order that smooth layers and abrupt interfaces are achieved; if temperatures are too low the growth surface becomes rough owing to lack of surface diffusion, whereas for too high a temperature interlayer diffusion occurs.

5.1.2 Dy/Y Multilayers

An advantage when growing epitaxial rare earths is that the bulk elements have very similar lattice parameters. Although some strain may exist between different layers the lattice mismatch is not large enough to prevent the growth of coherent crystalline multilayers. The lattice parameters of hcp dysprosium are a=3.593Å , c=5.655Å compared to a=3.650Å, c=5.641Å for yttrium, producing a 1.6% lattice mismatch in this

system. The rare earth elements are very reactive and tend to react with substrates and elements in the atmosphere. The breakthrough in the growth of rare earth multilayers came when it was discovered that (0001) Y could be grown epitaxially on a Nb (110) surface [69] which would not itself react with a sapphire substrate. $(11\bar{2}0)$ sapphire surface of area 1 cm^2 was used as the substrate, on to which 1500Å Nb buffer layer was grown. A seed layer of 500Å of Y was then used to allow relaxation of the lattice parameter from that of Nb to that of bulk yttrium. A thin film of pure Dy grown on a sapphire substrate with Nb buffer layer and Y seed layer will also experience strain owing to the presence of lattice mismatch between the Dy and Y. This strain arises when the basal plane of Dy is grown epitaxially on the Y lattice, which has a larger a parameter, and becomes expanded. Correspondingly its c-axis is contracted. This can be considered equivalent to applying a uniaxial stress along the c direction.

5.1.3 Bulk Dysprosium Properties

The ground state of the Dy^{3+} ion is $^6H_{15/2}$. The Dy 4f moments interact via an indirect exchange mechanism mediated by the conduction electrons. Below $T_N = 185K$ Dy orders antiferromagnetically in an in-plane incommensurate helical spin structure along the c-axis which is in this case also the growth axis. Each basal plane is ferromagnetically aligned but the angle between each successive plane rotates by a average turn angle which continuously decreases from 43.2° at its ordering temperature to 26.5° at 85K when the spin structure collapses into a ferromagnetic state. This is a first order transition resulting in a crystal distortion which occurs as a result of competition between exchange and magnetostriction. The helical distribution of spins can be ferro-aligned by the application of a sufficiently large external field in the basal plane. In general the field necessary is less than 1.5 Tesla. The helix has a characteristic length Λ_M which is defined as the distance in which the spiral turns through 2π radians.

Pressure dependent studies have shown that the spiral structure of bulk Dy is strongly strain-dependent [70]. For thin Dy films the first order ferromagnetic transition. seen at 88K for the bulk Dy, is suppressed owing to the lattice mismatch strain between

the Y seed layer and the subsequent Dy layer. For single layer Dy films the strain was not relieved for Dy thickness of less than 76Å [71]. For thicker films the strain is sufficiently relieved to allow a transition. The critical temperature decreases with decreasing film thickness. The spiral structure remains stable at low temperatures because the Dy basal planes are effectively clamped by their epitaxial growth on the Y seed layer. The elastic energy associated with the lattice distortion which accompanies the magnetic phase transition is larger than that of the corresponding change in magnetic free energy and the ferromagnetic transition is therefore energetically unfavourable.

5.1.4 Effects of Superlattice Modulation

On a simplistic level we would expect the introduction of non-magnetic spacer layers to cause a superlattice to behave in a significantly different manner from bulk Dy owing to the changes in magnetic interactions within the system. For a truly inert spacer layer the Dy layers would each have helical ordering but this helix would not exhibit coherence from one layer to the next. The width of the magnetic satellite, when deconvoluted from that of instrumental resolution, would correspond to that of a single Dy layer thickness. This contrasts with the results found from the neutron diffraction experiments of Saloman *et al* [72] which showed that the chirality and phase coherence was preserved across the spacer layer. This is clearly seen in [73] where the widths of the magnetic peaks are almost resolution limited indicating a coherence over many Dy layers. The coherence length for 9 Y atomic planes was found to be of order 600Å [74]. The coherence length for 20 Y planes was 100Å. It is postulated that the information about the phase of the helix is transmitted via a RKKY type indirect exchange interaction through the non-magnetic Y spacer layer to form a coherent spin structure whose coherence length decreases with increasing Y layer thickness. The RKKY interaction has a r^{-3} dependence. It is therefore expected that the introduction of a sufficiently thick Y spacer layer into a Dy/Y system should result in a breakdown of communication between two consecutive Dy layers. This would be evidenced by a loss of coherence between the magnetic spin helix in successive Dy layers.

The nature of the helical ordering also changes from that seen in the bulk. The turn angle decreases with weaker temperature dependence than for bulk Dy and can lock-in to a particular turn angle at lower temperatures [74],[75]. In order to calculate the Dy turn angle, an angle of 50° per atomic plane of Y was assumed [76], [77] [75]. Rhyne *et al* fitted data to produce a value of 51° [74]. We have assumed a value of 51° in our calculations.

5.2 Neutron diffraction

Neutron scattering methods have been used to look at the structure of Dy/Y multilayers. Neutron diffraction patterns provide magnetic structure information due to the interaction of the neutrons intrinsic spin with the moments of the Dy atoms present in the film. These interactions with the magnetic structure give rise to extra peaks in the resulting diffraction pattern enabling information concerning the magnetic periodicities of the samples, the spin configurations and magnetic coherence lengths to be extracted.

5.2.1 Theory

In order to predict the appearance of diffraction peaks it is necessary to consider the reciprocal lattice and construct an Ewald sphere. The reciprocal lattice is defined by the reciprocal lattice vectors:

$$\mathbf{a}' = 2\pi \frac{\mathbf{b} \times \mathbf{a}}{\mathbf{a}.\mathbf{b} \times \mathbf{c}} \tag{5.1}$$

The incident beam is represented by the vector $\mathbf{K}$ which terminates at a reciprocal lattice point chosen as the origin of reciprocal space where the length of $|\mathbf{K}|$ is given by

$$|\mathbf{K}| = \frac{2\pi}{\lambda} \tag{5.2}$$

where λ is the wavelength of the incident neutrons and is of order Angstroms. An Ewald sphere is then drawn about the origin of the vector $\mathbf{K}$. A diffracted beam is observed if the sphere passes through any other reciprocal lattice point. The diffraction condition can be expressed as

$$\mathbf{K}' = \mathbf{K} + \frac{\mathbf{G}}{2} \tag{5.3}$$

where **G** is a reciprocal lattice vector that connects two lattice points. Assuming that K=K' then angle 2θ between the incident and emergent beam can be found using

$$\sin\theta = \frac{G}{2}.\frac{1}{K} \tag{5.4}$$

more usually expressed as

$$2K\sin\theta = G \tag{5.5}$$

where θ is the angle which the incident beam makes with the diffracting planes.

Using the relations above, the corresponding repeat distance of the structure in real space, is given by

$$\Lambda = \frac{2\pi}{G} \tag{5.6}$$

Thus a small repeat distance in real space produces widely spaced associated reciprocal lattice points, and correspondingly widely spaced Bragg peaks.

5.2.2 Diffraction Patterns

Single crystal Dy/Y neutron diffraction patterns illustrate many of the features that may be found. First consider a single crystal of a pure material. The lattice containing only one type of atom regularly spaced, gives rise to Bragg peaks only. The position of these diffraction peaks is governed by the Bragg equation

$$2dsin\theta = n\lambda \tag{5.7}$$

where d is the atomic layer spacing n is the order of diffraction.

In the case of Dy/Y, the n = 1 order diffraction peaks are missing because of destructive interference between layers in the hcp unit cell. The only diffraction peaks occur at (002) and about the origin (000). For a multilayer film the structure consists of alternating layers of Dy and Y, and gives rise to a characteristic chemical repeat distance, Λ_c, which corresponds to the bilayer thickness.

A further modulation on the system is produced by the presence of a helical magnetic structure in the Dy layers below the transition temperature $T_N = 185K$ which

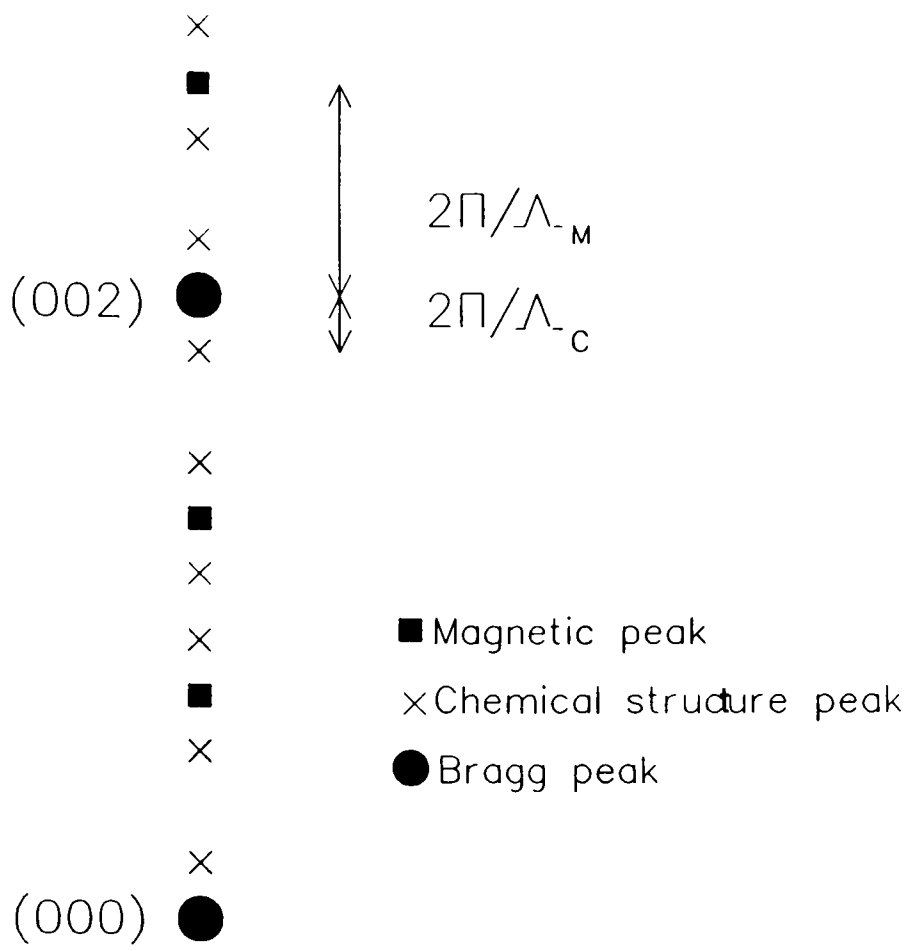


Figure 5.1 A typical diffraction pattern

causes a set of magnetic peaks to appear. The coherence length of the spiral can also be obtained from the inverse of the width of the magnetic peak.

Figure 5.1 is a typical map in reciprocal space of the diffraction peaks produced by neutron scattering from a [Dy/Y] multilayered structure showing characteristic lengths arising from structural and magnetic repeat distances.

5.3 Experimental Methods

5.3.1 The Chemical Modulation

The samples that were investigated were of nominal composition $[Dy_{100\mathring{A}}Y_{15\mathring{A}}]_{50}$ and $[Dy_{42.7\mathring{A}}Y_{42.7\mathring{A}}]_{80}$ which are identified as SL13 and SL25 respectively. Using these results the weighted average lattice parameter $\bar{c}$ was calculated, and was used to predict the diffraction peak positions for the subsequent neutron diffraction experiments. The

weighted average lattice parameters were found to be $\bar{c}$=5.6585Å and 5.6897Å for SL13 and SL25 rspectively assuming c_{Dy}=5.6475 for bulk Dy and c_{Y}=5.7318 for bulk Y.

5.3.2 Scanning electron microscopy

Scanning electron microscopy (SEM) has been used to look at the surface structure of the multilayers. Figure 5.2 (a) and (b) respectively feature scanning electron micrographs of the samples SL13 and SL25 taken using a Jeol JSM840A scanning electron microscope. The electrons used were of energy 10kV and 15kV respectively.

Structure is clearly seen on a scale of 1μm for all samples. As Fig 5.2 shows, the earlier samples such as SL13 feature small islands with deep troughs between them in an almost 3-D structure. Later samples (eg. SL25) are of much better quality and exhibit very little structure although shallow troughs are apparent. A recent Monte-Carlo simulation [78] has shown that unstrained growth occurs in a layer-by-layer manner. Increasing strain within the model results in increasing islanding with deeper troughs. It is therefore possible that strain is responsible for the difference in quality between the samples.

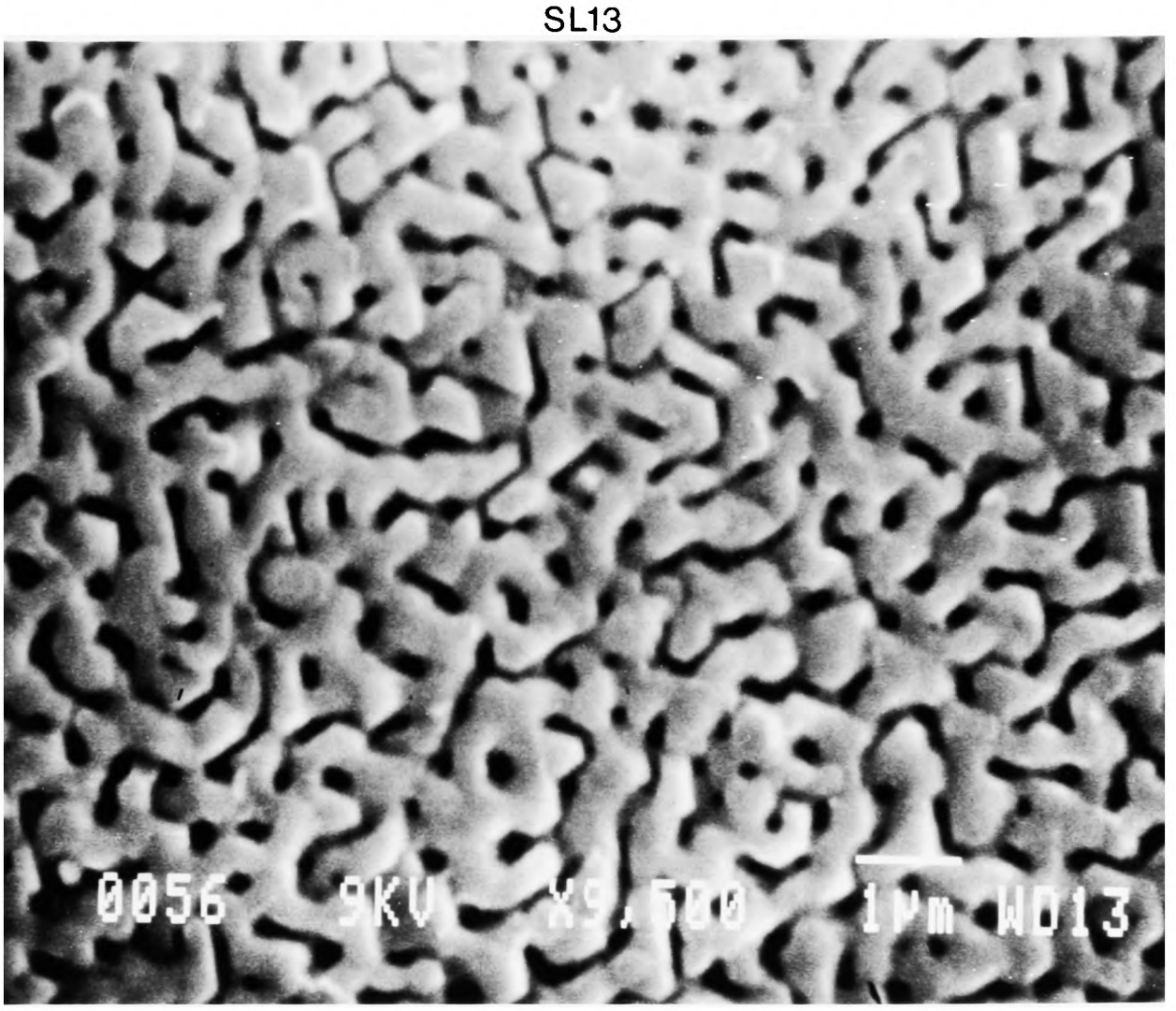
5.3.3 Methods of Neutron Diffraction

There are two methods of neutron diffraction that we have used in these studies. High angle diffraction is widely used for single crystal structural analysis. The samples we studied include m.b.e. films which consist of large crystallites. Neutron scattering from such a structure gives rise to intense well defined Bragg peaks. High angle diffraction gives poor intensity diffraction peaks for polycrystalline samples and study of such materials is more profitably undertaken using low angle diffraction which examines structural and magnetic peaks about the origin in k-space.

The experiments were performed on a double axis spectrometer PADA (G2-2) on the Orphée reactor at CEN Saclay. The resolution of the diffractometer was 10 minutes of arc. The wavelength of the neutrons was between 4.8Å and 4.9Å , whilst the neutron flux was of order 4500 neutrons per second.

The incident and emergent beams were collimated by an evacuated collimator

SL13



SL25



Figure 5.2 (a)SL13 (b)SL25

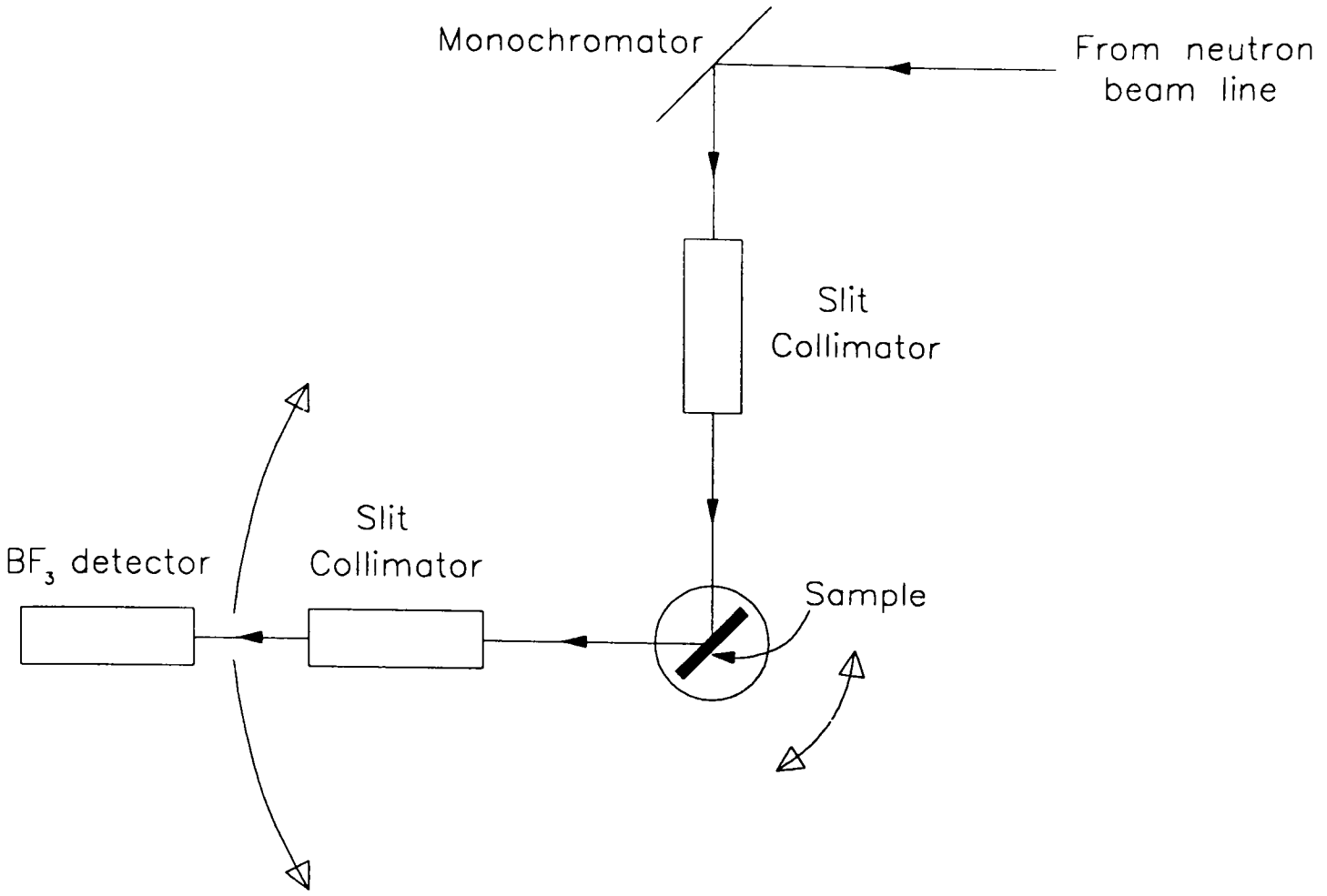


Figure 5.3 The Spectrometer

containing 5 neutron-absorbing cadmium grids containing slits 3 mm wide. It was found that although better beam collimation could be obtained by reducing slit widths to 1 mm, the mean strength was reduced by a third, which was a disadvantage considered to outweigh the improved collimation. The height of these slits was approximately 10cm. This produces a beam well defined in the horizontal plane only. The sample area can also significantly affect the detected peak size. An increase of sample surface area from 10 mm^2 to 17mm^2 can double the peak height for the same counting period. The detector was of a BF_3 type. A variable temperature liquid nitrogen cryostat was used to cool the sample; the temperature stability was 0.1K.

The beam was scattered from the sample and passed through a second collimator to the detector. The detector alignment was calibrated using reflections from a (111) epitaxial silicon substrate. The sample was then placed in the beam and vertically and horizontally aligned by taking rocking curves about the (002) Bragg peak to give the

maximum neutron flux at the detector.

5.3.4 Data Collection

The apparatus and data collection were computer controlled. Data was collected at 0.10° intervals for a period of 200s at each position of the arm. The scanning involves a $\theta, 2\theta$ scan. Thus in order for the end point of K to continue moving along the line shown, the detector arm rotates through 2θ degrees. It is important that the incoming and scattered neutron beams do not cross at the circumference of the cryostat as this introduces diffuse scattering and increases the background signal.

The neutron scattering factor, b, affects the size of peak detected, by an amount proportional to b^2. The values for the element used in our films are [79]

$b_{\mathrm{Dy}} = 16.9$

$b_{\mathrm{Y}} = 7.75$

It can be seen that there is a large difference between the value of b^2 for Dy and Y. This produces good chemical contrast between the layers.

5.4 Experimental Results-SL13

Figure 5.4 shows a typical scan around (002) at 110K. showing the magnetic satellite, structural satellite and the (002) Bragg peak at 2.027Å^{-1}, 2.110Å^{-1} and 2.252Å^{-1} respectively. The position of the structural peak relative to the magnetic peak indicates that the chemical repeat distance is in fact 76Å; sample SL13 was one of the initial multilayers made during the period in which the thickness measurement calibrations were being adjusted. It was therefore likely that a discrepancy between the actual and nominal thickness would arise.

5.4.1 Temperature Dependence

The sample was cooled and scans made at 10 Kelvin intervals in the range 170K to 100K. Assuming a value for the Y turn angle of 51Å, the value Λ_M was used to calculated the Dy turn angle which was found to vary from 44.65° at 170K to 35.28° at

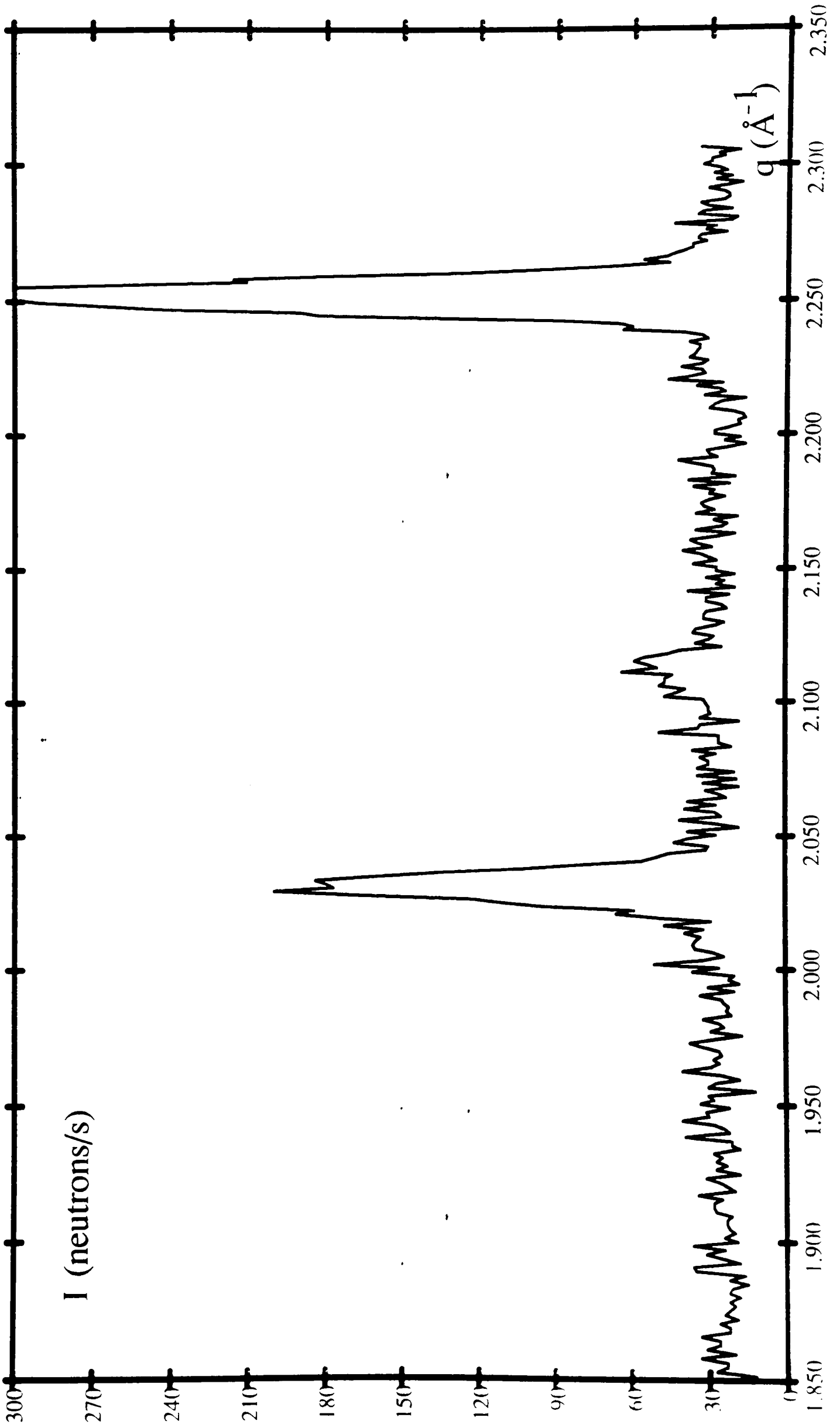

I (neutrons/s)
q (Å^{-1})
300
270
240
210
180
150
120
90
60
30
0
1.850
1.900
1.950
2.000
2.050
2.100
2.150
2.200
2.250
2.300
2.350

Figure 5.4

100K. Figure 5.5 shows these points plotted as a function of T.

Spin lock-in did not occur for this temperature range. The bulk Dy data is shown for comparison. The turn angles measured show satisfactory agreement with those seen by Rhyne *et al* [74] for multilayers of structure $[Dy_{16}$ - $Y_{20}]_{89}$, $[Dy_{16}$ - $Y_9]_{100}$ and $[Dy_{15}Y_{10}]_{64}$. Much larger turn angles at low temperatures were seen for samples of large Y spacer thickness [75] for samples $[Dy_{38\mathring{A}}Y_{120.4\mathring{A}}]_{80}$ and $[Dy_{38\mathring{A}}Y_{38.6\mathring{A}}]_{80}$. A general trend can be seen in these results. For constant Dy thickness larger Y thicknesses have larger turn angles and are less temperature dependent, having spin lock-ins at higher temperatures.

5.5 Experimental Results-SL25

Sample SL25 was cooled in the cryostat. Figure 5.6 and Figure 5.7 show high angle diffraction data for sample temperatures of 115K and 139K respectively.

The peak sizes are an order of magnitude larger than those found for sample SL13. This improvement could be due to improved film quality as seen from the SEM photos in Section 5.3.2.

In Fig. 5.6 the Bragg peak is seen to occur at q=2.21$\mathring{A}^{-1}$which corresponds to an average c-axis parameter of 5.686Å in good agreement with the calculated values. Two magnetic satellites are seen at Q=1.955$\mathring{A}^{-1}$ and Q=2.029$\mathring{A}^{-1}$. The chemical satellite is seen at Q=2.283$\mathring{A}^{-1}$. The position of the chemical satellite and the separation of the magnetic satellites correspond to a bilayer thickness of approximately 15.2 atomic layers of each metal corresponding well with the nominal multilayer composition. The profile of the magnetic satellites corresponds to a turn angle in the Dy layer of 38° at 115K.

In figure 5.7 a diffraction pattern of similar form is observed. The turn angle is found to be 39.3° at 139K. However an additional structure is seen in the magnetic satellites. Each magnetic peak now appears to consist of 5 or more distinct peaks within an envelope of the same width as the original peak. This splitting is not evident for the Bragg peak or chemical satellites, suggesting a purely magnetic origin. An identical

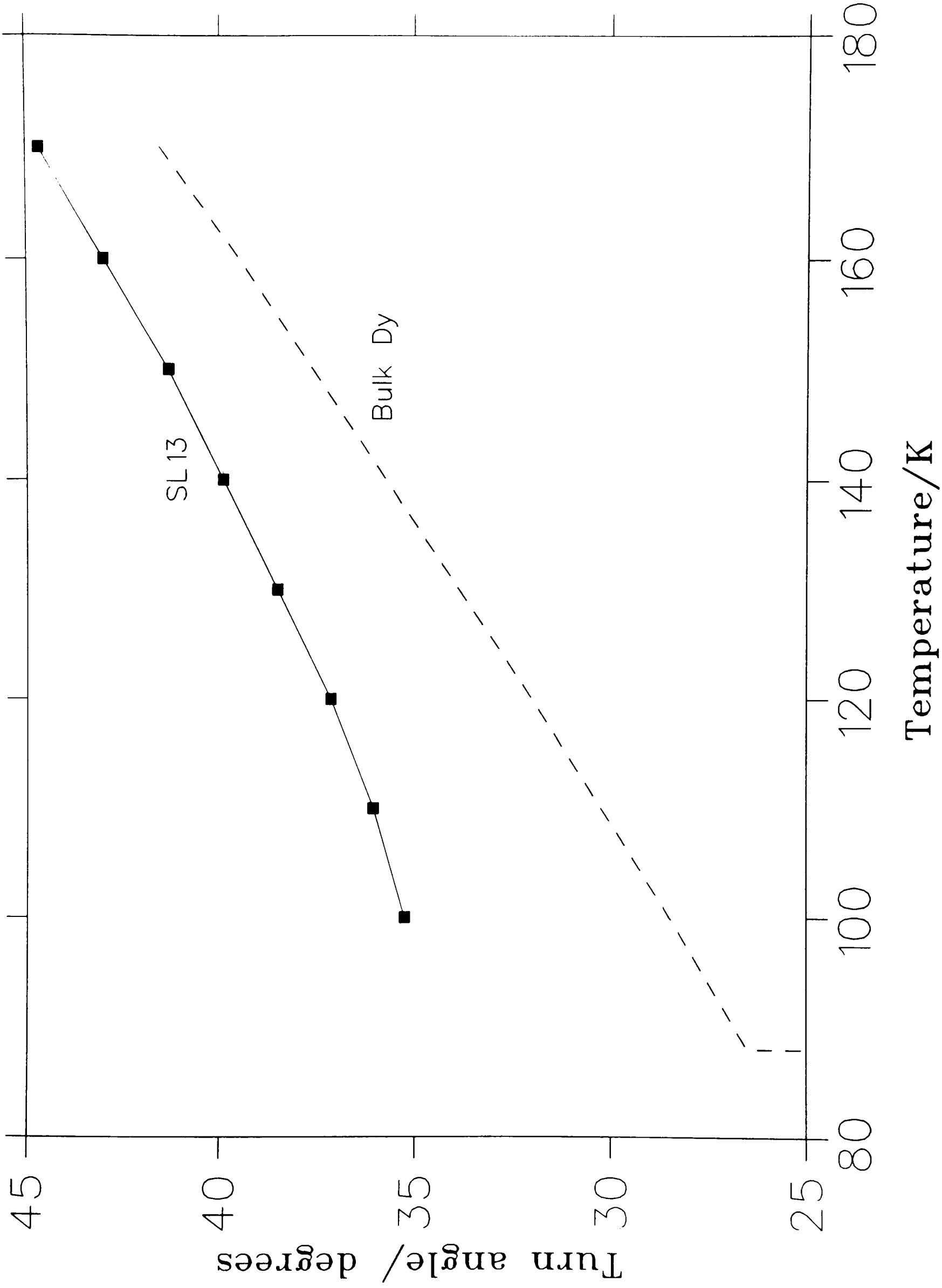

SL13
Bulk Dy
Turn angle/ degrees
45
40
35
30
25
Temperature/K
80
100
120
140
160
180

Figure 5.5

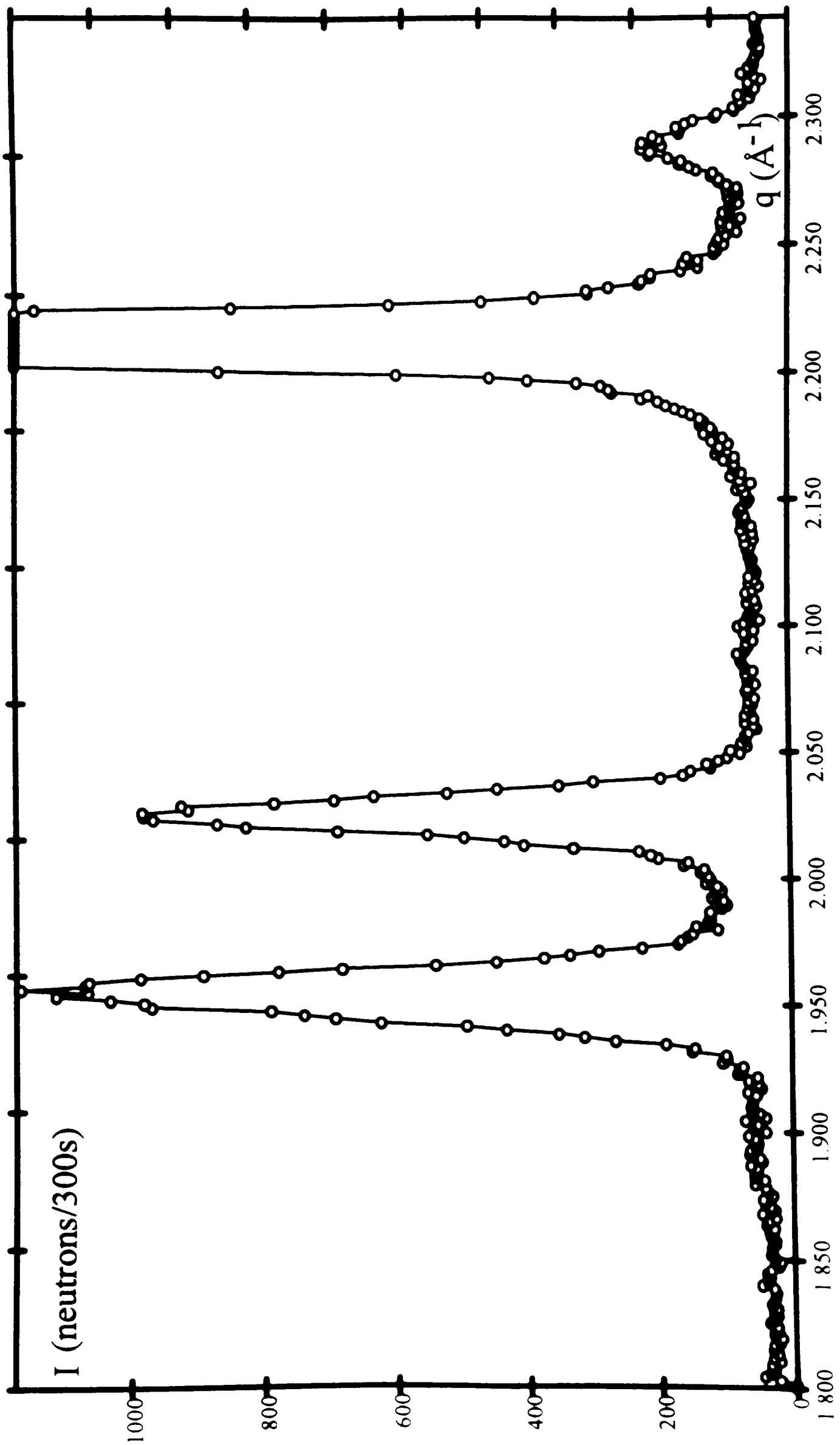

I (neutrons/300s)
0
200
400
600
800
1000
1 800
1 850
1.900
1.950
2.000
2.050
2.100
2.150
2.200
2.250
2.300
q (Å-1)

Figure 5.6

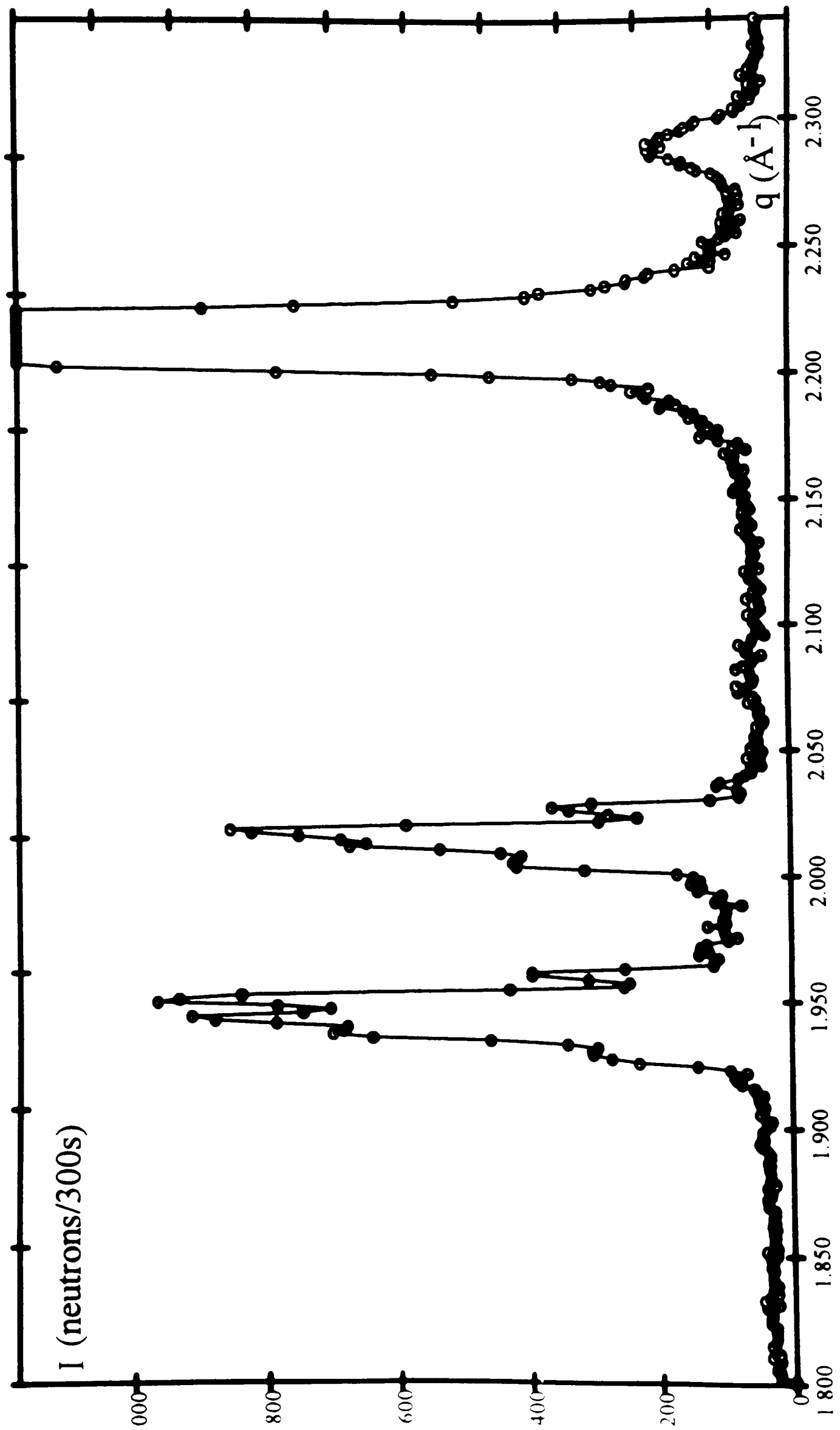

I (neutrons/300s)
1000
800
600
400
200
0
1.800
1.850
1.900
1.950
2.000
2.050
2.100
2.150
2.200
2.250
2.300
q (Å-1)

Figure 5.7

modulation of the magnetic peaks was seen in the low angle diffraction pattern. This new structure was observable over a temperature range of about 2 Kelvin, and corresponds to a periodicity of 700Å± 40Å in real space. This agreess closely with the thickness of eight bilayers (8 x 84.9Å= 679Å).

5.6 Possible Origin of the New Magnetic Structure

A magnetic structure of this characteristic length has not previously been seen for a Dy/Y multilayer or other regularly structured rare-earth multilayer. Similar structure has been observed in a diffraction pattern of Fibonacci sequenced multilayers of Gd/Y [71]. However in this case the deliberately quasiperiodic chemical structure was made in attempt to induce an unusual magnetic periodicity. In our case no such chemical modulation was imposed during growth and neither is any apparent from the subsequent measurements. It is possible that the lower resolution of previous experiments has not permitted observation of these features for similar samples [75]. Of the other 9 Dy/Y samples measured none exhibited similar long coherence length magnetic effects. It therefore seems likely that the results for sample SL25 derive from the precise chemical structure. It seems likely that at around 139K the magnetic structure is commensurate with the eight bilayer repeat distance and moreover that the apparent stability of this structure over a range of several Kelvin suggests that a lock-in occurs owing to this chemical periodicity.

The additional satellites are numerous and of large amplitude indicating that the underlying magnetic periodicity contains a relatively sharp feature. It has been reported [80] that for sufficiently thick Y layers, the magnetic chirality can change sign from one Dy layer to the next. It is therefore not inconceivable that the observed periodicity arises from a change in chirality which occurs every four bilayers giving rise to an eight bilayer characteristic length. This would indeed be an abrupt feature as the change would in effect occur within the non- magnetic spacer layer thereby minimising the energy cost of this chirality change. It may be significant that the 15 layers of Y correspond exactly to a phase change of 4π for a turn angle in the Y of 50.66°. Further experiments are

in preparation on other samples with different geometry which also exhibit this feature. The origins of the lock-in structure are unclear, but could possibly be magnetostatic in origin or arise from in plane anisotropy induced during growth by stray magnetic field or strain. Similar helical reversals are exhibited by the helifan structures in bulk holmium under the influence of a Zeeman driving term in the basal plane.

5.7 Diffraction Pattern Simulation

Taking a model of alternating helicity every 4 bilayers to be a likely possible explanation of the data, a simple simulation has been made of the nearest integral bilayer multilayer structure (i.e. 15 Dy and 15 Y) atomic planes assuming a perfect crystal. The Dy spin phase advance is assumed uniform but the helicity is reversed every four bilayers. The results are compared with the experimental data in Fig.5.8 . Taking into account the idealisations of the model good agreement is obtained between the experimental results and the calculated diffraction pattern for this idealisation.

5.8 Conclusions

A novel magnetic structure has been observed in a multilayer structure of composition $[Dy_{15}Y_{15}]_{80}$. The structure has a long range periodicity and is stable over a temperature range of order a few degrees. That similar structures have not been found for other DyY multilayers suggests that the stability may arise from a lock-in of the magnetic helicity to the chemical structure. Further experiments are under way to help confirm the proposed model of helicity reversal and to investigate the stability of the structure against magnetic fields applied in the basal plane.

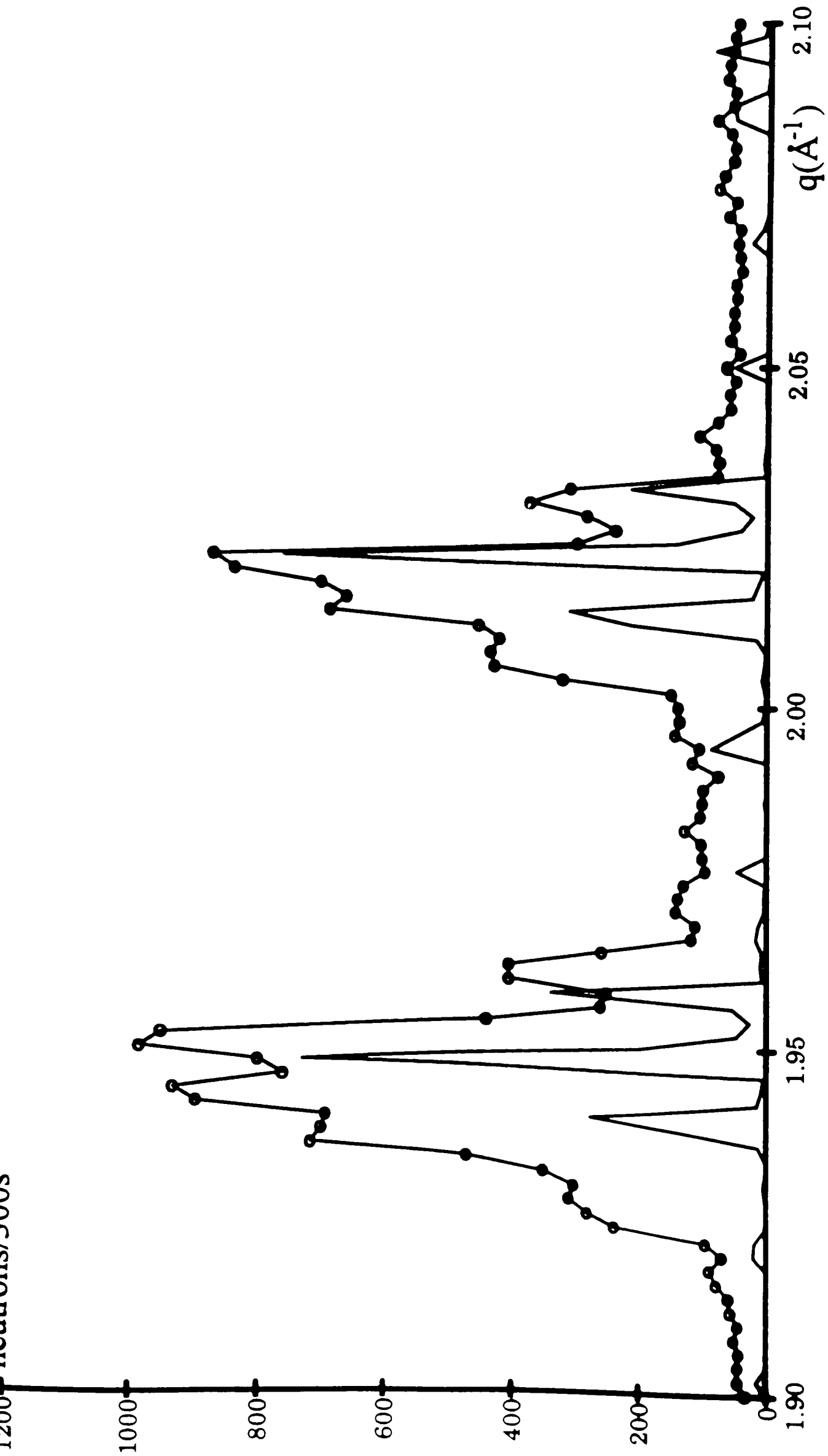

neutrons/300s
1200
1000
800
600
400
200
0
1.90
1.95
2.00
2.05
2.10
q(Å^{-1})

Figure 5.8

Chapter 6

Microwave Ultrasonic Interferometry

6.1 Introduction

Acoustic waves have been widely used in the past to investigate the magnetic properties of systems [81]. Such acoustic waves may be produced by applying an ac voltage to a transducer consisting of piezoelectric material coupled to the magnetic sample. In the reverse situation the application of an acoustic wave signal to a piezoelectric material leads to the generation of an electrical signal.

In the past many of the transducers used were slices of single crystal quartz bonded to the material under investigation. The acoustic mismatch between the transducer, bonding compound and sample reduces the electro-mechanical conversion efficiency particularly at high frequencies; the use of high frequency ultrasonic waves is important because it results in greater sensitivity and accuracy in the measurements. The lack of efficiency at high frequencies is further compounded by the difficulty of cutting and bonding sufficiently thin quartz slices. For an efficient transducer to be produced its thickness should be approximately one quarter wavelength at the desired operating frequency (depending on the acoustic impedance of the substrate and top electrode loading), although less efficient higher harmonics can also be used. To produce a 100 MHz transducer a 20μm thick slice of quartz would be needed; this is not easily achievable.

Microwave ultrasonic interferometry [82] is the acoustic analogue of the Michelson interferometer and uses ZnO transducers grown directly onto the sample which immediately results in a higher efficiency owing to better acoustic coupling. The ZnO film thickness can be adjusted to give operating frequencies up to the order of 2GHz and consequently the technique has a much improved sensitivity over more conventional interferometry which operates in the region of tens of MHz. High frequency ultrasonic pulses can be injected into a parallel-faced sample producing a series of echoes, which are

extracted for analysis by the same transducer. Changes in the acoustic time of flight provide information about changes in sample length or elastic coefficients within the sample. At high frequencies the wavelength is small, and by observing interference between the acoustic pulse emerging from the sample and a reference signal of the same frequency very small changes in the path length of order 1 part in 10^{10} can be measured. The microwave ultrasonic interferometry technique has been used to investigate several magnetic systems, which will be discussed in this and the following chapter.

6.2 The Acoustic Interferometer

A zinc oxide piezoelectric transducer is sputtered onto one face of an optically polished plane parallel sided crystal. An electrical signal applied to the transducer is converted by the piezoelectric material into an acoustic wave which propagates through the crystal. The signal is largely reflected by the opposite face; the returning signal is incident on the transducer and is mostly reflected, but some is reconverted into an electrical signal. The continuation of this process gives rise to a train of echoes which are then amplified to produce a measurable signal. The measurements that can be made on this echo train include:

(i) the attenuation of the signal,

(ii) the change of phase.

Attenuation of the echo train however may contain a mixture of information. Geometrical walk-off due to non-parallelism of the two faces must be avoided in our experiments as this gives rise to destructive interference between different parts of the returning wavefront at the transducer and this in turn causes oscillations in amplitude of the emergent wave train. Secondly, echoes from the wave trains of two different modes may coincide within the limit of resolution. Neither the amplitude nor phase of such echoes can provide much useful information in this case. Any returning transverse (T) echo may be partially reflected in the form of a longitudinal (L) mode and vice versa, thus producing an echo with transit times corresponding to the sum of the two modes. Such

echoes are easily distinguishable and are experimentally found to have small amplitudes as expected.

Higher order echoes in general have the advantage of larger phase shifts as they correspond to longer times of flight in the crystal. However the signal decreases roughly exponentially with distance travelled in the crystal thus reducing the signal to noise ratio. The optimum echo number for study is theoretically found to occur when the amplitude has fallen to a factor of $1/e$ of the first echo amplitude [83].

6.3 The Experimental Apparatus

The ultrasonic interferometer is shown in Figure 6.1.

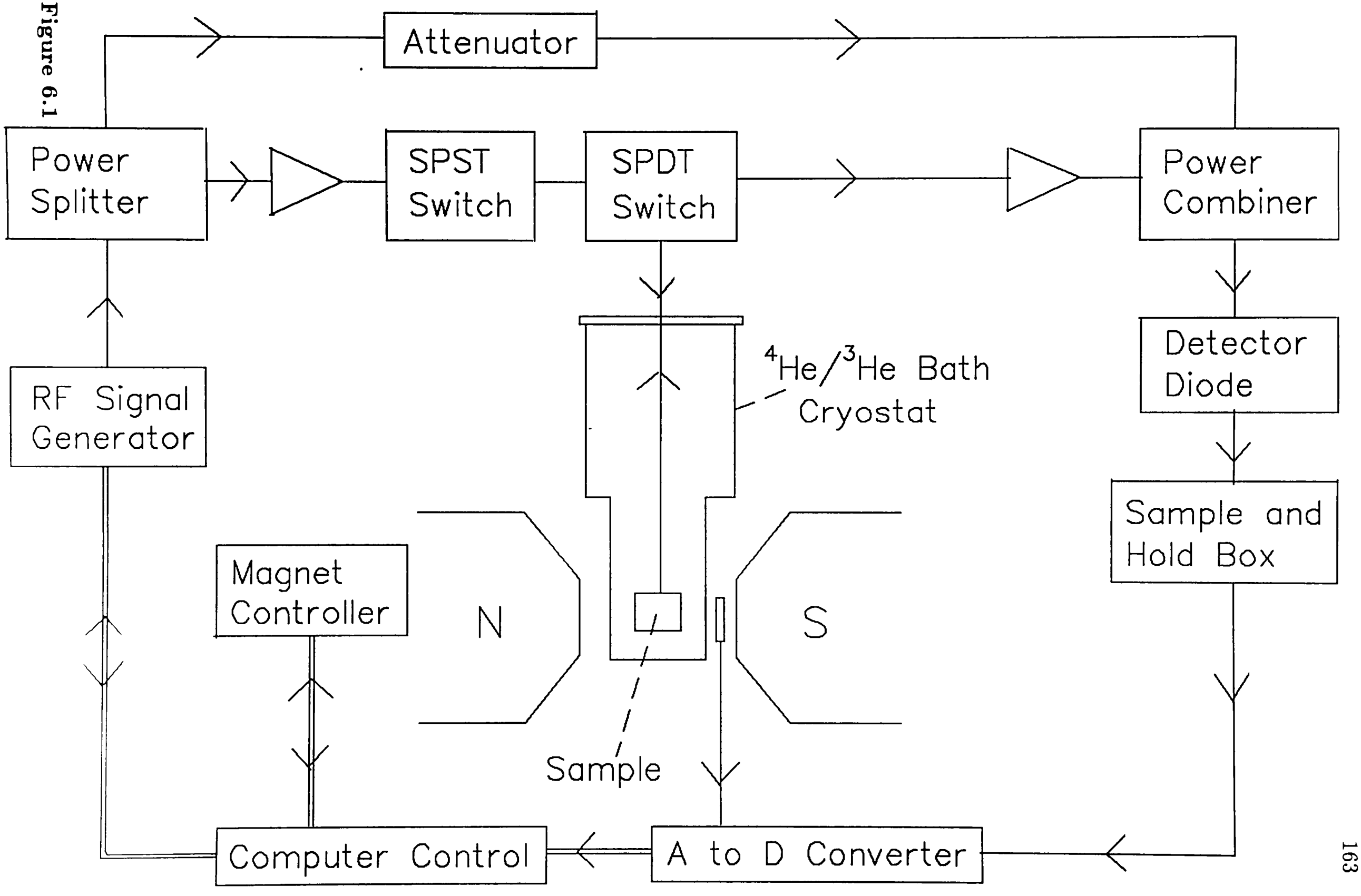
A pulsed high frequency (MHz) signal is produced by a specially designed pulsed signal generator [84]. The signal is initially split using an electronic power splitter; one half is used as a reference with which the phase of the returning echo train can be compared, whilst the other is passed through a SPST switch to produce 100ns pulses spaced by 10μs. The pulses are injected into the crystal using an SPDT switch which also collects the returning train of echoes. Using a power combiner the reference signal and echo train are recombined giving rise to an interference signal from which the phase shift due to the path length travelled in the crystal can be deduced. (The reference beam is attenuated and the echo train is amplified so that the two signals are of the same order of magnitude).

A detector diode is used to generate the amplitude envelope of the signal, which is then passed onto a sample-and-hold circuit. This produces an instantaneous value of the signal voltage for a chosen point on the wave train.

The echo train can be displayed on a digitizing oscilloscope (HP54111D) and measurements taken from this display, but it is found that measurements made using the sample and hold box have a better signal to noise ratio and have therefore been used for the following results. The reason for this is that such results are averaged over 1000 readings whereas the oscilloscope result is that of a single shot measurement.

INTERFEROMETER SCHEMATIC DIAGRAM

Figure 6.1



6.4 Production of a Zinc Oxide Transducer

An optically polished parallel faced crystal is required. The surfaces are initially cleaned in a 3:1 solution of Decon (an alkaline industrial detergent) in distilled water, and then rinsed several times in distilled water, to remove traces of grease and other substances which may prevent proper adhesion of the deposited materials. The crystal face to be coated is then subjected to an ion beam of 1000eV Ar ions to further clean the surface at an atomic level. Surface cleanliness is of great importance as metallic layers deposited without ion-cleaning tend to peel when ZnO is deposited on top. This peeling is due to strain within the ZnO film and is a general characteristic of sputtered oxide films.

Once the sample has been prepared it is placed in the substrate holder of the sputtering apparatus using tweezers to avoid any further contact. Layers of Cr and Au are flash evaporated at a base pressure of less than 1×10^{-6} torr. A metal film (in this case Au) is required to form a ground plate electrode for the transducer. The gold film is approximately 3000nm thick and forms the growth surface for the piezoelectric ZnO. The gold is evaporated to produce an amorphous film onto which the ZnO can deposit according to its natural growth habit, which consists of densely packed crystalline needles whose c-axis is approximately parallel to the direction of arrival of the sputtered material [85]. Any structure present in the gold film that did not match that of ZnO would disturb its natural growth habit. The Cr layer is also needed as gold is a soft metal and has a tendency to peel in common with most noble metals. This Cr film is of order 10nm thick (Fig. 6.2).

The direction of growth of the piezoelectric (c-axis) is important. If grown normal to the plane surface purely longitudinal modes are produced, whilst an angle of $\sim 40°$ gives rise to the generation of predominately transverse waves. An angle of $\sim 20°$ gives rise to a mixture of both modes with approximately equal amplitudes. This film should be about a quarter wavelength thick i.e. approx. 10μm for a 400MHz signal. The ZnO is presputtered for 15 minutes to remove the contaminated surface layer from the target before the film is deposited.

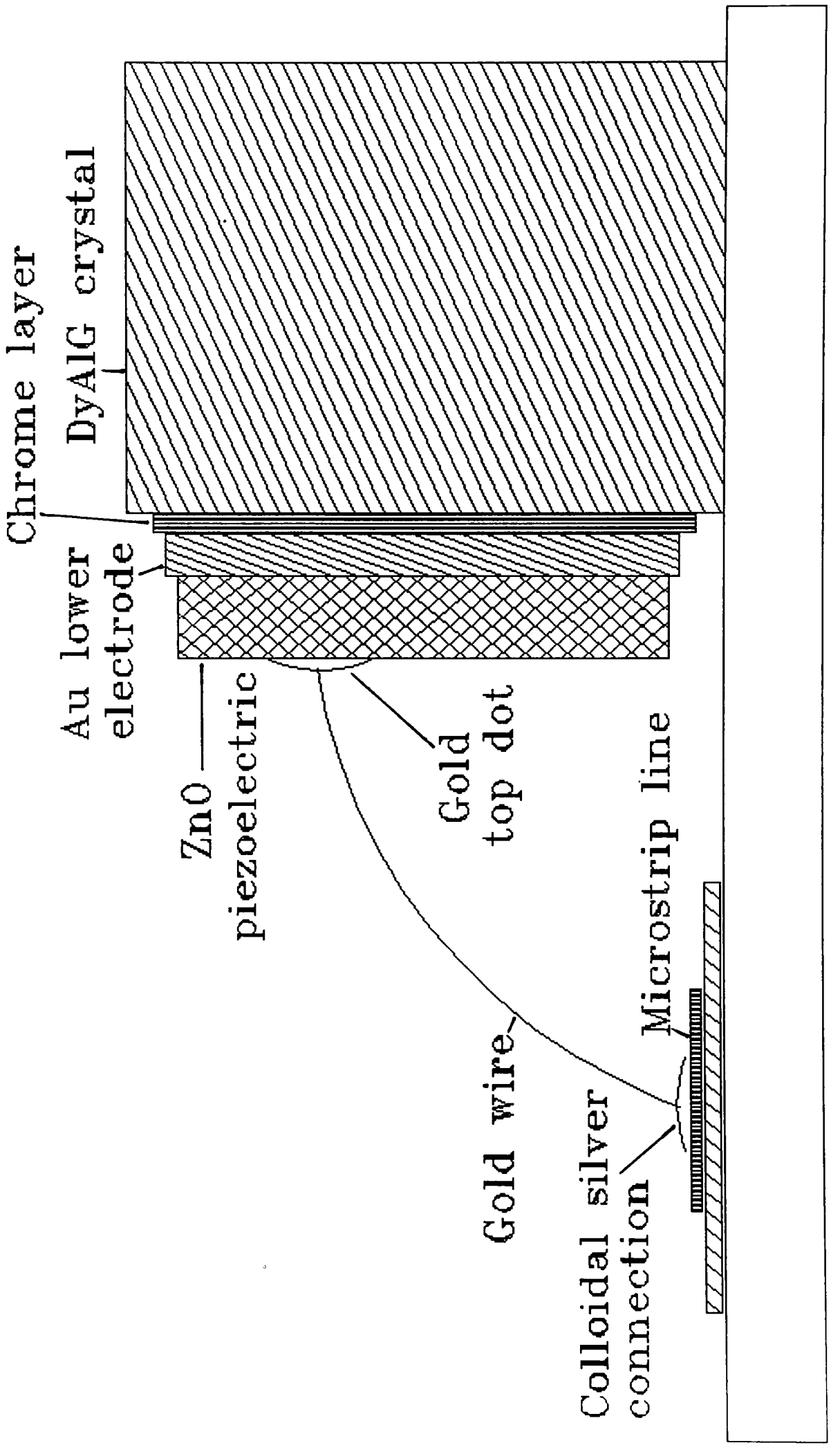

Chrome layer
DyAlG crystal
Au lower electrode
ZnO piezoelectric
Gold top dot
Microstrip line
Gold wire
Colloidal silver connection

Figure 6.2

Because the ZnO transducers used are grown directly onto the material under investigation the problems of bonding and acoustic mismatch are avoided. No mechanical strength is required from the transducer and therefore the ZnO layer can be made as thin as required so that high frequency modes are obtained without resorting to the use of overtones of a lower frequency transducer. This technique has resulted in an increase of resolution in ultrasonic experiments to 3 parts in 10^{10} compared with 1 part in 10^8 as found previously [81].

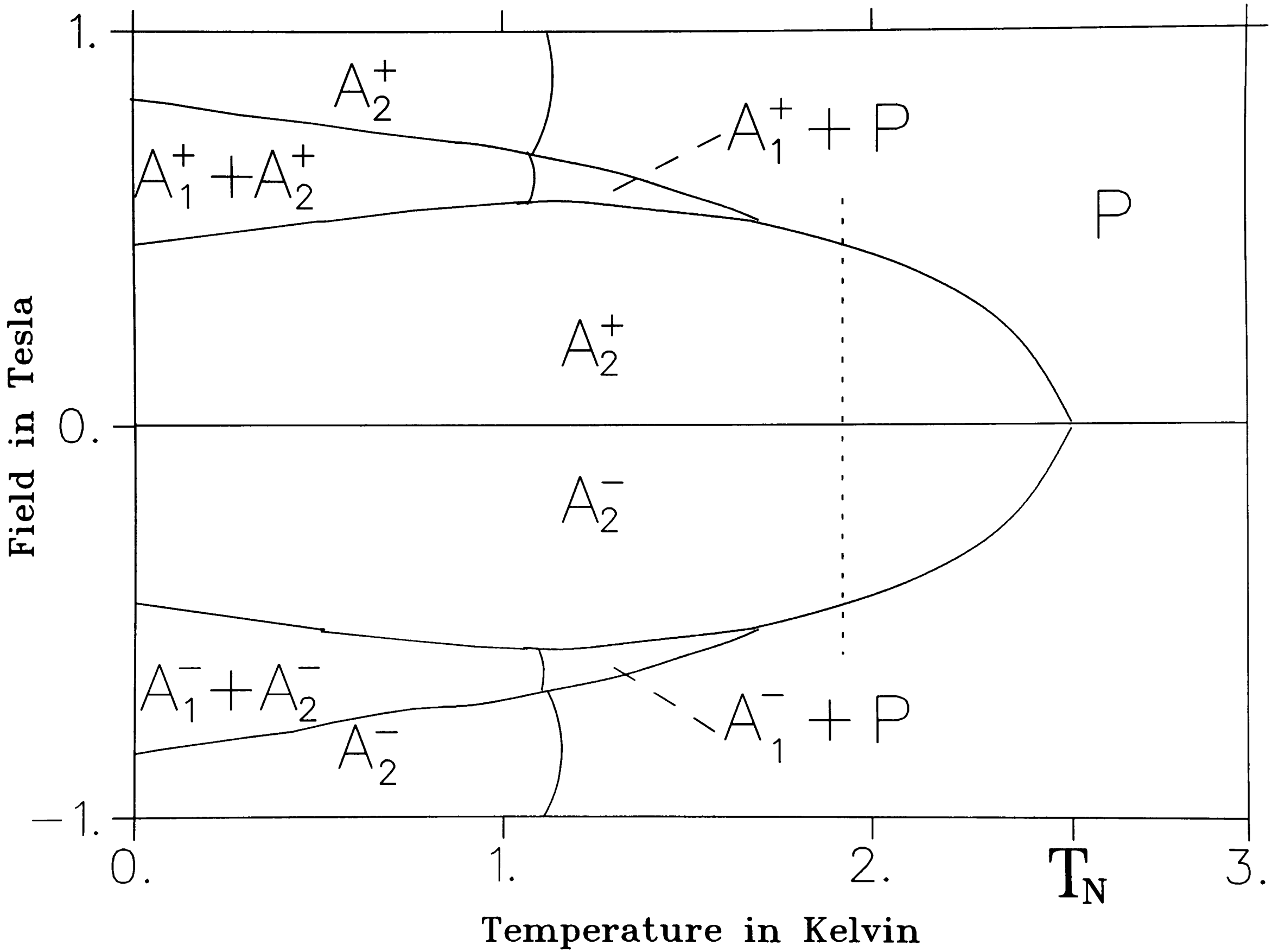
6.5 Dysprosium Aluminium Garnet

Dysprosium aluminium garnet ($Dy_3Al_5O_{12}$) has been extensively studied using techniques such as magnetometry and susceptibility measurements and as a result its phase diagram is well known Fig.6.3 [86].

Below the Néel temperature two magnetically inequivalent antiferromagnetic states exist, which are time-reversed conjugates. These are degenerate in zero field but this degeneracy can be lifted by applying a field, stabilizing one of the two states. Ultrasonic interferometry has been used to investigate the domain growth behaviour and the dynamics of these metastable states, which are of great theoretical interest. Verification of theoretical models is experimentally difficult because a simple system is required which can be easily measured and which will produce quantitative results. Despite its apparent complexity $Dy_3Al_5O_{12}$ nevertheless lends itself to simple mathematical modelling owing to its being a strongly Ising-like system with well understood magnetic properties. Ultrasonic interferometry provides quantitative information on time evolution under a controllable driving force; this is of great interest for comparison with domain growth theory predictions. The results have been related to the Lifshitz phenomenological model of domain growth, the Johnson-Mehl-Avrami-Kolmogorov Law and to numerical Monte-Carlo computer simulations of spin systems described by Glauber dynamics in Section 6.9.

6.6 Magnetic Properties

Figure 6.3


1.
0.
−1.
A_2^+
$A_1^+ + A_2^+$
$A_1^+ + P$
P
A_2^+
A_2^-
$A_1^- + A_2^-$
A_2^-
$A_1^- + P$
0.
1.
2.
T_N
3.
Field in Tesla
Temperature in Kelvin

$Dy_3Al_5O_{12}$ is a metamagnet with cubic symmetry which is antiferromagnetic below T_N=2.53K. There are 12 Dy^{3+} ions per unit cell, which are arranged in 3 pairs of crystallographically inequivalent sublattices. The spins are highly anisotropic; each of the three sublattices has its large g value (of approximately 18) parallel to one of the cubic axes with perpendicular much smaller and unequal g values ($\sim 0.3, \sim 0.7$). As previously mentioned, below T_N there are two crystallographically inequivalent antiferromagnetic states that are degenerate in zero field. This degeneracy may be lifted by applying an external magnetic field with components along all 3 cubic axes, or by a magnetic field in conjunction with an internal strain. The external magnetic field induces an internal staggered field and the resulting non-degenerate magnetic states are time reversed conjugates, defined as A^+ and A^-. The order parameter ,η , is chosen such that it has positive and negative values for these two states respectively.

Giordano and Wolf [87] have discussed the origins of the energy difference between the two states. Two possible origins have been considered to account for the lifting of degeneracy by field not aligned with the cubic axes. One process involving non-Ising interactions, which arise from unequal perpendicular g-values, was found to be too small an effect to explain experimental data in $Dy_3Al_5O_{12}$.

An alternative and more viable mechanism considers the interactions between three-spin clusters. Consider a pure Ising system at low temperatures. The free energy term in the Hamiltonian can be expanded in powers of $e^{-}E/kT$. If a field with components in the x, y and z-direction is applied the A^+ ground state and A^- ground state are found to have the same terms. However excited states exist which involve the reversal of clusters of three nearest neighbour spins. These clusters have a different configuration in each metastable state and the energy of a reversal is not the same, giving rise to different free energies for the A^+ and A^- states.

The magnetic and chemical unit cells in $Dy_3Al_5O_{12}$ are coincident; this is a necessary condition for the appearance of an internal staggered field. From symmetry considerations, in order that the applied field can couple to the order parameter, it is also necessary that the magnetic structure is invariant under inversion. For an external

field applied in a direction other than along the cubic axes a staggered field is induced. The magnitude of this staggered field is proportional to $B_x B_y B_z$ and contributes a term in the free energy equation of the form

$$\delta F_m \propto B_x B_y B_z \eta \tag{6.1}$$

By manipulating the external field direction it is possible to arrange that one state is made metastable with respect to the other. An applied field of magnitude close to B_c will cause the experimentally observed relaxation to the stable state.

The presence of an internal strain can also lift the degeneracy; the corresponding contribution to the free energy term is given by $\delta F_s \propto e_{xy} B_z \eta$. However, as will be shown later, the magnetically induced staggered field can easily be made to dominate this term.

6.6.1 Magnetoacoustic Interactions

The ultrasonic experiments involve the measurement of the change in time-of-flight, $\Delta\tau$, for an injected acoustic pulse.

$$\frac{\Delta\tau}{\tau} = \frac{\Delta l}{l} - \frac{\Delta v}{v} \tag{6.2}$$

where v is the acoustic wave velocity and l the path length within the crystal.

The velocity of acoustic waves in a solid depends on the elastic constant C and the density of the sample ρ, via the equation,

$$\frac{\Delta v}{v} = \frac{1}{2}\frac{\Delta C}{C} - \frac{1}{2}\frac{\Delta \rho}{\rho} \tag{6.3}$$

In an applied field each of the AF phases has different elastic constants thus giving rise to different values of Δv. The first term in equation (6.2) is due to magnetostrictive effects within the sample. Available data shows that for $Dy_3Al_5O_{12}$ the magnetostriction effect provides only a small contribution ($\sim 2\%$) to the overall time of flight measurement and, as such, no corrections have been made for this. Experimental sensitivity is important because the difference in ultrasonic velocities, and therefore the ultrasonic refractive indices of the two phases can be less than a few parts in 10^5. It should be noted that a

greater sensitivity (1 part in 10^8) can be achieved by using a higher rf power. However, in order to avoid the possibility that the acoustic waves perturbs the relaxation process, we reduced the power until the signal to noise ratio was just sufficient to produce reasonable measurement accuracy. In this way the effects of the ultrasonic pulse on the relaxation processes under investigation were minimized.

Wolf and Huan [88] developed a theory of magnetoelastic effects in $Dy_3Al_5O_{12}$, based on 58 terms found in the magnetoelastic Hamiltonian derived from order and strain parameters, and the applied magnetic field. For fields applied in symmetry directions many of the terms vanish. The acoustic waves were propagated along a cubic [100] axis, with the applied field along or close to this direction. The velocity shift found from the tensor representing the elastic constant is (for transverse waves),

$$\frac{\Delta v}{v} = \frac{1}{2C_{44}}(\Delta C_{44} + \alpha \Delta C_{55}) \tag{6.4}$$

The dominating term in the anti-ferromagnetic region is found to be,

$$\frac{1}{2}\frac{\Delta C_{45}}{C_{44}} = d_t M_x \eta + e_t H_x \eta \tag{6.5}$$

using the notation of Wolf and Huan.

This can be more simply written as

$$\frac{\Delta v}{v} \propto \eta B \tag{6.6}$$

Plotting change of velocity versus applied field, $\frac{dv}{dB}$, measured at zero field, the gradient is therefore identifiable as a quantity proportional to the magnitude and sign of the order parameter, η.

6.7 Experimental Method

The sample was mounted on a specially designed holder. The connections to the ZnO transducer were made to one of the top dots using a commercial gold wire ball bonder (Fig. 6.4).

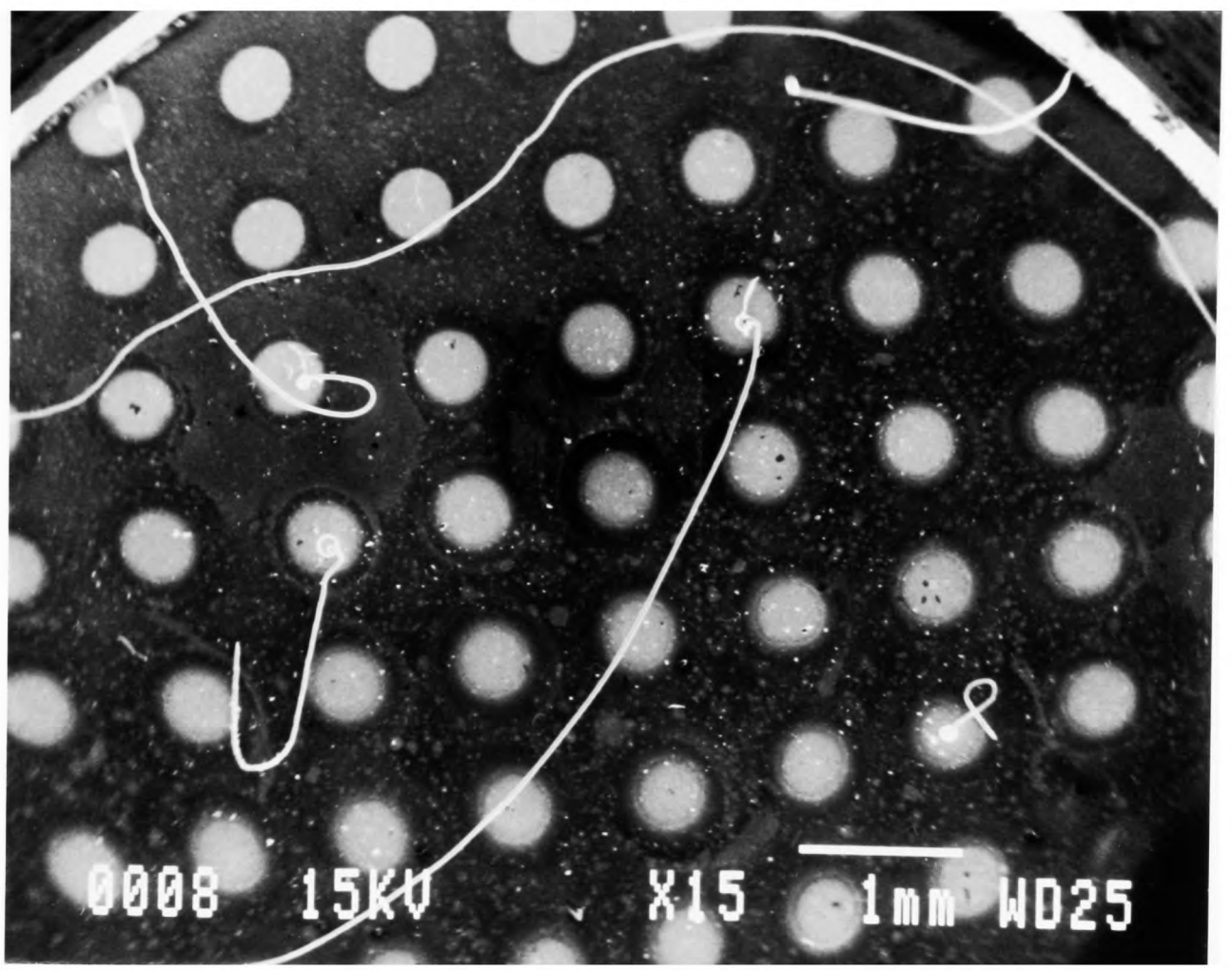


Figure 6.4 SEM picture of ZnO transducer array

This wire was then connected to the central pin of an rf connector. The rf connection was made to the external rf circuit as described in Section 6.4 . After dissolving a small area of the ZnO with weak HCl acid solution to reveal part of the gold film, the earth plane was connected to the rf earth via the sample holder, using Biorad colloidal silver.

The sample holder was mounted at the bottom of the cryostat insert and protected by a metal can which was then sealed using Wood's metal to prevent the sample from coming into direct contact with the liquid helium. A ^{4}He bath cryostat was used which could be pumped via a manostat to produce excellent and accurate temperature stabilization in the range 1.4K to 4.2K. The temperature was measured using a mercury manometer and vapour pressure calibration tables. The sample space was filled with 25

mmHg of helium at room temperature to provide thermal conduction between the liquid helium and the sample. The carrier frequency was kept constant at 425 MHz, whilst the pulse frequency was 10kHz. The phase of the 20th transverse echo was recorded as a function of either field or time for relaxation measurements. The time of flight was measured using the HP54111D digitizing oscilloscope to be 494.5 ns, giving a velocity of 4044 ms^{-1}.

In practical terms $Dy_3Al_5O_{12}$ is an ideal material for ultrasonic experiments as it is a hard crystal that can be optically polished and is mechanically strong enough to provide a substrate for a thin film transducer. The antiferromagnetic transition occurs at $T_N = 2.53K$ which is within the temperature range experimentally available by pumping on liquid ^4He. The sample is a rectangular plate of dimensions 4mm × 4mm × 1mm. The orientation of the axes were confirmed by backscattered X-ray diffraction. A [100] axis is normal to the largest (optically polished) faces. The [010] and [001] axes lie at 45° to the edge of the plates. The transducer was grown at an angle of ∼ 20° in order that both transverse and longitudinal echo trains would be generated [85]. The sample was vertically mounted such that the magnetic field could be rotated anywhere in the plane containing [100] and [011] axes. The electromagnet used provided fields in the range ± 1.4T and was calibrated using nuclear magnetic resonance of ^{19}F nuclei.

6.8 Experimental Results

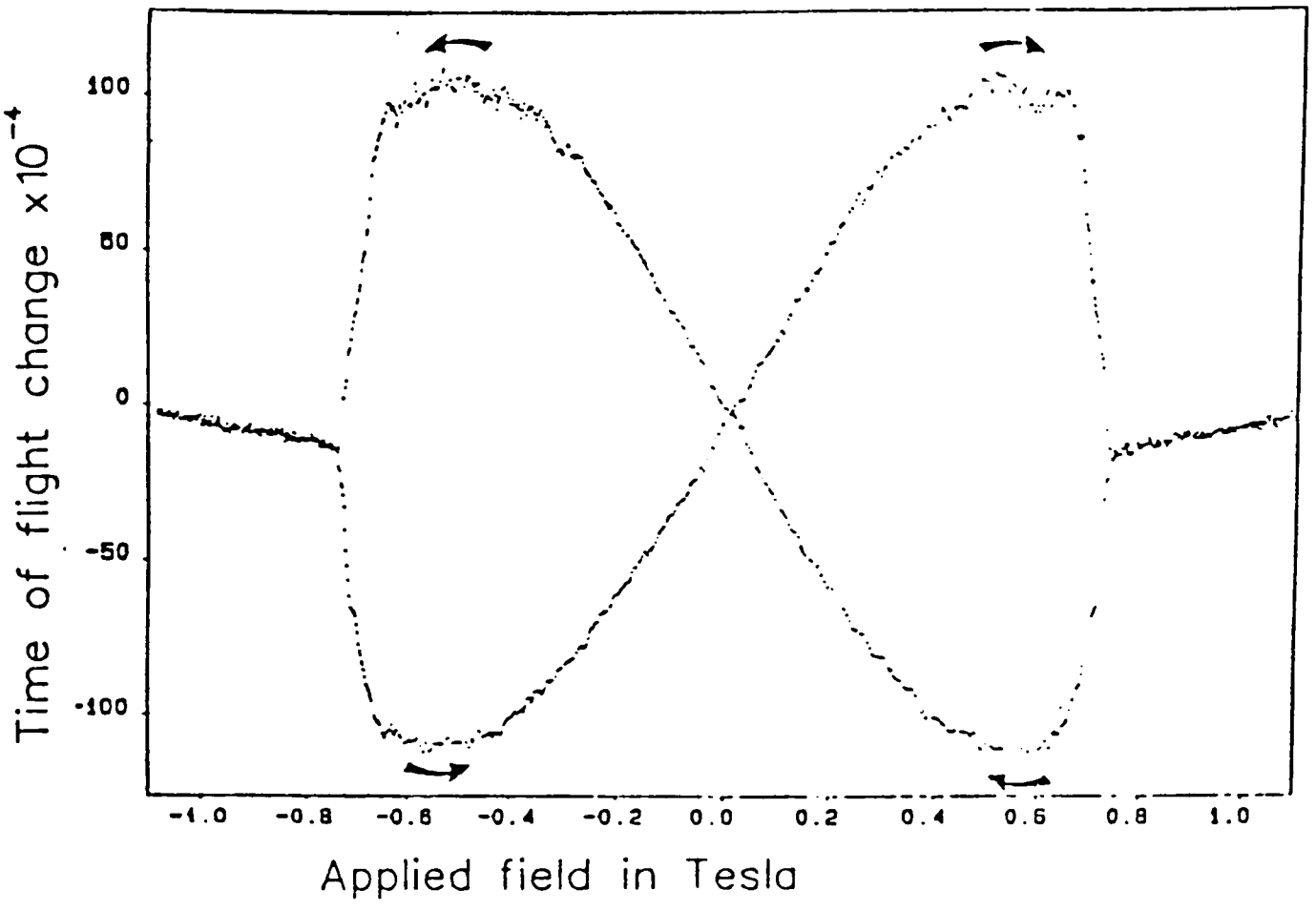
For many of the experiments shown later it is necessary first to create a meta-stable state. This is achieved using the following field cycling procedure represented by the dashed line in Fig. 6.3. The crystal is cooled below its Néel temperature into the antiferromagnetic state. A magnetic field is applied close to but not precisely along a (100) axis, producing a small driving force of magnitude $\propto B_x\ B_y\ B_z$ as given by equation (6.1) The magnetic field is increased to above B_c thereby driving the sample into its paramagnetic phase. In the paramagnetic phase the increasing and decreasing field sweeps coincide indicating no hysteresis. It is found that in both the positive and

negative sweep regions the velocity change is of the same small magnitude and sign. The field is then lowered through the antiferromagnetic- paramagnetic phase boundary causing the system to collapse into the state with the lowest energy. The energy difference may be due to any slight field misalignment producing a non-zero energy term proportional to $B_xB_yB_z$ and to strain within the crystal. If the A^+ state is stabilized the material will stay in this state as the field decreases until it passes through zero field into a field region of opposite sign. The A^+ state is now metastable, because the sign of the product $B_xB_yB_z$ has reversed. The field is now increased through the negative critical field, B_c, and the system is driven into the paramagnetic state. If the field magnitude is decreased again the sample collapses into the stable A^- state. This can be seen in the graph (Fig. 6.5a) which we have termed a "butterfly" curve owing to its distinctive form. However if in an identical situation the field sweep is halted in the AF phase just short of the phase boundary the metastable A^+ state will relax to the stable A^- state at a rate which increases with the size of the driving force (Fig. 6.5b). Fig.6.6 shows a similar butterfly curve made with the field applied in the [111] direction. The phase boundary occurs in a smaller field than when the field was applied in the [100] direction and the metastable state relaxes to the stable state at a field well below the phase boundary. There is also a large field dependent change in the time of flight in the paramagnetic phase.

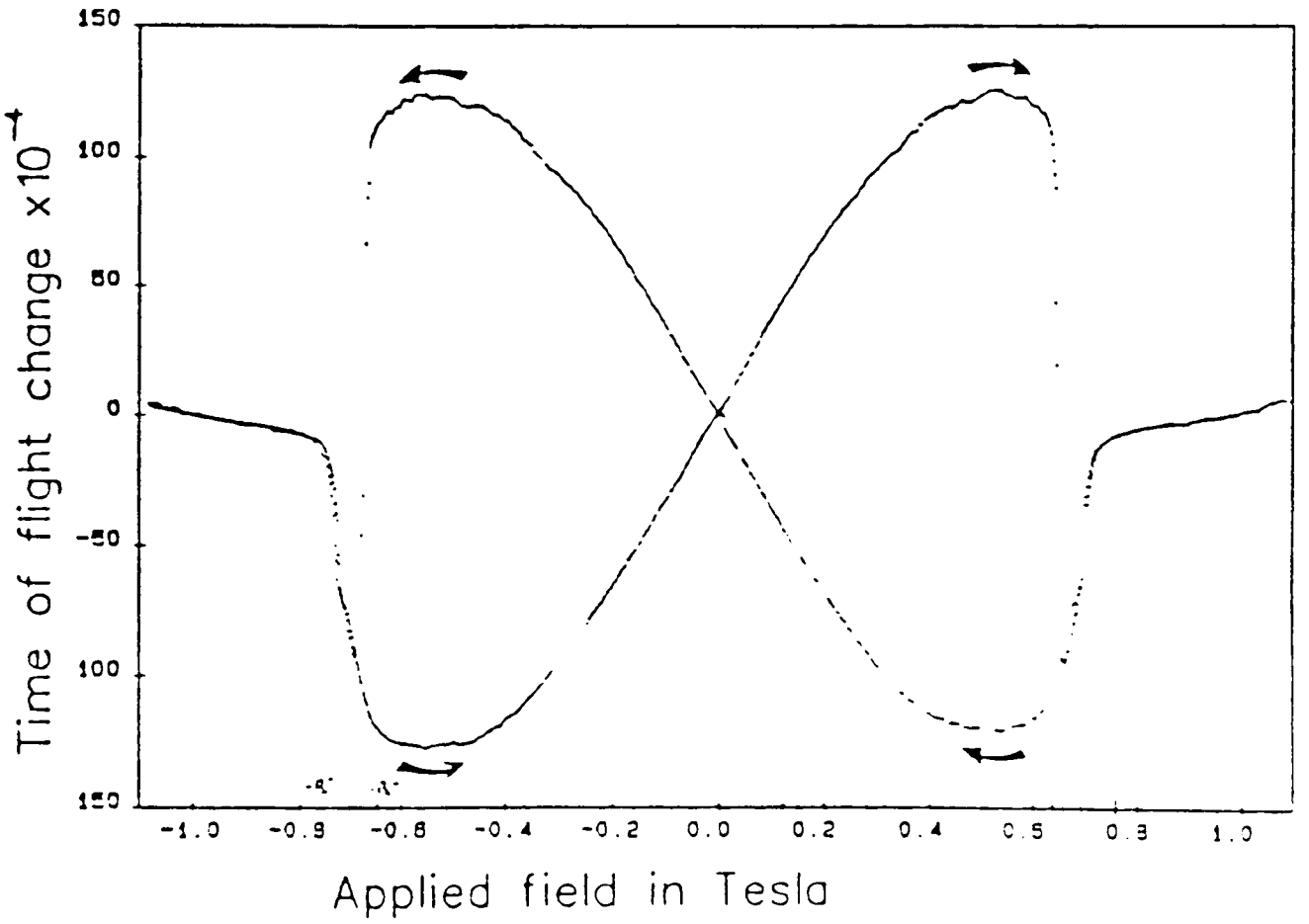
It can be seen from Figure 6.5 that at a given temperature the ultrasonic velocity varies linearly as a function of applied field. The order parameter for the A^+ phase, whether stable or metastable, is constant away from a phase boundary as seen from the fact that the signal is roughly linear in B. It can be seen from equation 6.6 that the magnetoelastic Hamiltonian is of the form $\propto \eta B$. The order parameter is then simply proportional to the gradient of the butterfly curve about zero field. At the critical fields, $\pm B_c$, the order parameter collapses. A plot of the field and temperature at which this collapse occurs describes the phase diagram for the DyAlG system.

6.8.1 The Strain Contribution

As discussed in Section 6.5 there are 2 significant contributions to the samples



Transverse waves – field aligned.to [001].



Transverse waves field misaligned by 1.4°
Metastable state decays close to $\pm B_c$

Figure 6.5

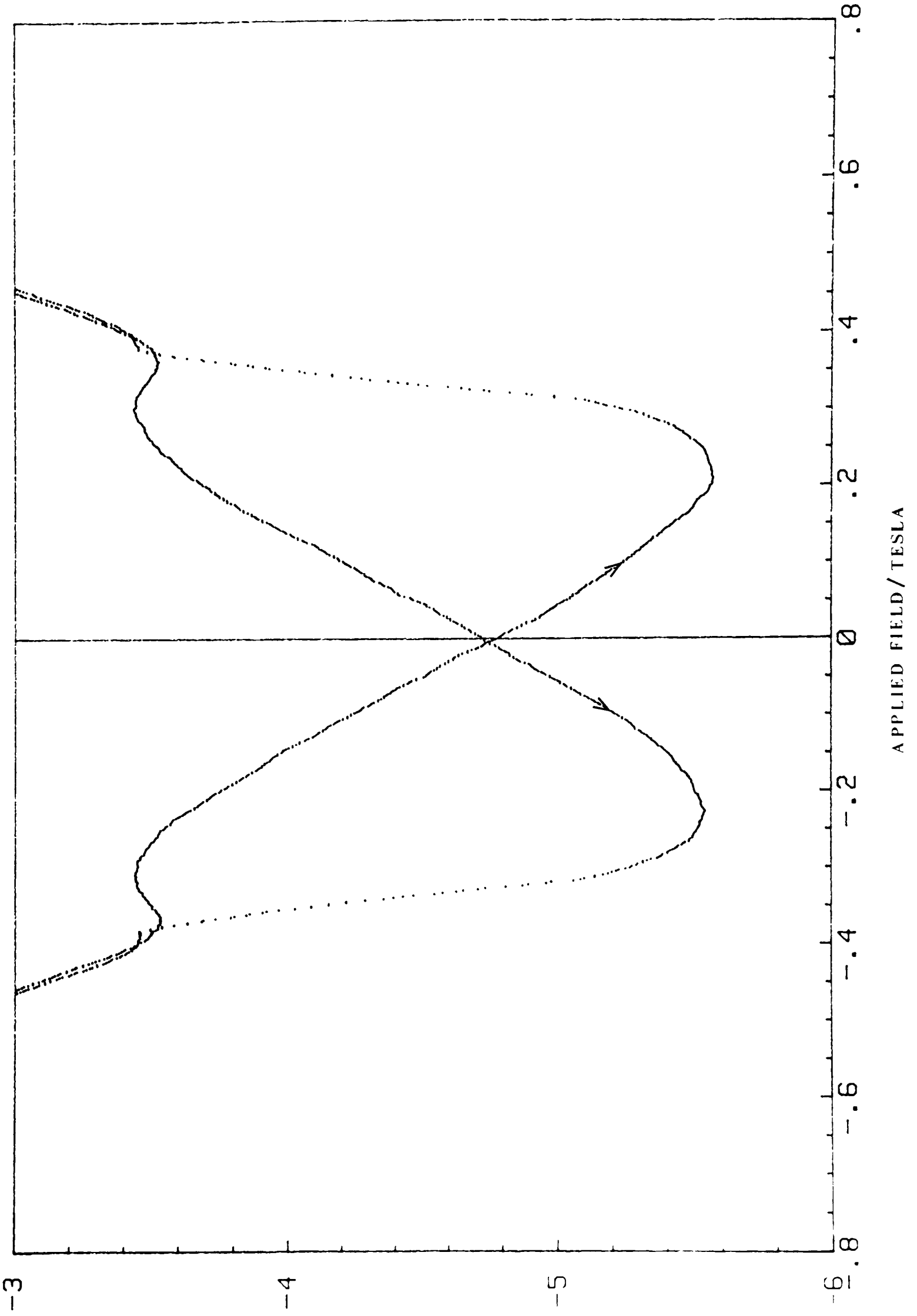


Figure 6.6

magnetic free energy. In the experiment described below the relative magnitude of the magnetically induced and strain contributions can be ascertained [89].

If a pure A^+ state is subjected to a small positive external driving force the state is stable. However if there is a strain contribution to the free energy the sign of the stable state will depend on the relative magnitude of the two competing energy terms. For a non-uniform strain distribution, in which the strain and external driving force free energy terms are of similar size, partial relaxation of the A^+ may occur in regions where the strain free energy term is of opposite sign to and dominates the externally applied driving force. Similarly a metastable A^- will not undergo a complete relaxation into an pure A^+ state under the same conditions. This occurs because in some regions the negative strain cancels out or dominates the positive driving force.

An attempt at quantifying the distribution and spread of random strain has been made. The behaviour of the system has been observed under the effect of very small positive and negative staggered fields. Fig 6.7 shows the angular field dependence of the acoustic echo phase with field at several angles close to the [011] direction.

All sweeps were taken in the same sense from -1T to +1T, at a temperature of 1.988K for which $B_c = 0.4T$. For field orientations greater than 123.5° the A^+ state is stable, while for angles less than 122.0° the A^- phase is stable. The values given for the angles are relative measurements only. The angular separation over which variation occurs between the 2 stable states may be taken as a indication of the strain distribution.

6.8.2 Relaxation Processes

As discussed previously, relaxation can occur from the metastable state to the stable state. The progress of this relaxation process can be monitored by measuring the change in the ultrasonic velocity as a function of time. This is possible because the change Δv is directly proportional to the volume fraction of the growing phase (e.g. A^+).

6.8.3 Arrhenius Plots

Relaxation times were measured as a function of applied magnetic field. The characteristic time was measured from the time at which this field value was reached to

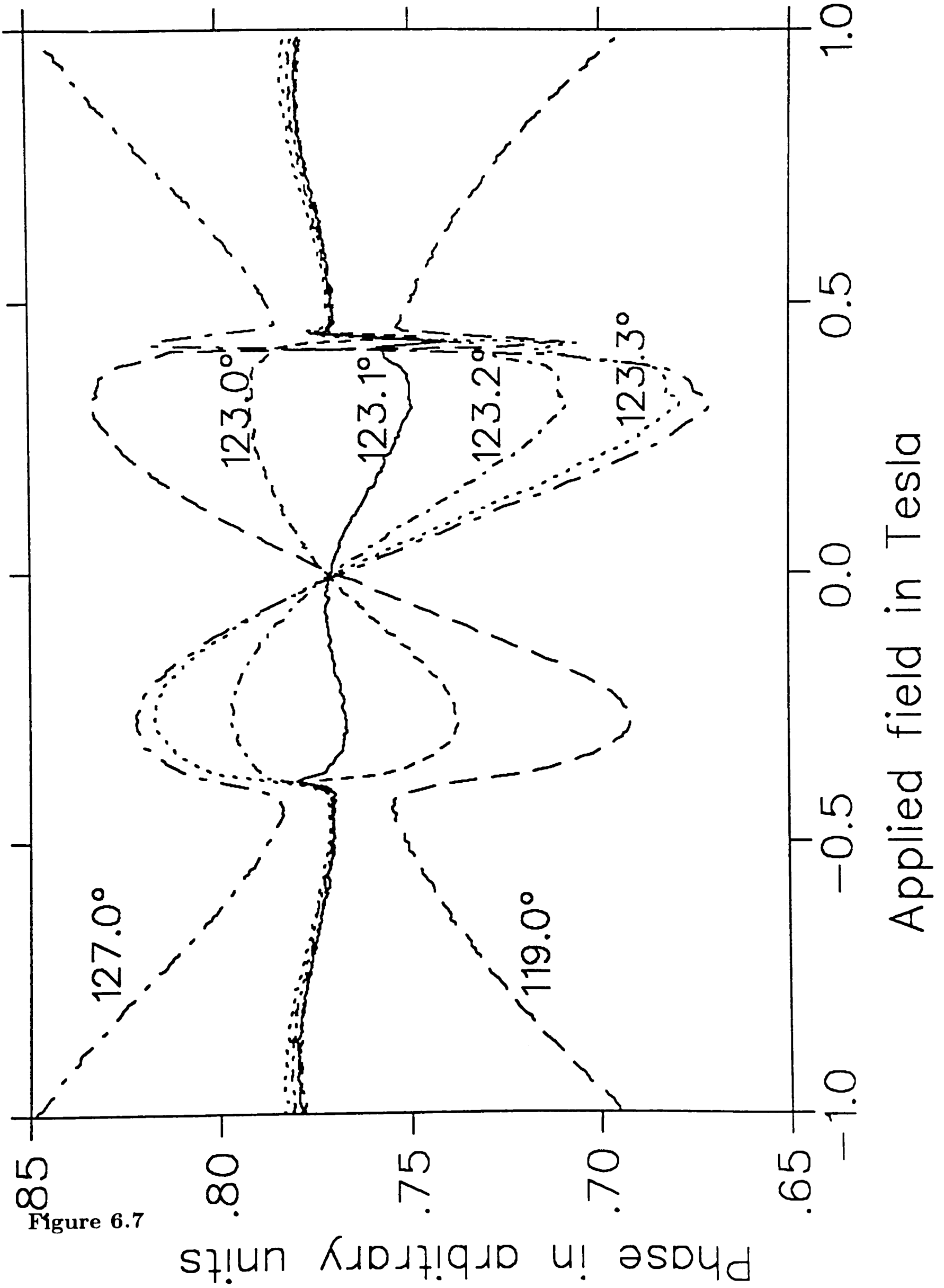

123.0°
123.1°
123.2°
123.3°
127.0°
119.0°
1.0
0.5
0.0
−0.5
−1.0
Applied field in Tesla
.85
.80
.75
.70
.65
Phase in arbitrary units

Figure 6.7

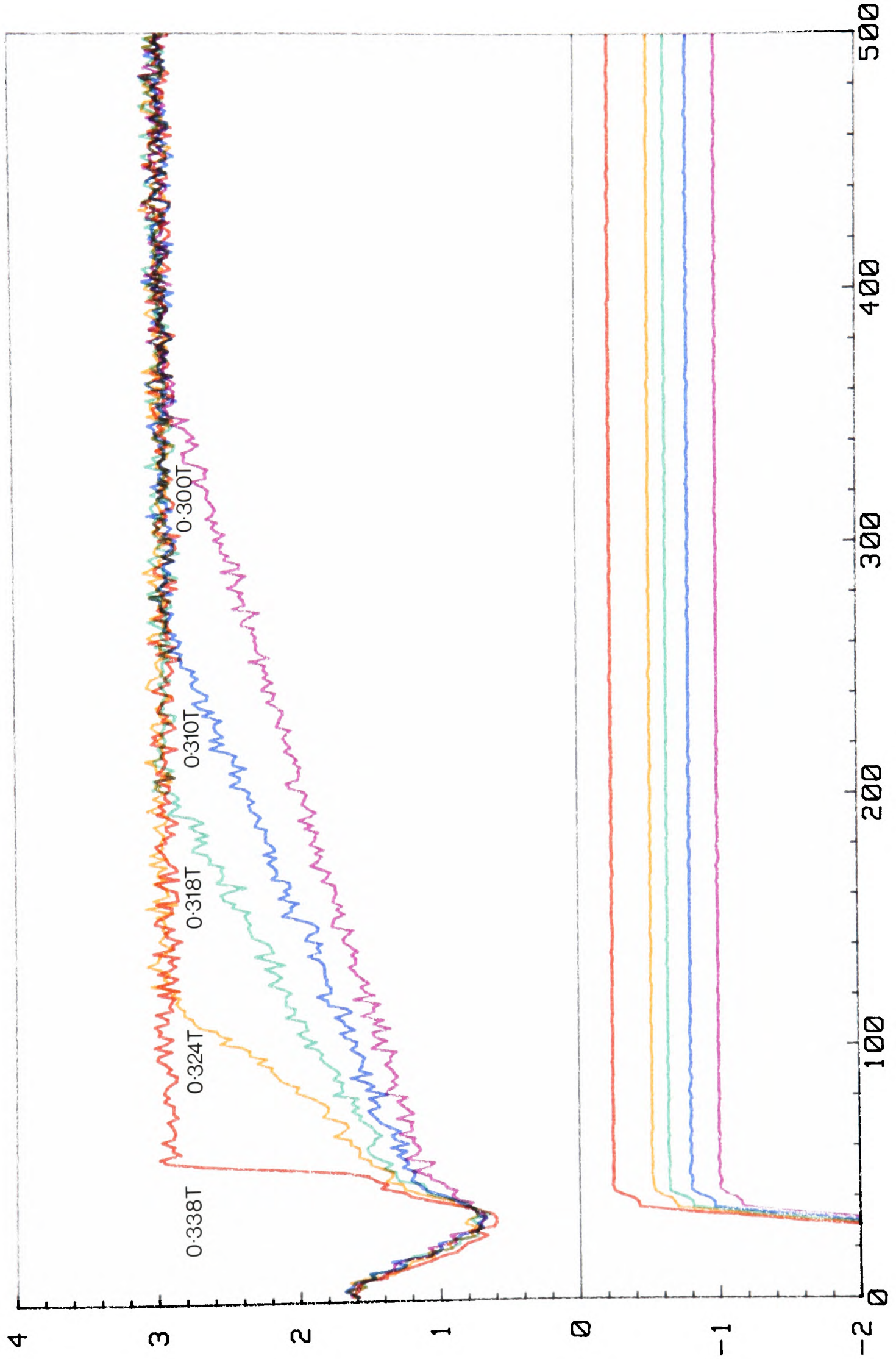

0·300T
0·310T
0·318T
0·324T
0·338T
4
3
2
1
0
−1
−2
0
100
200
300
400
500
ctime / s
scopephase / rad

Fig. 6.8

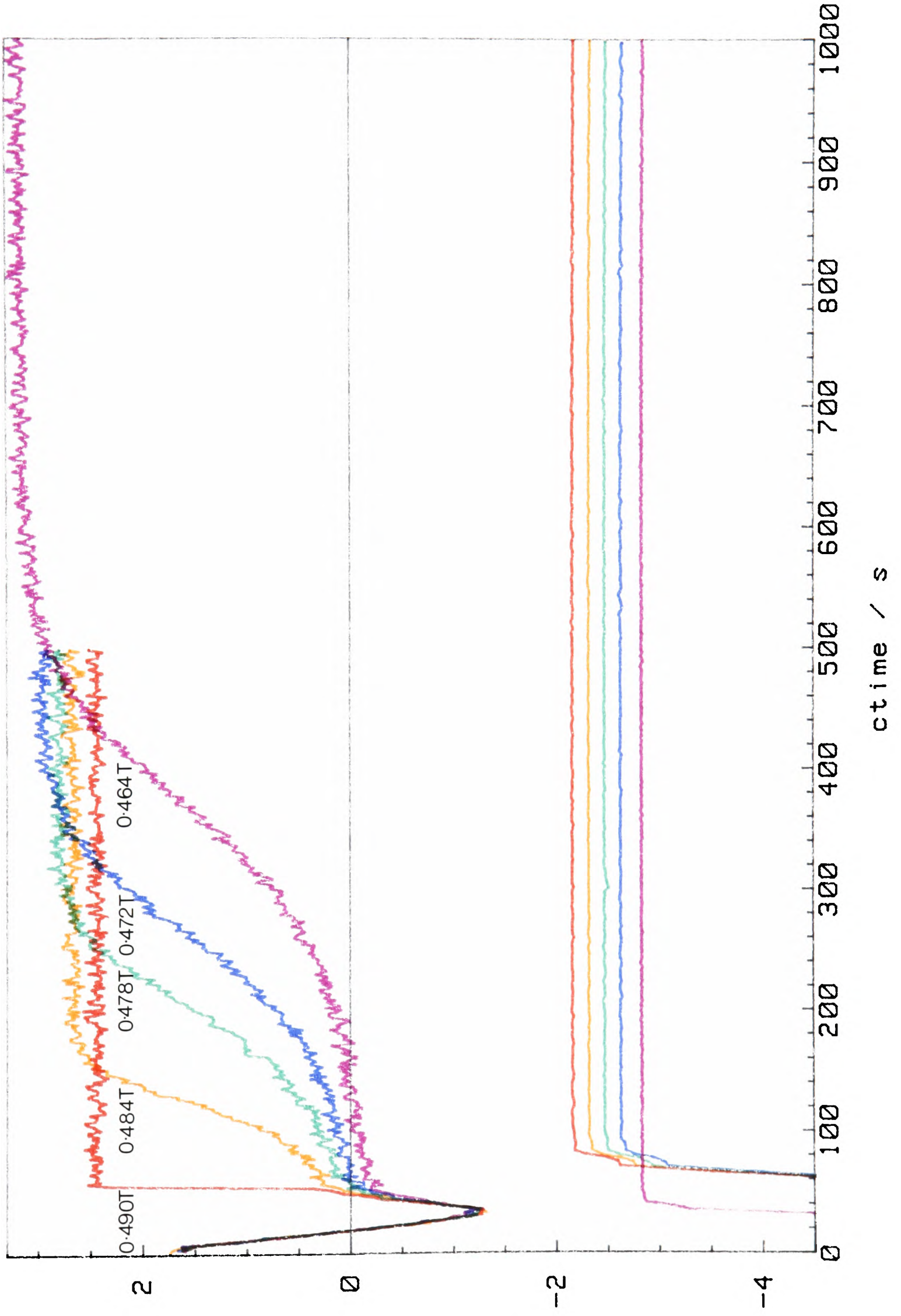

0·490T
0·484T
0·478T
0·472T
0·464T
2
0
−2
−4
scophase / rad
0
100
200
300
400
500
600
700
800
900
1000
ctime / s

Fig. 6.9

the end point of the relaxation. Measurements were made at temperatures of 2.0K, and were made with the field applied along the [111] axis (Fig.6.8) and along the [100] axes (Fig.6.9). The change in ultrasonic phase in radians is plotted as a function of time. The field sweeps were stopped at 0.338T, 0.324T, 0.318T, 0.310T and 0.300T (from left to right) for the for the applied field in the [111] direction, and 0.490T, 0.484T, 0.478T, 0.472T and 0.464T (from left to right) for the field applied in the [100] direction. The lower traces in both figures show the field sweeps as a function of time.

A process which has a specified activation energy (which is in this case proportional to B_0-B) can be fitted to an equation of the following form

$$\frac{1}{\tau} = P.e^{\frac{A(B_0-B)}{KT}} \tag{6.7}$$

where B_0 is a field value close to the phase boundary from which the fastest relaxation will occur. An Arrhenius plot showing ln τ versus B was drawn for each of the above cases. Fig.6.10 shows the results for the [111] direction whilst Fig.6.11 shows the results in the [100] direction.

In the [111] direction the end of the relaxation was clearly indicated by a sharp corner. The graph of ln (τ) plotted against B showed two distinct linear regions which both fitted the relation. On initial inspection it appears that there are two processes occurring with different activation energies. However the crossover region is very sharp; a relaxation involving two processes with similar activation energies is likely to give rise to a more gradual transition region between the two gradients owing to competition between them. Another possible explanation for this effect could follow from the presence of complex demagnetising effects.

In the [100] direction there was no clear end point to the relaxation and no obvious relationship between τ and B. For the longer relaxation times, the relaxation time was found to vary linearly with B. Again demagnetising effects within the whole sample could cause complex applied field dependencies in the volume under investigation.

Attenuation measurements

Figure 6.10

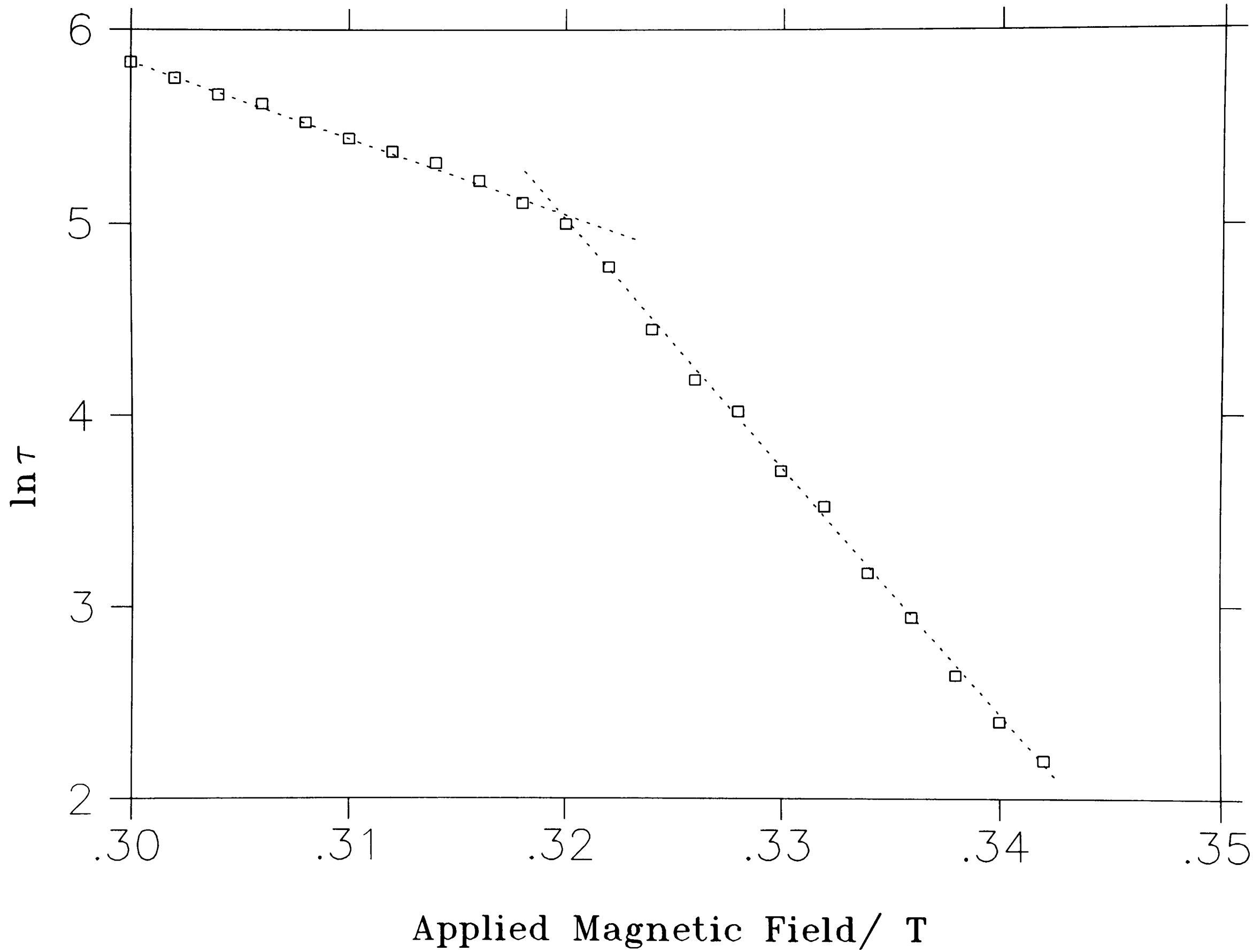
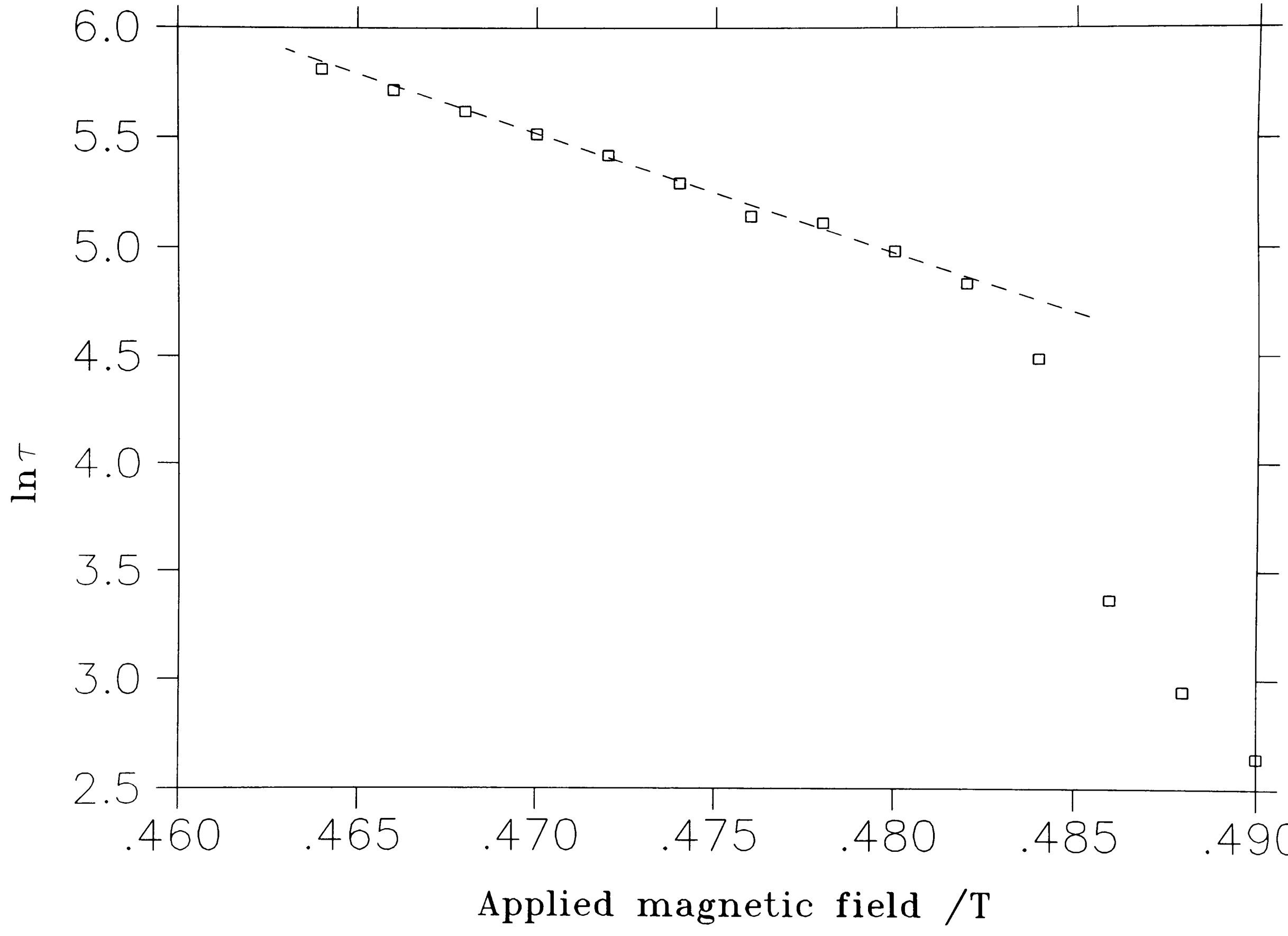


Figure 6.11


6.0
5.5
5.0
4.5
4.0
3.5
3.0
2.5
ln τ
.460
.465
.470
.475
.480
.485
.490
Applied magnetic field /T

The attenuation of the ultrasonic signal for the relaxations were also measured as a function of time. Fig.6.12 shows the amplitude of the ultrasonic signal (in mV) for a relaxation with a 0.478T magnetic field applied in the [100] direction. It is seen that the maximum attenuation is slightly displaced from the region of greatest ultrasonic phase change.

6.9 Domain Nucleation and Growth:Theory

A simple scaling law was found for the relaxation curves. The time axes were scaled and the data successfully collapsed onto the same line for the whole range of driving forces. This result strongly suggests that a single time constant is appropriate to describe the relaxation mechanism and that the process is amenable to simple mathematical modelling.

There are several theoretical models available to describe domain growth:

• A regular lattice of domain nucleation sites which nucleate at time t=0. The domains have zero volume at t=0 and grow linearly with time in all directions so that the volume of the domains at any time t is proportional to t^3. The Lifshitz phenomenological model predicts this kind of behaviour for a volume driven relaxation energy and with negligible surface energy terms. The form of the resulting curve is a cubic relation

$$\overline{\eta} = -1 + A(t - t_0)^3$$

until the percolation threshold is reached and all the domains touch. For the case of regularly spaced domains the relaxation will have a well defined end point when all the voids between the domains simultaneously vanish.

• A randomly spaced lattice of domain nucleation sites which nucleate at time t=0 and grow linearly with time. The resulting curve is of the form

$$\overline{\eta} = -1 + 2\exp(\rho(t - t_0)^3)$$

. For small times this expression reduces to the t^3 law as described above. but deviations occur as the domains begin to touch, resulting in the exponential form shown [90].

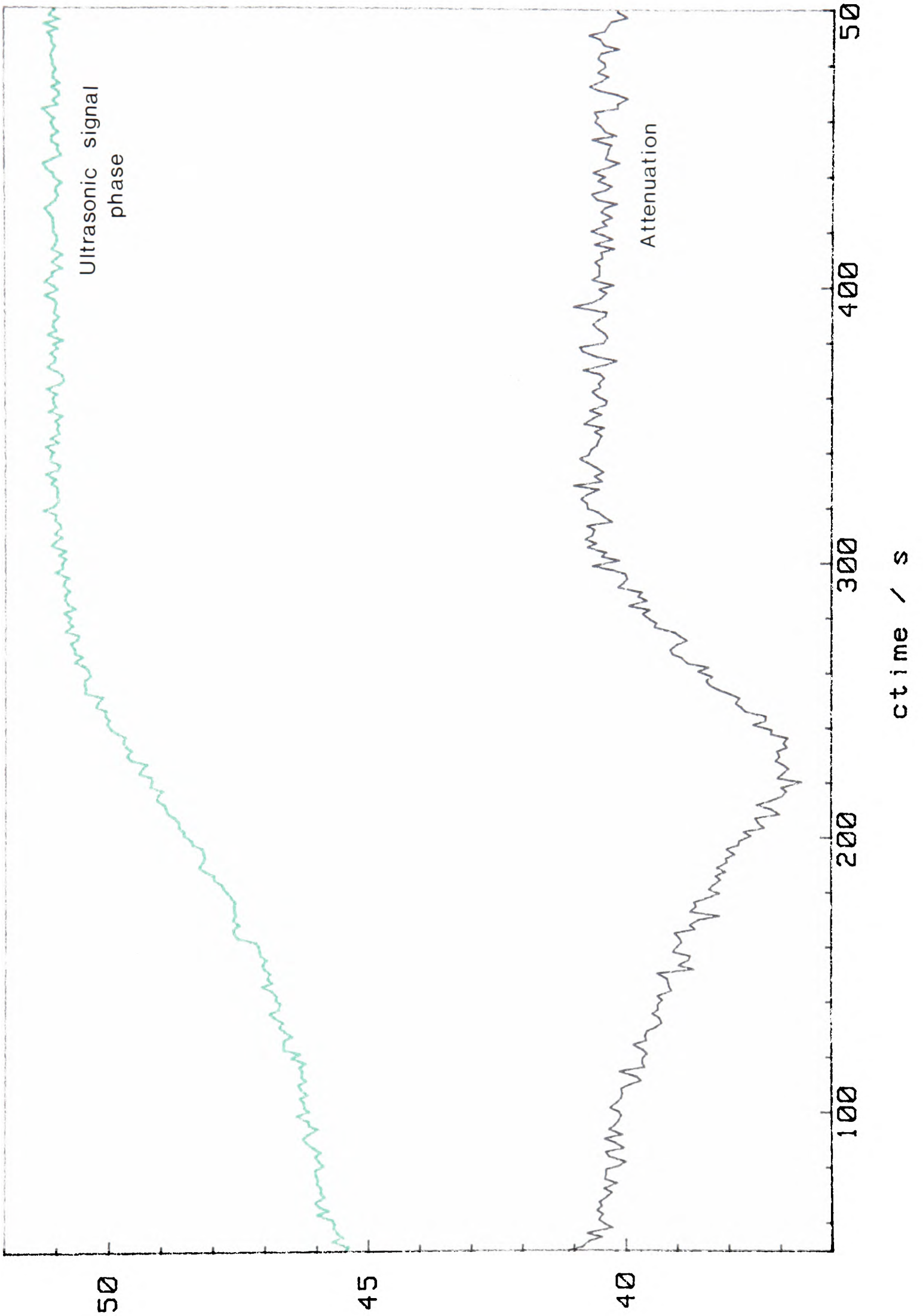

Ultrasonic signal phase
Attenuation
50
45
40
300
400
500
200
100
scopeamp / mV
time / s

Fig.6.12

• A constant rate of nucleation of new domains, at random positions, which grow linearly with time. Initially the number of domains present increases linearly with time and the volume of any one domain grows as a cubic function of time. The total volume of the stable state therefore increases as t^4. As the domains begin to touch a deviation from this form arises giving a result of the form

$$\bar{\eta} = -1 + 2\exp(\rho(t - t_0)^4)$$

.

The most general case is described by the Johnson-Mehl-Avrami-Kolmogorov (JMAK) law [91], [92], [93] which allows for initial and continuous nucleations and an arbitrary growth law of the nucleated domains. The described equation is of the general form

$$n = 1 - 2exp(f(t))$$

where f(0) = 0 and f(∞) = ∞ and f(t) is dependent on the nucleation rate N(t) per unit time and the growth law R(t).

The JMAK law reduces with appropriate simplifications to the models discussed previously. For the special case of homogenous nucleations and linear growth described above,

$$f(t) \propto t^p$$

where p = 3 for N(t) = $N_0\delta(t)$ where $\delta(t)$ is a delta function at time = 0

and p = 4 for N(t) = const. corresponding to continuous nucleations.

For the case of randomly sited nucleation centres nucleated at t = 0 the domains will begin to touch from time zero to the end of the relaxation. For this case it has been found that the t^3 law is replaced by $\exp(-at^3)$ as previously discussed.

6.9.1 Comparison with Experimental Results

The experimental relaxation data was initially fitted using a five parameter JMAK model,

$$m(t) = mexp(-\frac{t - t_o}{\tau}p) + m_1$$

The time origin and initial order parameter cannot be experimentally determined owing to the finite field cycling time. Note that the exponent, p, of the power law was used as a fit. Despite that fact that 5 fit parameters were used a satisfactory fit to the data was not obtained over the whole relaxation range.

It is conceivable that the the initial and final stages of the relaxation may require the use of different fits. Considering the ends of the relaxation first it is found that an exponential decay is the most satisfactory fit to the tail of the relaxation. (A t^3 fit will be considered later and is found to be a satisfactory fit for the end of the relaxation.)

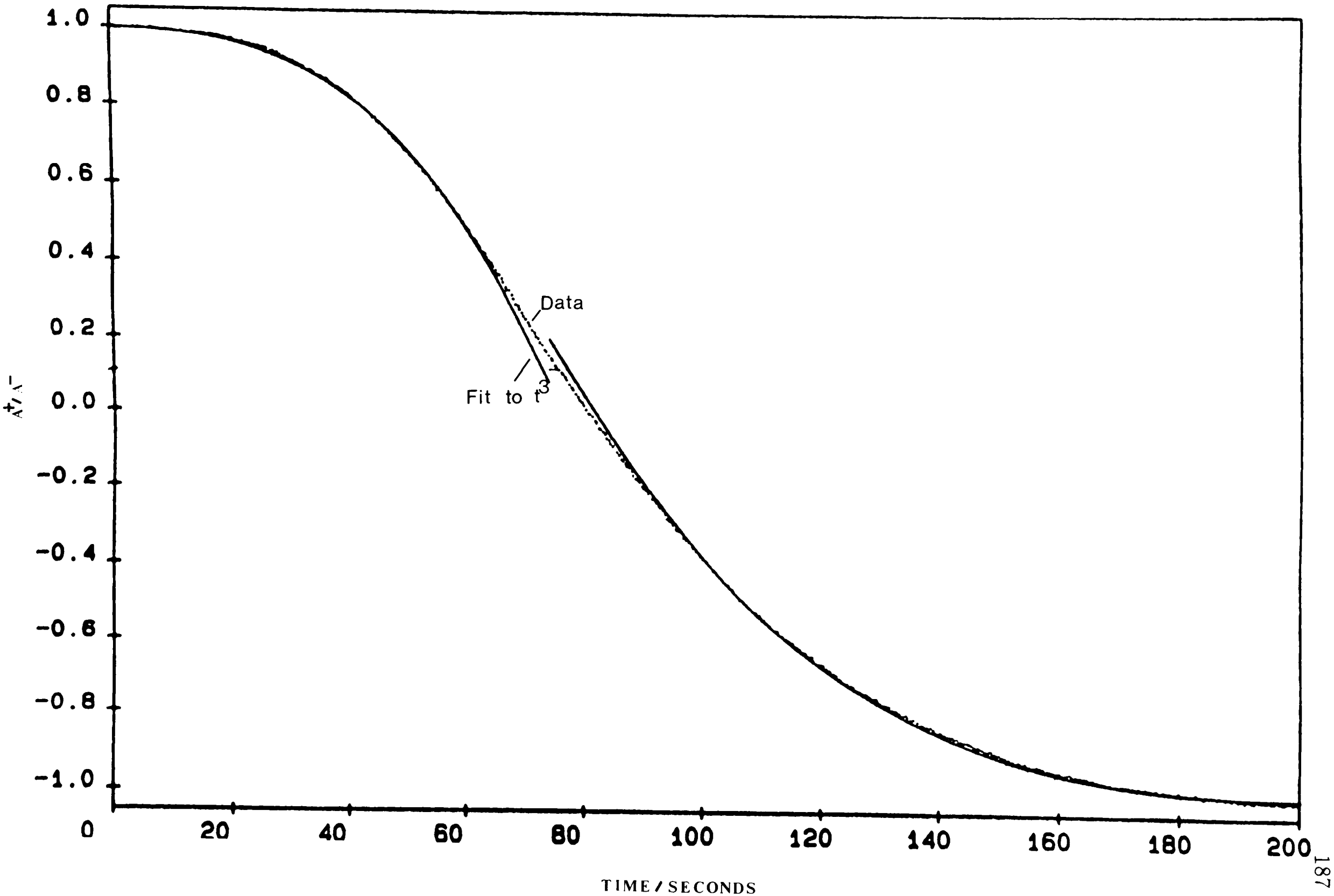
Simple numerical simulations for systems, which are mathematically similar to ours, have exhibited sigmoidal behaviour. A Monte Carlo process was used by Binder *et al*[94] to model magnetic nucleation processes in a 2-D ferromagnetic Ising model. The field was switched on at t=0 for a system just below T_c. The model produced a simple exponential law for the later stages of the relaxation. This agrees very satisfactorily with the experimental findings and also with the predictions of simple linear response theory. It should be noted that this model starts in a non-equilibrium state and as such the initial evolution of the state cannot be compared with experimental data for this sample.

Time cubed fits to the start and end of the relaxation were found to provide reasonable agreement over a wide range of times.

Physically such fits are consistent with a regular array of monodispersed spherical domains whose linear dimensions grow at a constant velocity. It is arguable whether fits of $e^{-\alpha t^3}$ give better agreement with the data; this would correspond to the time evolution of a random array of such domains. In any event, for small t both functions are of the same form; the discrepancy between the two arises for larger t values when domains progressively overlap as the relaxation proceeds in the random case. That the end stages of the relaxation also display t^3 behaviour can be understood by the collapse at constant velocity of regular shaped voids remaining between the growing domains.

This t^3 behaviour is significant because, following from the above discussion it corresponds to the evolution expected from a system described by the Lifshitz phenomenological model in which the surface driving term is totally absent. An experiment

Figure 6.13


1.0
0.8
0.6
0.4
0.2
0.0
-0.2
-0.4
-0.6
-0.8
-1.0
0
20
40
60
80
100
120
140
160
180
200
Data
Fit to t3
TIME / SECONDS

was therefore devised to test for the existence of a surface driving term. Given that the volume energy difference between the A^+ and the A^- phases can be almost arbitrarily small and that a large exchange energy is expected between spins at the domain walls, it seems reasonable to suppose that experimental conditions should be possible in which the surface term manifests itself.

6.9.2 Frozen relaxations

The relaxation can be frozen at any required A^+/A^- volume ratio by reducing the applied field to zero and hence removing the driving force. This results in a stabilized mixture of domains of relaxed and unrelaxed material. When the field is reapplied, it is found that the relaxation continues from the same volume fraction that existed when the driving force was removed (Fig 6.14).

It is possible that a surface energy term could also exist which would cause the domains to evolve at constant volume into a more energetically favourable spherical shape even in the absence of a volume driving term. However the relaxation behaviour observed following the freezing process is identical to that of the continuous relaxation. The lack of evolution of the domains in zero field is an important result and one which has two possible explanations. The simplest explanation is that there is no surface driving term. The second explanation is that the surface term is so large as to maintain the spherical domain shape throughout the relaxation. However this is inconsistent with the Lifshitz phenomenological model which predicts a $t^{\frac{3}{2}}$ time dependence for domain growth with a surface driving term.

6.10 Frustrated Relaxations

Section 6.9 discussed theoretical models which used parameters such as the nucleation rate per unit time and the growth law. Before seeking to draw comparisons between these theoretical pictures and the experimental data, some attempt should be made to establish the likely values for these parameters in this particular experimental system. To this end we now describe further measurements on more complicated

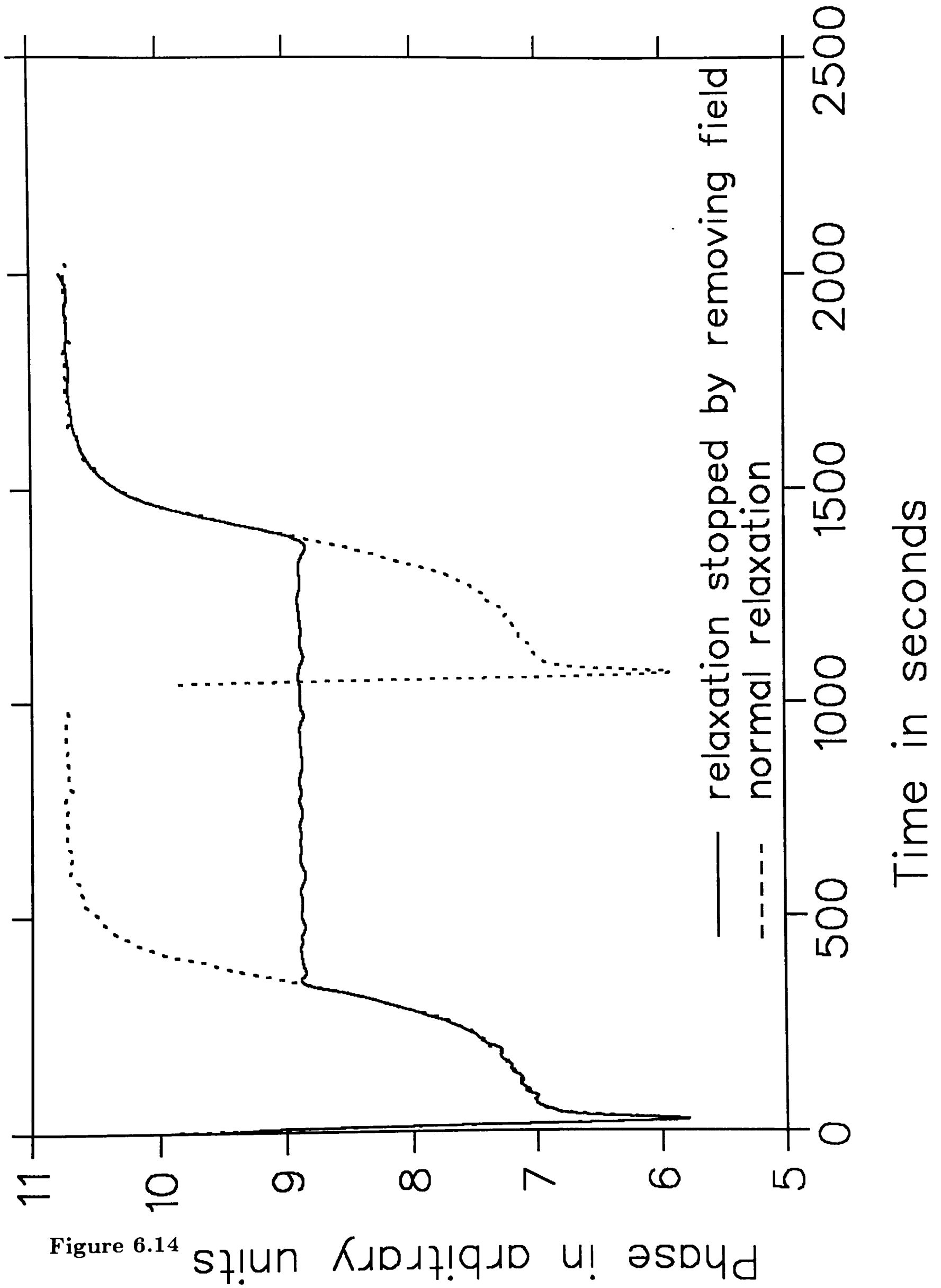

Phase in arbitrary units
11
10
9
8
7
6
5
0
500
1000
1500
2000
2500
Time in seconds
relaxation stopped by removing field
normal relaxation

Figure 6.14

relaxation sequences.

A relaxation was allowed to run to completion from eg. the A^+ to A^- state, and then the field direction was reversed. It was found that rate of return relaxation from the A^- to A^+ occurred at exactly the same rate. However if the applied field is reversed before completion, the relaxation is forced to proceed in the reverse direction and is said to be "frustrated". It was found that in such a case the returning relaxation rate was roughly twice as fast as that of the initial relaxation.

It is possible in turn to frustrate the return relaxation. This doubly frustrated relaxation was found to proceed at a still faster rate. As a general rule the greater the number of relaxations the faster the relaxation rate. Fig.6.15 shows a series of frustrated relaxations for a relaxation with a magnetic driving force along the [111] direction.

6.10.1 "Onion Skin" Domains

The increasing relaxation rate for successive frustrated relaxations can be explained by postulating that the same nucleation sites (eg. impurity atoms, dislocations) are involved in each relaxation. Consider a metastable A^- state relaxing to the stable A^+ state. The A^+ domains nucleate at given points in the lattice at time t=0 and grow spherically out from these points. If the field direction is reversed the A^- domains nucleate from the same points and grow in a similar fashion. Thus new concentric spheres of A^- grows outwards and the original A^- domains start to grow inwards to meet them. The A^+ domains become concentric "rings" of decreasing volume. Because there are now two domain walls moving the volume of A^+ domains decreases twice as fast, leading to an effective doubling of the relaxation rate. The effect of multiple frustrated relaxations is then to have N+1 moving domain walls (where N is the number of frustrations) thus increasing the relaxation rate to N+1 times that of the original relaxation (Fig. 6.15).

Checks on the validity of this model can be made by postulating that the domains grow with a constant surface velocity, v, so that domains growing out from from the nucleation sites have a radius given by r=vt. Certain critical points corresponding to the mutual annihilation of two concentric moving domain walls (indicated by filled arrows

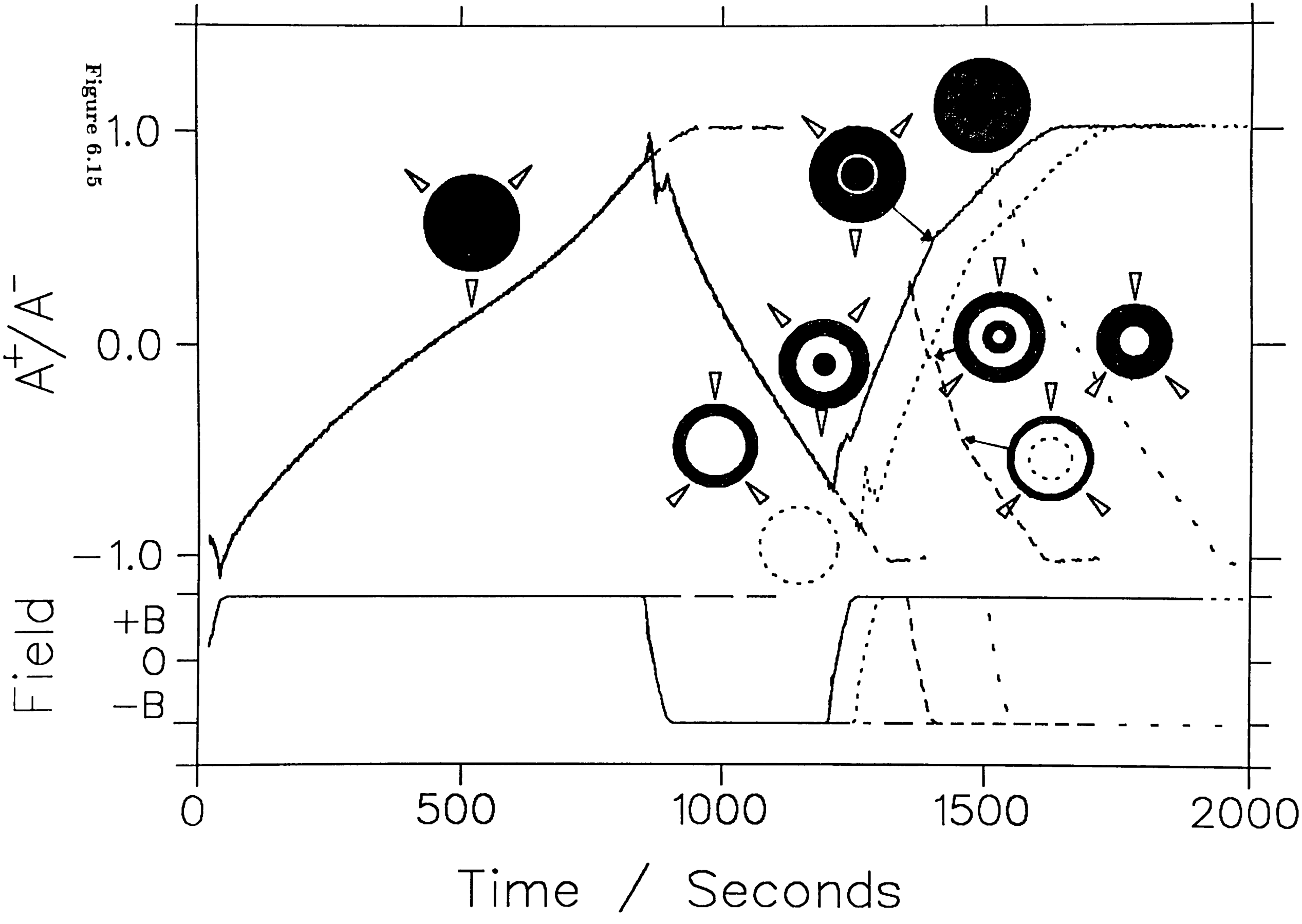


Figure 6.15

in Fig 6.15) can therefore be predicted. For the case of a single relaxation from a pure A^- state, which is frustrated after 900s, the critical point which marks the end of of the singly frustrated relaxation can be calculated to occur at time t+$\frac{t}{2}$=900+450=1350 s. This is in very good agreement with the experimental result.

For relaxations involving several moving domain walls the annihilation of two walls results in a change in gradient of the relaxation curve. The two doubly frustrated relaxations each show a clear point of inflection. This point coincides with the meeting of two of the three moving domain walls, resulting in only a single moving domain wall and a much slower rate for the remainder of the relaxation. In conclusion good agreement occurs between experimental and predicted relaxation rates based on a model of

- site specific rather than spontaneous domain nucleation,
- simultaneous nucleation at the start of the relaxation,
- similar and constant growth rate for all domains.

6.10.2 Weakness in the Experimental Method

The possible weakness of the method and hence the interpretation of the results derives from the fact that only one small cylinder (300μm x 1mm) of the crystal is probed [95]. It is possible that the almost linear relaxation curves, produced when the driving force was in the [111] direction, could be due to a single domain nucleated by perturbations to the system produced at the transducer and growing out from it. However we have checked that the ultrasonic power is sufficiently small that it does not perturb the relaxation rate (The relaxation rate was found to be independent of the power). Moreover if the transducer is acting as a nucleation site it is probable that it should do so for all geometries; this is clearly not the case for the sigmoidal relaxation curves seen for the [100] direction. Optical measurements by Dillon [96] under different conditions showed domains of order of 10μm apart; this suggests that the volume of the sample probed by the beam contains a statistically significant number of domains. An additional complication is the presence of demagnetising fields which result in the region under test being affected by changes of internal field in other regions of the sample. There are two contributions

to this effect. Firstly the static demagnetising fields result in a varying internal field throughout the sample. Secondly, dynamic effects occur in the course of a relaxation process; the internal field at a given point in the sample varies as a function of the global relaxation because of the variation of magnetisation in adjacent regions as a function of time. The fact that only a small sample volume is investigated can then be considered an advantage of the ultrasonic method, as the demagnetising field might be expected to be approximately uniform in this case.

6.10.3 Weakness in the Application of Numerical Solutions

Any simulation of a magnetic system will obviously be based on a great simplification of the interactions with the system. Typical simplifications include

- large driving forces
- a small array of spins
- only nearest neighbour interactions are included (Glauber dynamics)

These are necessary in order for a result to obtainable on a reasonable time scale. As discussed above the initial state is not an equilibrium state, so that at small times the evolution of the state cannot be compared to the experimental data. It is important to realise that in any case the use of increased driving forces may affect the validity of a comparison with results from the experimental system. In addition, edge effects become of increased importance and the use of Glauber dynamics results in the effects of long range interactions and elastic couplings being ignored.

6.11 Conclusions

Ultrasonic interferometry is a powerful technique capable of extracting a wide range of information about magnetic systems. In the case of the $Dy_3Al_5O_{12}$ system discussed, it has been possible to define the phase diagram and extract information concerning the behaviour of the order parameter as a function of temperature. It is in the quantitative study of dynamic effects, however, that this technique has a particular advantage over other experimental methods.

Quantitative measurements of the phase proportions can be made during the relaxation of the metastable phase. The interferometer is therefore particularly useful in extracting information concerning domain growth dynamics. The experimental data suggests that the beginning and end of the relaxation are best fitted by time-cubed laws with an $e^{-\alpha t}$ term at the extreme tail of the relaxation. This provides clues as to the nature of the driving terms of the relaxation. The t^3 behaviour is consistent with the predictions of the Lifshitz phenomenological model for a system which is volume driven only, i.e. there is no surface driving term present. This implies constant domain wall velocity. The t^3 fit also suggests that the domains are monodispersed spheres and hence that all nucleation occurs at the start of the relaxation. This is strongly confirmed by the results of the "onion skin" experiment which further indicates that these nucleations are strongly site specific, and are probably defect or impurity driven.

As discussed in Section 6.10.2 the origin of the different shaped relaxation curves for applied magnetic field in the [111] and [100] directions is not well understood. It is hoped that further optical imaging studies and the use of different transducer geometries will help to clarify these points. At present a study of a spherical $Dy_3Al_5O_{12}$ sample is beginning; it is anticipated that the study of this system with its well known demagnetising factor will enable a clearer understanding of the system to be obtained.

Chapter 7

Ultrasonic Investigation of $DyPO_4$

7.1 Introduction

Metamagnets are characterized by a type of magnetic field-induced phase transition, which occurs only in highly anisotropic systems. This metamagnetic transition occurs when the free energy of the anti-ferromagnetic state equals that of the ferromagnetic state. For small applied magnetic fields the sublattices are unaffected by an external parallel field. At low temperature, when a magnetic field is applied with a sufficiently large component in the direction of the anisotropy axes a first order transition occurs from an AF state (with zero or low magnetisation) to an aligned state (with high magnetisation). At higher temperatures (below the Néel temperature) the transition is second order. In both the AF and paramagnetic phases the anisotropy forces the spins to lie along the easy axes. This type of transition is distinct from field-induced transitions found in isotropic or weakly anisotropic systems in which spin flop occurs. The point on the phase diagram at which the first order and second order critical lines meet is known as the tri-critical point (TCP), and can be defined as the point in (M, H_i, T) space where the discontinuity of magnetisation as a function of internal field, H_i, associated with the first order transition vanishes.

A multi-critical point is a special point on the phase boundary where competition between 2 or more types of order leads to a new kind of co-operative behaviour. A tri-critical point was first observed in ^{3}He -^{4}He system by Griffiths [97] who pointed out that such an effect may be seen in other physical systems. A metamagnetic system is a good example of an experimental system which can be used to verify theoretical predictions of behaviour near tri-critical points.

7.1.1 Theory

Mean field theory can be used to qualitatively predict the magnetic properties of the metamagnetic system. The early work of Landau [98] and Néel [99] established two essential criteria for a material to be metamagnetic. Firstly a strong anisotropy must be present to confine the spins in a direction parallel or anti-parallel to the system's easy axis. Secondly there must be competing interactions present in order that the phase transition is first order for T greater than 0K. In this case this is manifested as an AF interaction between nearest neighbours and a ferromagnetic interaction between next nearest neighbours.

The mean field theory applied to such an Ising model has a Hamiltonian of the form

$$H = |J| \sum_{<nn>} S_{jz} S_{kz} + J' \sum_{<nnn>} S_{jz} S_{kz} - \mu H_i \sum_{j} S_{jz}$$

where S_{jz} is the component of the jth spin in the z direction with values $\pm 1/2$, and H_i is the internal magnetic field.

An important parameter in determining the behaviour of the system is R where $R = \frac{Z'J'}{ZJ}$ where Z and Z′ are the number of nearest neighbours (n.n.) and next nearest neighbours (n.n.n.) respectively. For a value of R less than 0 the interactions are competing. For R less than $-\frac{3}{5}$ the behaviour is qualitatively like that of $DyPO_4$ as previously described with regions of first and second order transitions meeting at a TCP.

7.1.2 Demagnetising Effects

For all finite samples the applied field H_0 is not equal to the internal field within the sample. Consider the simple case of an ellipsoidal sample for which the demagnetising factor, N, is homogeneous throughout the sample.

$$H_i = H_0 - NM \tag{7.1}$$

The demagnetising field has an important effect on the first order transition. For a small change in H_0 and M then

$$\delta(H_i) = \delta(H_0) - N\delta(M)$$

and so at a first order transition $\delta(H_i)=0$,

$$\delta(M) = \frac{1}{N}\delta(H_0)$$

resulting in the transition becoming spread out over a range of applied fields. This can be seen from equation (7.1). At the first order transition M increases discontinuously. This however will cause the internal field to drop below the value required for the transition to occur, and therefore the transition has to take place gradually. Accordingly the sample forms domains of the two phases which coexist at the first order transition and as the transition proceeds, one set of domains grows in the size at the expense of the other. Thus in a real system the first order transition is broadened into a mixed phase region [100].

7.2 Measurement of Critical Behaviour

Of the metamagnetic systems for which detailed data is available (eg $FeCl_2$, $Dy_3Al_5O_{12}$, $CsCoCl_3.2D_2O$ and $DyPO_4$) only the results on $Dy_3Al_5O_{12}$ are in good agreement with theory [101], [102], [103], [104].

The TCP and first order transition are experimentally difficult to locate. Most experiments on magnetic systems have utilized discontinuities in the gradient of the bulk magnetisation to locate the position of the first order phase transition after correcting for demagnetising factors for non-ellipsoidal samples. This is made more difficult because the susceptibility diverges near the tri-critical point making the discontinuities less distinct and the demagnetising corrections also become more important for larger susceptibilities. The presence of inhomogeneous demagnetising factors means that kinks in the magnetisation are not infinitely sharp.

Neutron and optical techniques have been used to study non-ellipsoidal samples with some degree of success. Masking can be used in order that the neutron or optical beam only interacts with the central region of the sample. Using neutron diffraction experiments and magnetic resonance methods it is fairly easy in practice to locate the upper boundary of the mixed phase region as the sublattice magnetisation M_S goes to

zero at this point. However there are still problems in locating the lower boundary of the mixed phase, and this is the main source of experimental difficulty in this field. In response to this problem, new techniques have been developed which are not dependent on the measurements of magnetisation.

The new measurement techniques are based on direct optical observation of domains [105], and light scattering techniques to detect the presence of domains [104]. Dynamic magnetisation processes in this coexistence region are fundamentally different to those in single phase regions in which magnetisation occurs by spin reversal. In the mixed phase region a slower macroscopic response to the changing applied field would be expected because domain wall motion is involved and hysteresis effects would be also expected to come into play. This was found to be the case in Giordano and Wolf's paper [101]. However for temperatures close to the TCP these hysteresis effects were found to be too small to observe.

7.2.1 The Ultrasonic Technique

The ultrasonic method, as described in Chapter 6, does not involve direct measurement of the magnetisation. The phase change of the returning echoes is dependent on the elastic constants within the system and the sample length, both of which may be affected by the changing magnetic order within the sample. It was hoped that the ability of this technique to detect small changes in the signal phase, and hence the magnetic ordering, would enable a very accurate measurement of the location of the onset of the mixed phase region to be obtained. In addition the attenuation of the ultrasonic signal may be taken as an indication of scattering of the wave train by growing domains.

7.3 Dysprosium phosphate

Dysprosium phosphate, $DyPO_4$, has a zircon crystal structure with a tetragonal unit cell of dimensions a_o=6.719 Å , c_o=6.053 Å and of space group D_{4h}^{19} I4/amd. Below the Néel temperature, T_N=3.4K, $DyPO_4$ orders antiferromagnetically into a two sublattice configuration in which the moments are aligned along the c axis. The ground

state is a Kramers doublet. There is a large anisotropy ($g_{||} = 19.3 \pm 0.5$, $g_{\perp} = 0.7$), making the system a good approximation to an s=1/2 Ising model. This has been verified experimentally [107], [106]. The zero field susceptibility and specific heat have been well described by a nearest neighbour interaction Ising model. It has thus been concluded that under these conditions the next nearest neighbour (n.n.n) and higher order interactions are very small. This has been experimentally verified by Wright *et al* [107] to be less than 3.4% of the nearest neighbour interactions. However for $B \neq 0$ these n.n.n interactions play a significant role because of their AF nature and are the cause of metamagnetic behaviour. It should be noticed that in contrast to $Dy_3Al_5O_{12}$ the order parameter, η, is odd under inversion. $DyPO_4$ is a simpler system to study than DyAlG because from symmetry considerations no staggered field should exist. This is the origin of the difference in properties between the two systems. However this simple theory would seem to imply that no magnetoelastic effects should be expected in materials such as $DyPO_4$, but as will be described below the $DyPO_4$ AF order parameter exhibits quite significant strain-dependent and unexpected hysteresis effects. This suggests that higher order factors (eg. inhomogeneous strain gradients) may provide a coupling mechanism between AF order and elastic strain. The only condition that is necessary is that the order parameter must be translationally invariant (i.e. the magnetic and chemical unit cells should coincide)[108].

The $DyPO_4$ metamagnetic transition and TCP have been investigated using many techniques including optical methods [109], [110], [105], magnetothermal resistivity [111], neutron scattering [112], [113] and magnetocaloric measurements [114]. The value of the tri-critical point has been experimentally found to be in the range 0.75K [106] to 2.4K [115]. It has been shown that stress caused by polishing [115] causes a variation in the value of TCP for otherwise similarly treated crystals. Jahn *et al* [115] found that samples that had been roughly polished had significantly higher T_{TCP} (2.05K, 2.18K, 2.4K) when compared to those which had not undergone this treatment (1.57K, 1.85K). Similarly Millhouse *et al* [116] investigating $DyPO_4$ crystals under hydrostatic pressure found that as the applied pressure was increased the TCP approaches T_N. It

can be therefore concluded that stress is a very important factor in determining the temperature of the TCP.

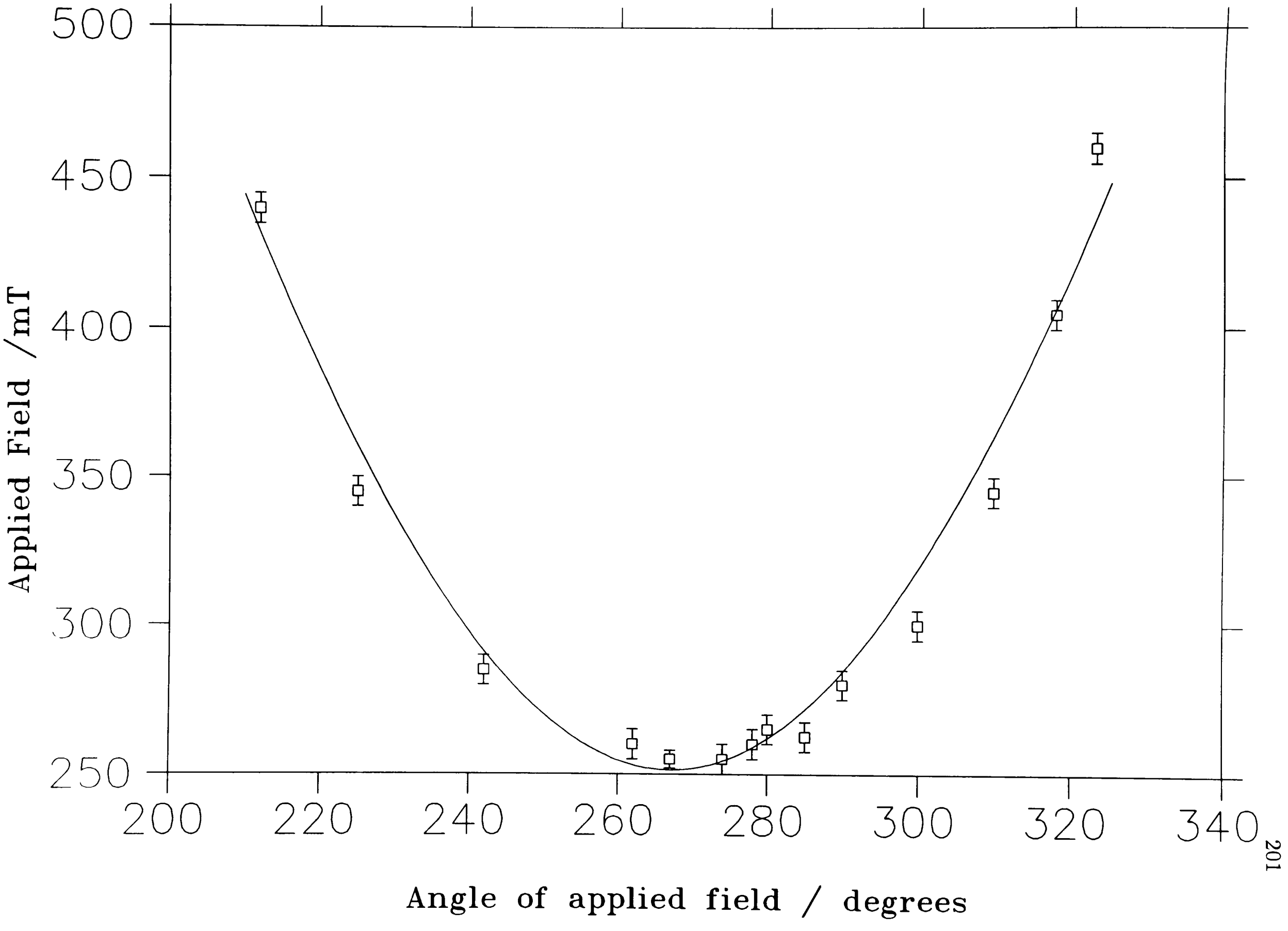
7.4 Experimental Method

ZnO transducer was deposited on one of the optically polished pair of long faces of a $DyPO_4$ needle shaped crystal of dimensions 0.9 x 0.9 x 4 mm as measured using a travelling microscope. Echoes were found for operating frequencies in the range 160 MHz - 1940 MHz. There were two modes present with characteristic time of flights of 240 ns ($7500ms^{-1}$) and 1000 ns ($1800ms^{-1}$) measured using the HP54111D Digitizing Oscilloscope. These modes have been identified as longitudinal and transverse respectively. The sample was mounted as described in Section 6 using silver dag with the c-axis in the plane of the field and cooled in a pumped ^4He bath cryostat to 3.5K, slightly below the acknowledged Néel temperature. The temperature was stable to within 0.01K.

The fifth longitudinal echo was monitored using carrier mixing to provide interference. The frequency of oscillation was optimized at 996.27 MHz to provide the maximum sensitivity to the changes in path length or elastic constants measured. This frequency was chosen because a train of more than twenty 240 ns echoes was seen, the maximum number of echoes found.

The sample was roughly oriented with the c-axis of the specimen in the plane of the field. Its precise orientation in the plane was determined by rotating the field direction and finding (for a constant temperature below the transition temperature) the angle for which the phase transition occurred at the lowest applied field value. This orientation was assumed to be the point at which the applied field was aligned along the c-axis. Fig.7.1 shows the field value, B_c at the transition point against the angle of the magnet in arbitrary units at T=2.0046K The variation of B_c is of the form $\cos\theta^{-1}$. where θ is the angle between the field and the c-axis, as expected for a strongly Ising-like system such as $DyPO_4$.

Figure 7.1


500
450
400
350
300
250
Applied Field /mT
200
220
240
260
280
300
320
340
Angle of applied field / degrees

7.5 The Phase Diagram

At a constant temperature below T_N a sharp discontinuity in the phase of the ultrasonic signal was found as the applied field is swept through the phase boundary (Fig. 7.2). The traces in Fig.7.2 correspond to data taken at 3.346K, 3.314K, 3.221K, 3.144K, 3.012K, 2.864K, 2.647K, 2.461K, 2.15K, 1.98K, 1.739K and 1.46K from left to right respectively.

Below the temperature of 2.5K it was seen that the discontinuity became visibly broadened into a region of fast change in phase. This region is thought to consist of a mixed phase with domains of paramagnetic (aligned) spins growing at the expense of the antiferromagnetic domains. The phase diagram was found to vary from one cooling to the next but to remain of the same general form; this was probably due to the variations in the strains produced on cooling.

From the phase diagram the TCP appears to be clearly (2.6 ± 0.1)K. This value is higher then any value reported in the literature. The closest published results are those of Jahn *et al* [115] for a needle-like sample of dimensions (0.9mm×1.31mm×2.51mm) who quotes a value of 2.18K for the TCP and observes splitting up to 2.6K. The temperature dependence of the splitting is qualitatively different to the data described here; in Jahn's data the lack of temperature variation in the splitting above 2.18K led him to discard these higher temperature results. Fig.7.4 shows the temperature dependence of the width of the mixed phase region, which clearly indicates a well-defined TCP.

7.5.1 Attenuation Measurements

The transition across the mixed phase region also gives rise to attenuation of the ultrasonic signal (Fig. 7.5). The maximum attenuation occurs at a field slightly displaced from the field value at which the maximum change in phase occurs. The attenuation is explained by scattering from the growing domains.

The disadvantage of this method for measuring the phase diagram is that the attenuation near the edges of the mixed phase region is small and the signal to noise ratio is low. It is therefore difficult to define the limits of the mixed phase region. The phase

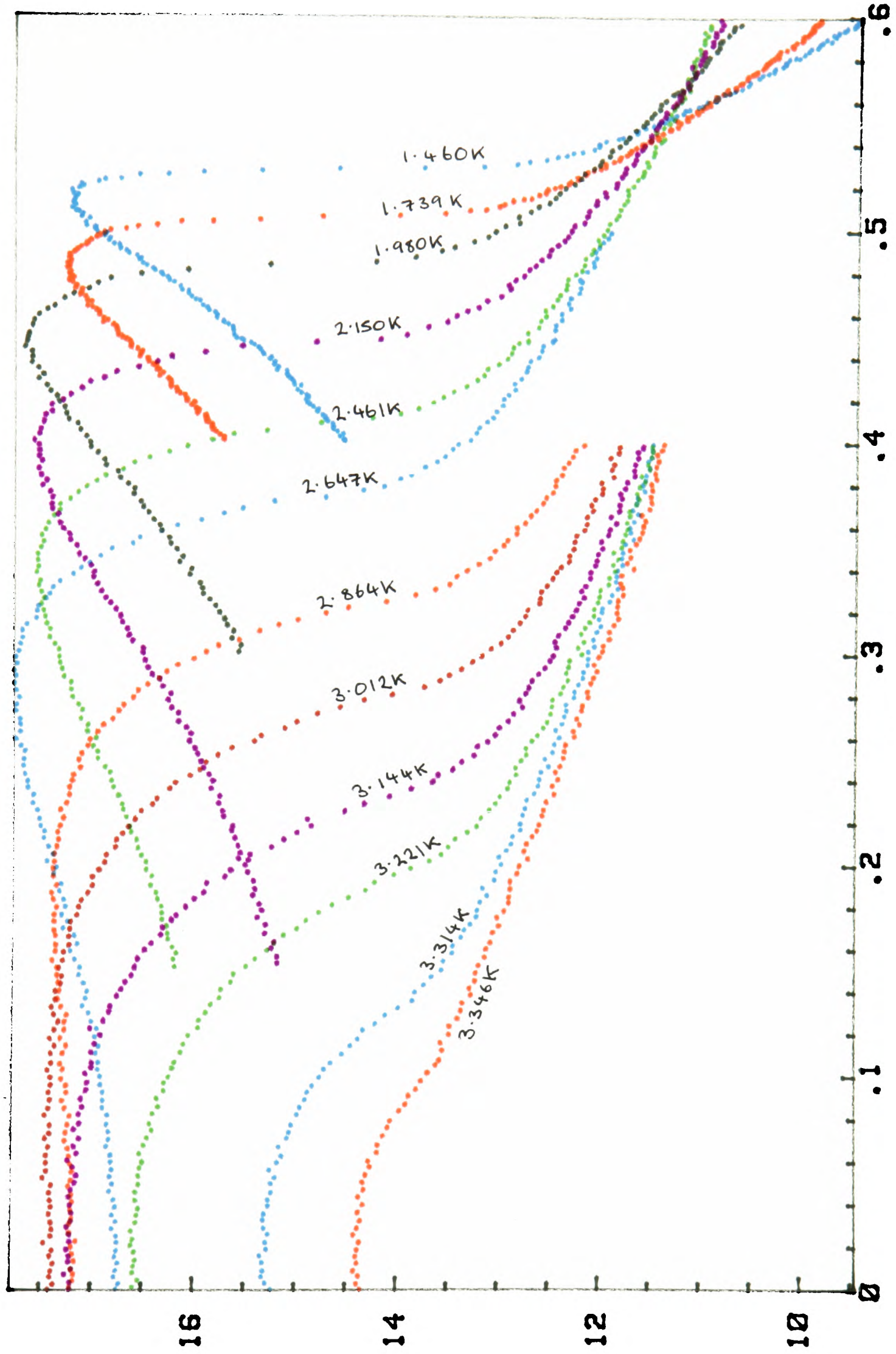

1·460K
1·739K
1·980K
2·150K
2·461K
2·647K
2·864K
3·012K
3·144K
3·221K
3·314K
3·346K
.6
.5
.4
.3
.2
.1
0
field / T
16
14
12
10
signal / mV

Fig. 7.2

Figure 7.3

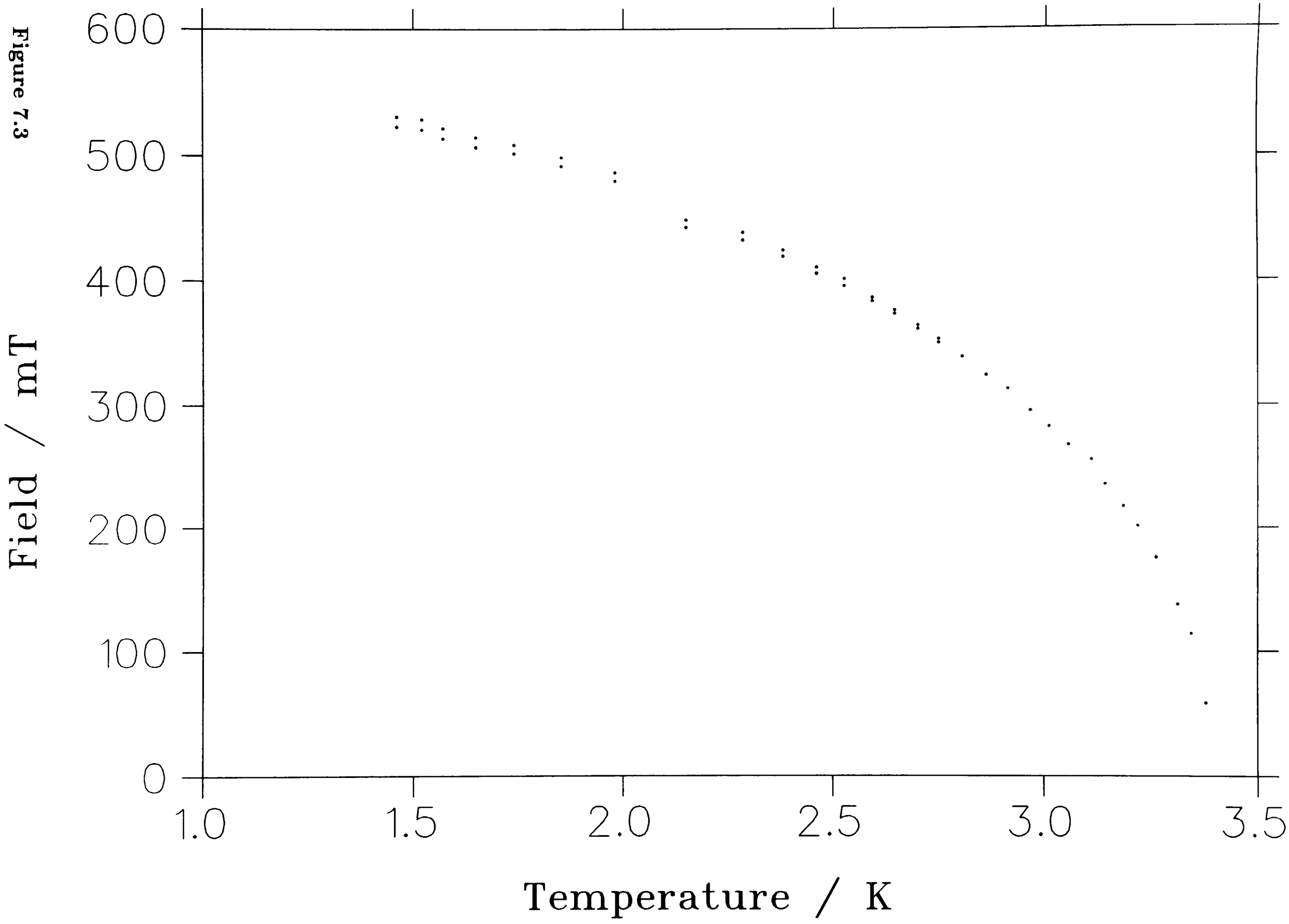
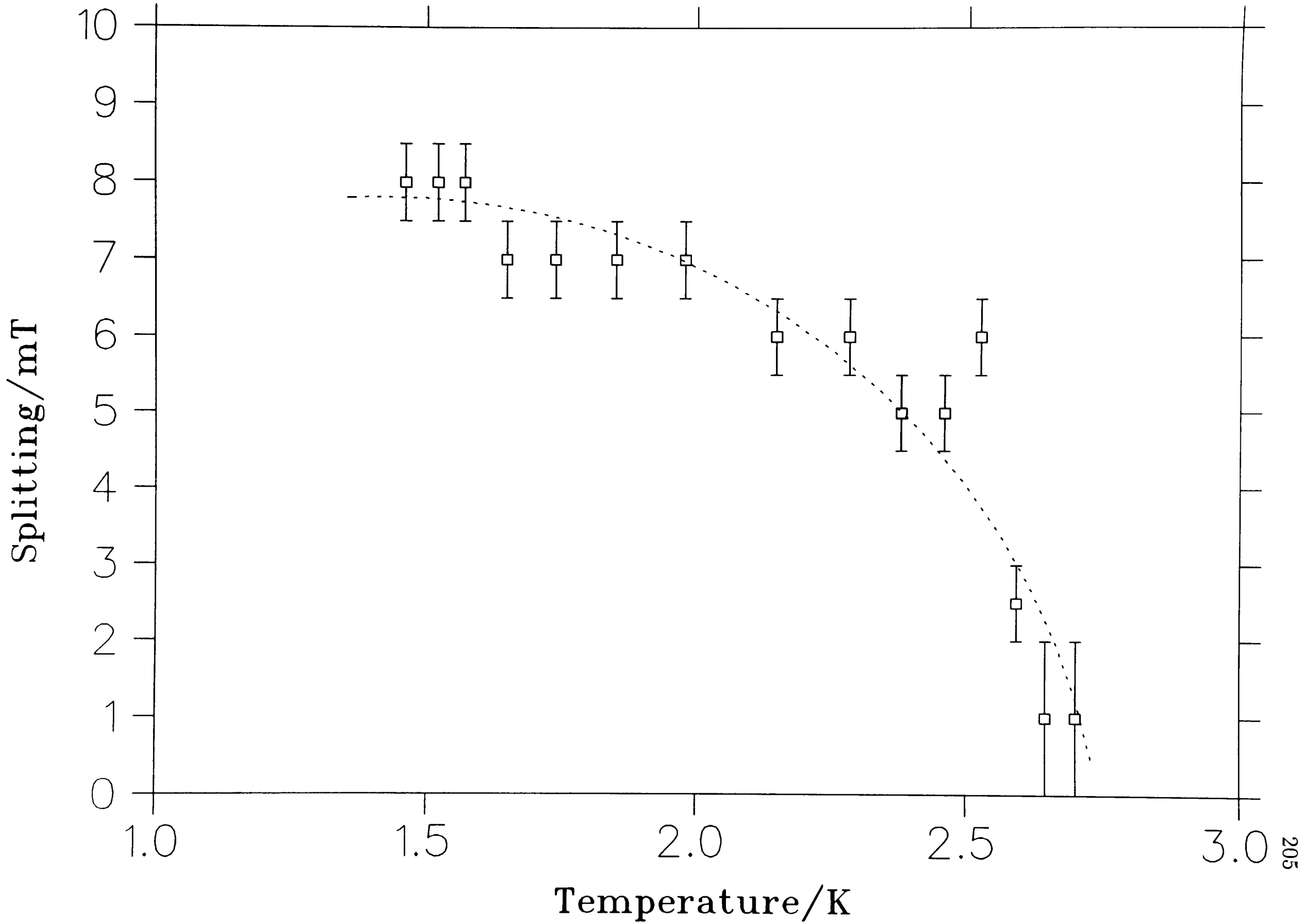
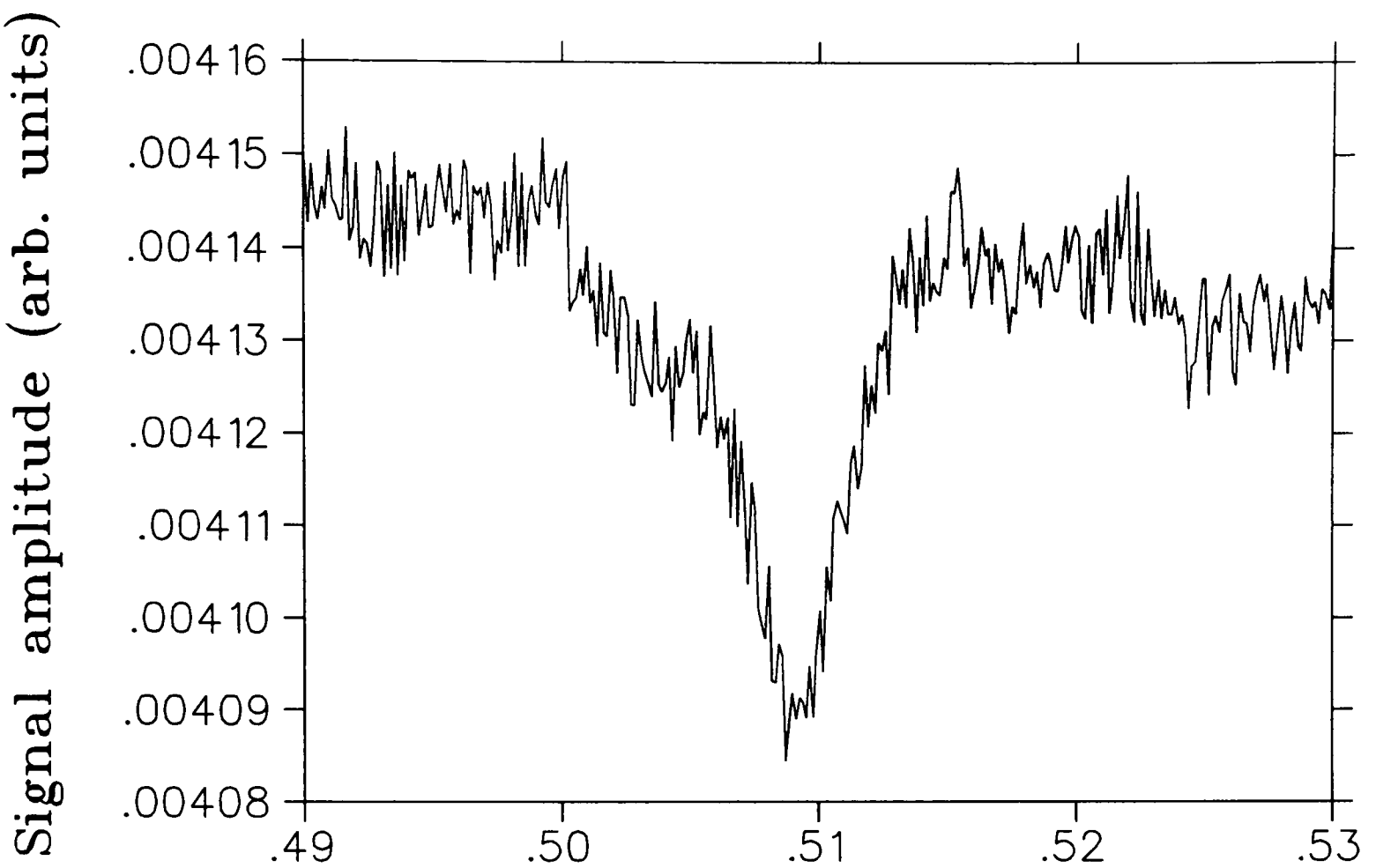

600
500
400
300
200
100
0
Field / mT
1.0
1.5
2.0
2.5
3.0
3.5
Temperature / K

Figure 7.4




Signal amplitude (arb. units)
.00416
.00415
.00414
.00413
.00412
.00411
.00410
.00409
.00408
.49
.50
.51
.52
.53
Field/T

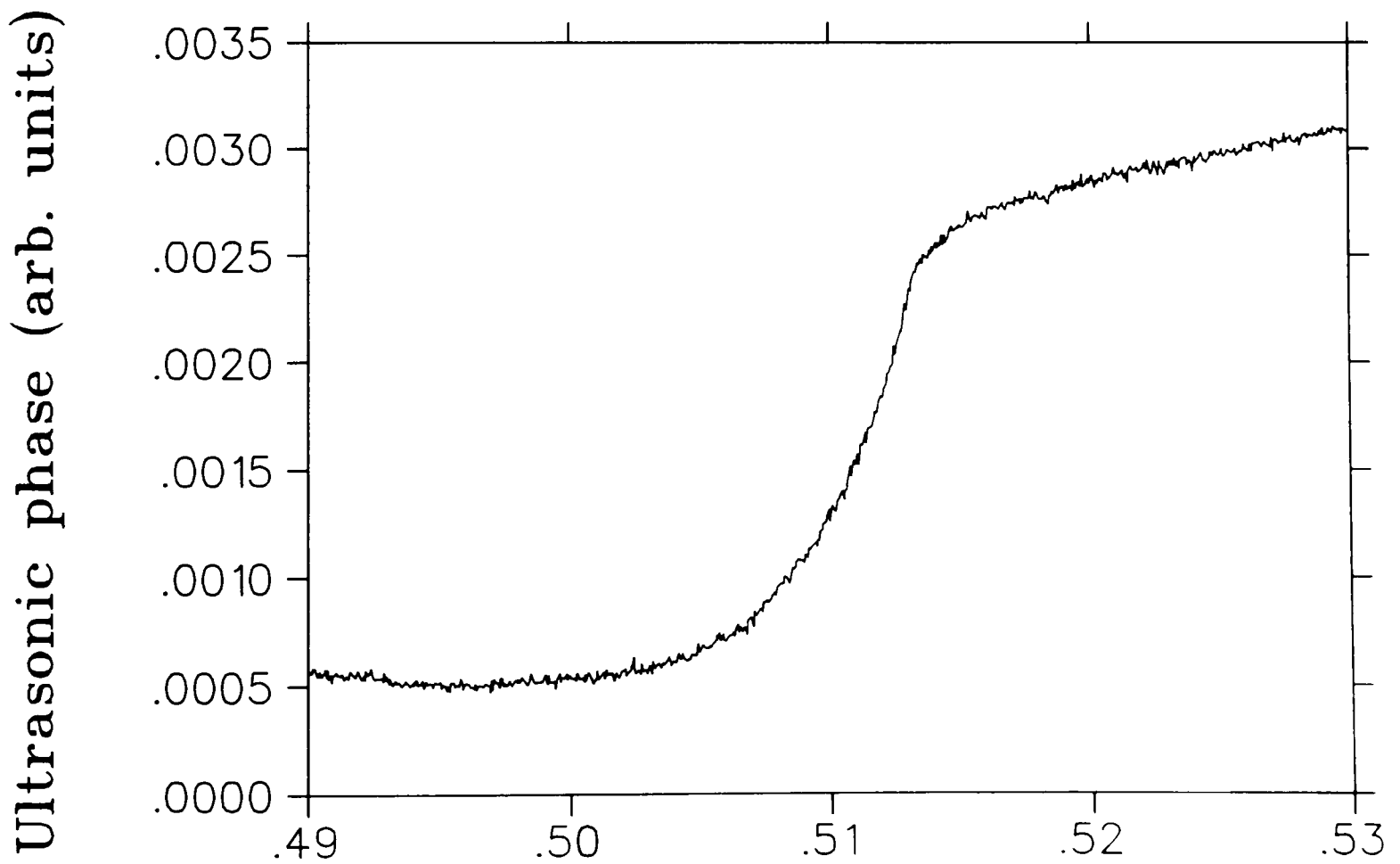

Ultrasonic phase (arb. units)
.0035
.0030
.0025
.0020
.0015
.0010
.0005
.0000
.49
.50
.51
.52
.53
Field/T

Figure 7.5

is shown in
diagram (Fig. 7.3)

7.6 The Mixed Phase

In the region of the first order phase transition much evidence for the existence of the mixed phase was found, taking the form of hysteresis effects not found either above or below this area of the phase diagram. As expected the applied field value at which the phase boundary occurred was found to increase with increasing field sweep speed, and was found to occur at a lower fields for decreasing field sweep (Fig.7.6). The blue, green and red traces represent the ultrasonic phase plotted as a function of field at T=3.2639K for sweeps taking 20 minutes, 50 minutes and 100 minutes from 0T to 1T.

The greatest hysteresis was seen for the fastest sweep speeds, as is to be expected. However even at the slowest sweep rates (100 mins for 0 to 1T) there is still a visible hysteresis effect of the order 5mT between increasing and decreasing field sweeps.

In order to define the mixed phase region, and hence the phase diagram of the sample, it was necessary to try to define the regions in which domains existed. It was found that hysteresis effects can be used to define the extent of the mixed phase region.

The upper bound of the traces was found to be quite distinct and appeared as a sudden gradient change. From Fig.7.7 it can be seen that the mixed phase region exists over a field range of 435mT-530mT at T=1.521K. The outer solid trace shows a sweep process in which the applied field value is cycled through the mixed phase region and then the sweep direction is reversed to sweep back down through the region again. These sweeps were made at a very slow sweep rate (0 to 1T in 250 minutes) to ensure that hysteresis arising from the sweeping process as described above was kept to a minimum. It can be clearly seen that there is still a significant amount of hysteresis present. There is of order 20 mT difference between the field value of the upper bound in an increasing field (520 mT) and the upper bound in a decreasing applied field (500 mT).

Several similar field cycles were made in which the applied field value did not reach that necessary to enter the paramagnetic region. The resulting traces are shown as

Fig.76

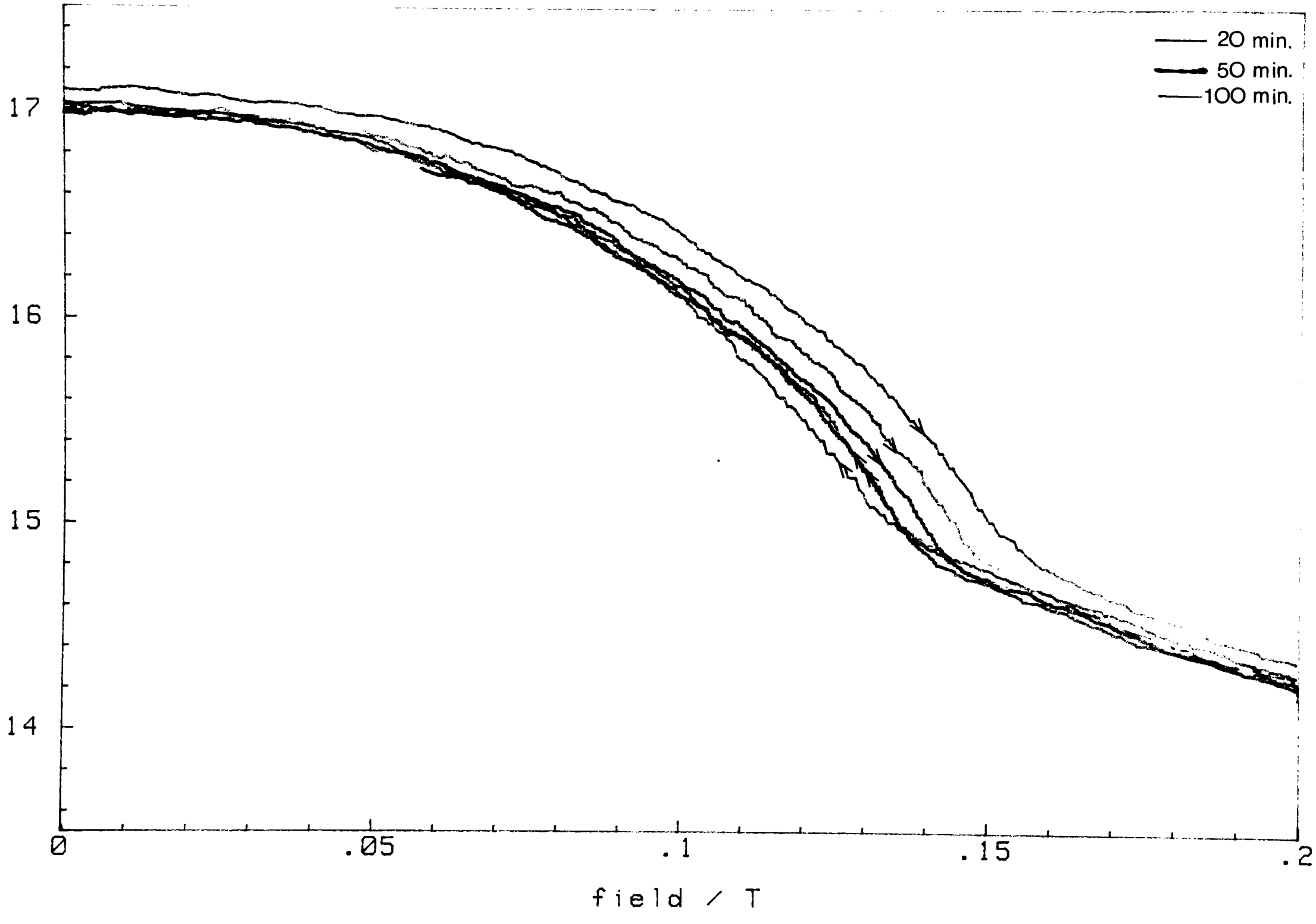
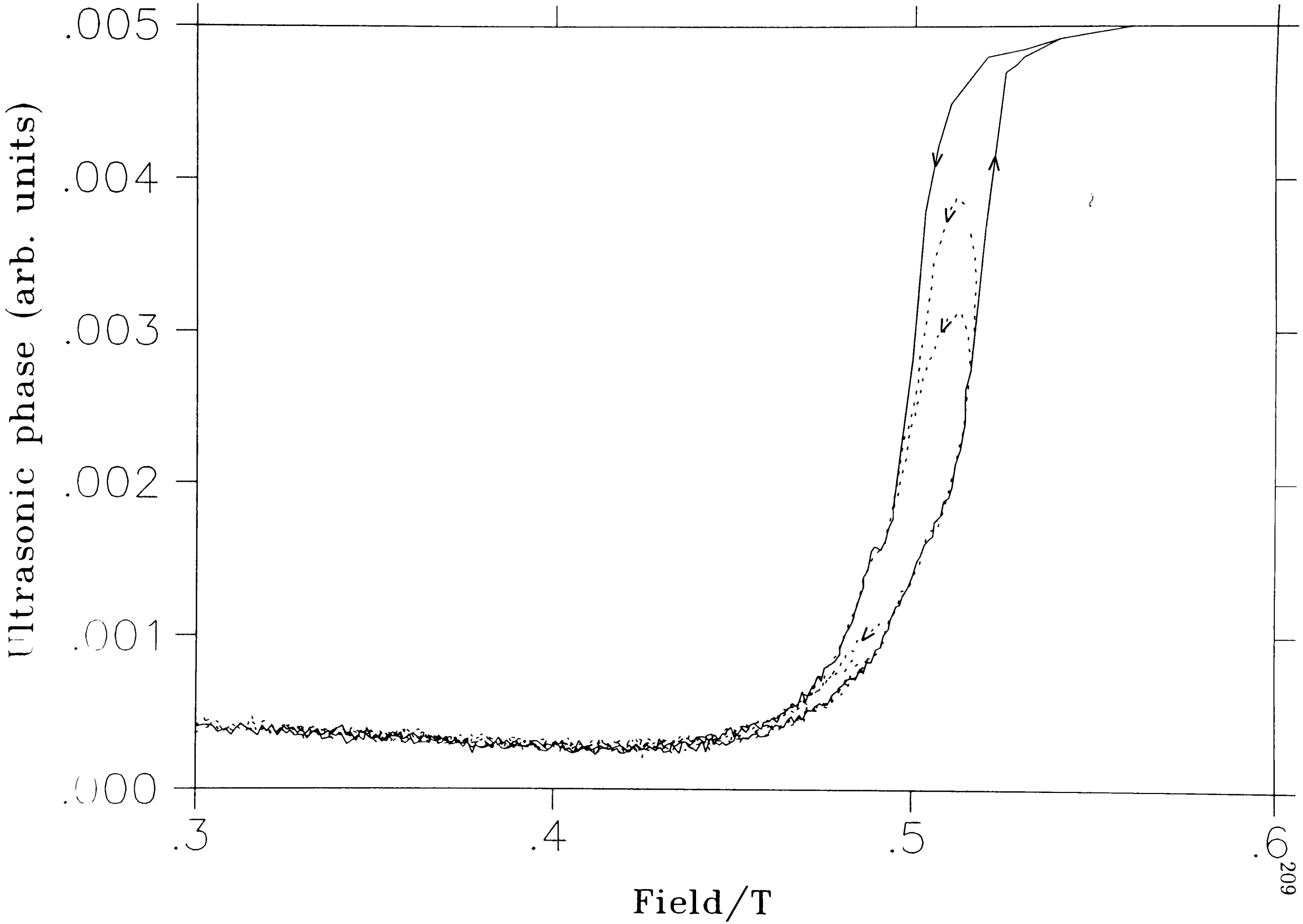


Figure 7.7


Ultrasonic phase (arb. units)
.005
.004
.003
.002
.001
.000
.3
.4
.5
.6
Field/T

dotted lines in Fig. 7.7. All traces lie within the solid line of the trace described above. It is interesting to note that the signal height continues to increase even after the applied field direction has been reversed. This will be discussed further in Section 7.6.1 below.

These results indicate quite accurately the location of the mixed phase state. Unfortunately for temperatures close to the TCP it is found that the hysteresis is too small to be accurately observed and that it is difficult to accurately define the mixed phase region close to the TCP.

7.6.1 Halted sweeps

It is found that if the field sweep is stopped at a field value b_F which lies close to the lower boundary of the transition then the system will proceed into the mixed phase region reaching a steady state in a time period that depends approximately linearly on the sweep speed whilst approaching the final field value.

The transition does not progress into the paramagnetic state unless B_F is close to the upper boundary of the transition region. An intermediate mixed phase can therefore be stabilized.

Figure 7.8 shows the results of a slower sweep speed (0 to 1T in 50 minutes) stopping at 495.0mT, 498.5mT, 499.9mT and 501.6mT. The upper trace is again a sweep which was not stopped. The signal height continues to increase for up to 70 seconds after the field sweep has been stopped. Figure 7.9 shows results taken at T=1.5914K following a 2 minute sweep speed stopping at a final field B_F with values 479.8mT, 493.3mT, 497.2mT, 504.2mT and 511.25mT, respectively from the lower trace upwards. The upper solid trace shows a sweep that continues right through the transition region. The approach to a stable state occurs more quickly for higher final field values and appears roughly linear in all cases. However it should be noted that the y-axis of these graphs is non-linear and cannot be considered to be directly proportional to the composition of the mixed phase. This is because in order that the transition through the mixed phase should appear as a monotonic function of ultrasonic signal magnitude the lower critical field was arranged to coincide with the minimum signal height. A linear and maximum

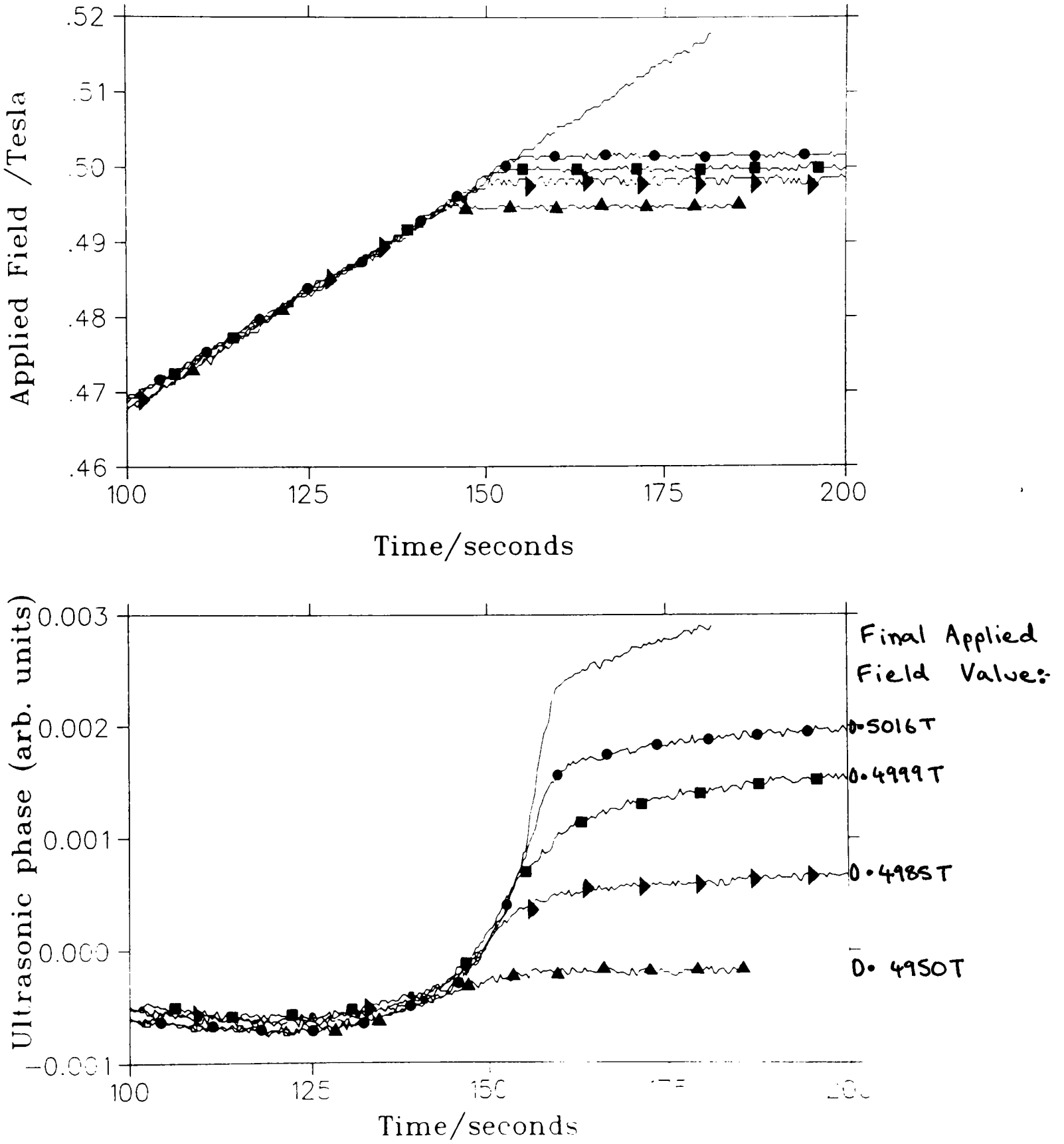

Applied Field /Tesla
.52
.51
.50
.49
.48
.47
.46
100
125
150
175
200
Time/seconds
Ultrasonic phase (arb. units)
0.003
0.002
0.001
0.000
−0.001
100
125
150
Time/seconds
Final Applied
Field Values:
0·5016T
0·4999T
0·4985T
0·4950T

Figure 7.8

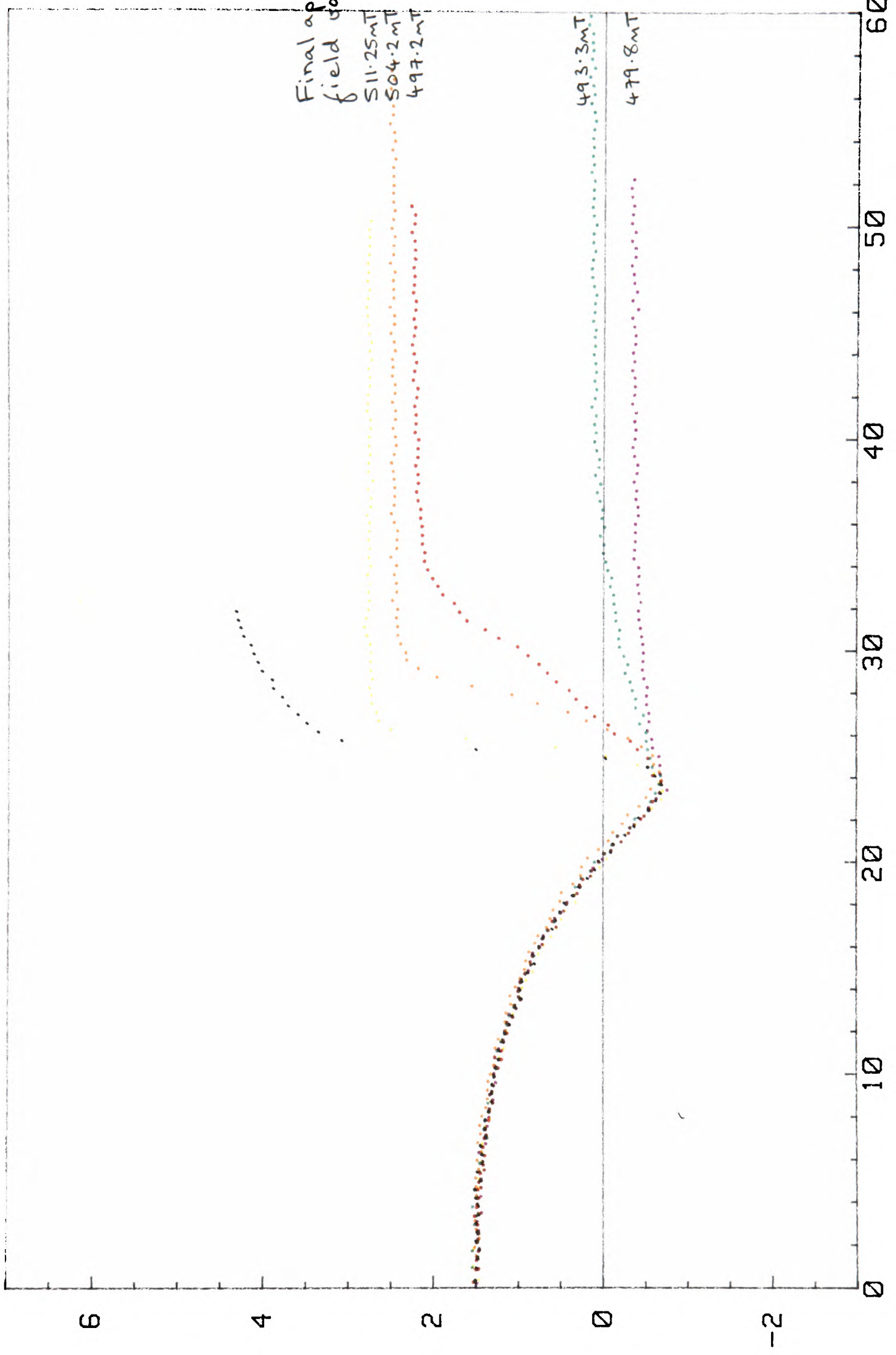

Final applied field value:
511·25mT
504·2mT
497·2mT
493·3mT
479·8mT
signal / mV
6
4
2
0
-2
0
10
20
30
40
50
60
time / s

Fig. 7.9

sensitivity is found half way between the two signal extremes.

It can therefore be concluded that the continuation of the process beyond the end of the field sweep is not due to a heating effect as this would lead to a larger change in peak height after the end of the faster field sweep; the gradual change in peak height after the field sweep has been stopped may be caused by the presence of slow equilibrium effects. These figures do in any case provide evidence of a mixed phase region and shows that the mixture of the paramagnetic and AF phases can be stabilized.

7.7 Conclusions

It has been seen that the location of the TCP can be well defined using the ultrasonic technique. However the position of the TCP and the degree to which the first order transition is broadened varies with each cooling process. This indicates the large degree to which the behaviour of such a system is dependent on the strain present as found by [115], [116].

It has been seen that sample polishing [115] is an important factor in the increase of strain within a sample, and hence strain will be intrinsically high in a sample which has been optically polished to provide two parallel faces. Sample mounting may also introduce strain as result of either the bonding process and the different thermal expansion coefficients of the sample and holder on cooling. The prepared sample was held using a small amount of silver dag to the conducting sample holder. This connection was necessary to earth the ground plane of the transducer. It is therefore difficult to envisage a way in which the strain within the sample could be reduced whilst maintaining this experimental technique. It should be noted that internal strain can also arise from imperfections in the growth of the crystal. The value found for the TCP will therefore always be higher than for a sample containing no internal strain and with no applied external strain. Although a definitive value of the TCP cannot be realised it has been shown that using the ultrasonic method it is possible to precisely define a region of domain coexistence from hysteresis measurements and hence the location of the first order

transition at low temperatures.

References

[1] Hofler and Wellerdick *Balzers Technical Report* (Balzers AG, 1983)

[2] C.M.Horwitz, *J.Vac.Sci.Tech.* **1**, 60 (1983)

[3] C.Weissmantel *et al*, *J.Vac.Sci.Tech.* **17**, 812 (1980)

[4] J.F.Gregg, S.J.Dawson and C.R.Staddon (A Novel Magnetron Design, Patent pending, 1992)

[5] P.D.Reader and H.R.Kaufman, *J.Vac.Sci.Tech.* **12**, 1344 (1975)

[6] S.M.Rossnagel and J.J.Cuomo, *Vacuum* **73**, (1988)

[7] T.Spalvins, *J.Vac.Sci.Tech.* **17**, 315 (1980)

[8] S.Aisenberg and R.W.Chabot, *J.Vac.Sci.Tech.* **10**, 104 (1973)

[9] H.T.G.Hentzell *et al*, *J.Appl.Phy.* **58**, 556 (1985)

[10] G.J.Kominiak *et al*, *J.Vac.Sci.Tech.* **13**, 1193 (1976)

[11] Leybold (Vacuum Technology:Its Foundations,Leybold AG)

[12] L.T.Lamont Jr, *J.Vac.Sci.Tech.* , 251 (1973)

[13] P.L.Kapitza, *Proc.Roy.Soc.* **A 123**, 292 (1929)

[14] S.S.P.Parkin *et al* (Digest of 13th International Colloquium on Magnetic Films and Surfaces, 1991)

[15] S.S.P.Parkin *et al*, *Phys.Rev.Lett.* **66**, 2152 (1991)

[16] S.S.P.Parkin *et al*, *Phys.Rev.Lett.* **64**, 2304 (1990)

[17] S.S.P.Parkin, *Phys.Rev.Lett.* **67**, 3598 (1991)

[18] D.H.Mosca *et al*, *J.M.M.M.* **94**, L1 (1991)

[19] A.Cebollada *et al*, *Phys.Rev.B* **39**, 9726 (1989)

[20] E.Fullerton *et al*, *Phys.Rev.Lett.* **68**, 859 (1992)

[21] A.Chaiken *et al*, *J.Appl.Phys.* **70**, 5864 (1991)

[22] B.Dieny *et al*, *J.Appl.Phys.* **69**, 4724 (1991)

[23] Y.Wang *et al*, *Phys.Rev.Lett.* **21**, 2732 (1990)

[24] D.M.Deaven and D.S.Rokshar, *Phys.Rev.B* **44**, 5977 (1991)

[25] R.E.Camley and J.Barnas, *Phys.Rev.Lett.* **63**, 664 (1989)

[26] P.Levy *et al*, *Phys.Rev.Lett.* **65**, 1643 (1990)

[27] B.A.Jones and C.B.Hanna (preprint)

[28] W.F.Egelhoff *et al*, *Phys.Rev.B* **45**, 7795 (1992)

[29] F.C.Nortemann *et al* (preprint)

[30] M.T.Johnson *et al*, *Phys.Rev.Lett.* **68**, 2688 (1992)

[31] D.M.Edwards *et al* (preprint)

[32] S.Araki *et al*, *J.Phys.Soc.Jap.* **60**, 2827 (1991)

[33] Y.Saito *et al*, *Appl.Phys.Lett.* **60**, 2436 (1992)

[34] S.S.P.Parkin *et al*, *Appl.Phys.Lett.* **58**, 2710 (1991)

[35] M.E.Tomlinson *et al* (Proceedings of CMMP,1991)

[36] R.A.Hajjar *et al*, *J.Appl.Phys.* **69**, 4686 (1991)

[37] E.Tatsumoto *et al*, *J.Phys.Soc.Jap.* **15**, 1703 (1960)

[38] M.Goto *et al*, *J.M.M.M.* **104-107**, 1789 (1992)

[39] F.Giron *et al*, *J.M.M.M.* , 101 (1991)

[40] B.Dieny *et al*, *Phys.Rev.B* **43**, 1297 (1991)

[41] B.Dieny *et al*, *J.M.M.M.* **93**, 101 (1991)

[42] V.S.Speriosu *et al*, *Phys.Rev.B* **44**, 5358 (1991)

[43] R.V.Coleman *et al*, *Phys.Rev.B* **8**, 317 (1973)

[44] G.R.Taylor, *Phys.Rev.* **165**, 621 (1968)

[45] G.G.Cabrera and L.M.Falicor, *phys.sta.sol.(b)* **61**, 539 (1974)

[46] T.R.McGuire and R.I.Potter, *I.E.E.E.Trans.Mag.* **11**, 1018 (1975)

[47] A.Fert *et al*, *J.M.M.M.* **104**, 1712 (1991)

[48] G.Suran (Private communication)

[49] K.O'Grady (Private communication)

[50] R.J.Hicken and G.T.Rado, *J.M.M.M.* **104-107**, 1743 (1992)

[51] M.N.Baibich *et al*, *Phys.Rev.Lett.* **61**, 2472 (1988)

[52] A.E.Berkowitz *et al*, *Phys.Rev.Lett.* **68**, 3745 (1992)

[53] J.Q.Xiao *et al*, *Phys.Rev.Lett.* **68**, 3749 (1992)

[54] M.J.Carey *et al*, *Appl.Phys.Lett.* **61**, 2935 (1992)

[55] S.S.P.Parkin *et al*, *Appl.Phys.Lett.* **64**, 2710 (1991)

[56] S.H.Liou *et al*, *J.Appl.Phys.* **70**, 5882 (1991)

[57] G.T.Rado and H.Suhl *Magnetism Vol.3* (Academic Press, 1963)

[58] Tsoukatos *etal*, *Appl.Phys.Lett.* **61**, 3059 (1992)

[59] B.Dieny *et al*, *Phys.Rev.B.* **43**, 1297 (1991)

[60] E.Kneller, *J.Appl.Phys.* **33S**, 1355 (1962)

[61] S.Zhang, *Appl.Phys.Lett.* **61**, 1855 (1992)

[62] M.Hansen *Consitution of Binary Alloys* (McGraw-Hill, 1958)

[63] K.O'Grady *et al*, *IEEE Trans.Magn.* **27**, 5061 (1991)

[64] B.Dieny *et al* (Conference on Novel Magnetic Properties in Thin Films, Kyoto, 1993)

[65] J.A.Barnard *et al*, *J.M.M.M.* **114**, L230 (1992)

[66] W.P.Pratt *et al*, *Phys.Rev.Lett.* **66**, 3060 (1991)

[67] E.F.Kneller and F.E.Luborsky, *J.Appl.Phys.* **34**, 656 (1963)

[68] E.P.Wolfarth *Ferromagnetic materials* (North-Holland, 1980)

[69] J.Kwo *et al*, *Phys.Rev.Lett.* **55**, 1402 (1985)

[70] Bartholin *et al*, *J.Appl.Phys.* **42**, 1679 (1971)

[71] C.F.Majkrzak et al, *Adv.in Phys.* **40**, 99 (1991)

[72] M.B.Salamon *et al*, *Phys.Rev.Lett.* **56**, 259 (1986)

[73] R.W.Erwin *et al*, *Phys.Rev.B* **35**, 6808 (1987)

[74] J.J.Rhyne *et al*, *J.Appl.Phys.* **61**, 4043 (1987)

[75] M.Hong *et al*, *J.Appl.Phys.* **61**, 4054 (1987)

[76] R.P.Gupta and A.J.Freeman, *Phys.Rev.B* **13**, 4376 (1976)

[77] N.Wakabayashi and R.M.Nicklow, *Phys.Rev.B* **10**, 2049 (1974)

[78] B.G.Orr et al, *Europhys.Lett.* **19**, 33 (1992)

[79] V.F.Sears, *Methods of Experimental Physics* **23**, 521 (Part A)

[80] J.Bohr *et al*, *Physica B* **159**, 93 (1989)

[81] R.J.Pollina and B.Luthi, *Phys.Rev.* **177**, 1394 (1969)

[82] J.F.Gregg *et al*, *J.de Phys.* **C8 49**, 2027 (1988)

[83] C.H.A.Huan *Thesis* (Oxford, 1987)

[84] J.S.Lord *Thesis* (Oxford, 1990)

[85] I.D.Morris *Thesis* (Oxford, 1989)

[86] D.P.Landau and B.E.Keen, *Phys.Rev.B* **19**, 4805 (1979)

[87] N.Giordano and W.P.Wolf, *Phys.Rev.* **21**, 2008 (1980)

[88] W.P.Wolf and C.H.A.Huan, *Phys.Rev.B* **37**, 2033 (1988)

[89] S.J.Dawson *et al*, *J.M.M.M.* **90**, 184 (1990)

[90] W.Kob (private communication)

[91] W.A.Johnson and R.F.Mehl, *Trans.Am.Inst.Min.Eng.* **135**, (1939)

[92] M.Avrami, *J.Chem.Phys.* **7**, 1103 (1930)

[93] A.E.Kolmogorov, *Akad.Nauk.S.S.R.IZVSer.Mat.* **1**, 355 (1937)

[94] K.Binder and H.Muller-Krumbhaar, *Phys.Rev.B* **9**, 2328 (1974—)

[95] S.J.Dawson *et al*, *J.M.M.M.* **104**, 373 (1992)

[96] J.F.Dillon *et al*, *Phys.Rev.Lett.* **33**, 98 (1974)

[97] Griffiths *et al*, *Phys.Rev.Lett.* **24**, 715 (1970)

[98] L.Landau, *Phys.Z.Sowj.Un.* **4**, 675 (1933)

[99] L.Neel, *C.r.hebd.Séanc.Acad.Sci.Paris.* **242**, 1549 (1956)

[100] A.F.G.Wyatt, *J.Phys.C* **1**, 684 (1968)

[101] N.Giordano and W.P.Wolf, *Phys.Rev.Lett.* **35**, 799 (1975)

[102] N.Giordano, *Phys.Rev.B* **14**, 2927 (1976)

[103] N.Giordano and W.P.Wolf, *AIP Conf.Proc.* **29**, 459 (1976)

[104] N.Giordano and W.P.Wolf, *Physica,'s Grav B* **86**, 593 (1977)

[105] J.E.Battison *et al*, *Sol.Stat.Comm.* **17**, 1363 (1975)

[106] C.S.Koonce *et al*, *Phys.Rev.B* **4**, 4054 (1971)

[107] J.C.Wright *et al*, *Phys.Rev.B* **3**, 843 (1971)

[108] W.P.Wolf and C.H.A.Huan, *J.Appl.Phys.* **63**, 3904 (1988)

[109] C.J.Ellis *et al*, *J.Phys.C* **4**, 2937 (1971)

[110] M.Regis *et al*, *Physica B* **86-88**, 599 (1977)

[111] M.J.Metcalfe and H.M.Rosenberg, *J.Phys.C* **5**, 450 (1972)

[112] N.Schubiya *et al*, *Sol.Stat.Comm.* **17**, 1305 (1975)

[113] A.H.Millhouse, *J.Appl.Phys.* **50**, 2011 (1979)

[114] J.Hoffmann, *Phys.Stat.Sol.B* **165**, 517 (1991)

[115] I.R.Jahn *et al*, *Sol.Stat.Comm.* **28**, 421 (1978)

[116] A.H.Millhouse *et al*, *J.M.M.M.* **15-18**, 1513 (1980)